The Muon Puzzle and the Neutron Component in Extensive Air Showers

For the attainment of the academic degree of

Doctorate in Science

from the KIT-Fakultät für Physik of the
Karlsruhe Institute of Technology (KIT)
and the Instituto de Tecnología "Prof. Jorge A. Sábato" of the
Universidad Nacional de San Martín (UNSAM)

accepted

Dissertation

of

M. Sc. Tobias Schulz

from Karlsruhe

Day of the oral examination: 06. 12. 2024
Referee: Prof. Dr. Ralph Engel
Co-referee: Prof. Dr. Federico Andres Sanchez
First Supervisor: Dr. David Schmidt
Second Supervisor: Dr. Darko Veberič
Third Supervisor: Dr. Markus Roth

The Muon Puzzle and the Neutron Component in Extensive Air Showers

Zur Erlangung des akademischen Grades eines

Doktors der Naturwissenschaften (Dr. rer. nat.)

von der KIT-Fakultät für Physik des
Karlsruher Instituts für Technologie (KIT)
und des Instituto de Tecnología "Prof. Jorge A. Sábato" der
Universidad Nacional de San Martín (UNSAM)

genehmigte

Dissertation

von

M. Sc. Tobias Schulz

aus Karlsruhe

Tag der mündlichen Prüfung: 06. 12. 2024
Referent: Prof. Dr. Ralph Engel
Korreferent: Prof. Dr. Federico Andres Sanchez
1. Betreuer: Dr. David Schmidt
2. Betreuer: Dr. Darko Veberič
3. Betreuer: Dr. Markus Roth

The Muon Puzzle and the Neutron Component in Extensive Air Showers

Tesis presentada para optar por el título de

Doctor en Astrofísica

de la KIT-Fakultät für Physik del
Karlsruhe Institute of Technology (KIT)
y del Instituto de Tecnología "Prof. Jorge A. Sábato" de la
Universidad Nacional de San Martín (UNSAM)

por

M. Sc. Tobias Schulz

de Karlsruhe

Fecha de la defensa oral: 06. 12. 2024
Director: Prof. Dr. Ralph Engel
Co-director: Prof. Dr. Federico Andres Sanchez
Primer Colaborador: Dr. David Schmidt
Segundo Colaborador: Dr. Darko Veberič
Tercer Colaborador: Dr. Markus Roth

No man is an island,
Entire of itself.
Each is a piece of the continent,
A part of the main.
If a clod be washed away by the sea,
Europe is the less.
As well as if a promontory were.
As well as if a manner of thine own
Or of thine friend's were.
Each man's death diminishes me,
For I am involved in mankind.
Therefore, send not to know
For whom the bell tolls,
It tolls for thee.

- *John Donne*

The content of this thesis reflects my own work. However, the AI assistive tools *ChatGPT*, *Grammarly*, and *DeepL Write* were used to improve the text flow and grammar of parts of the text of the thesis.

Abstract

The Pierre Auger Observatory is the largest cosmic ray observatory in the world and has made a significant contribution to our understanding of ultra-high-energy cosmic rays during its 20 years of operation. Although the existence of these ultra-high energy cosmic rays is known already for more than half a century, many questions, including their origin, remain unanswered. Additionally, they enable the study of hadronic interactions at energies far beyond those achievable with human-made accelerators through the measurement of the air showers they produce upon interacting with the Earth's atmosphere. A significant discrepancy exists between observational data and simulations, with the measured abundance of muons exceeding predictions from current interaction models. This work aims to study this discrepancy using measurements and simulations of the surface detector of the Pierre Auger Observatory. Two sources for the discrepancy between measured and simulated signals that are not specific to the muon content itself are explored: one related to the calibration and processing of measurements with respect to the reconstruction of signals from time traces. An algorithm to determine the baselines of traces is developed based on a realistic model of the response of the photomultipliers and the electronics of the surface detectors. Furthermore, the estimation of the ratio in the gain of two readout channels for the photomultiplier signals is identified to contribute to a bias in the surface detector signals. With a better understanding of the signals measured by the detectors, the origins of specific features in time traces are examined, and their impact on the muon deficit is determined. The second source of the discrepancy between measured and simulated signals is the possible contribution of neutrons to the signal in the water-Cherenkov detectors. The neutron component is first characterized from the measurements of late pulses in the time traces of the new surface-scintillator detectors. The arrival-time distribution, pulse spectrum, and other characteristics of these late pulses are studied. Furthermore, the measured signal spectrum of late pulses is compared with dedicated air shower simulations including neutrons over the complete range of energies to validate the plausibility of the latter. Finally, the measurements of late pulses are used to provide an upper estimate of the possible contribution of neutrons to the total signal in the water-Cherenkov detectors and to determine if neutrons could account for a meaningful fraction of the discrepancy between measured and predicted signals that has thus far largely been attributed to a lack of muons in the latter.

Zusammenfassung

Das Pierre-Auger-Observatorium ist das größte Observatorium für kosmische Strahlung der Welt und hat in seinen 20 Jahren Betrieb erheblich zu unserem Verständnis von kosmischen Strahlen mit ultra-hoher Energie beigetragen. Obwohl die Existenz dieser kosmischen Strahlen mit ultra-hoher Energie seit mehr als einem halben Jahrhundert bekannt ist, bleiben viele Fragen, einschließlich ihrer Herkunft, weiterhin unbeantwortet. Darüber hinaus ermöglichen sie das Studium von hadronischen Wechselwirkungen bei Energien, die weit über die mit menschengemachten Beschleunigern erreichbaren Energien hinausgehen. Dabei werden Luftschauer gemessen, die die kosmische Strahlung bei der Wechselwirkung mit der Erdatmosphäre erzeugt. Es gibt eine signifikante Diskrepanz zwischen den beobachteten Daten und den Simulationen, wobei die gemessene Häufigkeit von Myonen die Vorhersagen der aktuellen Wechselwirkungsmodelle übertrifft. Diese Arbeit hat das Ziel, diese Diskrepanz mithilfe von Messungen und Simulationen des Oberflächendetektors des Pierre-Auger-Observatoriums zu untersuchen. Zwei Quellen für die Diskrepanz zwischen gemessenen und simulierten Signalen, die nicht spezifisch auf den Myon-Gehalt selbst zurückzuführen sind, werden untersucht: eine im Zusammenhang mit der Kalibrierung und Verarbeitung der Messungen in Bezug auf die Rekonstruktion von Signalen aus Zeitverläufen. Ein Algorithmus zur Bestimmung des Untergrundsignals wird entwickelt, der auf einem realistischen Modell der Reaktion der Photomultiplier und der Elektronik der Oberflächendetektoren basiert. Darüber hinaus wird festgestellt, dass die Schätzung des Verhältnisses der Verstärkung von zwei Auslesekanälen für die Photomultipliersignale zu einer Verzerrung der Oberflächendetektorsignale beiträgt. Mit einem besseren Verständnis der Signale werden bestimmte Pulssignale vom Nachpulsen der Photomultiplier in den Zeitverläufen der Wasser-Cherenkov-Detektoren untersucht und deren Einfluss auf das Myon-Defizit ermittelt. Die zweite Quelle der Diskrepanz zwischen gemessenen und simulierten Signalen ist der mögliche Beitrag von Neutronen zum Signal in den Wasser-Cherenkov-Detektoren. Die Neutronenkomponente wird zunächst anhand der Messungen von späten Pulsen in den Zeitverläufen der neuen Oberflächen-Szintillatordetektoren charakterisiert. Die Ankunftszeitverteilung, das Pulsspektrum und andere Eigenschaften dieser späten Pulse werden untersucht. Zudem wird das gemessene Spektrum der späten Pulse mit speziellen Luftschauersimulationen, die Neutronen über den gesamten Energiebereich einschließen, verglichen, um deren Plausibilität zu überprüfen. Schließlich werden die Messungen der späten Pulse verwendet, um eine obere Schätzung des möglichen Beitrags von Neutronen zum Gesamtsignal in den Wasser-Cherenkov-Detektoren zu liefern und festzustellen, ob Neutronen einen bedeutenden Teil der Diskrepanz zwischen gemessenen und vorhergesagten Signalen ausmachen könnten, die bisher weitgehend einem Mangel an Myonen in letzteren zugeschrieben wurde.

Resumen

El Observatorio Pierre Auger es el observatorio de rayos cósmicos más grande del mundo y, durante sus 20 años de operación, ha contribuido significativamente a nuestro entendimiento de los rayos cósmicos de ultra-alta energía. Aunque la existencia de estos rayos cósmicos de ultra-alta energía ya se conoce desde hace más de medio siglo, muchas preguntas, incluida su origen, siguen sin respuesta. Además, los rayos cósmicos permiten el estudio de las interacciones hadrónicas a energías muy superiores a las alcanzables con aceleradores creados por el hombre, mediante la medición de las cascadas atmosféricas que producen al interactuar con la atmósfera terrestre. Existe una discrepancia significativa entre los datos observados y las simulaciones, donde la abundancia medida de muones supera las predicciones de los modelos de interacción actuales. Este trabajo tiene como objetivo estudiar esta discrepancia mediante el uso de mediciones y simulaciones del detector de superficie del Observatorio Pierre Auger. Se exploran dos fuentes para la discrepancia entre las señales medidas y simuladas que no están específicamente relacionadas con el contenido de muones: una relacionada con la calibración y el procesamiento de las mediciones en cuanto a la reconstrucción de señales a partir de trazas temporales. Para evaluar la primera posibilidad, se desarrolla un algoritmo para determinar las líneas base de las trazas, basado en un modelo realista de la respuesta de los fotomultiplicadores y la electrónica de los detectores de superficie. Además, se identifica que la estimación de la relación entre el canal de baja y alta ganancia de las señales de los fotomultiplicadores contribuye a una distorsión en las señales del detector de superficie. Con una mejor comprensión de las señales medidas por los detectores, se examinan los orígenes de características específicas en las trazas temporales y se determina su impacto en el déficit de muones. Para investigar la segunda hipótesis, la componente de neutrones se caracteriza primero a partir de las mediciones de pulsos tardíos en las trazas de tiempo de los nuevos detectores de superficie con centelleador. Se estudian la distribución de tiempos de llegada, el espectro de pulsos y otras características de estos pulsos tardíos. Además, el espectro de señal medido de los pulsos tardíos se compara con simulaciones específicas de cascadas atmosféricas que incluyen neutrones en todo el rango de energías, para validar su plausibilidad. Finalmente, se utilizan las mediciones de los pulsos tardíos para proporcionar una estimación superior de la posible contribución de los neutrones a la señal total en los detectores Cherenkov de agua y para determinar si los neutrones podrían representar una fracción significativa de la discrepancia entre las señales medidas y las previstas, que hasta ahora se ha atribuido en gran medida a una falta de muones en estas últimas.

Contents

Chapter I

Introduction

In the early 20th century, scientists increasingly studied various physical phenomena related to radiation. In 1912, building on the work of Domenico Pacini, who demonstrated that radiation intensity decreases underwater, Victor Hess conducted a series of balloon experiments that revealed that radiation intensifies with altitude [1, 2]. Hess hypothesized that particles from extraterrestrial sources were entering the atmosphere and ionizing its molecules. This discovery of cosmic rays earned him the Nobel Prize in Physics in 1936.
Numerous new experiments were conducted to study the properties and origin of these cosmic rays. In 1939, Pierre Auger became the first to measure the lateral distributions of extensive air showers, which are cascades of particles initiated by the interaction of a primary cosmic ray with Earth's atmosphere [3]. Theoretical models of these showers are typically calibrated using data from particle accelerators, such as the Large Hadron Collider, which operates at maximum center-of-mass energies of approximately $\sqrt{s} = 14\,\text{TeV}$ for proton-proton collisions. However, cosmic rays with energies as high as 10^{20} eV have been observed, offering a unique opportunity to probe hadronic interaction models at energy scales far beyond those achievable by modern accelerators [4, 5, 6, 7]. Despite this potential, several experiments have reported a significant discrepancy between simulations and measurements, namely an apparent deficit of muons in simulations [8]. Although numerous studies have advanced the understanding of this "muon puzzle", it remains an open question [9, 10, 11, 12, 13, 14, 15].
The Pierre Auger Observatory is the world's largest facility for measuring extensive air showers [16]. Its hybrid design enables the simultaneous measurement of the longitudinal development of the showers in the atmosphere and the lateral distribution of particles that reach the ground. In an upgrade of the Pierre Auger Observatory, new surface-scintillator detectors were installed on top of the existing water-Cherenkov detectors. These detectors have different sensitivities to various particle types, which aids in disentangling the signals from different shower components. This enhanced capability offers the potential to investigate the muon puzzle further. In 1984, John Linsley reported the detection of pulses, delayed by several microseconds after the main signal, in the scintillator time traces of the Volcano Ranch experiment. He assumed that these so-called sub-

luminal pulses could correspond to neutrons traveling at speeds slightly below the speed of light, an idea previously suggested by Kenneth Greisen[17]. Air shower simulations typically do not fully model the neutron spectrum, primarily due to their long time delays and broad energy range. However, neutrons can generate large, non-negligible pulses in scintillators, making their contribution significant in some instances.
This work aims to describe the apparent muon deficit between the measurements of the Pierre Auger Observatory and simulations using only measurements of water-Cherenkov detectors and to explore if neutrons could contribute to the differences between simulations and measurements. In Chapter 2, a general overview of cosmic rays and the physics of extensive air showers is given, and the detection methods of the Pierre Auger Observatory are presented. Chapter 3 centers around a new method to determine the apparent muon deficit and the improvement of the signal reconstruction of the measured data of the Pierre Auger Observatory used in this thesis. The correct estimation of the signal in the surface detectors is of great importance if one wants to determine the differences between measured and simulated signals for estimating the muon deficit. Therefore, in Section 3.1 and Section 3.2, the baseline algorithm for the time traces of the surface detectors is visited and reworked to be based on a realistic description of the behavior of the photomultipliers and the electronics. In addition to correctly estimating the baseline, determining the gain ratio of the photomultipliers is equally crucial for the signal calculation. In Section 3.3, biases in the gain ratio are determined and corrected for. With sources of error in the reconstruction process of signals being resolved, features in the time traces of the water-Cherenkov detectors themselves are analyzed in Section 3.4 and determined to originate from afterpulsing. Furthermore, the contribution of these afterpulses towards the total signal is determined. Next, in Section 3.5, the improved measurements are used to implement an alternative estimation method of the apparent muon deficit, using only the water-Cherenkov detector data. In Chapter 4, the contribution of the signal generated by neutrons in the water-Cherenkov detectors towards the apparent muon deficit shall be explored. First, measurements of subluminal pulses in the surface-scintillator detectors are investigated and characterized in Section 4.1 to determine if these delayed pulses could originate from a late hadronic component. For this, the population of late pulses in the traces is characterized based on their rate, time distribution, and pulse spectrum in relation to the primary energy, shower zenith angle, and distance to the shower axis. In Section 4.2, the simulation framework is adjusted to include hadronic interactions and quenching for the proper accounting of neutrons in the surface detector simulations of the Pierre Auger Observatory. The measurement of the late neutron component is then further analyzed in Section 4.3 by looking at the lateral distribution of late pulses and the pulse spectrum. Additional simulations of neutrons are performed to study the scintillator response to neutrons, its detection efficiency, and the impact of quenching. These results are then used to forward-fold a neutron energy spectrum from simulations and compare the resulting pulse spectrum to the measurements. Finally, in Section 4.4, the combined results from the simulations and measurements are used to estimate the contribution of the

signal generated by neutrons to the total signal in the water-Cherenkov detectors and if this signal could contribute to explaining the apparent muon deficit.

Chapter II

Ultra-High-Energy Cosmic Ray Physics

Cosmic rays (CR) are relativistic, charged particles of extraterrestrial origin. They can reach energies beyond 10^{20} eV, thus being the most energetic particles known to date. Cosmic rays with energies above 10^{18} eV are also referred to as *ultra-high-energy cosmic rays* (UHECR). At these energies, the rate of these cosmic rays is as low as 1 particle per square kilometer per year. While various, strong candidates exist for galactic sources of low-energy cosmic rays, the origin of UHECRs remains unclear.

A brief introduction about cosmic rays, their properties and their detection is given in Section 2.1. In Section 2.2 is an overview of the Pierre Auger Observatory, whose measurements are used in this thesis.

2.1. Cosmic rays

2.1.1. The Flux of Cosmic Rays

The energy spectrum of cosmic rays spans a wide range from 10^{10} eV up to more than 10^{20} eV [18]. As the energy of CRs increases, the flux decreases, and at the highest energies, fewer than one particle per square kilometer per century can be detected. The differential flux approximately follows a broken power-law, with varying values of the spectral index γ to reflect changes in the steepness of the spectrum

$$\frac{\mathrm{d}N}{\mathrm{d}E\,\mathrm{d}A\,\mathrm{d}t\,\mathrm{d}\Omega} \propto E^{-\gamma}. \tag{2.1}$$

Here, $\frac{\mathrm{d}N}{\mathrm{d}E\,\mathrm{d}A\,\mathrm{d}t\,\mathrm{d}\Omega}$ represents the differential flux, i.e. the number of CRs detected per unit energy E, area A, time t, and solid angle Ω of the cosmic rays. Several prominent features within the CR spectrum provide insights into the nature and distribution of their sources. Fig. 2.1 shows the flux, which is scaled by E^2 to highlight these features better.

One distinct feature of the spectrum is the steepening of the flux at energies around 3×10^{15} eV, known as the *knee*. At this point the spectral index γ changes from ≈ 2.7 to ≈ 3.1. The *Karlsruhe Shower Core and Array Detector* (KASCADE)

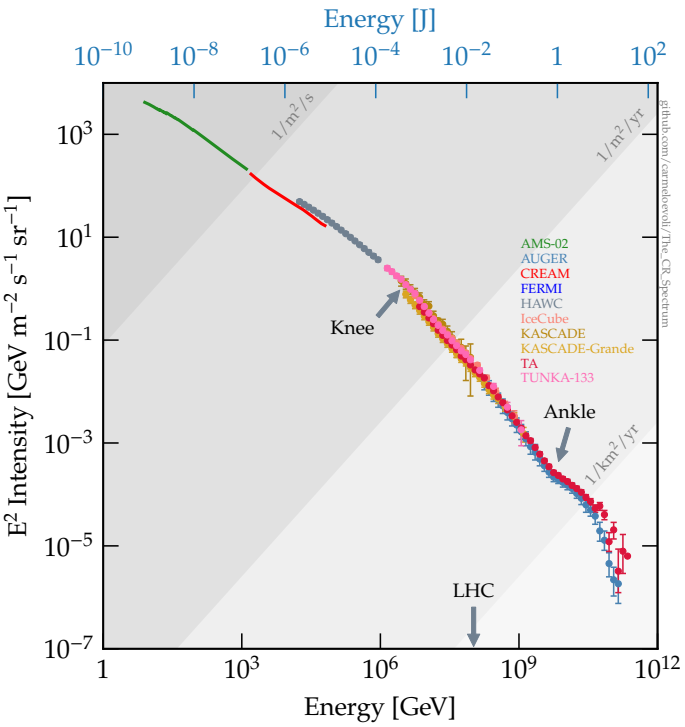

Figure 2.1: The energy spectrum of cosmic rays, as measured with different experiments. Figure taken from Ref. [19].

experiment measured a transition from lighter to heavier elements in this energy region [20]. This observation is compatible with the assumption of galactic *supernova remnants* (SNR) reaching the maximum energy to which they can accelerate light nuclei, such as protons. A less pronounced feature, the *second knee*, is observed for heavier particles like iron nuclei and is also attributed to the maximum acceleration energy of SNRs [21]. The knee and second knee are important for understanding the acceleration limits of various cosmic ray sources and the transition to other potential sources.

The next distinct feature of the spectrum is the *ankle*, found around an energy of 5×10^{18} eV, where the hardening of the flux is observed. A possible explanation for the ankle is the transition from galactic to extragalactic cosmic ray accelerators. The absence of a directional origin in the galactic plane for cosmic rays at this energy further supports the shift to extragalactic sources. The ankle region is particularly interesting for studying the origins and propagation of ultra-high-energy cosmic rays, as it could mark the transition between different cosmic ray populations. A recently discovered feature is the so-called "instep" at around 10^{19} eV, which could be the result of combined fluxes of light to intermediate nuclei [7].

The third prominent feature of the spectrum is at energies above 5×10^{19} eV, where a strong suppression of the energy spectrum is observed. This suppression could be caused either by the cosmic ray sources reaching their acceleration limit or propagation effects such as the photodisintegration or the theoretically predicted *Greisen-Zatsepin-Kuzmin* (GZK) cut-off [22, 23]. The GZK cut-off describes

the interaction of ultra-high-energy cosmic rays with the CMB photons, leading to energy loss through pion production via the Δ-resonance

$$p + \gamma_{CMB} \rightarrow \Delta^+ \rightarrow p + \pi^0, \tag{2.2}$$

$$p + \gamma_{CMB} \rightarrow n + \pi^+. \tag{2.3}$$

This amounts to an average energy loss of about 20%, and the maximum distance a proton can traverse with an energy above 10^{20} eV is estimated to be around 100 Mpc. Consequently, cosmic rays with energies above the GZK cut-off cannot travel large distances without significant energy loss. For heavier nuclei, such as iron, photodisintegration via the giant dipole resonance would lead to a similar energy loss length as for protons [24]. The detection of particles above 10^{20} eV implies the possible existence of particles with even higher energies or a propagation distance smaller than the GZK limit [25]. However, it remains unclear whether the observed suppression is due to the GZK cut-off or the maximum acceleration limit of cosmic ray sources [26].

2.1.2. Sources and Propagation

Mechanisms for the acceleration of particles to such high energies were described by Enrico Fermi in 1949 [27]. He proposed that charged particles gain energy through elastic scattering off magnetic irregularities in moving, magnetized "clouds". This process effectively leads to an energy gain proportional to the square of the velocity of the cloud [28]. Due to the small energy gain per scattering event, it was further suggested that particles could be accelerated in the shock fronts of supernovae, resulting in an energy gain that scales linearly with the shock wave velocity [29, 30, 31]. Considering the escape probability of particles from these systems, the resulting energy spectrum matches a power-law with a spectral index of $\gamma \approx 2.2$, which is almost compatible with the observation of $\gamma \approx 2 - 2.7$ [32].

For the sources themselves, the Hillas confinement condition provides an estimate of the maximal acceleration energy [33] given by

$$E_{max} \sim \beta Z B R. \tag{2.4}$$

Thus, the maximal acceleration energy of a particle is primarily proportional to the size, or radius, R of the acceleration region, its magnetic field B as well as to the charge Z, and velocity β of the acceleration region. A collection of potential sources, along with their size and magnetic field strength, is shown in Fig. 2.2.

2.1.3. Extensive Air Showers

When entering Earth's atmosphere, the cosmic rays interact with the nuclei in the air, initiating a shower of further particles that lead to subsequent interactions. The development of an *extensive air shower* (EAS) can be divided into two components (see Fig. 2.3), as described by the shower model proposed by Heitler and Matthews [35, 36]. Detecting these air showers can be achieved by either directly measuring energy deposits of particles on the ground with surface detectors or through measuring the yield of the emission of fluorescence light of

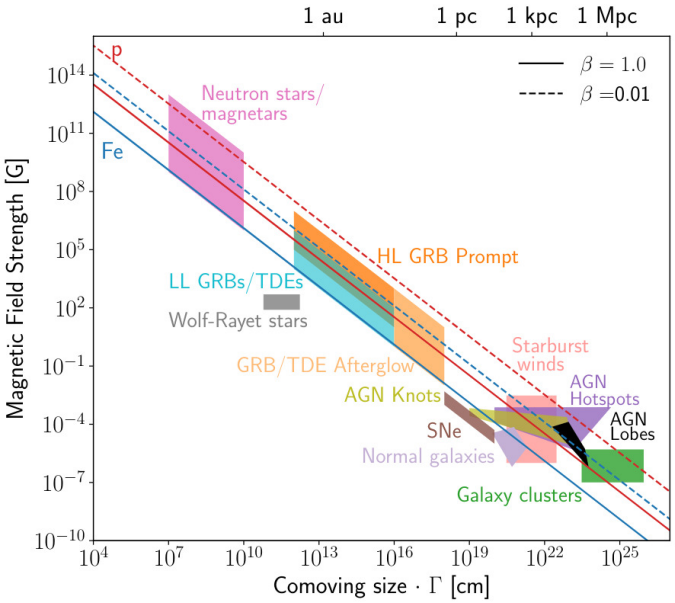

Figure 2.2: The Hillas plot describes the size and magnetic field strength of potential UHECR sources. Figure taken from Ref. [34].

excited nitrogen particles due to the shower passing through the atmosphere. The longitudinal evolution of the shower in the atmosphere can be described by the atmospheric depth X

$$X = \int_h^\infty \rho(h)\,\mathrm{d}h, \tag{2.5}$$

where $\rho(h)$ is the density of air in the atmosphere relative to the height h above sea level. The central region, or the core of the shower, consists mainly of either neutral or charged pions as well as kaons, neutrons and a few heavier nuclei, which are created in the early stages of the shower development. These particles originate from high-energy hadronic interactions, feeding the other components of the shower. Neutral pions decay with a high probability into two photons, which then initiate an electromagnetic cascade through the pair-production of electron-positron pairs if their energy is sufficient. Electrons and positrons can then produce photons through bremsstrahlung, which can then again go on to the production of more electron-positron pairs. The electromagnetic component contributes to the majority of the secondary particles observed in an EAS with an estimated contribution of approximately 98%. With each of the processes mentioned above, two new particles are created, leading to a total of

$$N = 2^n \tag{2.6}$$

particles after n steps. Once the individual energy of the particles drops below the critical energy of $E_c = 85\,\mathrm{MeV}$ no further particles are produced, and the shower starts to get absorbed in the atmosphere. The maximum number of particles is, therefore, directly proportional to the energy E_0 of the primary particle

$$N_{\max} \propto E_0. \tag{2.7}$$

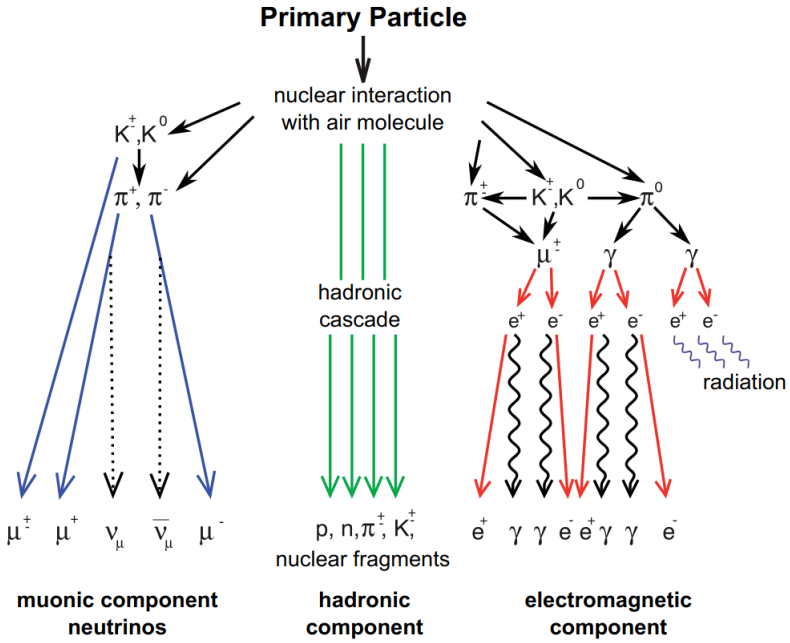

Figure 2.3: Depiction of an extensive air shower. Figure taken from Ref. [37].

The maximum number is reached at the depth $X_{\max}$ in the atmosphere, which corresponds to

$$X_{\max} \propto \ln E_0. \tag{2.8}$$

The charged pions, on the other hand, have a longer lifetime than the neutral pions and can undergo multiple interactions before their energy drops below the limit at which their decay into muons and neutrinos becomes more probable than further interactions. The muonic component of the hadronic component is created through the decay of charged pions and kaons, with the latter accounting for less than 2% of the air shower. The majority of these secondary particles reach the ground without further interaction. For the hadronic cascade, N_{tot} new particles are created at each interaction step, with a ratio of 2:1 of charged to neutral pions. Therefore, after n interactions, this will yield a total number of charged pions

$$N_\pi = \left(\frac{2}{3N_{\text{tot}}}\right)^n. \tag{2.9}$$

The critical energy E_c when the further production of pions ceases depends on E_0, as well as N_{tot}. For a shower with a primary energy of about 10^{17} eV, the critical energy is ≈ 10 GeV and further decreases with increasing primary energy. Assuming that all charged pions will decay into muons, the number of muons in the shower is

$$N_\mu = N_\pi \propto \left(\frac{E_0}{E_c}\right)^\beta, \tag{2.10}$$

where β depends on the multiplicity of pions [36].

2.1.4. Neutrons in Extensive Air Showers

Neutrons are the only relevant neutral particles of the hadronic component that remain stable over the timescales of air showers. They only lose their energy through hadronic interactions and quasielastic scattering processes and can reach the ground with delays of up to several seconds. Neutron measurements in air showers date back to the 1940s [38]. In 1984, Linsley reported the detection of late pulses in the scintillation detectors of the Volcano Ranch experiment [17]. Over the years, various experiments have been conducted to measure neutrons in air showers using dedicated detectors. An overview and discussion of these experiments can be found in Refs. [39, 40, 41]. Recent comparisons in Ref. [42] have shown a comparison between neutron energy spectra, generated using the Fluka simulation framework [43], and neutron measurements performed at the Zugspitze mountain in 1995 [44] and aboard an ER-2 Airplane in 1997 and 1999 [45]. These simulations [42] indicate that neutrons at the highest energies originate from the same hadronic interactions as pions and kaons. At neutron energies below a few GeV, the energy spectrum is mainly shaped by non-elastic neutron-nucleus interactions and neutron-nucleon elastic interactions. Below $\approx 20\,\mathrm{MeV}$ diffusion is used to describe the propagation of neutrons. The number of neutrons increases with the energy of the air shower. As the energy of the shower increases, the maximum of the shower occurs deeper in the atmosphere, which reduces the attenuation of neutrons. As a result, an almost linear scaling of the neutron flux can be expected at atmospheric depths of around $800\,\mathrm{g/cm^2}$.

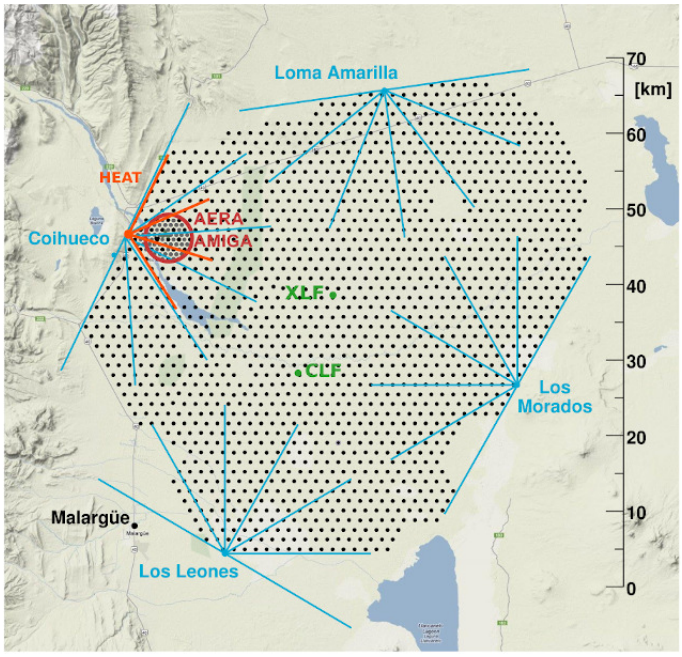

Figure 2.4: Schematic depiction of the detector array of the Pierre Auger Observatory. Each black dot represents one water-Cherenkov detector with a spacing of 1500 m in between. The field of view of the fluorescence telescopes at the 4 locations of the fluorescence detector is marked with blue lines and the view of the HEAT extension at Coihueco is in red. The Central and Extreme Laser Facilities for calibration of the fluorescence detector are marked with green dots.

2.2. The Pierre Auger Observatory

The *Pierre Auger Observatory*, located near Malargüe, Argentina, is the world's largest hybrid detector array. It is designed to study ultra-high-energy cosmic rays [16]. It was named after the French physicist Pierre Auger, who discovered extensive air showers in 1939. The observatory integrates both a *Surface Detector* (SD) [46] and *Fluorescence Detector* (FD) [47] to capture data on cosmic ray-induced air showers. The SD array consists of 1660 *Water-Cherenkov Detectors* (WCDs) to measure particles reaching the ground. They are arranged in a triangular grid, covering 3000 m^2. The FD consists of 24 telescopes positioned at four locations around the SD array. The telescopes measure fluorescent light emitted by air molecules that get excited by the particles of the evolving shower. Together, these two systems provide a comprehensive picture of air shower development, measuring both lateral and longitudinal distributions of particle cascades. In 2008, an additional set of *High Elevation Auger Telescopes* (HEAT) was installed to extend the detector sensitivity to cosmic rays of lower energies. A schematic depiction of the SD array and the locations of the FD sites is given in Fig. 2.4.

Initiated in 2015, the *AugerPrime* upgrade aims to address unresolved questions about cosmic ray composition and the origin of the flux suppression at the highest energies by further expanding the observatory's capabilities [48]. The upgrade involves enhancing existing detectors and deploying new instruments, such as

Surface-Scintillator Detector (SSD) and radio antennas, to provide deeper insights into the properties of cosmic rays.

2.2.1. Surface Detector

The SD array is designed to sample the lateral distributions of EAS as they reach the ground and to estimate the shower size. 1660 WCDs are deployed in a isometric triangular grid with spacing of 1500 m (SD-1500) between each station. The SD-1500 array reaches full efficiency above 3×10^{18} eV [49]. The WCDs are cylindrical tanks with a radius of 1.8 m and filled to a height of 1.2 m with purified water. Hence, the active detector volume is 12 m^3 [48]. A photograph of a station and a schematic can be seen in Fig. 2.5. Inside each WCD, thre 9-inch *photomultiplier tubes* (PMTs) are used to detect the Cherenkov light produced as particles of the EAS travel through the water. Relativistic, charged particles produce Cherenkov radiation when traveling through an electrically polarizable medium, like water. Electrons usually have not enough energy to penetrate more than only the first few centimeters of the water. Muons, on the other hand, have a much larger mass compared to electrons and traverse the complete tank, emitting photons along their whole way. The PMTs are read out at the anode and at the last dynode, which has a net difference to the anode by a factor of 32. The analog pulses are read out in the *Unified Board* (UB), which is placed on top of the WCD and are sampled with two 10-bit *Flash Analog to Digital Converters* (FADC) at a frequency of 40 MHz [48]. The low-gain channel (LG) is connected to the anode and the high-gain channel (HG) to the last dynode and together they cover a wide dynamic range [50]. The output is known as the FADC, or time trace, which is a block of 768 time bins. By integrating over the time trace, a signal can be acquired. This signal is then normalized to the most probable charge of a vertical, through-going muon, also referred to as *vertical equivalent muon* (VEM). For the AugerPrime upgrade, the UB electronics were replaced with the *Upgraded Unified Board* (UUB). Both gains are derived from the anode signal, with the HG amplified by a nominal factor of 32. The signal resolution is increased by a 12-bit FADC and the time resolution is improved to a sampling frequency of 120 MHz [51]. The HG channel may saturate if the shower energy becomes too large or if stations are close to the shower core. If the HG is saturated, the signal is estimated from the LG channel. An additional small PMT was added during the AugerPrime upgrade to extend the dynamic range of the WCD. This enhances the dynamic range from around 600 VEM to more than 30 000 VEM before the PMT and the electronics saturate. The increased dynamic range will allow for a measurement at distances closer to the shower axis for high-energy showers [48]. A GPS antenna allows for communication between the detector and the *central data acquisition center* (CDAS). To extend the possible observation energy downwards, a sub-array called the SD-750 was completed in 2011. It consists of 71 stations, with a spacing of 750 m between each WCD, lowering the energy threshold to 3×10^{17} eV. An additional array with a reduced spacing of 433 m was deployed in 2013 to lower the energy threshold further.

The SSD is mounted on top of the WCD to provide complementary measurements for better discrimination between muonic and electromagnetic signals. It

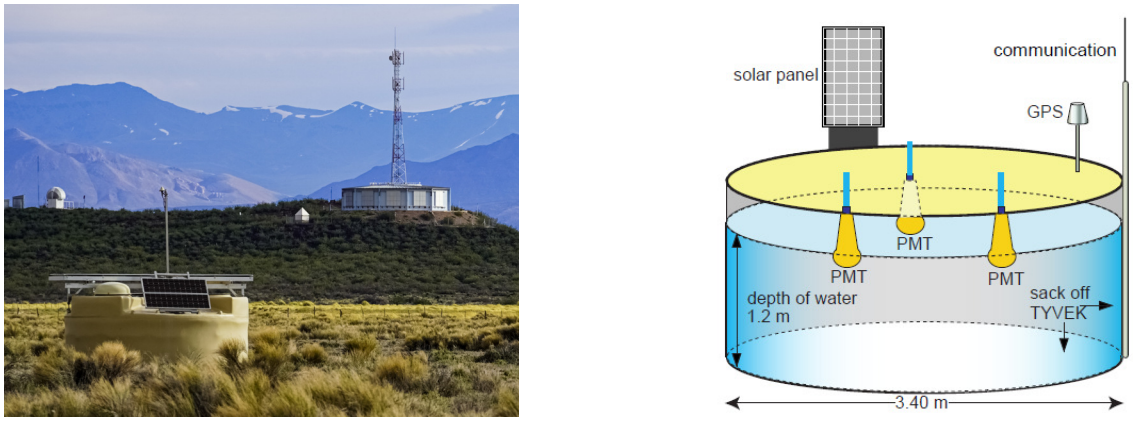

Figure 2.5: *Left:* Picture of a WCD with an SSD on top. The FD can be seen in the background. *Right:* Schematic view of a WCD with its components. The right picture is taken from Ref. [52].

comprises two planes containing a total of 48 plastic scintillator bars, each measuring 1.6 m in length, 5 cm in width, and 1 cm in thickness. These bars are housed within a protective enclosure to shield them from weather and external light. Wavelength-shifting fibers connect the scintillator bars to a PMT [48]. The SSD detects signals from both muons and low-energy electromagnetic particles [53]. It has a higher relative sensitivity to the electromagnetic component than to the muonic component than in the WCD. Electromagnetic particles penetrate only a few centimeters into the WCD, resulting in faint signals, whereas muons traverse the detector completely, producing larger signals. Conversely, most muonic and electromagnetic particles pass entirely through the SSD, generating similar signals. Signals measured by the SSD are calibrated to the charge deposited by a *minimum ionizing particle* (MIP) traveling vertically through the SSD. When particles deposit energy in a scintillator, the light yield is reduced due to an effect known as *quenching*, which is discussed in more detail in Section 4.2.2. Since both detectors sample the same fraction of an air shower, their complementary measurements enhance the accuracy of reconstructing the composition of EAS. The SSD operates in a subordinate mode to the WCD, meaning it is triggered by the WCD. In September 2016, twelve SSD prototypes were deployed as part of the *Engineering Array* (EA) and have been taking data since then [54]. Full-scale deployment of the SSDs began in March 2019 and continued throughout the year. In March 2019, 77 SSDs were deployed using the old UB electronics in the so-called *SSD Pre-Production Array* (PPA). Results of the performance and calibration of the upgraded stations have been discussed in Ref. [55]. The deployment of the SSDs and the UUBs effectively finished in 2023 [56].

2.2.2. Fluorescence Detector

While the SD measures the lateral distribution of a shower, the FD observes the longitudinal development of an EAS. The 24 telescopes are installed in 4 buildings, housing 6 telescopes each. The buildings are located on the perimeter of the SD array. Fig. 2.6-left shows a picture of one of the buildings. With a 30° by

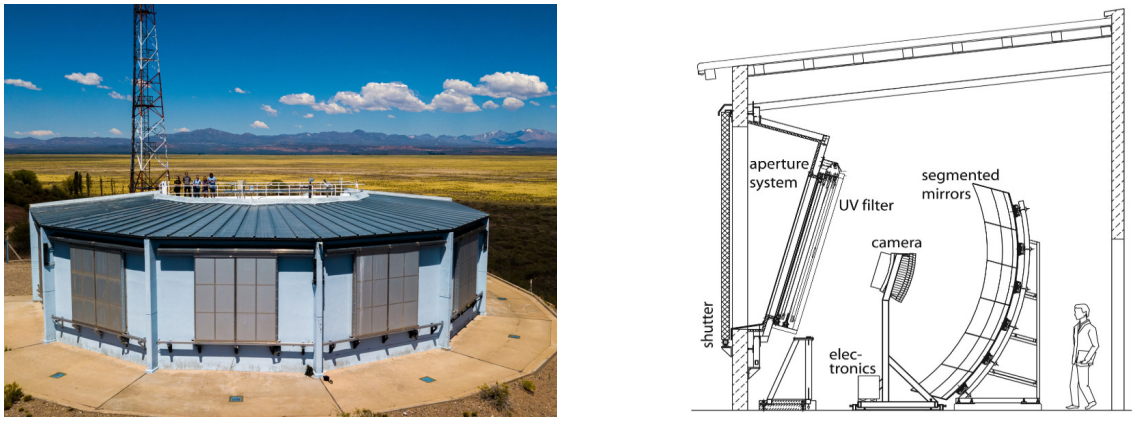

Figure 2.6: *Left:* The FD building houses the telescopes. The shutters are closed during the day to protect the electronics. *Right:* Schematic view of one of the telescopes. The right picture is taken from Ref. [16].

30° *field of view* (FoV) of each telescope, each building can cover a total azimuthal FoV of 180°. At one site, an additional three telescopes, named HEAT, are installed. These telescopes can be tilted upwards to extend the zenith FoV up to 60° for measuring showers from lower energy primaries that develop at a higher altitude [57]. Particles of EAS excite nitrogen molecules in the atmosphere that emit isotropically fluorescence radiation at the range of 300 to 400 nm. The photons from the radiation that enters the telescope bay are reflected by a segmented mirror of 13 m^2 onto a camera, consisting of hexagonal PMTs on a 22×20 grid. A schematic of a telescope is given in Fig. 2.6-right. Since the light intensity of the fluorescence radiation is directly proportional to the number of particles in the shower, the maximum shower depth and the energy of the primary particle can be directly estimated. The high sensitivity of the cameras limits the working time of the FD to clear and moonless nights with appropriate weather conditions. Therefore the duty cycle of the FD amounts to around 15% of the SD measuring time The *Central Laser Facility* (CLF) and the *Extreme Laser Facility* (XLF) are located at the center of the SD array. They are used for the measurement of the atmospheric conditions.

2.2.3. Further Improvements of the AugerPrime Upgrade

In the SD-750 array, the so-called *Underground Muon Detector* (UMD) was deployed. It consists of scintillation detectors buried 2.3 m below the ground at the locations of 61 WCD stations within the array. This underground placement reduces the background of other particles and environmental factors. With this, a more direct measurement of the muon content is possible [58, 59]. Furthermore, detector extension will improve the composition sensitivity of the energy spectrum in the ankle region, which is important for understanding the transition between galactic and extragalactic cosmic rays.

In addition to the SSDs, radio antennas will be deployed at each SD station in the array. Air showers produce extensive radio emissions, particularly at zenith angles above 60°. While the SSD and WCD are primarily sensitive to non-inclined

air showers, combining WCD and radio antennas will extend the composition sensitivity to more inclined air showers [60].

Chapter III

Improvements to SD Signals & Impact on the Apparent Muon Deficit

Estimating the mass of cosmic rays is one of the goals of UHECR physics. Because the muon content of air showers is directly coupled to the mass of the primary particle, a precise estimation of the muons is helpful. This muon content can be estimated by tuning different hadronic interaction models to the measurements of human-made accelerators and extrapolating them to the energy range of UHECRs. However, measurements of different experiments show a statistically significant deviation from the predictions of the muonic component from the hadronic interaction models [8, 9]. This apparent muon deficit is also referred to as the "muon puzzle". Hybrid measurements using the FD and SD show that air shower simulations contain 30% to 60% fewer muons than measurements. The exact value depends on the energy of the primary, the zenith angle, the hadronic interaction model, and assumptions about the composition [10, 11]. Throughout several analyses, a wide range of methods has been employed to estimate the muon content of air showers, e.g., by using the characteristic risetime of the SD signals [13] or models based on air shower universality [61]. Additionally, direct measurements of the muon content, using the UMD of the Pierre Auger Observatory, have shown a discrepancy with simulations [12]. With AugerPrime, new methods have been tested to estimate the muon signal by combining the measurements of the WCD and SSD with the so-called matrix formalism [62, 63]. One of the main objectives of this thesis is to estimate the difference in the muon content between measured and simulated air showers using only the data of the WCD. Therefore, a wide energy range from $10^{18.5}$ eV up to $10^{20.0}$ eV and beyond can be covered. To estimate the muon deficit, it is necessary to fully understand the signals in the SD and remove any sources of biasing the signal estimation. For this, an improved baseline-finding algorithm for the time traces of the SD is presented in Section 3.1 of this chapter. It is based on a realistic model of the PMT response, which is robust to sporadic early and late signal contributions in the trace and accounts for undershoot. A major part of the AugerPrime upgrade is the switch from UB to UUB electronics, making it necessary to adjust the algorithm to the new electronics. The adjusted algorithm will be explained in Section 3.2.

These adjustments to the baseline-finding procedure significantly reduce the bias between the high-gain and low-gain signals. Additionally, using the new baseline algorithm allows for a better identification of late pulses. Section 3.3 addresses the remaining bias that could not be resolved from the baseline algorithm updates. With the new baseline algorithm, peak structures at characteristic times can also be better analyzed in saturated WCD traces. In Section 3.4, these features are investigated, and it is shown if they are caused by afterpulsing of the PMTs and could account for any discrepancies between measurements and simulations. Finally, a novel, SD-only estimate of the apparent muon deficit is presented in Section 3.5 and the impact of the previously described improvements in the signal estimation is studied.

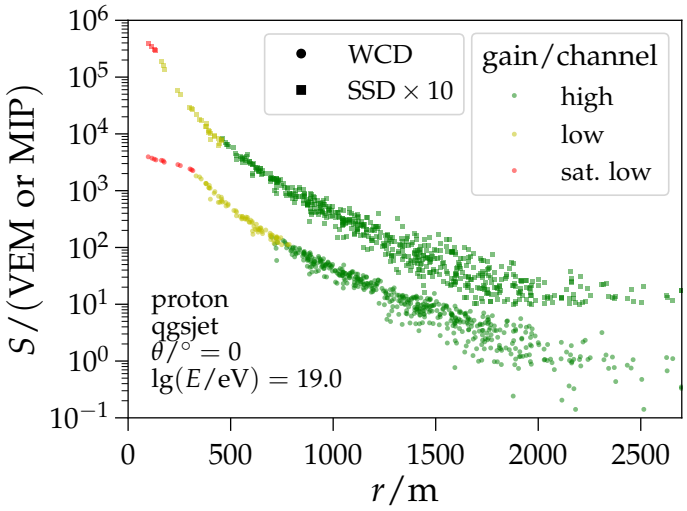

Figure 3.1: Simulated lateral distributions of WCD and SSD measurements. At distances far away from the shower axis the high gain is used (green points). Closer to the shower axis, the HG saturates, and the low gain is used (yellow points). With increasing signal size also the LG saturates (red points). The gains of both detectors saturate at different points, as depicted by the transition between colors.

3.1. Improving the Estimation of Baselines

The identification and calibration of detector signals is crucial for minimizing systematic uncertainties in measurements. A constant offset, called the baseline, which is generated by the electronics, has to be estimated to properly compute the size of the signals. Various studies have reported systematic biases that might be due to a bias in the ratio between the signal of the HG and LG channels [64, 65]. With the AugerPrime upgrade, the new SSDs are used in addition to the measurements of the WCD. Both detectors have different signal thresholds for saturation. Thus, the transition point when the LG instead of the HG is used is different. Fig. 3.1 shows a simulation of a lateral distribution of WCD and SSD measurements for the estimation of the shower size S_{1000} and thus the energy of the shower. The existence of a systematic bias in the ratio of the signal from the two gains implies a shift of the signal used when fitting the lateral distribution at the transition point from HG to LG. Hence, it is important to understand this systematic bias and to reduce it.

The following analysis is performed on data that was recorded by WCDs using UBs. To estimate the systematic bias between the HG and LG, a data set of 770 664 events from years 2019 to 2021 of the full array with a total of 7 630 454 traces is analyzed. For each working PMT, the HG and LG traces are extracted. The maximum bin entry of the HG channel $\mathrm{HG_{max}}$ is an estimate of how close the trace is to the saturation of the HG channel. The range of ADC counts (adc) has a maximum at 1023 per time bin. Signals above this value are digitized as 1023 and the trace is thus saturated. The maximum time-bin entry of the full HG trace is denoted with $\mathrm{HG_{max}}$. At $\mathrm{HG_{max}} \equiv 1023$, the HG trace is saturated and the LG is used. The ratio of the calculated signal from the HG S_{HG} and LG S_{LG} as a function

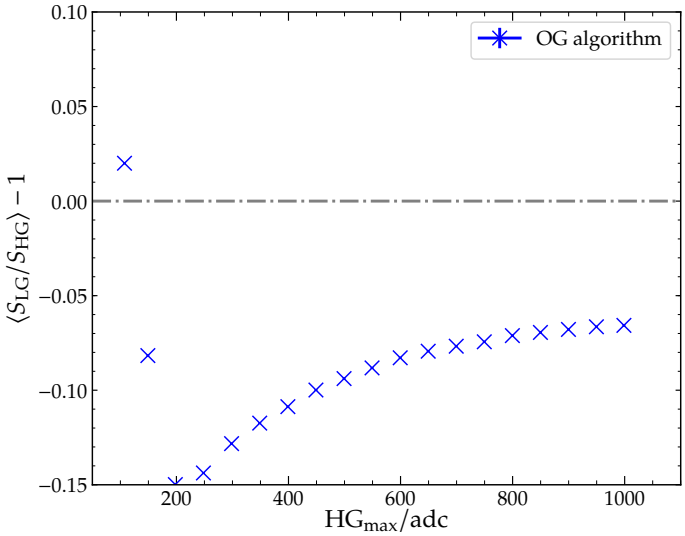

Figure 3.2: The ratio between signals from LG and HG traces as a function of the maximum bin entry in the HG channel, which provides an indication of how close the HG channel is to saturation. The algorithm used to determine the baselines of the time traces is referred to as the OG algorithm here. At low counts, the signals in the LG channel are too small to give reliable results, but at larger values and at the transition point from HG channel to the LG channel, the LG signals are on average 6.5% smaller than the HG signals.

of the maximum bin entry in the HG channel HG_{max} is shown in Fig. 3.2. For low HG_{max} ranging up to a few hundred adc, the signal is too small to perform a useful estimate of the signal from the LG channel. At the transition from HG to LG, there is a negative systematic bias of about 6.5% for the current standard OG algorithm. For the UB, this bias can have its origin in either the dynode-to-anode-ratio (D/A ratio, gain ratio) or in the calculation of the baselines from the traces and it has to be determined which is the main culprit.

The ratio of the LG and HG signals for different zenith angle, energy, and distance bins is shown in Fig. 3.3. The three bins in zenith angle cover a range of 0° to 56° and are uniform in $\sin^2\theta$. At the transition from HG to LG, the bias of the ratio is the smallest at approximately −6% for almost vertical showers. For the more inclined showers up to 56°, the bias at the transition is the largest with about −7.5%. In Fig. 3.3-right, the ratio is plotted in 3 energy bins, ranging from $\lg(E/\text{eV}) = 18.0$ up to an energy of $\lg(E/\text{eV}) = 19.5$. The difference between the 3 energy bins is larger than for the zenith bins at the transition point from HG to LG. For showers with a reconstructed energy between $\lg(E/\text{eV}) = 18.0$ and $\lg(E/\text{eV}) = 18.5$, the bias is the smallest at approximately −6%. In the largest energy bin, the bias increases up to almost −10%. In Fig. 3.3-bottom, the ratio is plotted in 3 distance bins, ranging from 500 m up to 1500 m. For stations that are far away from the shower axis, the bias is the largest at around −13% to −15%. At around 300 m to 700 m from the shower axis, the bias is at approximately −6%. These differences can be attributed to the shape of the trace that is different for the zenith, energy and distance bins. The electromagnetic component of the showers increases with decreasing zenith angle, thus broad signal shapes appear more

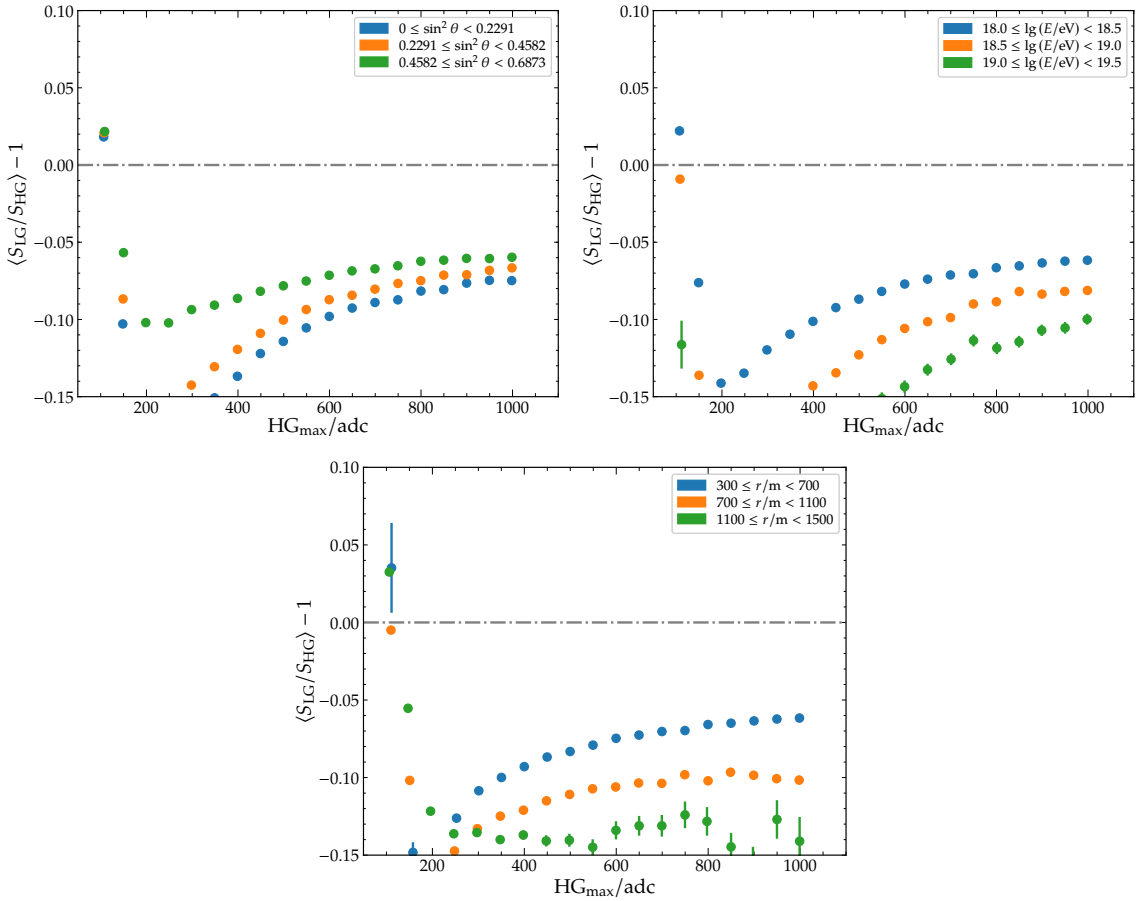

Figure 3.3: The ratio S_{LG}/S_{HG} between the signals calculated from the LG and HG traces binned in zenith angle θ (left), energy E (right), and distance r (bottom). For showers with smaller zenith angles, larger energies, and larger distances the biases are larger.

often in the traces. Similarly broad signal shapes appear in showers with larger energy and further from the shower core.

3.1.1. Current Baseline Algorithm

The current baseline algorithm of the baseline finder, which is based on the CDAS code, tries to identify flat segments in the trace and interpolates a baseline between them [66]. It has been shown that this procedure, in its current implementation, accidentally identifies parts of the signal as baseline pieces and thus gives an overestimation of the baseline and an underestimation of the signal [67]. A procedure by Ronald Bruijn was developed to resolve the so-called *stop-time problem*, which influences the calculation of the risetime of the signals. The risetime is defined as the time in which the integrated signal increases from 10% to 50% of its total value, which is determined by the start- and stop-time. This problem originates from the accidental inclusion of of signals in the flat baseline segments, resulting in an overestimation of the baseline. This procedure has been implemented in the CDAS and Offline reconstruction but could not fully resolve the problem that parts of the signal are included in the flat segments and is not

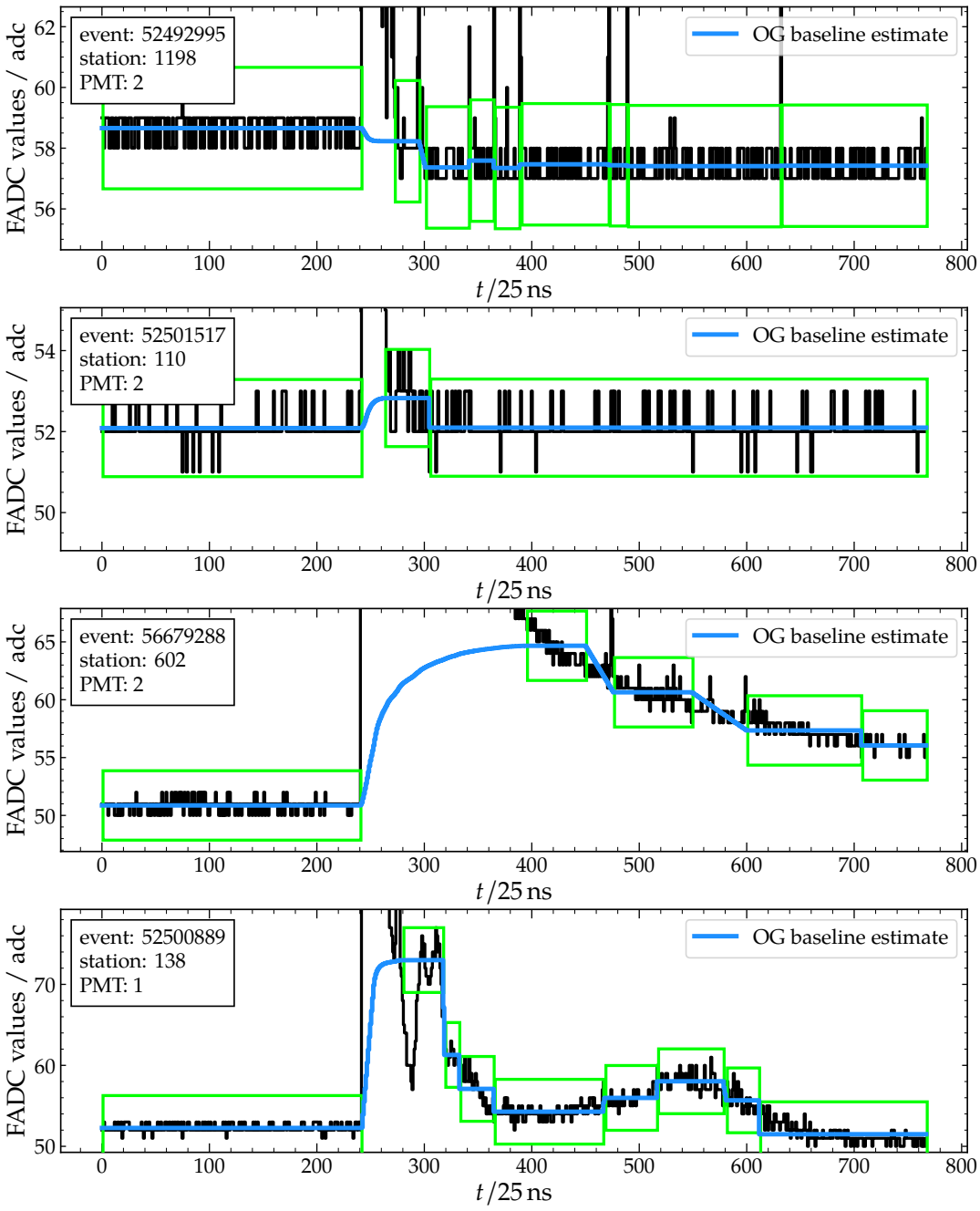

Figure 3.4: Example traces with the baseline estimate of the `BaselineFinderOG` module of Offline. The algorithm tries to find baseline pieces as flat trace segments, which are marked with green boxes, and interpolates between them. Part of the signal might be falsely identified as a flat piece and is consequently removed from the final trace.

used by default [67, 68]. The plots in Fig. 3.4 show examples of time traces and the estimation of their baselines, calculated by the `BaselineFinderOG` module of Offline. This baseline algorithm will be now referred to as the "OG algorithm". The first two traces of Fig. 3.4 show common examples of the misidentification of flat pieces. While the algorithm correctly finds large flat pieces at the front and end of the trace, it also misidentifies relatively flat signal contributions as a baseline. These misidentified baseline pieces result in multiple random jumps of the final, interpolated baseline, as shown in the first plot, or in single jumps, as shown in the second plot. In more extreme cases, the algorithm tries to identify flat pieces on extended tails of traces as in the third plot or on small, late signals as in the last plot of Fig. 3.4. This results in the unwanted removal of these signals. It is therefore of interest to find a baseline model that is based on the knowledge of the PMT response and does not remove relatively flat signal contributions.

3.1.2. New Baseline Algorithm

Physical Trace Model

PMT traces can exhibit various features that should be taken into consideration in the development of a new baseline-finding algorithm. Therefore, a physical trace model was developed as a first step. An example trace of one PMT of a WCD is shown in Fig. 3.5. In the first 40 time bins of the trace, a small peak is visible. This peak is very likely caused by an "accidental" particle entering the tank, which did not originate from the actual shower. Next follows a "flat" segment, where the baseline can be roughly estimated by eye to be about 58 adc. At around the time bin 240 the main part of the signal of the event is visible. After the main signal, at around the time bin 340, smaller peaks from shower components occurring later are visible. The baseline after the signal is lowered by approximately 1 adc, due to the undershoot of the PMT after a large signal. A description of the undershoot and a possible recovery method have been discussed in Ref. [69]. It has been shown that the recovery of the undershoot takes about 300 µs and is followed by an overshoot [70]. This overshoot then slowly decreases over a time span of up to 1 to 1.5 ms. The total trace length is 19.2 µs and thus, the baseline after the main signal can be assumed to be a constant undershoot. The undershoot ΔB can be calculated as the difference between the baseline at the end and at the beginning of the trace,

$$\Delta B = B_{\text{end}} - B_{\text{front}}. \tag{3.1}$$

This undershoot is proportional to the signal that causes the undershoot and thus to the total charge q_{tot} of the trace. Fig. 3.6 shows the coefficient of the linear proportionality

$$k = \frac{\Delta B}{q_{\text{tot}}}, \tag{3.2}$$

which turns out to be different for HG and LG traces. In considering such traces, a few requirements for the new baseline algorithm can be defined:

1. The calculation of the baseline should be stable against any signal contributions, as for example from accidental particles.

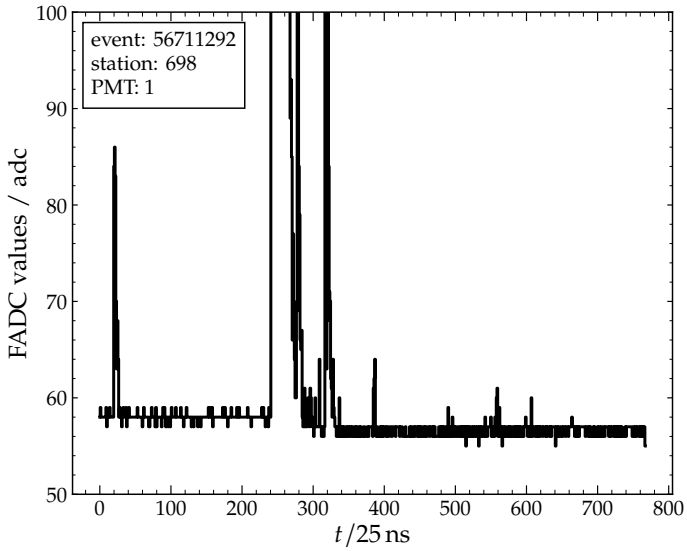

Figure 3.5: Zoomed-in example trace of an event. In the first 40 bins, a peak from an accidental particle is visible. After the main part of the signal, at around bin 340, the baseline of the trace is visibly lower than during the first 200 bins of the trace.

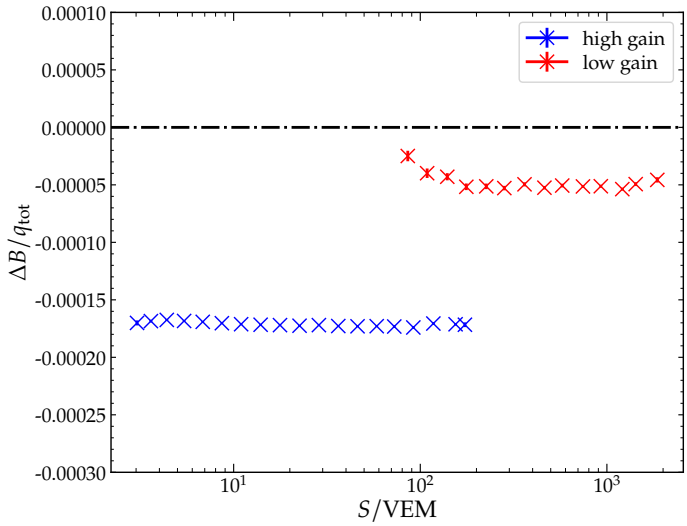

Figure 3.6: Ratio of difference ΔB and the approximate total charge q_{tot}. As the signal in the HG and LG increases, the linear relationship of the ratio between ΔB and q_{tot} becomes constant.

2. Two separate baseline estimates at the beginning and the end of the trace are required, to account for a possible undershoot.

A new, three step algorithm will be discussed in the following sections in more detail. The implementation of this new algorithm is done in a new module in Offline, named `BaselineFinderKG`. This new algorithm will be referred to as the "KG algorithm".

Table 3.1: Continuous Napoli library of Corsika simulations with different combinations of parameters. For each combination, 500 events were reconstructed.

primary	p, Fe
hadronic interaction model	Epos-LHC
lg(E/eV)	18.5 - 19.0, 19.0 - 19.5, 19.5 - 20.0
θ/°	0 - 65

Front and End Baseline Estimation

As an initial step, two separate estimates of the baseline are obtained. The algorithm that is used to derive these two estimates is adapted from the baseline estimation of the FUNK experiment [71]. The first baseline estimate B_{front} is performed at the beginning of the trace. It is defined as

$$B_{\text{front}} = \frac{1}{N} \sum_{i=1}^{N} T_i, \tag{3.3}$$

where N is the length of the beginning trace segment used to calculate the baseline. Due to the undershoot, the baseline fluctuates downwards after a large signal. Since the recovery time of the undershoot significantly exceeds the total trace length, the baseline can be assumed constant after the undershoot. The second baseline estimate can thus be evaluated at the end of the trace and is obtained as

$$B_{\text{end}} = \frac{1}{N} \sum_{i=L-N}^{N} T_i, \tag{3.4}$$

where $L = 768$ is the trace length of the UB stations[1]. The baseline should be estimated as the mean of only the trace bins that do not include any signal. The length N of this trace window, from which the baseline is calculated, has to be determined first. Optimally, the length of the trace window is chosen to be as short as possible to exclude possible signal contributions from accidental particles. To determine the optimal length, a set of 3000 simulated events with 98 457 traces is used. An overview of the simulated library is given in Table 3.1.

Even with a short trace window, some signals can still be included in the baseline calculation and the baseline will be overestimated when calculating the mean. Thus, an additional truncation is applied to the trace to exclude such signals from accidental particles. First, the mode m and the standard deviation σ of the trace window with a fixed number of bins are calculated, as shown in the first plot of Fig. 3.9. The histograms on the left and right side of the trace show the distribution of the ADC counts of the first and last 100 bins of the trace in the middle. The modes of the front and end are indicated with the green dash-dotted lines. Then the trace is truncated by excluding all bins with counts larger or smaller than

$$m \pm 2\sigma. \tag{3.5}$$

[1] For UUB $L = 2048$ and for Cyclon boards the trace length is only $L = 760$ bins [72].

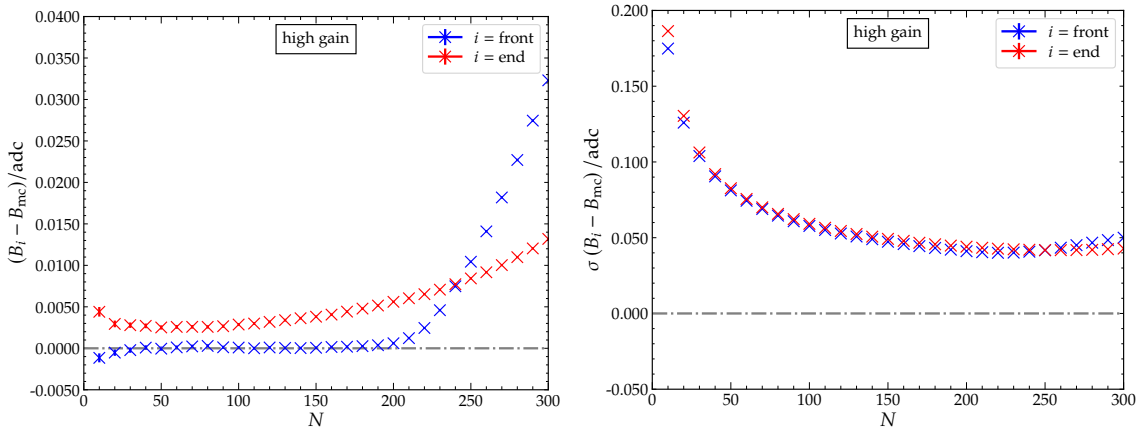

Figure 3.7: Bias and its resolution of the calculated baseline for various lengths of the trace window for HG traces. *Left:* The front baseline, which is depicted in blue, gets heavily biased by the shower signals starting at around time bin 200. The bias of the end baseline, shown in red, increases with larger window sizes, as more late shower signals are included. *Right:* By including more bins in the window, the resolution improves until shower signals start to be included in the window.

In the second plot of Fig. 3.9 the 2σ around the mode m are shown as grey area and the excluded bins are marked in red. To avoid the exclusion of all bins, the $m \pm 2\sigma$ is floored or rounded up, to always include the next smaller value at downwards fluctuations, or larger value at upwards fluctuations. The standard deviation of the truncated trace is calculated again and the truncation with $\pm 2\sigma$ relative to the mode is repeated until the number of excluded bins is not changing anymore, as shown in the plots 3 to 5 of Fig. 3.9. From the final truncated trace piece, a mean is calculated as an estimate of the baseline. The estimated baseline B_i is compared to the true, simulated baseline B_{mc} and the bias $B_i - B_{\mathrm{mc}}$ and the resolution $\sigma(B_i - B_{\mathrm{mc}})$ can be calculated. For different trace window lengths, the procedure is repeated, and the results are shown in Fig. 3.7 for the HG and in Fig. 3.8 for the LG. Due to the truncation, the signal from accidental particles is effectively excluded and the bias of the front baseline is minimized. For a trace window size larger than 200 time bins, the signal of the shower can already be included in the window, which cannot be fully filtered out by the truncation. As a result, the bias of B_{front} increases. The baseline estimation at the end of the trace is almost bias-free as well. This is due to small signal contributions of the shower, that can not be entirely filtered with the truncation. By increasing the trace window B_{end}, the bias increases as more signal from the shower is swept up.

For the LG traces, this bias is reduced, since small signals can not be resolved in the trace. The resolution of the baseline estimates improves with larger trace windows, as one would expect. As soon as the shower signal is included in the window, the resolution worsens. From this analysis, it is possible to choose a trace window between 10 and approximately 180 bins, without a significant increase in the bias.

Since the goal is to use as few bins as possible a trace window of 100 time bins

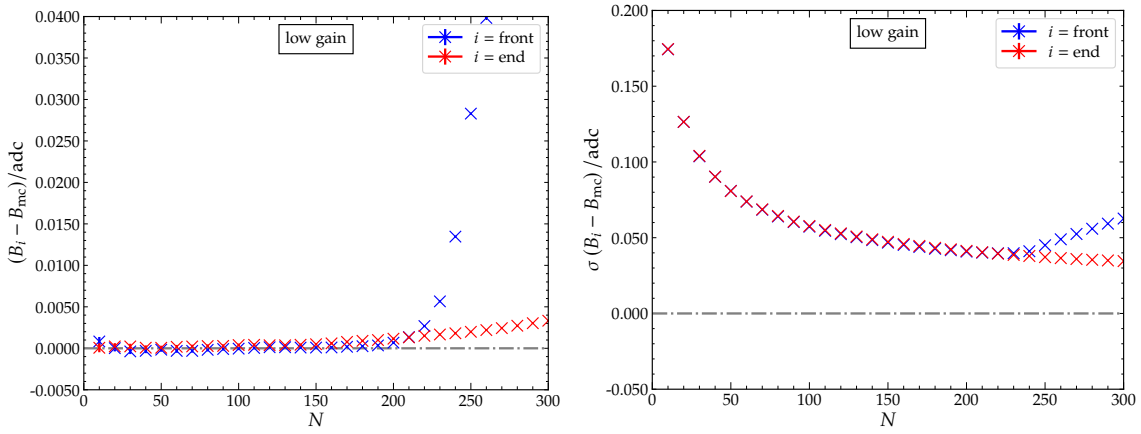

Figure 3.8: Bias and resolution of the calculated baseline for various lengths of the trace window for LG traces. The front baseline is shown in blue, the end baseline in red. B_{front} gets heavily biased by the shower signals, starting at around the time bin 200. Since the amplitudes in the LG traces (in adc units) are less than for their respective HG traces, the bias is smaller, although the resolution stays the same.

is considered as a good choice. The resolution of the baseline estimates with a trace window size of 100 time bins is approximately

$$\sigma(B_{\text{front}}) \approx 0.058\,\text{adc} \qquad \text{and} \qquad \sigma(B_{\text{end}}) \approx 0.059\,\text{adc}, \tag{3.6}$$

for the HG channel and

$$\sigma(B_{\text{front}}) \approx 0.057\,\text{adc} \qquad \text{and} \qquad \sigma(B_{\text{end}}) \approx 0.058\,\text{adc}, \tag{3.7}$$

for the LG channel.

Decision of Interpolation Method

After the front and end baseline estimates have been determined, the baseline difference ΔB is calculated. The left plot of Fig. 3.10 shows the distribution of ΔB of the traces from the SD data set from years 2019 to 2021 that did not saturate their corresponding channel. The HG traces show a long tail of the distribution to negative ΔB values, which corresponds to an end baseline that is below the front baseline. This is an expected behavior due to the undershoot that occurs at large signals. The tail is more prominent for HG traces. The right plot of Fig. 3.10 shows the distribution of the standard deviations σ_{front} and σ_{end}, calculated from the trace windows of the HG traces. The median of the distributions is approximately at a value of 0.49 for both the front and the end trace window. Due to the conversion of the analog signals to discrete adc values, some traces may have a $\sigma_{\text{front,end}}$ of zero since minimal fluctuations can not be resolved anymore.

In Fig. 3.11 the effects of the discretization from an analog to a digital signal are shown for baseline estimation. Multiple traces with the size of 10^6 time bins are created with varying analog means μ and standard deviations σ_{analog}. Each trace is then rounded to integer values and the mean $\langle T \rangle$ and standard deviation $\sigma(T)$ of each rounded trace is calculated. The calculated mean is shown as a function

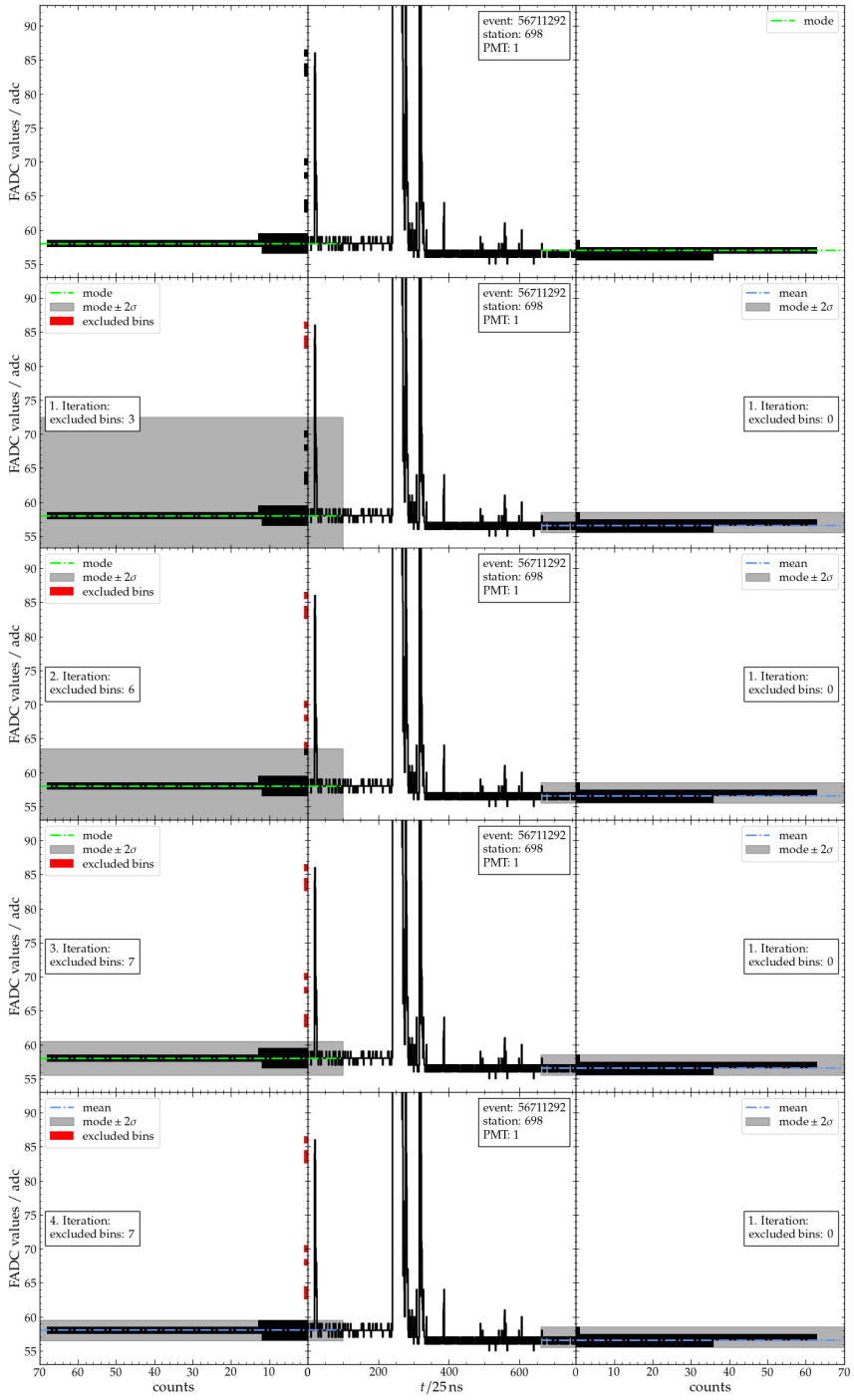

Figure 3.9: Example of the truncation procedure for the trace of Fig. 3.5. The left and right histograms show the distribution of the first and last 100 bins. *First plot:* The mode m of the front and end trace window is determined (green, dash-dotted line). *Second plot:* The standard deviation σ of both windows and all bins that are larger or smaller than $m \pm 2\sigma$ are excluded (red). *Plots 3-4:* σ of the truncated trace is recalculated and the exclusion of bins is repeated. *Plot 5:* If no more bins are excluded, the truncation procedure is stopped and the mean of the remaining bins is used as the baseline estimate (blue, dash-dotted line).

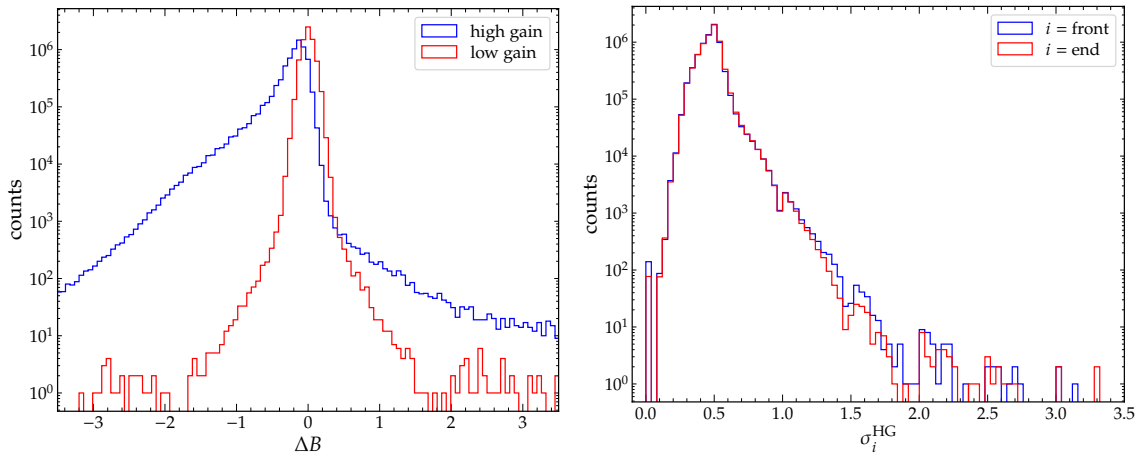

Figure 3.10: Anomalous traces can be found, based on values of their ΔB as well as σ_{front} and σ_{end}. Normally a negative ΔB is expected for the standard undershoot. A large positive ΔB or large values of σ_{front} and σ_{end} can indicate possible problems such as malfunctioning PMTs. *Left:* Distribution of the difference ΔB between the front and end baseline estimate for HG and LG traces. The tail at negative values of ΔB corresponds to the undershoot. *Right:* Distribution of the calculated standard deviations σ_i of the trace windows of the front baseline estimate (blue) and end baseline estimate (red) for HG traces.

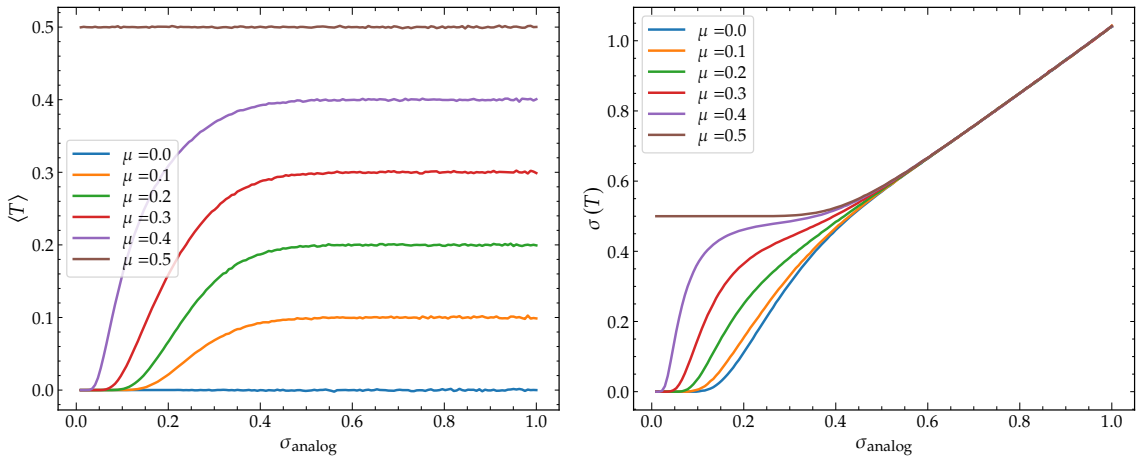

Figure 3.11: The analog signal of the PMT is by the ADC converted to a digital trace T, rounding analog values to integers. Due to this process, the mean $\langle T \rangle$ and the error of the mean $\sigma(T)$ of a baseline estimate change with respect to the true mean μ, if the fluctuations σ_{analog} of the analog trace are below a certain threshold, $\sigma_{\mathrm{analog}} \lesssim 0.5$. To prevent the error becoming artificially small, it was chosen according to Eq. (3.8). *Left:* Average $\langle T \rangle$ of rounded baseline for varying analog fluctuations σ_{analog} and mean values μ. Due to rounding of the traces, the mean $\langle T \rangle$ of a trace is biased if σ_{analog} is small. *Right:* Standard deviation $\sigma(T)$ of the baseline. This value can be compared to the error of the mean of the estimated baselines. Due to the rounding of the traces, the error changes depending on the value of the true mean μ of the baseline if the fluctuations are smaller than $\sigma_{\mathrm{analog}} \lesssim 0.5$.

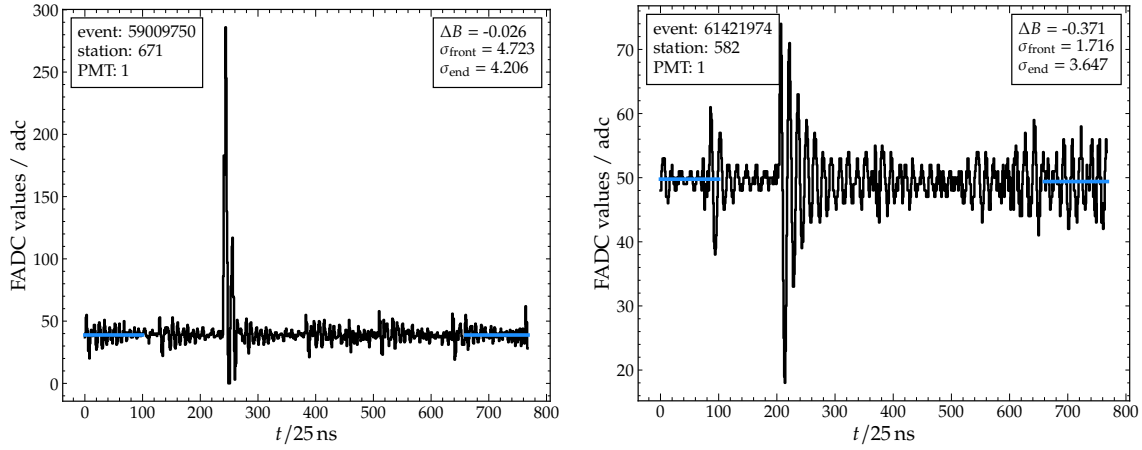

Figure 3.12: A large σ_{front} or σ_{end} can be caused by various effects, as for example by lightning events or malfunctioning PMTs. *Left:* An example of a noisy trace due to problems in electronics. *Right:* An example of a trace from a lightning event.

of the analog fluctuation σ_{analog} in Fig. 3.11-left. If the fluctuations of the analog values are sufficiently large, the mean $\langle T \rangle$ of the rounded trace will correspond to the true mean μ of the trace. However, with decreasing σ_{analog}, the mean of the trace will take the values of the half integers due to the rounding of the values. The standard deviation of the traces is plotted as a function of σ_{analog} in Fig. 3.11-right. If the true analog mean value μ lies close to the threshold of rounding upwards or downwards, even a very small σ_{analog} will cause the rounded trace to flip between both available integer values, leading to a standard deviation of exactly $1/2$. For a μ that is closer to an integer value, small fluctuations cannot cause flipping between the two integers, the fluctuations are suppressed, and the standard deviation drops to zero. To prevent the error of the mean of the baseline estimates artificially decrease to zero due to this discretization effect, an error of

$$\sigma_{b_{\text{front,end}}} = \frac{\max(0.5, \sigma_{\text{front,end}})}{\sqrt{n_{\text{front, end}}}}, \tag{3.8}$$

is used. Outliers that have either a large, positive ΔB or a large $\sigma_{\text{front,end}}$ can be investigated in more detail by analyzing the distributions from Fig. 3.10. Fig. 3.12 shows two example traces with a large σ_{front} and σ_{end}. The reasons behind the abnormal shapes of these traces might be either related to issues in the electronics or lightning conditions.

The value of the baseline difference ΔB is used to determine whether an undershoot or an anomalous overshoot is present in the trace. For this, the error of the baseline difference $\sigma_{\Delta B}$, which is dependent on the error of the front and end trace window is calculated as

$$\sigma^2_{\Delta B} = \sigma^2_{b_{\text{front}}} + \sigma^2_{b_{\text{end}}}. \tag{3.9}$$

Different interpolation methods between B_{front} and B_{end} can now be chosen depending on the actual values of ΔB and $\sigma_{\Delta B}$.

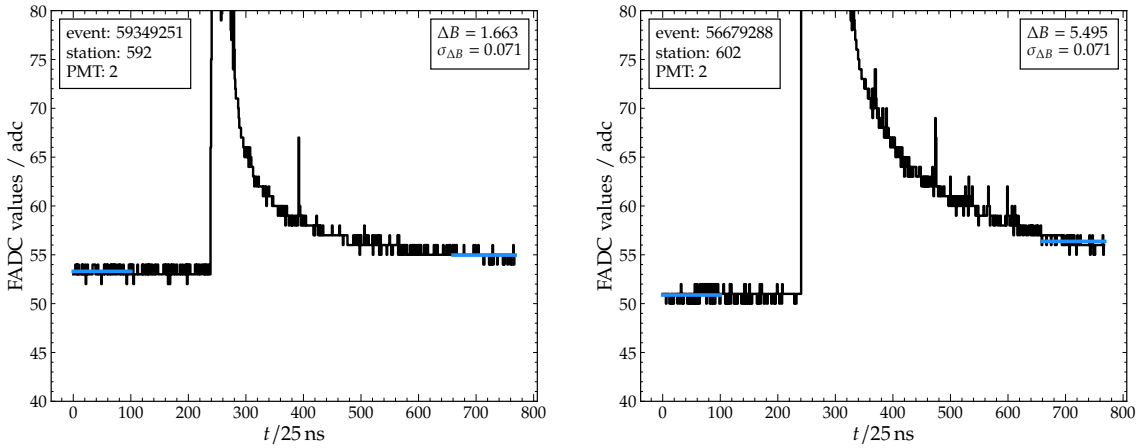

Figure 3.13: Anomalous traces can be filtered out by applying a threshold of $5\sigma_{\Delta B}$ as a maximum upwards fluctuation of the baseline estimate at the end of the trace when compared to the front. *Left:* An example of a trace from station 592 with $B_{\text{end}} > B_{\text{front}}$. *Right:* An example of a trace from station 602 with $B_{\text{end}} > B_{\text{front}}$.

Rejection of Anomalous Upward Fluctuations $\Delta B \geq +5\sigma_{\Delta B}$

If the end baseline is estimated to be more than $5\sigma_{\Delta B}$ larger than the front baseline, the trace is rejected as an anomalous trace. Aside from random fluctuations of B_{front} and B_{end}, there is no reason for the baseline to increase after a signal. A significant increase of the baseline indicates possible errors in the electronics and the resulting traces should not be considered for the estimation of a signal. In Fig. 3.13, two example traces with $\Delta B > +5\sigma_{\Delta B}$ are shown.

In both cases, the trace seems to have a long tail that decreases slowly over time but does not reach the original baseline and thus clearly deviates from the normal undershoot behavior.

Constant Approximation for Small Upward Fluctuations $+5\sigma_{\Delta B} > \Delta B \geq 0$

An increase of the baseline up to $+5\sigma_{\Delta B}$ is assumed to be a random fluctuation. In such cases, a reevaluation of the baseline based on the full trace is performed. The truncation method used for B_{front} and B_{end} is applied to the full range of the trace. The resulting robust estimate is chosen as a constant for the full baseline. Fig. 3.14-left shows an example trace where the B_{end} is larger than B_{front} but still smaller than the allowed $5\sigma_{\Delta\text{B}}$ upwards fluctuation.

Step-function Approximation for Small Downward Fluctuations $0 > \Delta B \geq -1\sigma_{\Delta B}$

Similar to the upwards fluctuations, B_{end} can be smaller than B_{front} due to downward fluctuations. However, traces are also expected to have an undershoot after a signal. Instead of calculating a robust constant, an interpolation between B_{front} and B_{end} should be performed. Since the undershoot is correlated with the signal size, small signals will cause only a small undershoot. However, these signals might be too small to correctly interpolate, thus a step-function is used instead. B_{front} is used as the baseline from the start of the trace to the bin with the maxi-

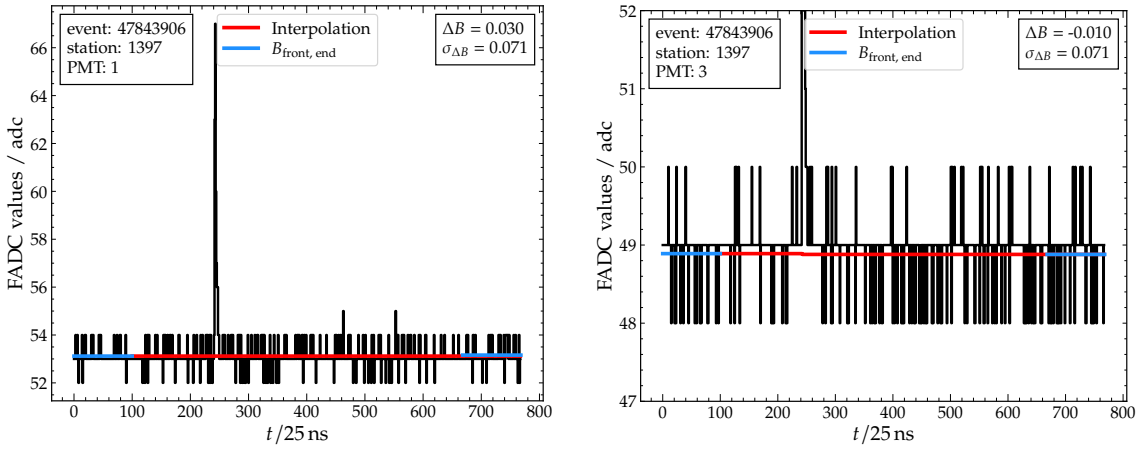

Figure 3.14: If the ΔB fluctuations are small compared to the error of the baseline difference $\sigma_{\Delta B}$, two cases are distinguished. For upwards fluctuations of up to $+5\sigma_{\Delta B}$, a robust constant is evaluated by applying the truncation procedure on the full trace (left). A step-function is used, if there are small downward fluctuations, where $0 > \Delta B \geq -1\sigma_{\Delta B}$ (right).

mum trace value. Then the baseline is set to B_{end} until the end of the trace. An example trace with a step-function is shown in Fig. 3.14-right.

Charge-linear Interpolation for Large Undershoots $-1\sigma_{\Delta B} > \Delta B$

If B_{end} is smaller than B_{front} by more than $-1\sigma_{\Delta B}$, a more refined procedure is used to model the baseline. As a first estimate the baseline is interpolated linearly in time between B_{front} and B_{end}, as shown in Fig. 3.15-left. Afterwards, the baseline is interpolated linearly as a function of integrated charge. Since the evaluation of the integrated charge itself requires the baseline, this procedure can be applied only in an iterative way. Fig. 3.15-right shows an example of the first iteration of the charge-linear interpolation. The interpolation is only executed if the bin with the most ADC counts exceeds a threshold of 50 adc relative to B_{front}. If the difference of the maximum of the trace and B_{front} is below 50 adc, the previously introduced step function is used to calculate the baseline instead.

The thresholds for deciding which interpolation method is used are not equally distributed. This can be explained with the physical trace model introduced earlier. A trace should never exhibit a significant overshoot; thus, a maximum upwards fluctuation of $+5\sigma_{\Delta B}$ is chosen. An undershoot, however, is expected and thus the step-function is used to describe the traces for small total trace charges and the charge-linear interpolation is used below the threshold of $-1\sigma_{\Delta B}$. These threshold values can be adjusted in the XML configuration of the `BaselineFinderKG` module in Offline.

Charge-linear Interpolation

The last step of the algorithm is to find an appropriate interpolation of the baseline between the front and end baseline estimates B_{front} and B_{end}. The baseline is set to be either a robust constant in the case of upward fluctuations of the end baseline or a step function for small downward fluctuations. For significant undershoot,

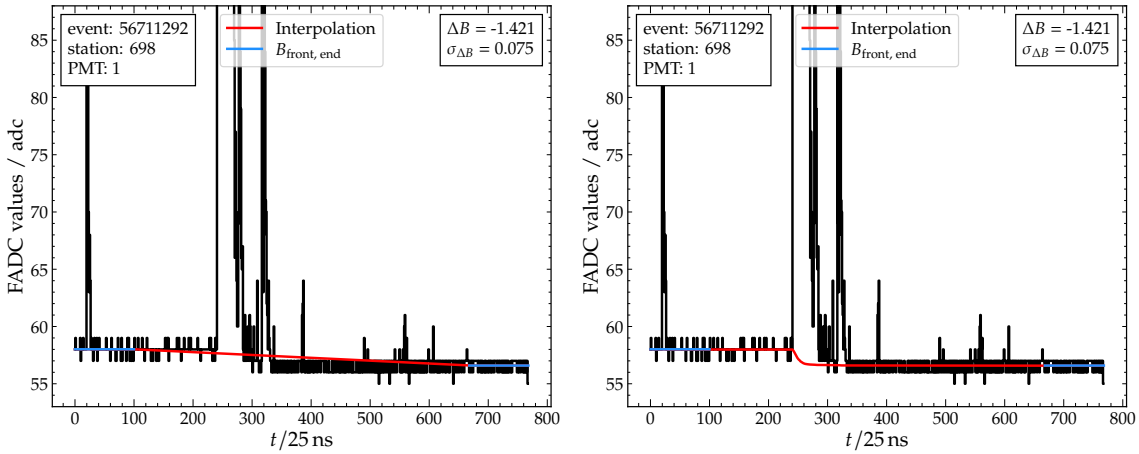

Figure 3.15: If the undershoot exceeds $-1\sigma_{\Delta B}$, several successive interpolation steps are used to find an appropriate baseline. In the first step, the baseline is interpolated linearly in time between B_{front} and B_{end} (left). Using this as a first approximation, a total charge q_{tot} of the trace is calculated and the baseline is reevaluated using a linear interpolation q_i in charge (right).

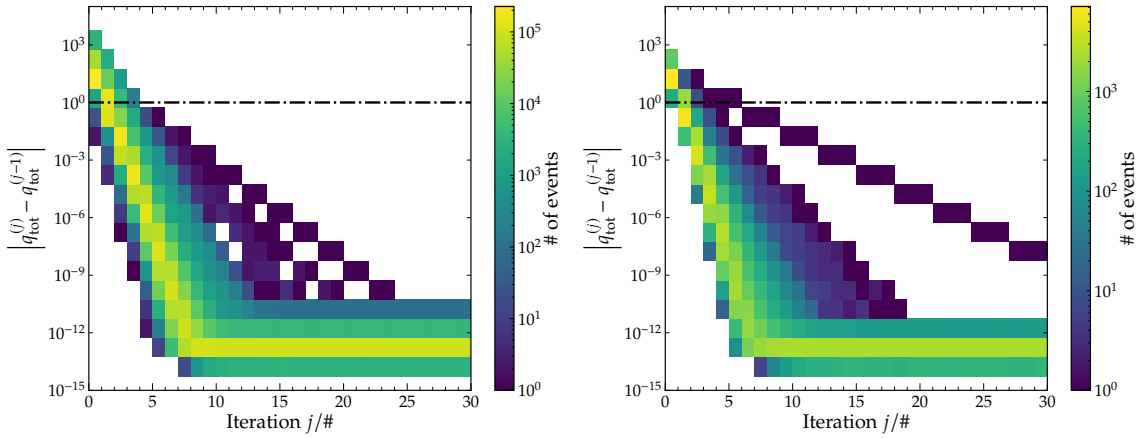

Figure 3.16: The absolute difference between the total charge $q_{\text{tot}}^{(j)}$ of the j-th iteration and the previous iteration $q_{\text{tot}}^{(j-1)}$ is decreasing with each step of the iteration. After about 5 iterations, the absolute difference becomes smaller than 1 and the procedure can be stopped. *Left:* Absolute difference for each iteration of HG traces. *Right:* Absolute difference for each iteration of LG traces.

an appropriate interpolation between B_{front} and B_{end} is needed. As a zeroth order approximation, the baseline $b_i^{(0)}$ is interpolated linearly in time between the end index b_{front} of B_{front} and the start index b_{end} of B_{end} as

$$b_i^{(0)} = B_{\text{front}} + (i - b_{\text{front}})\frac{\Delta B}{n_{\text{mid}}}, \tag{3.10}$$

where i denotes the current bin, $n_{\text{mid}} = (b_{\text{end}} - b_{\text{front}})$ is the length of the interpolated part of the trace. By subtracting the baseline from the trace, an approximate total charge $q_{\text{tot}}^{(0)}$ can be calculated by integrating the full baseline-subtracted trace

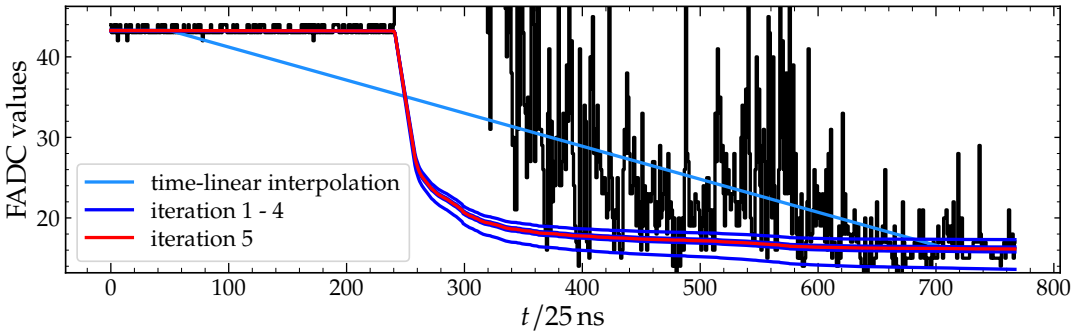

Figure 3.17: Example trace shown with several steps of the iterative baseline procedure. The first estimate is the time-linear interpolation (light blue). Afterwards the charge-linear interpolation procedure is repeated five times. Within the first four iterations (blue) the baseline estimate already in the fifth iteration converges very close to the final baseline (red).

T_i as

$$q_{\text{tot}}^{(0)} = \sum_{i=b_{\text{front}}}^{b_{\text{end}}} (T_i - b_i^{(0)}). \tag{3.11}$$

As previously shown in Fig. 3.6, the magnitude of the undershoot is proportional to the signal charge. After the linear interpolation between the baseline estimates, a new, j-th baseline approximation is calculated, which is linearly dependent on the integrated charge,

$$b_i^{(j+1)} = B_{\text{front}}(1 - \epsilon_i^{(j)}) + B_{\text{end}}\,\epsilon_i^{(j)}, \tag{3.12}$$

where the weight $\epsilon_i^{(j)}$ is defined as a relative fraction of the integrated charge

$$\epsilon_i^{(j)} = \frac{\sum_{k=b_{\text{front}}}^{i}(T_k - b_k^{(j)})}{q_{\text{tot}}^{(j)}}. \tag{3.13}$$

The total charge of the trace is recalculated using the new baseline estimation and the procedure is repeated. For the test data set, this procedure is repeated 30 times. If $q_{\text{tot}}^{(j)}$ is evaluated to be negative during the procedure, the procedure is stopped and the PMT is rejected. Fig. 3.16 shows the absolute difference between the calculated total charge $q_{\text{tot}}^{(j)}$ after the j-th iteration and total charge of the previous iteration $q_{\text{tot}}^{(j-1)}$. It runs out $q_{\text{tot}}^{(j)}$ varies the most in the first two steps and the relative difference reduces as the number of iterations increases. After about 5 iterations, the absolute difference becomes smaller than 1. Thus, for the KG algorithm a total number of 5 iterations is chosen to determine the baseline. Fig. 3.17 shows an example trace with the initial baseline estimate, that is determined with a time-linear interpolation, as well as the 5 iterations, using a charge-linear interpolation. During the first 4 iterations small changes of the baseline estimate are visible until it converges towards the final estimation.

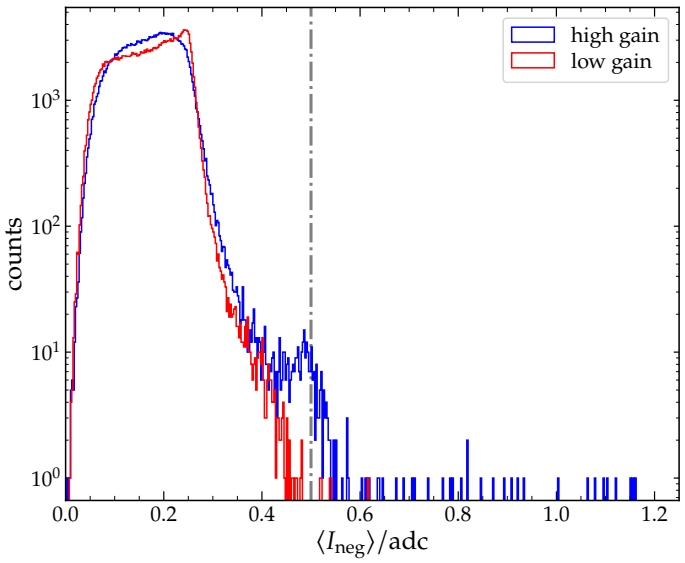

Figure 3.18: The mean negative amplitude $\langle I_{\mathrm{neg}} \rangle$ of the baseline-subtracted trace can be used for a fast check of the calculated baseline. If $\langle I_{\mathrm{neg}} \rangle$ exceeds a threshold of 0.5 adc (grey dot-dashed line), the trace might have an anomalous shape.

Limitations

After a baseline has been determined, a check is performed. The mean negative amplitude $\langle I_{\mathrm{neg}} \rangle$ of the baseline-subtracted trace is calculated as

$$\langle I_{\mathrm{neg}} \rangle = \frac{-q_{\mathrm{neg}}}{n_{\mathrm{mid}}}, \tag{3.14}$$

where q_{neg} is the sum of the negative values of the trace

$$q_{\mathrm{neg}} = \sum_{i=b_{\mathrm{front}}}^{b_{\mathrm{end}}} \lceil T_i - b_i^{(j)} \rceil \qquad \text{where} \qquad \lceil x \rceil = \begin{cases} x & ; x < 0 \\ 0 & ; x \geqslant 0 \end{cases}. \tag{3.15}$$

If variate x is distributed as $\mathcal{N}(x; 0, \sigma)$ then $-\lceil x \rceil$ is distributed as $\frac{1}{2}\delta(x) + \Theta(x)\mathcal{N}(x; 0, \sigma)$ with the mean $\langle -\lceil x \rceil \rangle = \sigma/\sqrt{2\pi} \approx 0.4\sigma$ and standard deviation $\sigma(-\lceil x \rceil) = \sigma\sqrt{(\pi - 1)/2\pi} \approx 0.58\sigma$. In the central limit $n_{\mathrm{mid}} \gg 1$, the mean negative amplitude is thus $\langle I_{\mathrm{neg}} \rangle = \sigma/\sqrt{2\pi n_{\mathrm{mid}}} \approx 0.4\sigma/\sqrt{n_{\mathrm{mid}}}$ with the standard deviation $\sigma(\langle I_{\mathrm{neg}} \rangle) = \sigma\sqrt{(\pi - 1)/2\pi n_{\mathrm{mid}}} \approx 0.58\sigma/\sqrt{n_{\mathrm{mid}}}$. If the estimated baseline matches the true baseline, $\langle I_{\mathrm{neg}} \rangle$ should not exceed the standard deviation of the trace.

For a trace without any signal, the mean negative amplitude should thus be of the order of the product of the standard deviation of the trace and half of the trace length. The standard deviation of the UB traces is around $\sigma \approx 0.5$ adc as can be seen in Fig. 3.10-right. A histogram of the mean negative amplitudes of 443 011 traces is shown in Fig. 3.18. About 99.9% of these traces have a mean negative amplitude smaller than 0.5 adc. Four example traces with a mean negative amplitude larger than this threshold are shown in Fig. 3.19. The

first plot shows an anomalous trace with a visible undershoot recovery, which should not be present in UB traces. In the second plot a trace with an oscillating baseline is shown. An example of a malfunctioning PMT is depicted in the third plot, where strong oscillations can be seen after the signal. The last plot of Fig. 3.19 shows anomalous glitches in the trace. These traces do not correspond to the physical trace model for UB traces that was introduced in Section 3.1.2 and therefore should not be used for any further analysis.

3.1.3. Evaluation with Simulated Data

The results of the KG baseline algorithm are compared to the OG baseline algorithm, which was the default algorithm until now. For the comparison non-saturated traces T_i were simulated in Offline. These traces have no undershoot, baseline, or noise and can be considered as pure Monte-Carlo traces. From these traces, the "true" total charge q_{tot}, as well as the true signal S_{mc} is calculated. Afterwards, an undershoot is simulated and added to the trace T_i, which results in a new trace

$$T_i' = T_i - k \lg q_{\mathrm{i}}, \qquad \text{where} \qquad q_i = \sum_{j=0}^{i} T_j. \tag{3.16}$$

and where k is a constant factor. The factor k can be determined from the previously described linear relationship between the undershoot ΔB and the total charge q_{tot}. This factor can be read off from Fig. 3.6 as approximately $-1.7{\times}10^{-4}$ adc/adct for HG traces and $-0.5{\times}10^{-4}$ adc/adct for LG traces. A baseline b_{mc} is added to the new trace T_i' along with artificial random noise with a standard deviation of 0.5 adc. In the last step, the values of the trace are floored to integer values to resemble a trace as it would be received from the ADC. An example simulated trace is shown in Fig. 3.20 together with the true baseline in blue and the estimated baseline from the KG baseline algorithm in red. The KG algorithm matches the true baseline in this example almost perfectly. This procedure is applied to all traces of the simulated library in Table 3.1. The signal S is determined using the OG baseline algorithm and the KG algorithm and compared to the true signal S_{mc}. A bias $\langle S/S_{\mathrm{mc}} \rangle - 1$ as well as the uncertainty $\sigma(S/S_{\mathrm{mc}})$ is then calculated. The results are shown in Fig. 3.21-left for the OG baseline algorithm and in Fig. 3.21-right for the KG algorithm. The HG data points include only traces that are below the saturation threshold of 1023 adc. For the LG data points, all traces where the HG is saturated are used. It is thus possible to read off the region of transition from HG to LG from these plots, which ranges from around 30 VEM up to 200 VEM.

For both versions of the baseline algorithm, the relative bias of the HG is below 1%. The bias $\langle S/S_{\mathrm{mc}} \rangle - 1$ of the LG for the OG algorithm, however, increases from around -0.5% down to -5%. While the bias is rather small at large signals at around 700 VEM, it is larger at the transition region from HG to LG. In the lower plots of Fig. 3.21, the signal uncertainty model σ_S/S is shown (in black) next to the uncertainties $\sigma(S/S_{\mathrm{mc}})$ from the baseline predictions. The uncertainty of the signal decreases with increasing signal. While for both algorithms the uncertainty

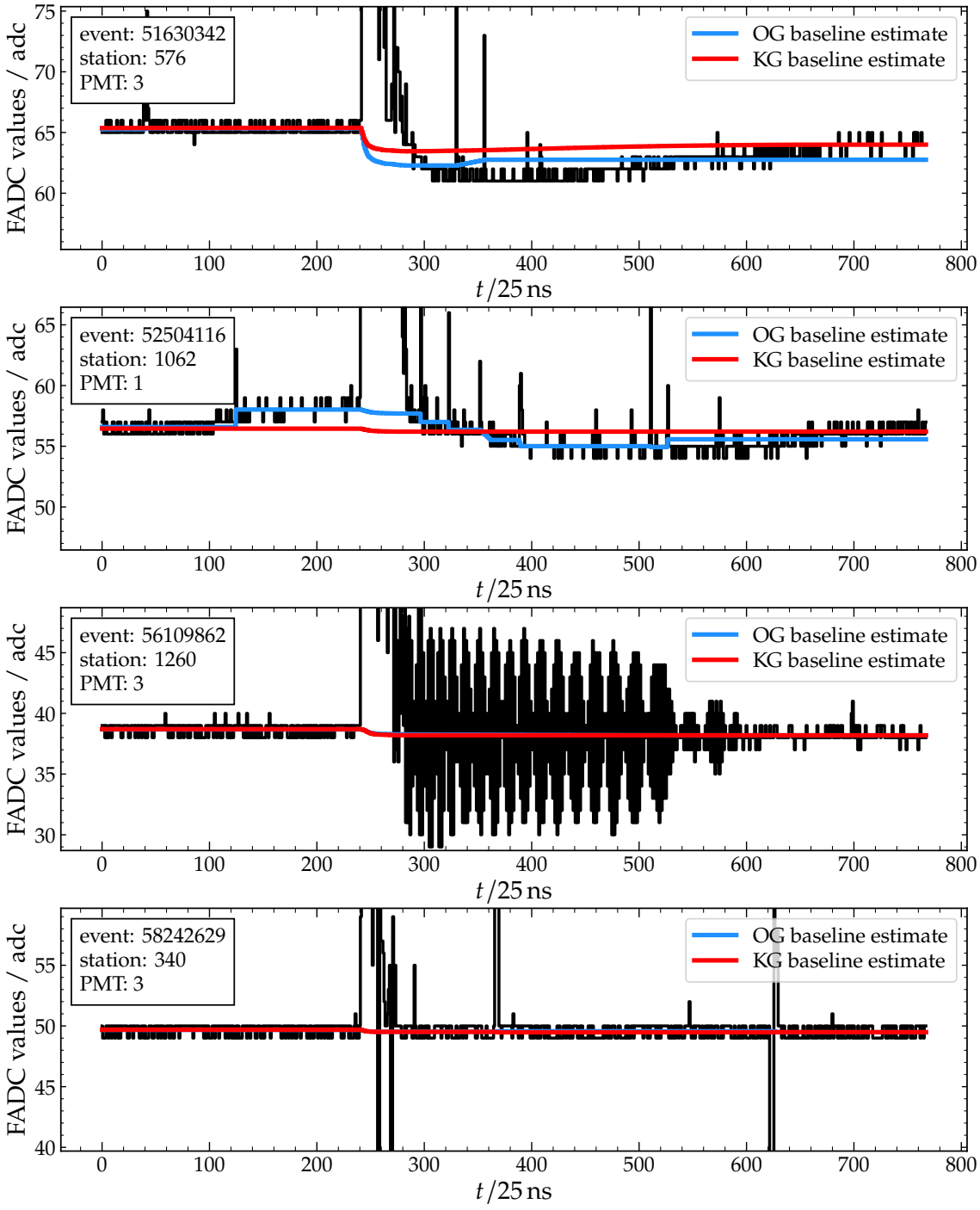

Figure 3.19: Examples of anomalous trace shapes. The mean negative amplitude $\langle I_{\text{neg}} \rangle$ of these traces exceeds the threshold of 0.5 adc and are therefore identified as anomalous. *From top to bottom:* Too-fast undershoot recovery of the baseline, since for UB the baseline should be constant after a signal. Oscillating baseline with a long wave. Malfunctioning PMT with high-frequency oscillations. Baseline glitches.

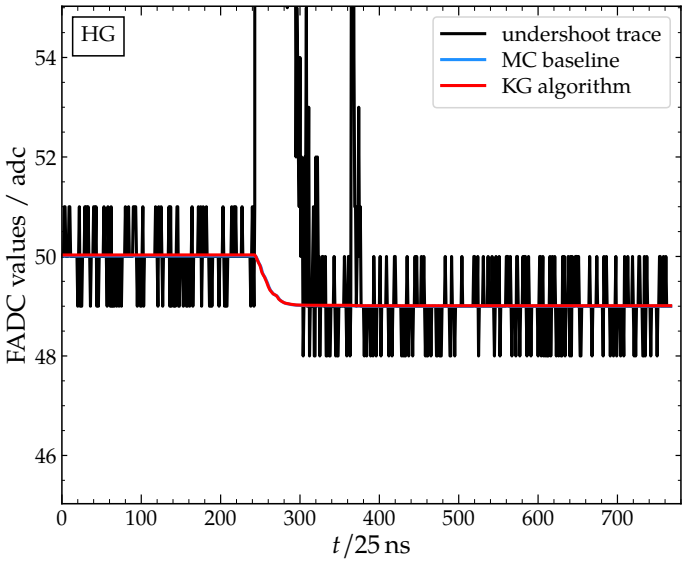

Figure 3.20: Simulated trace with artificial noise and undershoot. The estimated baseline from the KG algorithm (red) matches the simulated, true baseline (blue) very well.

is below the signal uncertainty σ_S/S, the uncertainty of the OG algorithm for the LG signals at around 200 VEM is nearly as large as the signal uncertainty. In contrast, the relative bias of the LG signals for the KG algorithm ranges from a maximum of around 1% at the transition region down to almost no bias for larger signals. The procedure thus gives an improved estimate of the true baseline, as compared to the OG algorithm.

The full functional form of the fits to the measured bias and uncertainty are given in Appendix A.1. While for the OG algorithm the uncertainty approaches the signal uncertainty and thus potentially should be included into the LDF fitting procedure, the uncertainties in the new KG algorithm are much smaller and are thus negligible as far as the LDF fitting is concerned.

3.1.4. Impact on Reconstruction

The estimated baselines from the OG algorithm can now be compared with the baselines estimated by the KG algorithm by using the data set of events between the years 2019 and 2021 from Section 3.1. Fig. 3.22 shows the traces and OG algorithm baselines from Fig. 3.4 with the baselines of the KG algorithm superimposed. For the baseline at the beginning of the trace, both algorithms produce similar estimates. In the `BaselineFinderOG` small humps can appear in the baseline due to the misidentification of flat pieces. These humps vanish with the charge-linear interpolation and constant baseline estimates, shown in Fig. 3.22. In the third plot of Fig. 3.22 the end baseline estimate is significantly larger than the front baseline estimate and the trace is classified as an anomalous trace and rejected as a result.

Fig. 3.23 shows the comparison of the ratio between the signals calculated from the LG and HG traces for both algorithms for 3 years of SD data. At the transition point from HG to LG, the bias of the OG algorithm of −6.5% improves to −1.5%

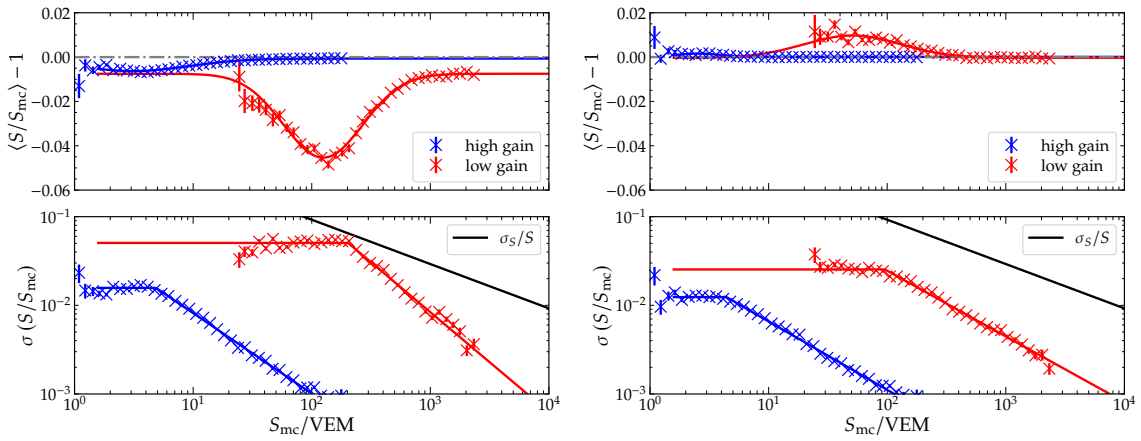

(a) OG (b) KG

Figure 3.21: Comparison between the signals estimated using the OG baseline algorithm (left) and the KG baseline algorithm (right). The upper plots show the bias, $\langle S/S_{mc}\rangle - 1$, relative to the true signal S_{mc} (crosses), which is simply fitted to an ad-hoc Gauss function (line). The lower plots show the relative uncertainty $\sigma(S/S_{mc})$ of the estimated signal, fitted to an ad-hoc broken power-law and compared to the signal uncertainty model σ_S/S used in LDF fitting in Offline (black line). The functional forms are given in Appendix A.1.

with the KG algorithm. This negative bias is in conflict with the expected positive bias of about 1% predicted by simulations for the transition region and hints at possible other sources of bias.

In Fig. 3.24, the ratios between LG and HG total signals S_{LG} and S_{HG}, binned in zenith angle θ, energy E, and distance to the shower axis r are compared between both algorithms. The ratio calculated with the current baseline algorithm depends on zenith angle, energy, and distance. Using the KG baseline algorithm, this dependence is reduced.. This minimal dependence of the ratio on proxies for the trace shape indicates that the remaining bias might originate from a bias in online estimation of the gain ratio by the local-station software, a claim that requires further investigation and will be addressed in Section 3.3.

A comparison between S_{1000} reconstructed with both algorithms is shown in Fig. 3.25 as a function of S_{1000}^{OG}. The KG algorithm results in a larger value for S_{1000} than the OG algorithm up to 5% on average. Although S_{1000} is used for the energy estimation, an energy calibration has to be done first for signals calculated with the KG algorithm, before final conclusions about a shift in the reconstructed energy can be made.

The absolute difference between the start and stop times is shown in Fig. 3.26. The start times do not change for most of the events. There are a few exceptions, which are more frequent at smaller signals. The stop times, however, have a broader distribution of outliers as compared to the start times. At larger signals, the average of the absolute difference increases by up to 50 time bins. This can be attributed to the inclusion of small, late signal contributions that were previously filtered out by the OG baseline algorithm.

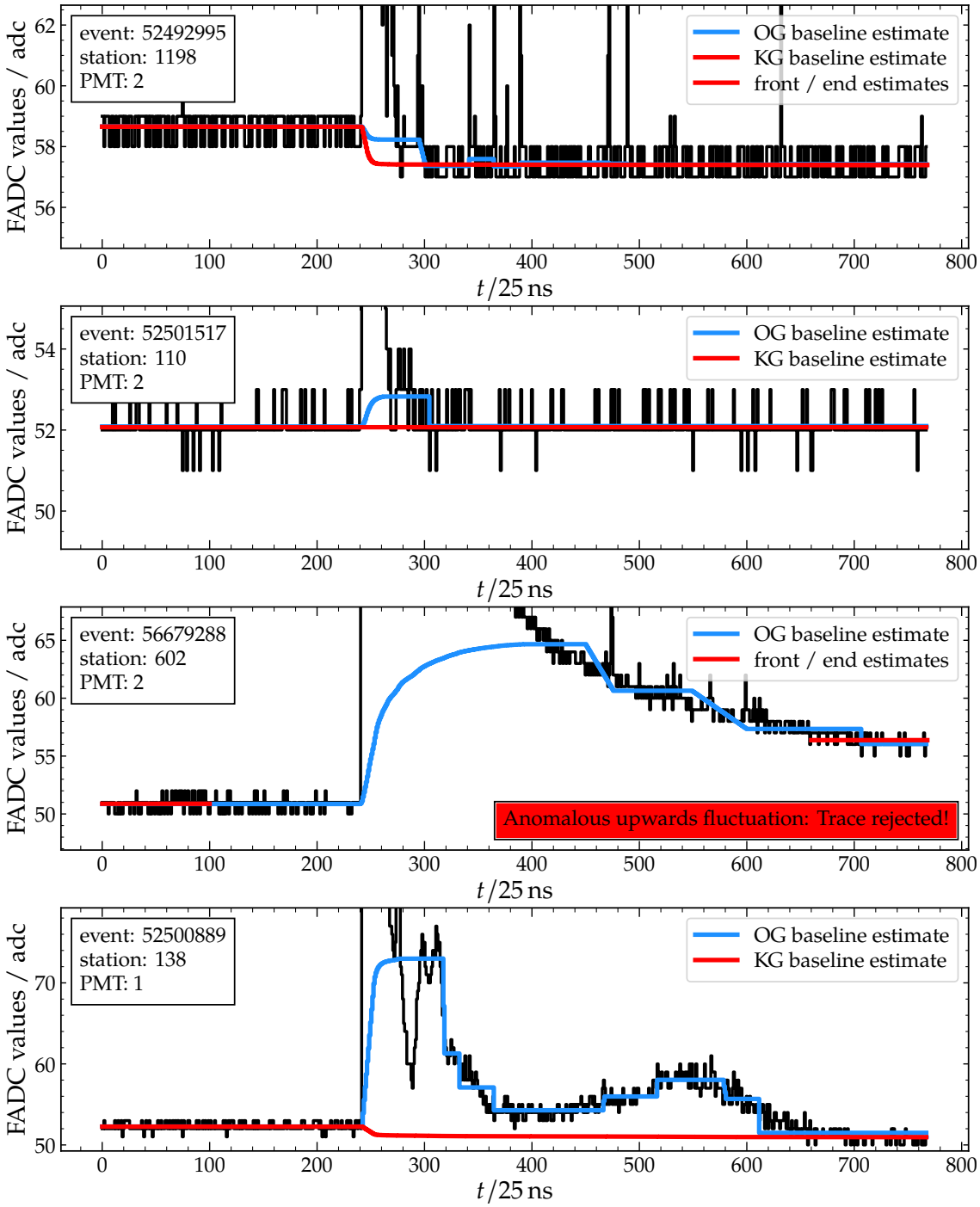

Figure 3.22: Example traces with the baseline estimate of the `BaselineFinderOG` module of Offline and the `BaselineFinderKG` module. At the beginning of the trace, the baseline estimates are similar but start to deviate as soon as the signal starts. *From top to bottom:* Charge-linear interpolation. Robust estimation of a constant baseline. Rejection due to anomalous upward fluctuation. Charge-linear interpolation.

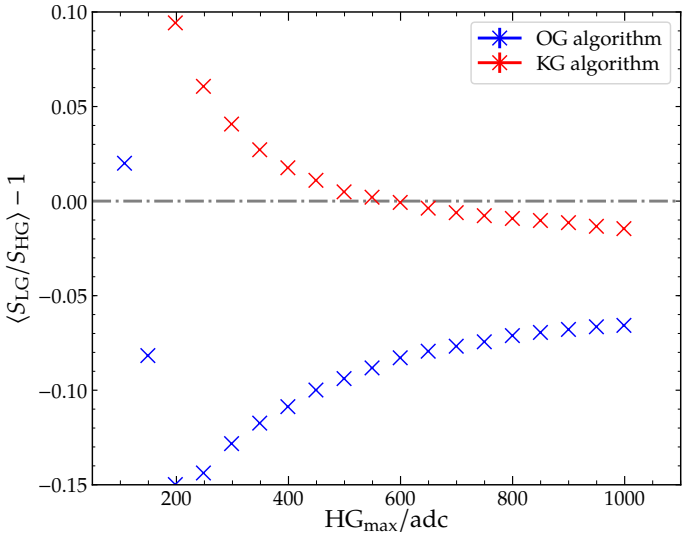

Figure 3.23: The KG algorithm (red) improves the systematic difference between the LG and HG signals. At the transition point from HG to LG at an $ADC_{max} = 1023$, a negative bias of approximately 1.5% remains.

3.1.5. Conclusions

It was shown that a large part of the systematic bias in the LG and HG signals originates from estimating the baseline of the time traces. The OG baseline algorithm, as well as the CDAS algorithm, tries to find flat signal pieces and connects them. A new physically-motivated KG baseline algorithm was introduced, which accounts for undershoot after large signals and is robust against accidental signal contributions outside the signal region. By determining two robust estimates of the baseline at the beginning and the end of the trace, the trace can be checked for anomalous baseline fluctuations. The PMT will be removed from the reconstruction in such cases. Depending on the relative difference between the two estimates, the magnitude of the undershoot was determined, and the interpolation method to use for the baseline was decided. The KG algorithm has been shown to work exceptionally well on simulated traces and also significantly improves the ratio between the HG and LG signals in measurements. This algorithm is now included in $\overline{\text{Off}}\underline{\text{line}}$ as the new `BaselineFinderKG` module and is part of the default reconstruction sequence.

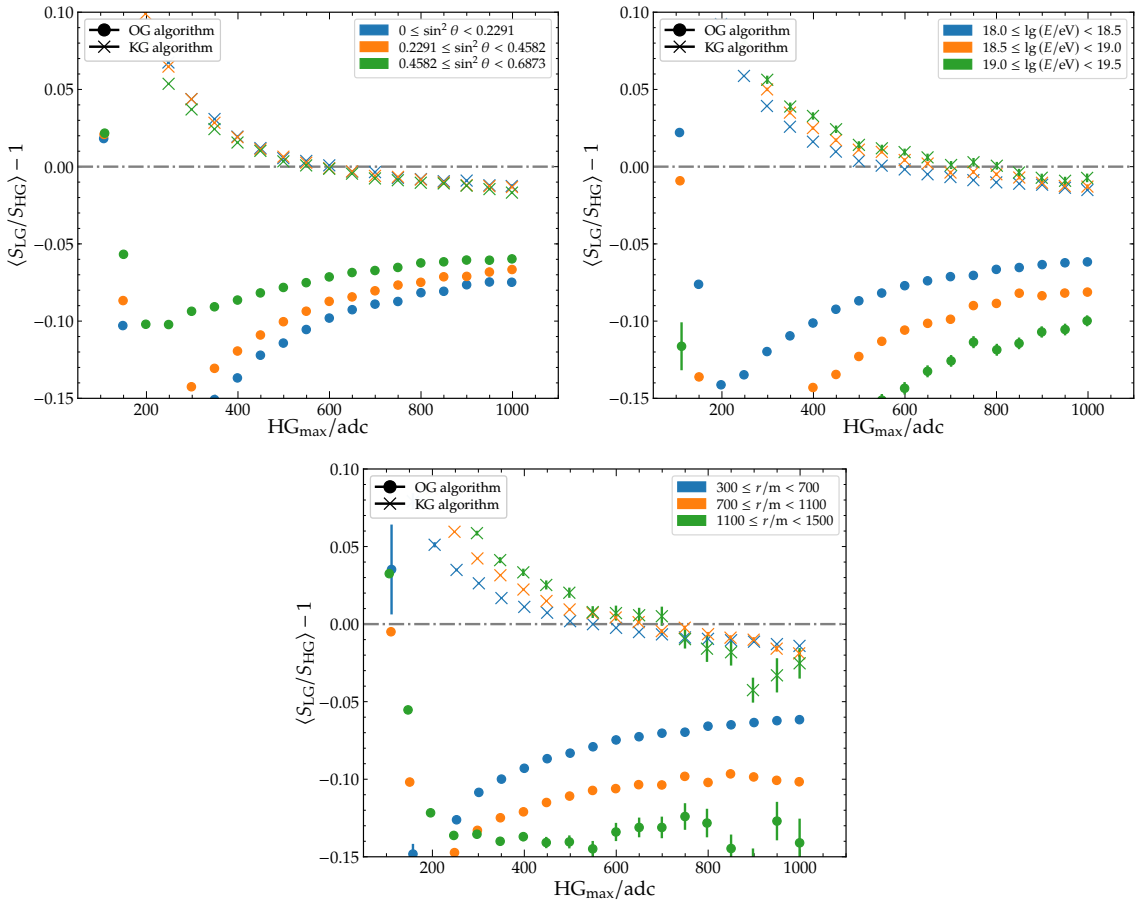

Figure 3.24: Comparisons of the low-to-high-gain ratio $S_{\mathrm{LG}}/S_{\mathrm{HG}}$ for different zenith angles θ, energies E, and distances r for the OG algorithm (circles) and the KG algorithm (crosses). While for the OG algorithm a strong dependence on zenith angle θ (left), energy E (right), and distance to the shower axis r (bottom) is visible, this dependency almost vanishes when using the KG algorithm.

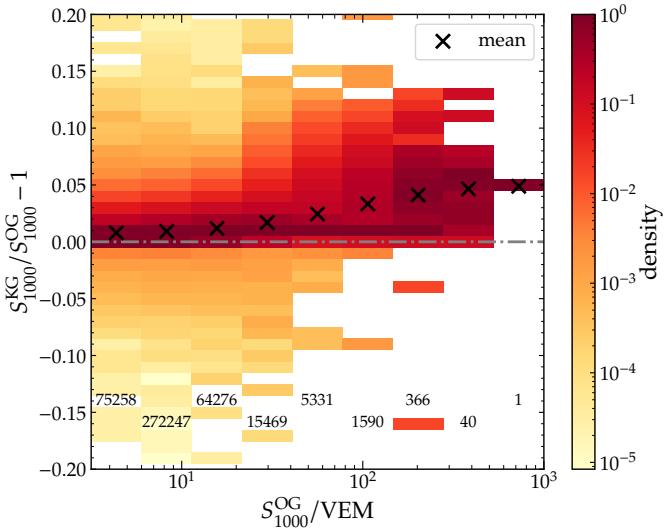

Figure 3.25: Comparison between the values reconstructed for S_{1000} using the OG (S^{OG}_{1000}) and the KG (S^{KG}_{1000}) algorithms. The color axis of each S^{OG}_{1000} column is normalized to the bin with the most entries. The total number of entries in each column is given at the bottom of the plot. With increasing values of S_{1000}, the KG algorithm leads to increasingly higher values of reconstructed S_{1000} than the OG algorithm.

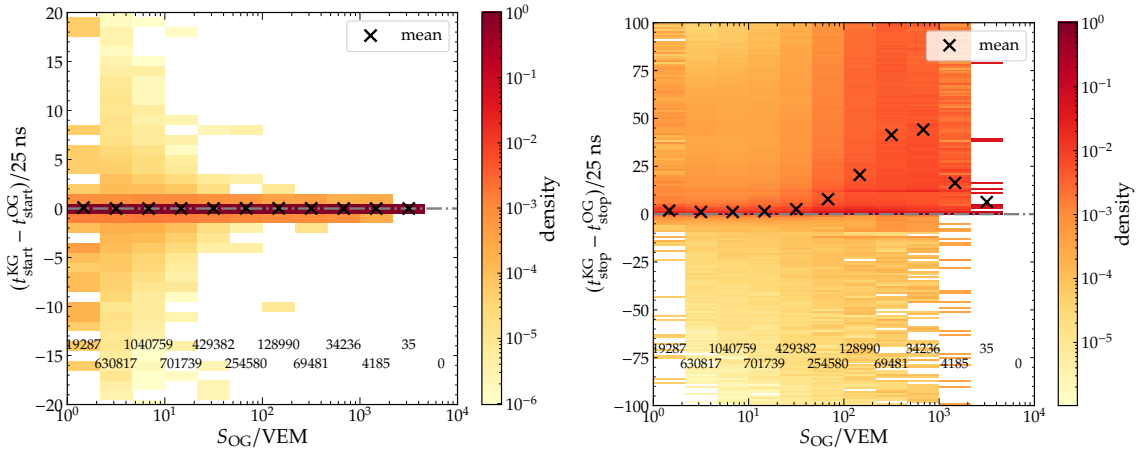

Figure 3.26: For large station signals S_{OG}, the start times t^{OG}_{start} and t^{KG}_{start} do not significantly change between both algorithms. The color axis of each S_{OG} column is normalized to the bin with the most entries. The total number of entries in each column is given at the bottom of the plot. The difference in the stop times t_{stop} between the two algorithms increases for larger station signals S_{OG}, reaching up to 50 time bins (1.25 µs) on average.

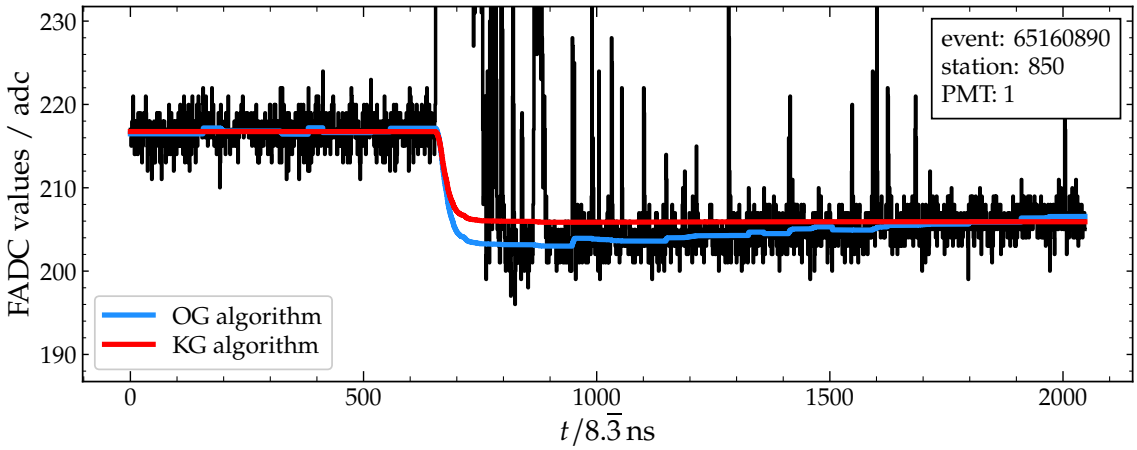

Figure 3.27: The KG algorithm for UBs computes a constant front and end piece of the time trace and makes a charge-linear interpolation between them. The OG algorithm tries to identify flat pieces in the trace and interpolates the baseline between these pieces, resulting in a varying baseline. For this example of a UUB trace both algorithms produce a sub-optimal estimate of the baseline, justifying an improvement.

3.2. Extensions for New Electronics and Detectors

The KG baseline algorithm was developed based on a physically motivated model of baseline behavior. Without any signal present in a trace, the baseline of such a trace can be assumed to be constant. Nevertheless, after a signal, the baseline of photomultipliers drops, resulting in an undershoot that recovers exponentially with a characteristic decay time τ. For the UB, the undershoot recovery takes about 300 µs, followed by an overshoot of the baseline, although with a smaller amplitude than for the undershoot. This overshoot slowly decreases over a time span of up to 1 to 1.5 ms [70, 69]. The total trace length of UB traces is 19.2 µs, and thus, comparing this time to the aforementioned time scales, the baseline after the undershoot can be safely assumed constant. On the contrary, in the UUB, the recovery of the undershoot is visible due to the shorter decay times, as can be seen in Fig. 3.27. The nominal decay times in the HG are around 100 µs and around 270 µs in the LG. However, this excludes the AC coupling at the PMT base, and thus, diverging results are to be expected for the decay times. The KG baseline algorithm for UBs cannot take the recovery of the undershoot into account. Only a constant front and end baseline estimate based on the truncated mean of the first and last 100 bins of the trace is calculated. Depending on the absolute difference ΔB between these estimates, a baseline is charge-linearly interpolated between the front and end estimates. On the other hand, the OG baseline algorithm identifies various flat pieces and interpolates between them, resulting in a varying baseline estimate that roughly follows the recovery seen in the UUB traces. However, as it was shown in the previous chapter, the baseline estimates of the OG baseline algorithm result in false estimates of the baseline due to erroneous flat piece determination and should not be used. Therefore, an extension of the KG baseline algorithm is needed to account for the shorter decay times of the UUB.

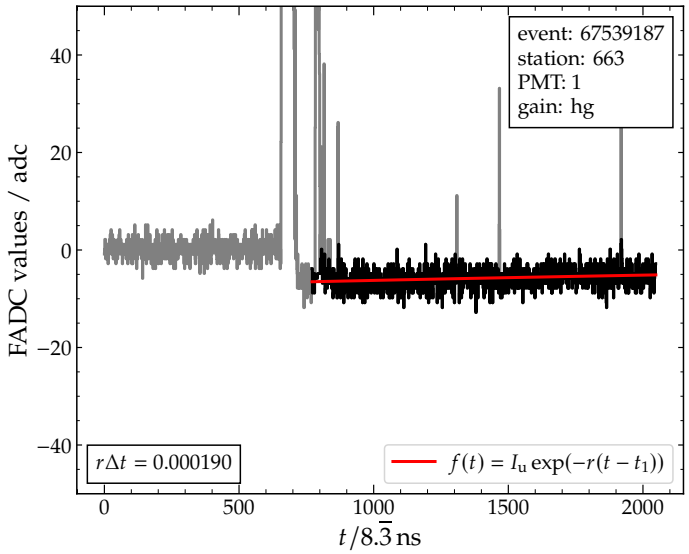

Figure 3.28: Example final fit of the decay rate r and undershoot amplitude I_u of a trace. After an initial fit, all signal contributions in the trace that do not belong to the baseline are removed (in grey) and a final fit of the decay function is performed.

3.2.1. Determination of the Decay Time of the Large PMTs

The decay times of multiple events between October 2021 and June 2022 are extracted from the UUB traces. The amplitude of the undershoot is proportional to the size of the signal that precedes them. A small signal will not produce a significant undershoot and thus the decay time can not be determined reliably. A cut on the charge of the preceding signal is applied to select events with a significant amplitude of the undershoot, such that the decay time can be fitted well. A detailed description of how this cut is chosen is given in Appendix A.2. This leaves us with a set of 134 313 HG traces. Since the data set is too small to include a sufficient number of LG traces with a significantly large undershoot, the following analysis is performed purely on HG traces. An exponential decay of the form of

$$f(t) = I_u \exp(-r(t - t_1)) \tag{3.17}$$

is used for the fit, where r is the decay rate (which is the inverse of the decay time) and I_u denotes the amplitude of the undershoot immediately after the preceding signal, i.e. at time t_1. First, a robust baseline estimate of the front baseline is performed, as it was previously described in Section 3.1.2. This estimate is then subtracted from the trace for the subsequent fit of the trace. As a rough approximation for t_1, the first bin after the trace maximum where the trace becomes negative is used and half a microsecond is added to avoid any remnants of the shower signal. The amplitude of the undershoot I_u and the decay rate r are determined in an initial fit. After the first fit has been performed, the trace can be cleaned from unwanted signal contributions to improve the quality of a second fit. Using the results from the initial fit, the decay term is subtracted from the trace. Similarly to the estimation of the robust baseline at the beginning of the trace, the mode of the trace is determined and all signal, exceeding a threshold of

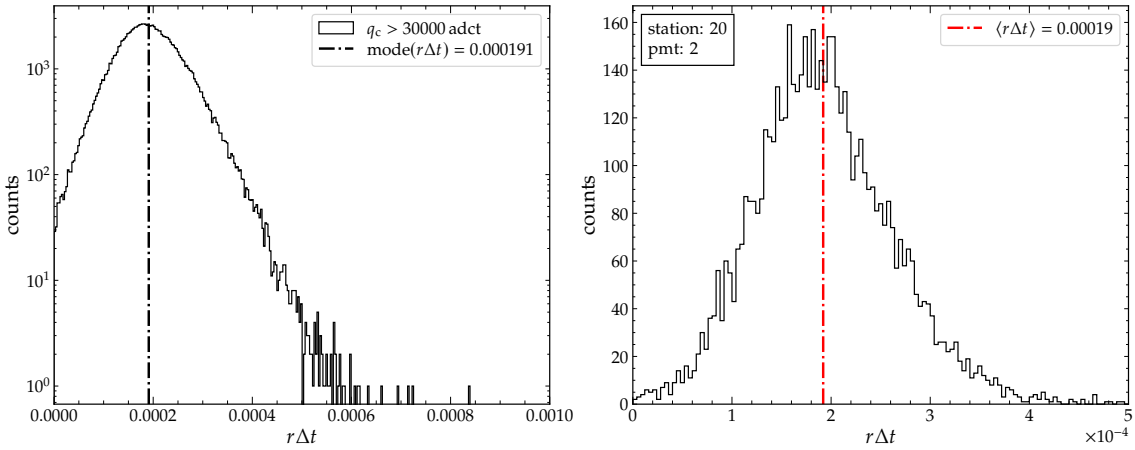

Figure 3.29: The distribution of $r\Delta t$ for all PMTs of all stations (left) and for specific PMTs (right) covers a wide range of decay rates.

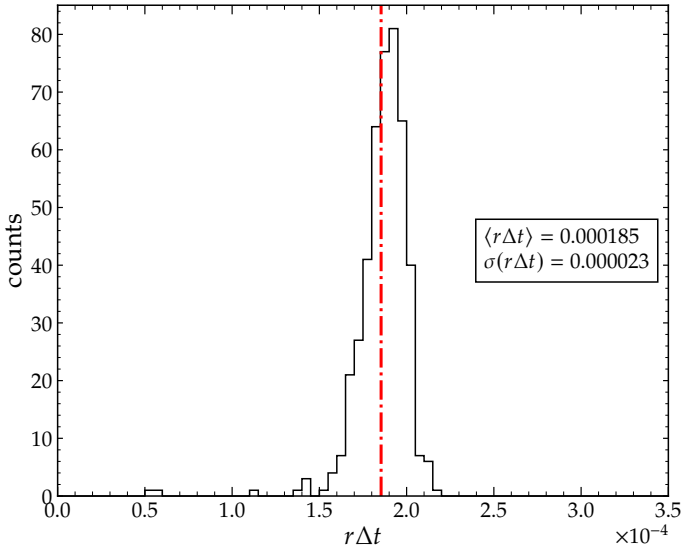

Figure 3.30: By calculating for each PMT of each station the most likely decay time, a universal constant, valid for all PMTs, can be estimated if the spread between the single PMTs is small enough. For 451 PMTs from 183 different UUB stations the average decay rate is $\langle r\Delta t = 1.85{\times}10^{-4} \rangle$ with a standard deviation of $\sigma = 0.23{\times}10^{-4}$, thus a universal and constant decay rate can be assumed for all PMTs.

$\pm 2\sigma$ relative to the mode is removed. The fit of I_u and r is then repeated with the cleaned trace. The resulting fit can be seen in Fig. 3.28. A further selection of the data and identification of "bad" PMTs can be done by using both fit parameters I_u and r, and is discussed in Appendix A.3.

The distribution of all fitted decay rates r is shown in Fig. 3.29-left. The maximum of this distribution is around $r\Delta t = 1.91{\times}10^{-4}$, with 95% of the decay rates being in the interval of $0.7{\times}10^{-4}$ to $3.4{\times}10^{-4}$. The sampling time of Δt for the UUB traces is $8.\bar{3}$ ns. For each station and PMT, the mode of $r\Delta t$ is determined, if at least 30 fits were performed. In Fig. 3.29-right the histogram and the mean is shown for a specific station and PMT.

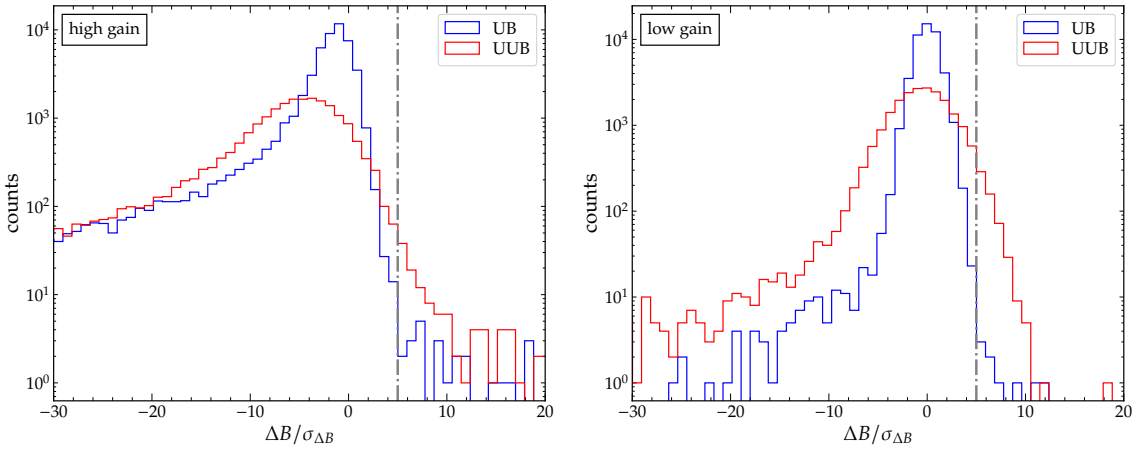

Figure 3.31: The distribution of $\Delta B/\sigma_{\Delta B}$ of 2 days of data for HG (left) and LG (right) traces varies for UB and UUB. For the UUB an increased fraction of traces have a ΔB larger than $+5\sigma_{\Delta B}$.

Fig. 3.30 shows the estimated decay rates for a total of 451 PMTs from 183 different UUB stations. The mean of the distribution is at $r\Delta t = 1.85{\times}10^{-4}$ with a standard deviation of $\sigma = 0.23{\times}10^{-4}$. Since this distribution is rather narrow, a global decay rate $r\Delta t = 1.85{\times}10^{-4}$, based on the mean of the distribution, is assumed. This rate can be converted to a decay time τ, which evaluates to

$$\tau = \frac{1}{r} = \frac{\Delta t}{r\Delta t} \approx 45\,\mu\text{s} \tag{3.18}$$

with the standard deviations of $\sigma = -4.9\,\mu$s and $\sigma = +6.4\,\mu$s.

3.2.2. Changes to the Core Algorithm

A few changes have to be implemented in the KG baseline algorithm in order to correctly estimate the baselines of UUB traces. While the total time length of the trace remains approximately the same, the sampling bin width is decreased from 25 ns down to $8.\overline{3}$ ns, which results in an increase of the number of bins from 768 to 2048. The sample window for the estimation of the front and end baseline is thus increased from 100 to 300 bins. After both baseline parts have been determined, the undershoot ΔB and baseline error $\sigma_{\Delta B}$ are determined and an interpolation method is chosen. While for the UB algorithm, a PMT is rejected if $\Delta B > +5\sigma_{\Delta B}$, for the UUB this threshold has to be raised due to an increase of the fluctuations in ΔB, as shown in Fig. 3.31. For two days of data, two sets of 50 926 traces from UB and 21 657 traces from UUB are analyzed. In the UB 0.07% of the HG traces and 0.02% of the LG traces have a ΔB larger than $+5\sigma_{\Delta B}$. For the UUB however, 0.63% of the HG traces and 2.63% of the LG traces have a ΔB larger than $+5\sigma_{\Delta B}$. This increase is a consequence of oscillations in the baseline. An example trace is shown in Fig. 3.32. The oscillation of the baseline leads to a bimodal distribution of the FADC values. During the calculation of B_{front} and B_{end}, the algorithm truncates the trace relative to its mode. However, if there are oscillations present in the baseline, a single mode can not be estimated and the trace will be truncated

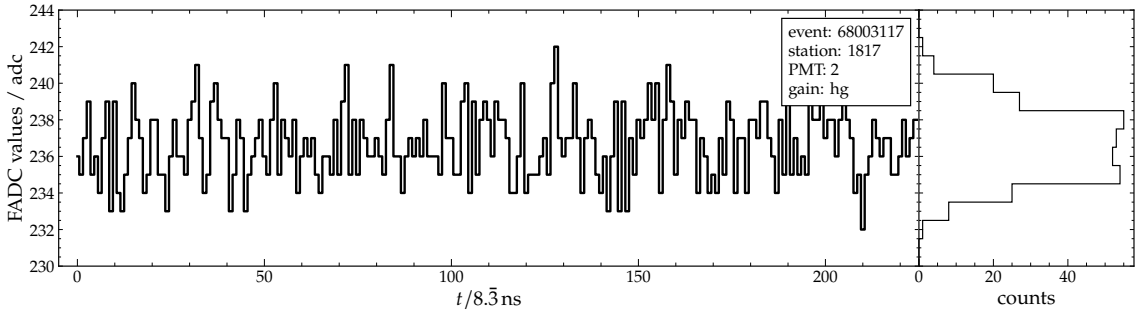

Figure 3.32: In UUB traces, oscillations of the baseline are visible (left), which causes a bimodal distribution of the FADC values (right). The estimation of a front and end baseline thus results in an increase of ΔB.

around one of the two modes of the distribution, leading to an increased difference between B_{front} and B_{end}. To compensate, the upper threshold for ΔB is therefore chosen as $+10\sigma_{\Delta B}$ for the UUB. In the case of a significant undershoot with $0 > \Delta B \geq -1\sigma_{\Delta B}$, a minimum difference of 200 adc counts between the trace maximum and the front baseline estimate B_{front} is needed to execute the charge-linear interpolation of the baseline with the modification described below. After a time-linear interpolation of the baseline has been performed, yielding a baseline $b_i^{(0)}$, the baseline of the charge-linear interpolation can be calculated as

$$b_i^{(j)} = B_{\text{front}} + \epsilon_i^{(j)} \Delta B, \tag{3.19}$$

where ϵ_i is the fraction of the cumulative charge q_i in the total charge q_{ref}

$$\epsilon_i = \frac{q_i}{q_{\text{ref}}}, \tag{3.20}$$

where $q_{\text{ref}} \equiv q_{1898}$ is the integrated total charge with a decay kernel of the baseline-subtracted trace and runs all the way up to the center bin of the end baseline estimate, which is at the index $i = 1898$. Since there is a decay of the undershoot after the signal, an exponential kernel has to be added when calculating q_i so that

$$q_i^{(j)} = \sum_{k=0}^{i} (T_k - b_k^{(j-1)}) \exp\left(-\frac{\Delta t(i-k)}{\tau}\right) \tag{3.21}$$

where the previously determined universal decay time is $\tau = 45\,\mu\text{s}$ and the indices run over the time bins of size Δt. In the case of large decay times, the exponential term becomes 1 and the equation is the same as for the UB baseline estimation. The UB algorithm can thus be reproduced by setting $r = 0$. The calculation of the

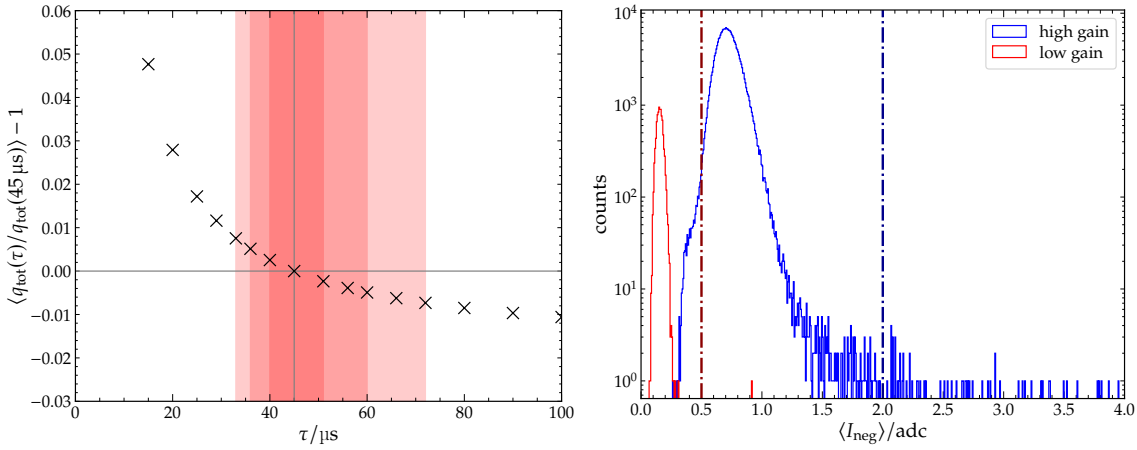

Figure 3.33: *Left:* Bias $\langle q_{tot}(\tau)/q_{tot}(45\,\mu s)\rangle - 1$ of the total charge relative to the total charge for $\tau = 45\,\mu s$. In red 1, 2, and $3\,\sigma$ deviations from $\tau = 45\,\mu s$ are shown. *Right:* Mean negative amplitude $\langle I_{neg}\rangle$ of the baseline-subtracted trace for HG (blue) and LG (red). The threshold of the maximum allowed $\langle I_{neg}\rangle$ is plotted in dash-dotted lines. If $\langle I_{neg}\rangle$ should exceed the threshold, the PMT is rejected.

baseline can be made more efficient with the following relation:

$$q_{i+1}^{(j)} = \sum_{k=0}^{i+1}(T_k - b_k^{(j-1)}) \exp\left(-\frac{\Delta t((i+1)-k)}{\tau}\right) \tag{3.22}$$

$$= (T_{i+1} - b_{i+1}^{(j-1)}) + \exp\left(-\frac{\Delta t}{\tau}\right) \sum_{k=0}^{i}(T_k - b_k^{(j-1)}) \exp\left(-\frac{\Delta t(i-k)}{\tau}\right) \tag{3.23}$$

$$= (T_{i+1} - b_{i+1}^{(j-1)}) + \exp\left(-\frac{\Delta t}{\tau}\right) q_i^{(j)}. \tag{3.24}$$

After a baseline has been determined, a check on the mean negative amplitude $\langle I_{neg}\rangle$ of the baseline-subtracted trace is performed, as previously described in Section 3.1.2. For the UBs the thresholds of the maximum $\langle I_{neg}\rangle$ are set to the standard deviation of the traces $\sigma \approx 0.5$. For the UUBs the standard deviation of the LG traces does not change. However, the HG traces have a higher standard deviation of $\sigma \approx 2$. If $\langle I_{neg}\rangle$ exceeds the standard deviation, the PMT is rejected as bad PMT.

3.2.3. Impact of the Improved UUB Algorithm

As shown in Section 3.2.1, the decay rate r, and thus the decay time τ, varies on the PMT level only to a small degree, justifying using only one universal decay rate for all PMTs for all stations. Nevertheless, the systematic errors have to be checked. For a set of 114 484 traces the baseline is estimated multiple times for a varying τ. The total charges $q_{tot}(\tau)$ of the traces are then calculated and compared to the trace with the baseline estimate that is performed with the universal decay time $\tau = 45\,\mu s$. The resulting bias relative to $q_{tot}(45\,\mu s)$ is shown in Fig. 3.33-left. For decay times that are larger than the estimated universal decay time, the observed

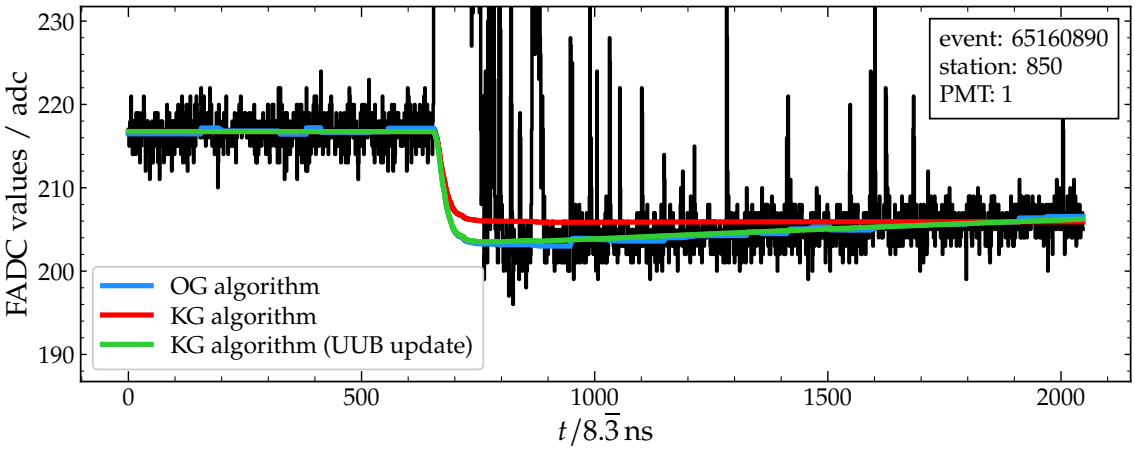

Figure 3.34: Comparison of the estimated baselines of OG algorithm (blue), KG algorithm (red), and the updated KG algorithm for UUBs (green). With the extension of the algorithm, the recovery of the undershoot of the trace is now estimated correctly.

bias asymptotically approaches the limit of −2%. If the decay times are smaller the bias increases exponentially. At approximately $\tau = 20\,\mu s$, the bias relative to the universal decay time is at around +2.7%. However, these biases hold only for the comparison of the total signal and can be much higher for certain time intervals of the traces. In Fig. 3.33-right the distribution of the mean negative amplitude $\langle I_{neg} \rangle$ of the baseline-subtracted trace is shown for HG and LG traces. More than 99% of the traces are below the threshold of 2 and 0.5 adc respectively.

Fig. 3.34 shows a comparison of estimated baselines between the OG algorithm, the KG algorithm, and the updated version of the KG algorithm. While previously the KG algorithm could not take the undershoot recovery into account, the extension now allows for an undershoot recovery, using a constant universal decay time.

In Fig. 3.35 the LG to HG signal ratio is shown as a function of the HG trace maximum HG_{max}, using 41 065 traces from 6507 events between October 2021 and July 2022. At $HG_{max} = 4096$ the HG saturates and the LG is used instead. The bias in the last bin, and thus the bias at the transition from HG to LG, is for the OG algorithm at around −0.6% and for the KG algorithm at around 0.6%.

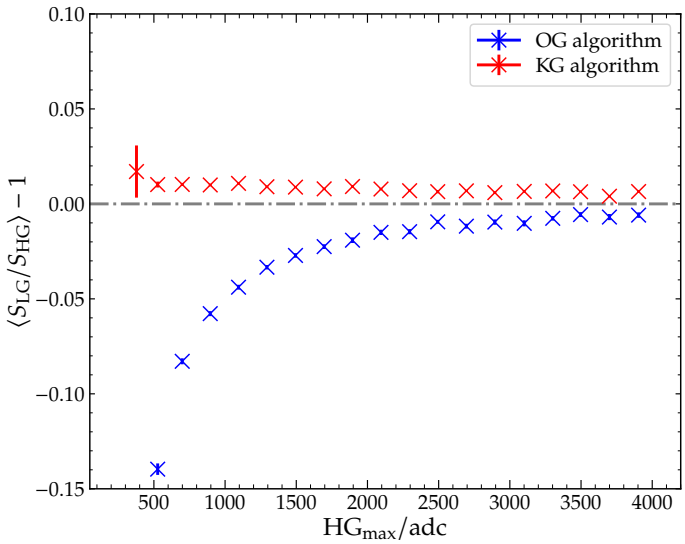

Figure 3.35: The ratio between signals from LG and HG traces as a function of the maximum bin entry HG_{max} in the HG channel, which indicates how close the HG channel is to the saturation. At the transition from HG to LG in the last bin 4095, the OG and KG algorithms for UUB both result in a similar bias of about 0.6%.

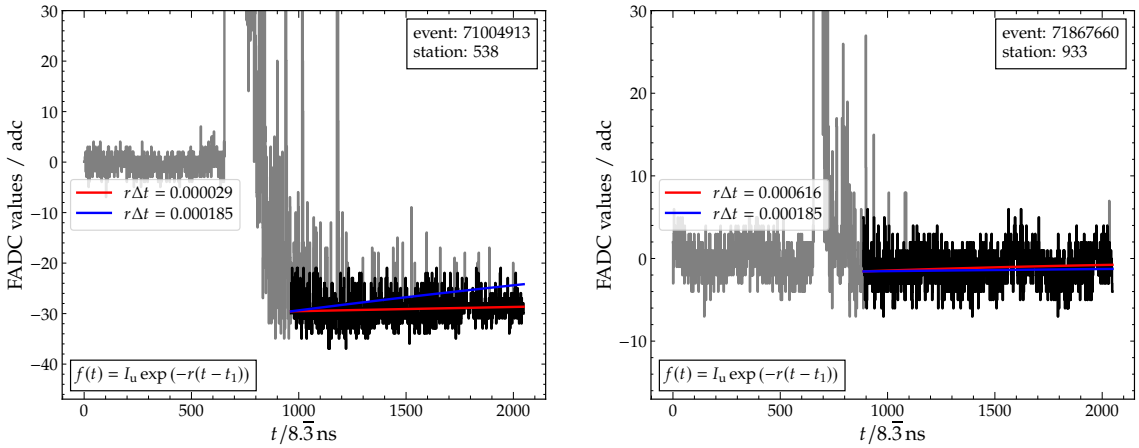

Figure 3.36: Final fit of the decay rate r and undershoot amplitude I_u of two sample traces. After an initial fit, all signal contributions in the trace are removed (in grey), and a final fit of the decay function is performed, shown with the red curve. For comparison, the blue curve shows the fit for a WCD decay rate using $r\,\Delta t = 0.000185$.

3.2.4. Adjusting the Algorithm for the SSD

In the previous chapter, a universal decay constant $\tau = 45\,\mu s$ was determined for the UUB WCD PMTs since station-to-station differences were determined not to be meaningful. However, an open question remains whether the SSD baseline can be assumed to stay constant after a significant signal is recorded or the decay time of the undershoot is small enough that a baseline algorithm with a decay of the undershoot similar to the WCD needs to be used.

The decay time is determined following the same procedure as in Section 3.2.1. The amplitude of the undershoot I_u and the decay rate r are determined in multiple fitting steps. The resulting fit for two sample traces is shown in Fig. 3.36. A fit is also included, using $r\,\Delta t = 0.000185$ (which corresponds to $\tau = 45\,\mu s$), which was determined for the WCD as a comparison. This value is incompatible with the SSD trace. The sampling time Δt for the UUB traces is $8.\bar{3}$ ns. The SSD trace of Fig. 3.36-right shows oscillations in the baseline. Due to these oscillations, the fit results of $r\Delta t$ can exhibit quite large fluctuations.

Small signals do not produce a significant undershoot, making them unreliable in determining the decay time. To select events with a significant amplitude of the undershoot, a cut on the charge q_c of the preceding signal is applied, which allows for a well-fitted decay time. The cut is set to require at least a charge of $q_c = 12\,000$ adct. This results in a set of 24 248 SSD traces. The distribution of all fitted $r\,\Delta t$ is shown in Fig. 3.37-left, with the maximum of this distribution being around $r\,\Delta t = 1{\times}10^{-5}$. Approximately 95% of the decay rates fall within the interval of $-3{\times}10^{-4}$ to $4{\times}10^{-4}$. In Section 3.2.1, the maximum of the distribution of $r\Delta t$ was found for the WCD to be around $1.91{\times}10^{-4}$. Thus, the rate of the SSD is about nineteen times smaller than that of the WCD. Additionally, the distribution of $r\Delta t$ for the SSD is centered around 0, which means that the decay of the undershoot cannot be observed in the traces and the baseline remains constant after a significant signal. A station decay rate is calculated to estimate whether

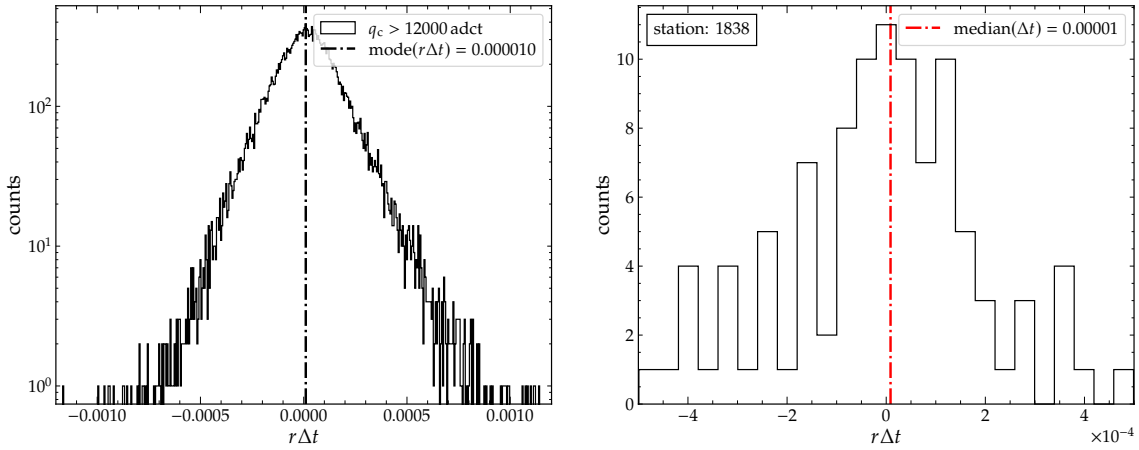

Figure 3.37: The distribution of $r\,\Delta t$ for measurements by the SSDs of all stations (left) and for station 1838 (right) covers a wide range of decay rates.

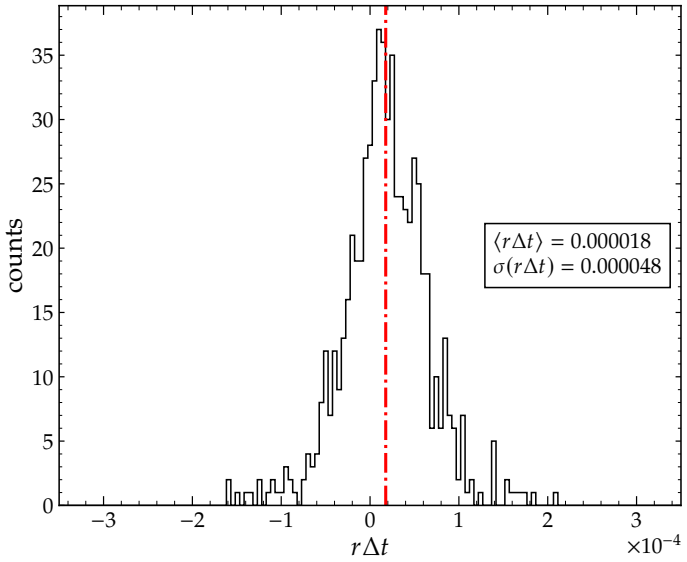

Figure 3.38: By calculating the most likely decay rate for each station, a universal constant, valid for all stations, can be estimated. For 648 UUB stations, the average decay rate is $\langle r\Delta t \rangle = 1.8{\times}10^{-5}$ with a standard deviation of $\sigma = 4.8{\times}10^{-5}$.

the decay rate is constant or fluctuating for individual stations. The median of $r\Delta t$ for each station is determined if at least 15 traces for a station are present. Fig. 3.37-right shows the distribution and the median of $r\Delta t$ for station 1838.

Fig. 3.38 displays the estimated median decay rates for 648 UUB stations. The mean of the distribution is at $r\Delta t = 1.8{\times}10^{-5}$ with a standard deviation of $\sigma = 4.8{\times}10^{-5}$. This mean rate can be converted to a decay time τ, which evaluates to

$$\tau = \frac{1}{r} = \frac{\Delta t}{r\Delta t} \approx 472\,\mu\text{s}. \tag{3.25}$$

This decay time exceeds the WCD decay time for the UUB by a factor of almost 10. For 5% of the stations, the estimated median decay times are smaller than 92 µs.

Table 3.2: The average decay times $\langle\tau\rangle$, as well as the 95th percentile $P_{95\%}$ changes for different selection cuts.

min. charge	min. traces	$\langle\tau\rangle$/µs	$P_{95\%}$/µs	N_{stations}	σ_{height} / adc	σ_q / %
$q_c > 8000$ adct	15	569	72	913	0.15	1.2
$q_c > 8000$ adct	30	448	86	482	0.12	1.0
$q_c > 12\,000$ adct	15	472	92	648	0.17	0.9
$q_c > 12\,000$ adct	30	351	96	271	0.17	0.9
$q_c > 16\,000$ adct	15	342	93	431	0.23	0.9
$q_c > 16\,000$ adct	30	257	90	90	0.24	0.9

For this case, the minimal error σ_{height} in the height of the peaks of a signal when using a constant baseline can be calculated. The constant baseline is calculated as the average of the last 300 bins of a trace. The start time t_1 is set at 0 µs, which will lead thus to the evaluation of the baseline estimate at $t_{\text{end}} \approx 10.83$ µs. σ_{height} can therefore be calculated as

$$\sigma_{\text{height}} = I_{\text{u}} \exp(-t_{\text{end}}/\tau) - I_{\text{u}} \exp(-t_1/\tau). \tag{3.26}$$

e_{height} is dependent on the undershoot amplitude I_{u} and, therefore, on the total signal of the trace. Using $q_c = 12\,000$ adct as an estimate, results in an error of $\sigma_{\text{height}} = 0.17$ adc. The maximum error σ_q of the total integrated signal of the trace can be calculated as 0.9%.

The total average decay times $\langle\tau\rangle$ will change depending on the cut on the charge q_c as well as the minimum number of required traces of a single station to evaluate the median decay rate and decay time. For different requirements on the minimal charge q_c and a minimum number of traces, the resulting average decay times $\langle\tau\rangle$, the 95th percentile $P_{95\%}$, the total numbers of stations in the dataset and the error on the pulse heights as well the total integrated signal is given in Table 3.2.

A histogram of the FADC values of several baseline-subtracted traces of the UUB SSDs at different time bins is shown in Fig. 3.39, using a constant baseline after the undershoot. Large shower signals or signal contributions of late-arriving shower particles can cause the tail in the distributions of the FADC values. The amplitude of the tail becomes smaller for distributions at later times. Additionally,a Gauss function is fit to each distribution between -6 and 6 adc to determine the mode and the standard deviation σ of each distribution. For all three fits, a mode between 0.01 and 0.04 adc is obtained and a standard deviation of around 2 adc. Thus, there is no significant difference in the estimated baseline at different time intervals after the undershoot observed. Therefore, the mean baseline in the traces of UUB SSDs after the undershoot can be assumed *constant* on the timescale of the SSD traces.

3.2.5. Conclusions

The KG baseline algorithm has been extended to properly estimate baselines for UUBs. An additional exponential kernel has been added to the charge integration

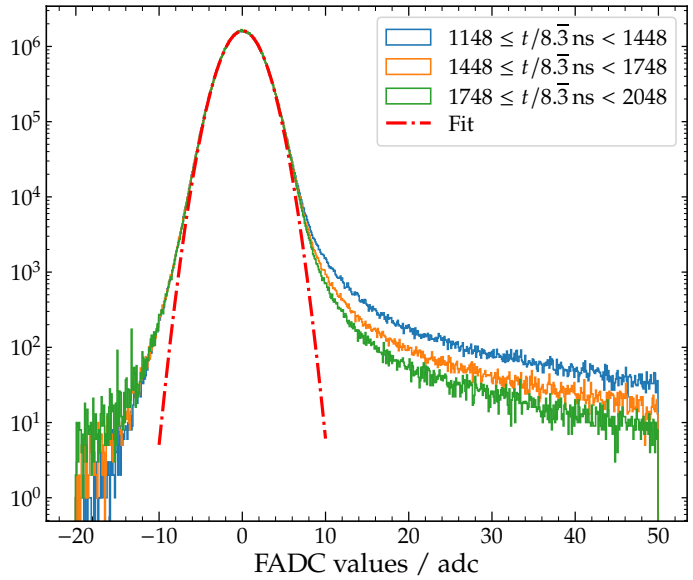

Figure 3.39: The distributions of the FADC values of baseline-subtracted traces between different time intervals after the undershoot are shown. The mode of all three distributions is between 0.01 and 0.04 adc and it is determined by a fit of a Gauss function to each distribution. Therefore, the assumption of a constant baseline in the traces of the UUB SSDs is favored.

to account for recovering the undershoot in the UUB traces. A universal decay constant τ that fits most PMTs has been determined to be $\tau = 45\,\mu\text{s}$ with the standard deviation of $\sigma = -4.9\,\mu\text{s}/+6.4\,\mu\text{s}$. An upper limit on the negative bias of the total signal, relative to the determined baseline with $\tau = 45\,\mu\text{s}$, is reached in the case of large decay times (as for UBs) at around 2%. For shorter decay times, this bias increases exponentially with a positive bias of 2.7% at around $\tau = 20\,\mu\text{s}$. It was shown that this updated algorithm reconstructs the trace shape and its baseline well and that the gain ratio $\langle S_{\text{LG}}/S_{\text{HG}}\rangle$ is on average biased only by 0.6% at the transition point from HG to LG. It was observed that while the undershoot in the UUB WCD traces showed visible decay, no decay was visible for the SSDs. The decay time for the UUB SSD was determined to be 472 µs, on average, which is far larger than the time window of the UUB traces. Therefore, using a constant baseline assumption for the SSD after large signals is suggested, as is done in the KG baseline algorithm for the WCD traces of the UB.

3.3. Correcting Residual Biases in the Gain Ratio

With the development of the KG baseline algorithm and its extensions in the previous chapters, the systematic bias in the LG and HG signals was reduced to -2.9% and 0.6% for the UB and UUB traces, respectively. The remaining bias shall also be resolved by further analyzing possible factors. In the following, the signal ratio is denoted as

$$R = \frac{S_{\mathrm{LG}}}{S_{\mathrm{HG}}}, \tag{3.27}$$

i.e. as the ratio of the LG signal to the HG signal. For the purposes of this study, the signals S_{LG} and S_{HG} do not have to be fully calibrated in VEM units, since the common VEM-peak or VEM-charge factors would cancel in the ratio R. The appropriate integral of the HG FADC trace T^{HG} with the corresponding baseline B^{HG} already subtracted is used as the S_{HG} signal

$$S_{\mathrm{HG}} = \sum_{i=a}^{b} (T_i^{\mathrm{HG}} - B_i^{\mathrm{HG}}), \tag{3.28}$$

where a and b are defining the integration window and are determined by the trace-cleaning algorithm in the Offline calibration modules. Denoting with s_{LG} the similar sum for the LG FADC trace,

$$s_{\mathrm{LG}} = \sum_{i=a}^{b} (T_i^{\mathrm{LG}} - B_i^{\mathrm{LG}}), \tag{3.29}$$

the HG-equivalent LG signal S_{LG} can be defined as

$$S_{\mathrm{LG}} = G\, s_{\mathrm{LG}}, \tag{3.30}$$

where G is the gain ratio with which the LG FADC trace has to be scaled to match the (analog) dynamic range of the HG channel. Therefore, one is left with

$$R = \frac{G\, s_{\mathrm{LG}}}{S_{\mathrm{HG}}}, \tag{3.31}$$

from where it is clear that the signal ratio R can be influenced by two factors:

(a) the estimation of the baselines B^{HG} and B^{LG}, and

(b) the gain ratio G.

The bias $\langle R \rangle - 1 = \langle S_{\mathrm{LG}}/S_{\mathrm{HG}} \rangle - 1$ is shown in Fig. 3.40 as a function of the maximum signal in the HG channel, $\mathrm{HG}_{\mathrm{max}}$, which provides an indication of how close the HG channel is to the HG-LG transition that takes place at $\mathrm{HG}_{\mathrm{max}} = 1023$ adc for the UB. The signal ratio R_{tr} at this HG-LG transition point is of interest, i.e.

$$R_{\mathrm{tr}} = \langle R \rangle|_{\mathrm{HG}_{\mathrm{max}} \equiv 1023}. \tag{3.32}$$

For the UUB the transition point is at $\mathrm{HG}_{\mathrm{max}} = 4095$ adc. Fig. 3.40-left shows the bias $\langle R \rangle - 1$ for the UB and Fig. 3.40-right shows the bias for the UUB. For the

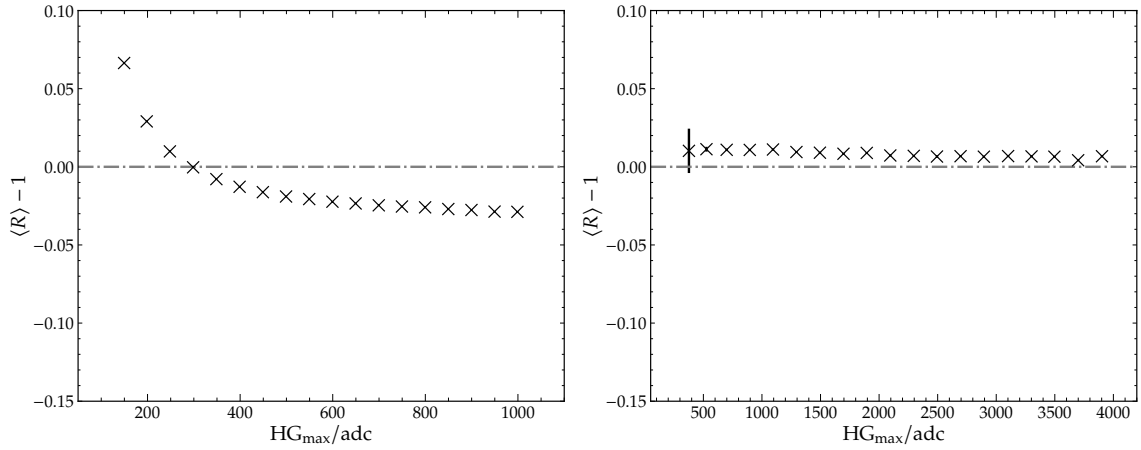

Figure 3.40: *Left:* The bias of the signal ratio $\langle R \rangle - 1$ of UB stations (where $R = S_{\mathrm{LG}}/S_{\mathrm{HG}}$) as a function of $\mathrm{HG}_{\mathrm{max}}$. The change from using the LG signal instead of the HG occurs when $\mathrm{HG}_{\mathrm{max}} \geqslant 1023$. Right before this transition, a residual bias of around −2.9% can be observed. *Right:* For comparison, the bias for the UUB stations is shown. A smaller residual bias of ∼+0.5% can be observed at the HG-LG transition.

UB a non-negligible bias $R_{\mathrm{tr}} - 1 = -2.9\%$ is observed at the transition, while for the UUB a small bias of $R_{\mathrm{tr}} \approx +0.5\%$ persists. Therefore, this remaining bias in R_{tr} might be caused by the gain ratio G, which is used to scale the LG signals when the HG channel is saturated. From this point onward, is is assumed that any remaining bias observed in the signal ratio R is only due to the bias in gain ratio G, defined in Eq. (3.30). In the preceding sections, the bias originating from the estimation of the baselines has been resolved. It can be assumed that with the new baseline algorithm only the factor (b) above remains relevant so that the relative online gain correction G'/G should be equal to the observed bias in the signal ratio at the transition point, i.e. $G'/G = R_{\mathrm{tr}}$, where G' is the corrected gain.

For the UB, the gain ratio G is estimated by an online algorithm of the local station software which is described in Ref. [73]. This online algorithm is not trivial, since the HG and LG traces are shifted in time by approximately one-third of the sampling period, i.e. ∼25/3 ns or ∼8 ns, and might still exhibit some residual biases. This algorithm is currently in the UUB running and so the stations are sending the online estimate of G. The gain ratio G was fixed by the choice of the electronic components and should thus nominally correspond to a value of about 32 [51]. Furthermore, there were calls to fix G to a nominal value, measured in the UUB test stand.

3.3.1. Correction of UB Gain Ratio

In order to correct the gain ratio G, its bias has to be determined from the available signal ratio R data. Furthermore, it should be determined whether a global correction is sufficient or if corrections for individual stations/PMTs must be performed. Fig. 3.41 shows the bias $\langle R \rangle - 1$ for all three PMTs of a chosen station. For PMT 3 (green markers), R_{tr} is almost bias-free, while R_{tr} of PMT 1 and 2 (red and blue markers) has a bias of about −12%. These differences could be caused

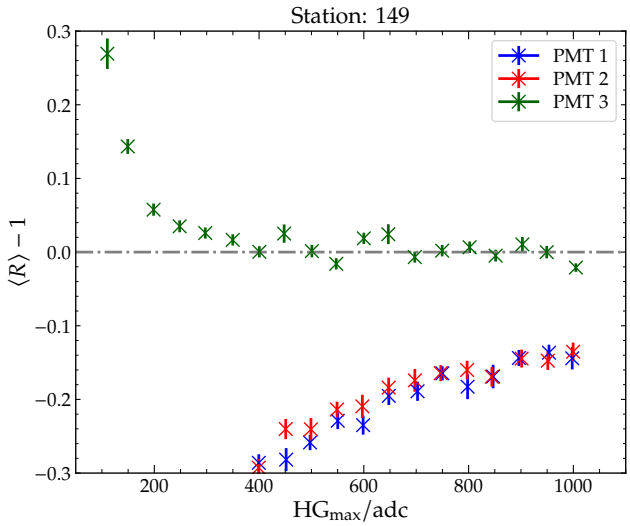

Figure 3.41: Bias $\langle R \rangle - 1$ as a function of the maximal signal in any single bin $\mathrm{HG}_{\mathrm{max}}$ in the HG channel for the three PMTs of station 149, using data between the years 2004 and 2022. The transition from HG to LG channel occurs for $\mathrm{HG}_{\mathrm{max}} \geqslant 1023$. PMT 3 is nearly bias-free at the point of the HG-LG transition, whereas the first two PMTs have a bias of about −12%.

by a non-optimal setting of the high voltage of the PMT or by a systematic error in the online gain-estimation algorithm. It can be concluded that a correction of the gain ratio has to be performed on the level of individual PMTs of each station.

Unfortunately, the signal ratio R seems to be changing with time. Fig. 3.42 shows the average bias $\langle R \rangle - 1$ for all PMTs of all stations as a function of $\mathrm{HG}_{\mathrm{max}}$ over many years. Between the years 2004 and 2005, the signal ratio R_{tr} at the transition has a bias of around −5%. This bias decreases to −3% in more recent years.

In Fig. 3.43, the signal ratio R_{tr} as a function of time is given for two chosen PMTs from two different stations for illustration purposes . For each year, an approximation for R_{tr} is obtained as an average of R of events with $\mathrm{HG}_{\mathrm{max}} \geqslant 650\,\mathrm{adc}$. The left plot shows an example of a PMT with a rather stable R_{tr}, which is not changing with time. The right plot shows an example of a PMT with a significant jump in R_{tr} between the years 2010 and 2011. These jumps are most likely caused by an exchange of the PMT or the electronics, or both. Since R_{tr} is not only different for each PMT but also varies with time, it was decided to build a small database and implement the gain-ratio corrections for each PMT of every station separately for each year.

For this database, the signal ratio R is extracted from all events for each station/PMT that has the HG trace with $\mathrm{HG}_{\mathrm{max}} \geq 650\,\mathrm{adc}$. Using a shorthand $x = (\mathrm{HG}_{\mathrm{max}}/\mathrm{adc} - 1023)/(1023 - 650 + 1)$, a linear function of the form

$$R(x) = k_{650}\, x + n_{650}, \tag{3.33}$$

is fitted to the N_{650} data points in each year separately to obtain an approximation of the signal ratio at the transition point $x \equiv 0$, i.e. $R_{\mathrm{tr}} \approx R(0) = n_{650}$. Additionally, the mean μ_{800}, as well as the median m_{800} and standard deviation σ_{800} of all R for

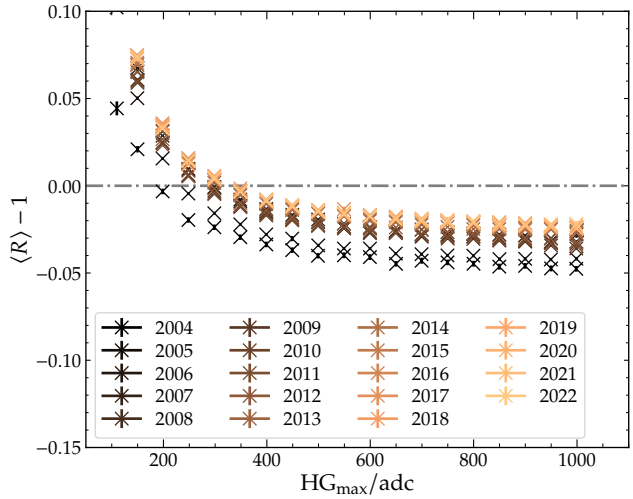

Figure 3.42: The signal-ratio bias $\langle R \rangle - 1$ as a function of the maximum signal $\mathrm{HG}_{\mathrm{max}}$ in the HG channel and its dependence over many years (early years darker, recent years lighter markers). The transition bias R_{tr} changes from around −5% to −3%. This is evidence, that a time-dependent correction of the gain ratio is necessary.

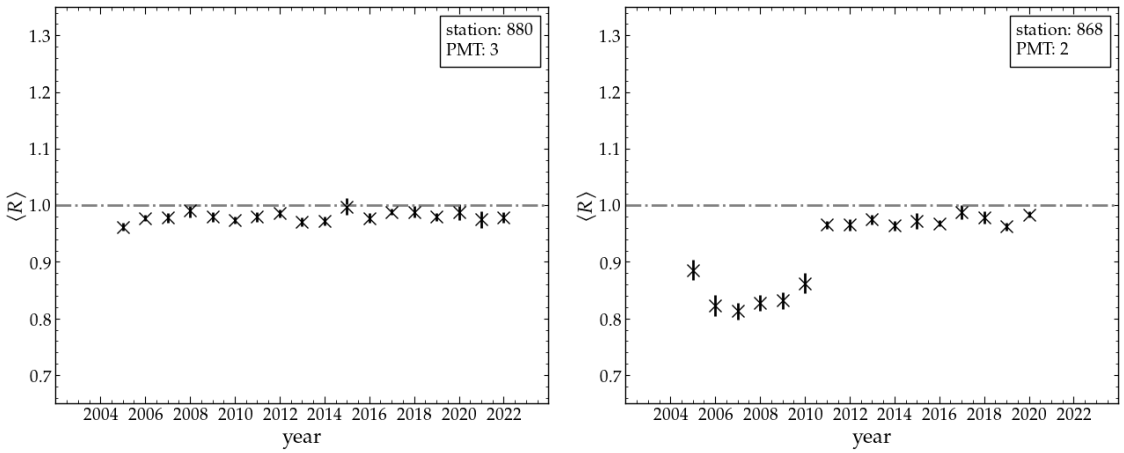

Figure 3.43: *Left:* PMT 3 of station 880 has a rather stable behaviour of R_{tr} over time. Note that an approximation to this R_{tr} is calculated for each year as an average of R of events with $\mathrm{HG}_{\mathrm{max}} \geqslant 650\,\mathrm{adc}$. *Right:* PMT 2 of station 868 which exhibits non-trivial changes in R_{tr}, possibly due to replacement of the PMT or the electronics.

N_{800} traces with $\mathrm{HG}_{\mathrm{max}} \geqslant 800\,\mathrm{adc}$ is calculated for each year. Fig. 3.44 shows an example of the fit for a chosen PMT in one selected year, where μ_{800} is given as a blue dash-dotted line while the fit from Eq. (3.33) is drawn as a red solid line. The offset n_{650}, the median m_{800}, and the mean μ_{800} are all suitable approximations for R_{tr} in a specific year. In the following, the criteria used to select between these three candidates is described.

The top-left plot of Fig. 3.45 shows the distribution of the number of events N_{800}. If N_{800} is larger than 5 (as indicated by the red dash-dotted vertical line), it is assumed that there is enough data to reliably determine the mean μ_{800}, the median m_{800}, and the standard deviation σ_{800}. To exclude strange outliers, which

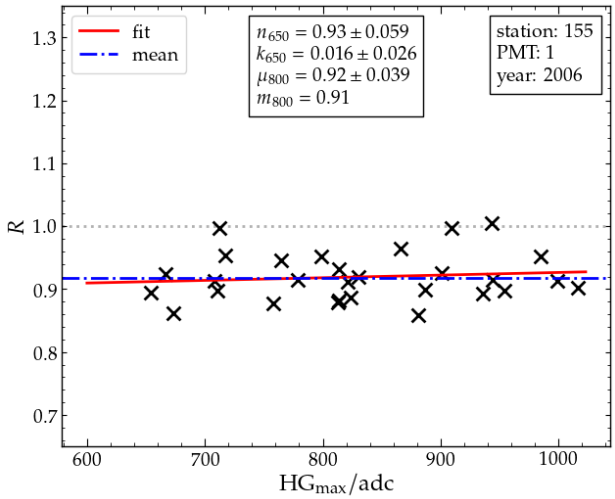

Figure 3.44: All signal ratios R (black crosses) as a function of the maximal signal HG_{max} found in the HG trace of PMT 1 of station 155 during the year 2006. A linear fit with the slope parameter k_{650} and n_{650} is shown in red. For $HG_{max} \geqslant 800$ adc the mean μ_{800}, median m_{800}, and standard deviation σ_{800} of R are calculated.

are mostly very noisy PMTs or PMTs with a very high baseline, the requirement that $N_{800} \leqslant 35$ is additionally imposed. The first criterion is thus $5 \leqslant N_{800} \leqslant 35$.

The top-right plot of Fig. 3.45 shows the distribution of the means μ_{800} (blue) and the medians m_{800} (red). It is required that the mean and median lie between 0.8 and 1.2 as the second criterion, which is the case for around 99.8% of all PMTs over all years. This immediately implies that the gain-ratio corrections will never be larger than 20%.

The bottom-left plot of Fig. 3.45 shows the distribution of the difference between the median and mean, $m_{800} - \mu_{800}$. When the electronics or the PMT are exchanged or altered during the course of a year, the distribution of R can have a large spread. To avoid these cases, it is additionally required $|m_{800} - \mu_{800}| \leqslant 0.085$, since otherwise these might be large outliers or the distribution has a fat tail or is bimodal. Only a fraction of 0.04% of all PMTs over the years do not fulfill this criterion.

The bottom-right plot of Fig. 3.45 shows the distribution of the standard deviation σ_{800}. $\sigma_{800} \leqslant 0.18$ is required to avoid distributions of R with a large spread, which is the case for 0.1% of all PMTs over the years.

If all the criteria above are met, the median m_{800} is used to correct the gain ratio of the PMT in this particular year.

Nevertheless, if the criteria above are not met and R_{tr} cannot reliably be determined from the data with $HG_{max} \geqslant 800$, i.e. close to the transition point (note that $1023 - 800 + 1 = 224$), the window of possible values to $HG_{max} \geqslant 650$ (now $1023 - 650 + 1 = 374$) is enlarged. In such a large window one cannot simply calculate the mean or the median since they will be biased by the trend in HG_{max}. This trend in $R(x)$ is removed in the first order if the dependence is fit with the linear function from Eq. (3.33). To use the result of this fit, additional quality criteria have to be applied.

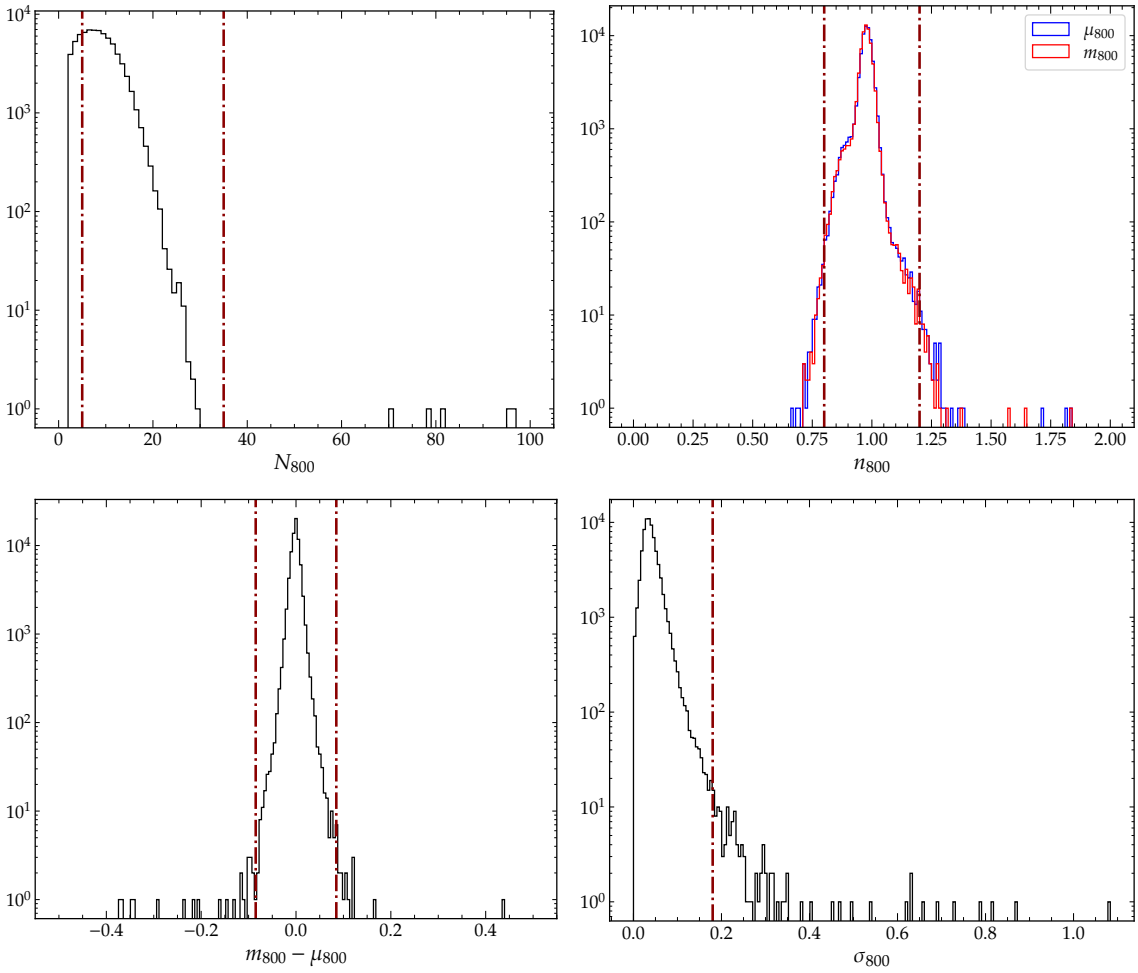

Figure 3.45: *Top-left:* The distribution of N_{800} for individual stations/PMTs/years. $5 \leqslant N_{800} \leqslant 35$ (vertical red lines) is required to reliably determine the mean μ_{800}, the median m_{800}, and the standard deviation σ_{800}. *Top-right:* The distribution of the mean μ_{800} (blue) and median m_{800} (red). Both values are required to lie between 0.8 and 1.2 (vertical lines). *Bottom-left:* The distribution of the difference $m_{800} - \mu_{800}$. An absolute difference smaller than 0.085 (vertical lines) is required. *Bottom-right:* The distribution of the standard deviation σ_{800}. σ_{800} must be smaller than 0.18 (vertical line).

For the fit, a minimum amount $N_{650} \geqslant 10$ of events is required, as well as a maximum amount of $N_{650} \leqslant 50$ events. The top plots of Fig. 3.46 show the distribution of the slope k_{650} and its fit error δk_{650}, along with the chosen threshold values as vertical lines. To avoid cases with a large change of R in the data, $|k_{650}| < 0.4$ and $\delta k_{650} < 0.2$ is required.

The bottom plots of Fig. 3.46 show the distributions of n_{650} and its fit error δn_{650}. Similarly to the $\mathrm{HG}_{\mathrm{max}} \geqslant 800$ constraints above, $0.8 < n_{650} < 1.2$ and $\delta n_{650} < 0.4$ is also required.

If these criteria are fulfilled, n_{650} is used as an approximation for R_{tr} for this station/PMT/year.

If none of the criteria above are met, R_{tr} is assumed and the gain ratio is effectively not corrected. In this case, the PMT signals stay unchanged and thus

identical to the previous data productions. The criteria can be summarized briefly:

condition	**use as R_{tr}**
$5 \leqslant N_{800} \leqslant 35$ and $0.8 < \mu_{800} < 1.2$ and $0.8 < m_{800} < 1.2$ and $\lvert m_{800} - \mu_{800} \rvert < 0.085$ and $\sigma_{800} < 0.18$	m_{800}
else	
$10 \leqslant N_{650} \leqslant 50$ and $\lvert k_{650} \rvert < 0.4$ and $\delta k_{650} < 0.2$ and $0.8 < n_{650} < 1.2$ and $\delta n_{650} < 0.4$	n_{650}
else	1

The station/PMT/year database, the criteria above, and the correction of the gain ratio R have been implemented in the new `SdGainRatioCorrector` module in the SD reconstruction sequence of Offline .

If the median m_{800} is used for the gain-ratio correction, the average correction and its spread can be obtained by calculating the mean and standard deviation of all m_{800} values in Fig. 3.45-top-right that remain after applying the selection criteria. In this case, an average correction of $(-2.88 \pm 3.44)\%$ is applied. If the offset n_{650} is chosen as the correction factor the corresponding mean correction and its spread is $(-2.92 \pm 3.93)\%$.

The results of the corrections are displayed in Fig. 3.47. Fig. 3.47-left shows the average signal ratio of the entire data set without (black) and with the correction (red) applied. The initial bias of -2.9% is with the corrections reduced to only -0.3%, thus the HG-LG transition is now almost bias-free. Fig. 3.47-right shows the distribution of the individual gain ratios R of the last two $\mathrm{HG}_{\mathrm{max}}$ bins of the left plot without the applied correction (black) and with the correction (red). Also given are the mean and standard deviation of the two distributions. Along with the reduction of the bias $\langle R \rangle - 1$, $\sigma(R)$ is also reduced from 0.055 down to 0.048 when applying the correction.

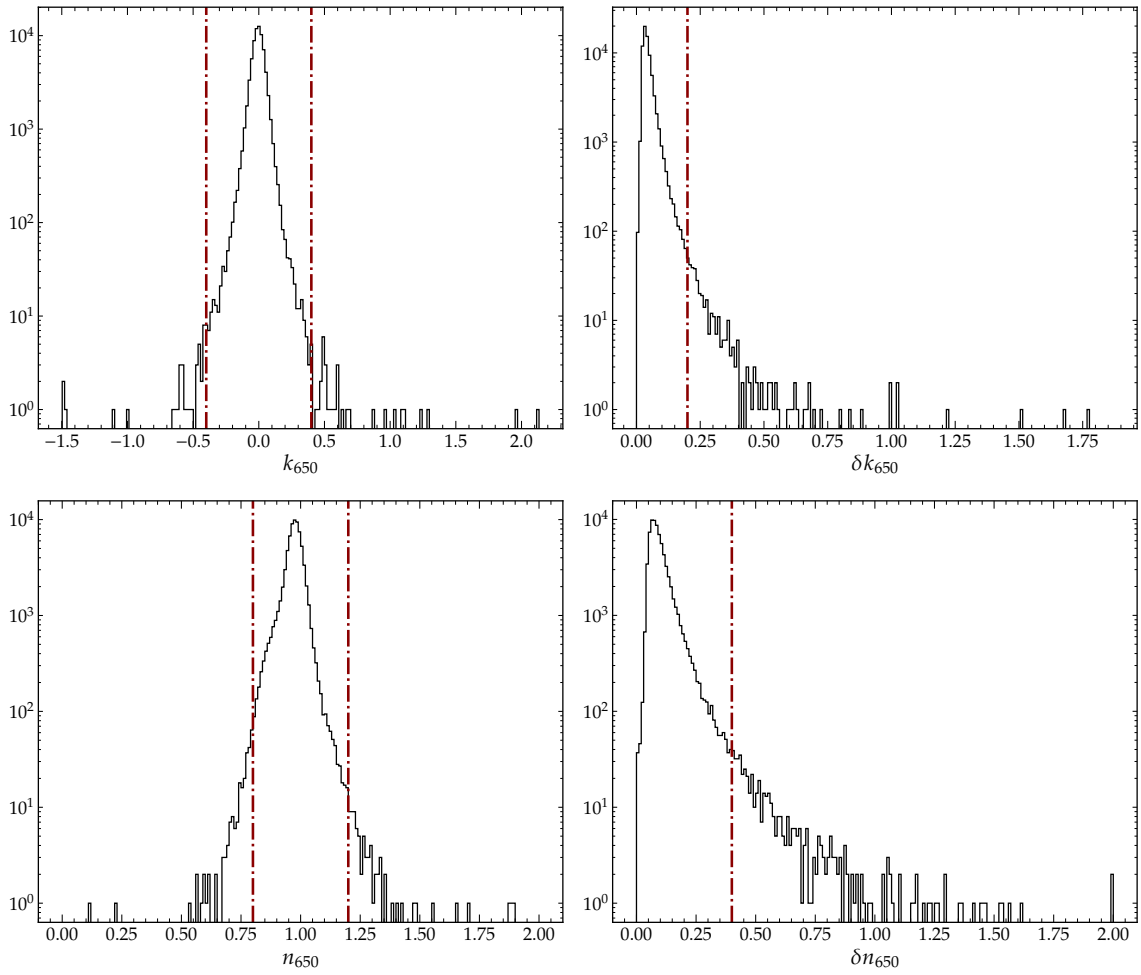

Figure 3.46: *Top-left:* Distribution of the slope k_{650} of the fits. *Top-right:* Distribution of the fit error δk_{650}. *Bottom-left:* Distribution of the offset n_{650} of the fits. *Bottom-right:* Distribution of the fit error δn_{650}. All selection criteria are denoted with vertical lines.

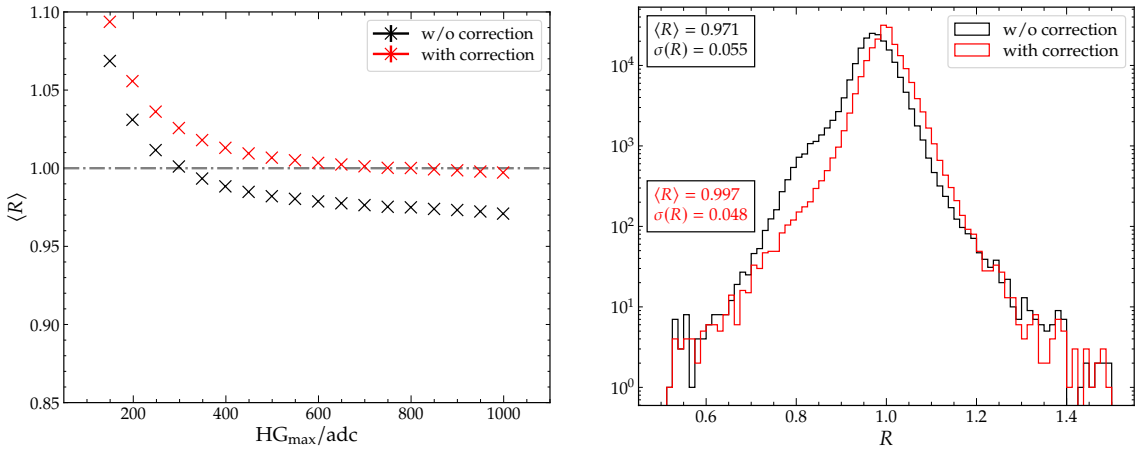

Figure 3.47: *Left:* Comparison of the mean $\langle R \rangle$ in HG_{max} bins with (red) and without (black) the correction of the gain ratio. *Right:* The distribution of all R entries in the last two bins of HG_{max} of the left plot. Without any correction, there is a residual bias of about -2.9% remaining. Applying the gain-ratio correction removes the bias and decreases the standard deviation of the distribution of R from 0.055 to 0.048.

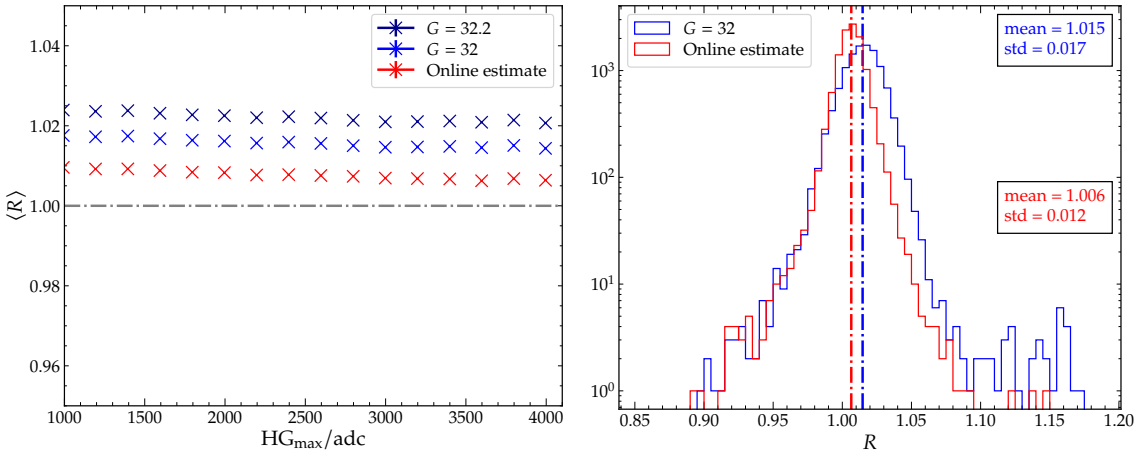

Figure 3.48: *Left:* The mean signal ratio $\langle R \rangle$ of all UUB stations (where $R = G\, s_{\mathrm{LG}}/S_{\mathrm{HG}}$) as a function of $\mathrm{HG}_{\mathrm{max}}$. The transition from HG to LG occurs when $\mathrm{HG}_{\mathrm{max}} \geqslant 4095$. *Right:* The distribution of all measured values of R of the last three bins of $\mathrm{HG}_{\mathrm{max}}$ from the left plot. The distributions for $G = 32.2$ and $G = 32$ are similar but shifted in R and thus only the distribution for $G = 32$ is included for better readability of the figure.

3.3.2. Correction of UUB Gain Ratio

In contrast to the UB, where the gain ratio is partially a property of individual PMTs, in UUB, only the electronic components determine the gain ratio G, which were chosen so that G approximately corresponds to 32. During a new set of measurements at the ESS test bench in Prague, the gain ratio G has been re-evaluated and is now estimated to be 32.2. For the UB, the signal ratio R was individually estimated for each PMT and each year due to the time dependence of G. The corresponding bias correction in the signal estimation is now in the `SdGainRatioCorrectorKG` module of Offline also applied on a per-PMT and per-year basis. For the UUB, it must be determined whether a correction factor for the gain ratio G is also needed and what kind of correction should be used. The possible choices are:

(a) use one globally fixed value of G for all PMTs and stations,

(b) use G from the online algorithm,

(c) use unique time-independent values of G for each PMT, or

(d) use individual gain corrections for each station and each year, as it is done for UBs.

The data set consists of 584 959 UUB traces from the years 2020 to 2023. The traces are taken from events with a reconstructed shower energy $\lg(E/\mathrm{eV}) \geqslant 18.0$, zenith angle $\theta \leqslant 56°$, and with a distance to the shower axis $\rho \leqslant 1500\,\mathrm{m}$. Fig. 3.48-left shows the dependence of the signal ratio R on the maximum signal $\mathrm{HG}_{\mathrm{max}}$ in the HG channel. This value indicates how close the HG channel is to the HG/LG transition, which occurs when $\mathrm{HG}_{\mathrm{max}} = 4095\,\mathrm{adc}$. At the point of transition from the HG to the LG, the signal ratio R has a smaller systematic difference between LG and HG when using the online estimate (red) instead of the gain ratio G fixed

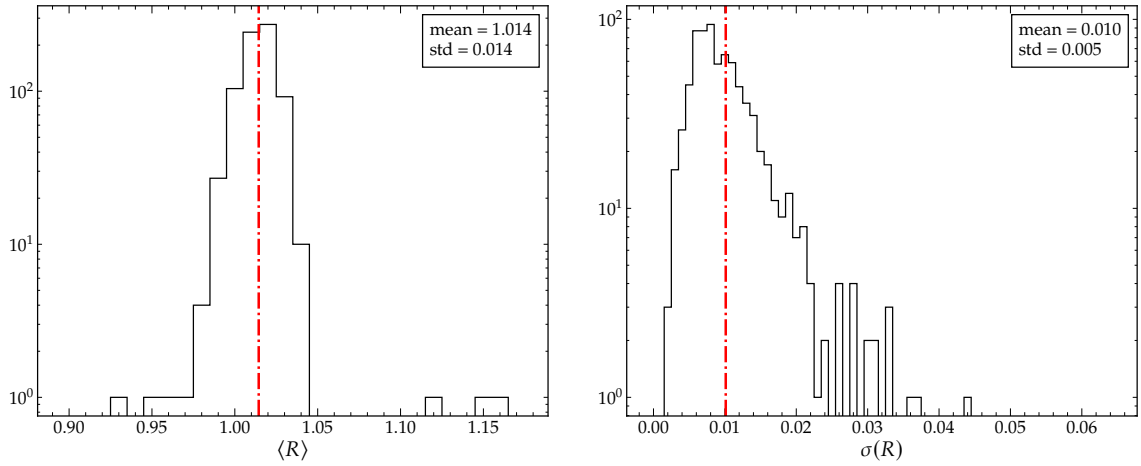

Figure 3.49: *Left:* Average signal ratio R as calculated for each PMT while using fixed gain ratio $G = 32$. The outliers above $\langle R \rangle = 1.1$ could be identified from the PMTs of a station with ID 1739. The outliers below $\langle R \rangle = 0.95$ could be identified from the PMTs of the station with ID 1221. *Right:* On average, the standard deviation of R for each station is around 1%, which consistent with the Prague measurements.

to the nominal value of 32 (blue) or globally optimized value of 32.2 (dark blue). In Fig. 3.48-right, the distribution of all entries from the last 3 bins of HG_{max} in Fig. 3.48-left is displayed. The standard deviation of R is approximately 1.2% when using the online estimate of G. However, the variance increases to 1.7% if G is fixed to 32.

The average value of R is calculated for each PMT when G is fixed to 32. The distribution of the average gain ratio $\langle R \rangle$ for each PMT is shown in Fig. 3.49-left, and the standard deviation of the gain ratio $\sigma(R)$ over the PMTs is shown in Fig. 3.49-right. Based on the distributions presented, it can be concluded that fixing G to 32 results in an average systematic difference between the HG and LG signal by 1.4% with a standard deviation of the mean signal ratios of 1% over the PMTs. Since the latter variation is relatively small, it can be concluded that the suggested options (c) and (d) above are not needed.

The values for the gain ratio G, obtained by the online algorithm, are presented in Fig. 3.50-left. G is approximately 31.7 on average, with a standard deviation of 0.4. These values show a discrepancy with the measured values obtained at the test bench in Prague. Outliers with $G < 30$ and $G > 33$ were identified, and it was found that they all belong to the PMTs of the station with ID 1739 and PMT 3 of the station with ID 1221. The distribution of G obtained by dividing HG and LG signals is shown in Fig. 3.50-right. The mean value of G is approximately 31.5 with a standard deviation of $\sigma_{\text{online}} = 0.5$. The measurements and those obtained in Prague have an average discrepancy of 2.2%. The fluctuation σ_{online} is substantially smaller than the corresponding fluctuations observed with a fixed $G = 32$. It can thus be safely concluded that option (a) is not the optimal choice.

The variation of the gain ratio G for different years, plotted in Fig. 3.51, indicates no significant time dependence. The mean values of G are approximately 31.60, 31.57, 31.56 and 31.53 for 2020 to 2023. A time-dependent gain-correction factor,

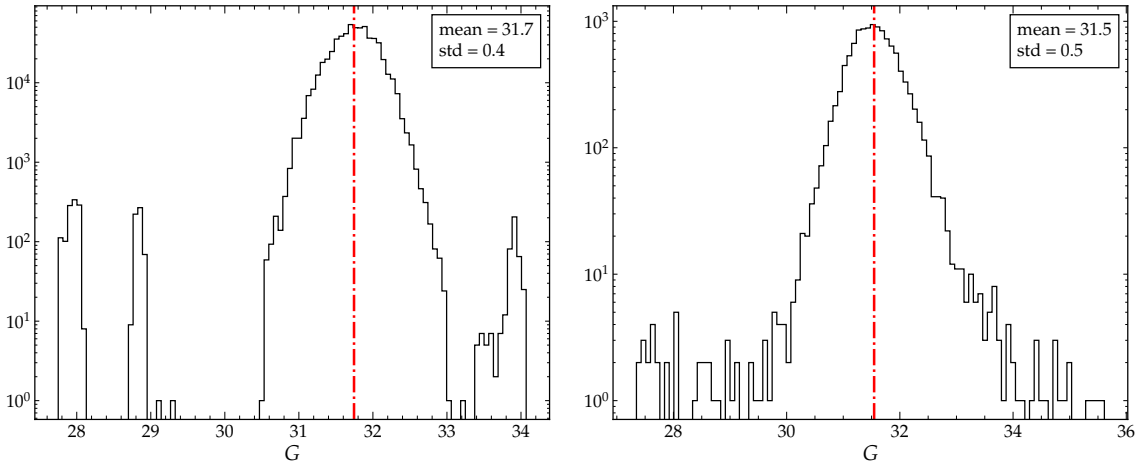

Figure 3.50: *Left:* The distribution of the estimated values of the gain ratio G from the online algorithm. G is on average around 31.7 and thus lower than the nominal value of 32 and the Prague measurement of 32.2. *Right:* The distribution of G, obtained by dividing the HG and LG signals.

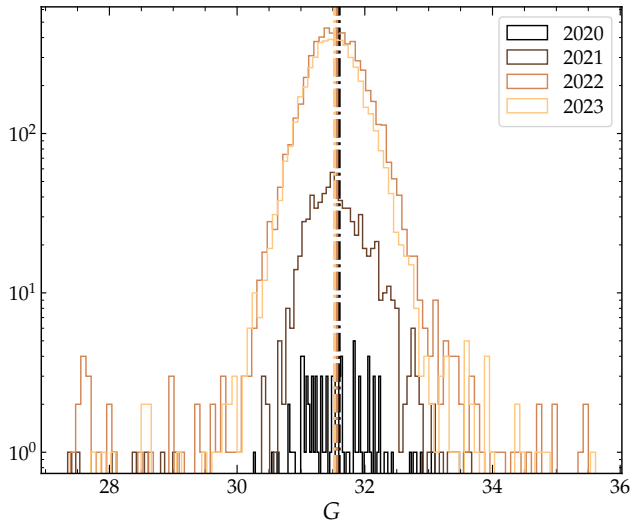

Figure 3.51: Evolution of the gain ratio G from years 2020 to 2023. In contrast to the UB, no significant change can be observed in UUBs over the four years; thus, no time-dependent correction is planned for now.

as was implemented for the UB, is not needed for the UUB, and for the time being, option (d) can be eliminated. However, using the online estimate of G instead of a globally fixed value results in slightly lower fluctuations $\sigma(R)$. Considering all the above results, (b) is proposed as the best option.

3.3.3. Conclusions

It was shown that the bias in the signal ratio R in the UB is due to biases in the gain ratio that differ from PMT to PMT and can be, in principle, different in each year. To unbias R, the gain ratio was determined individually for each PMT of each station in each year. A database of several useful correction-related parameters

was built and their necessary selection criteria were determined before applying them as the gain-ratio corrections. The new gain-ratio correction is implemented in the `SdGainRatioCorrector` module of Offline , which is now part of the standard SD reconstruction sequence of the Phase I data productions. The previously reported mean residual bias of −2.9% in the PMT signals close to the HG-LG transition is now reduced to −0.3%. In contrast, the standard deviation of the signal ratios is now reduced from 0.055 to 0.048.

For the UUB, a discrepancy of about 2.2% was shown between the gain ratio reported from measurements at the ESS test bench in Prague and estimates based on air shower measurements of the current AugerPrime data set taken since 2020. An individual correction for each PMT, as applied to the UB data, does not appear necessary because the standard deviation of the average R is only ∼1%, and no significant time-dependent changes were (yet) observed. The gain ratio obtained from the online algorithm of the local station software leads to a bias in R of approximately 0.5%.

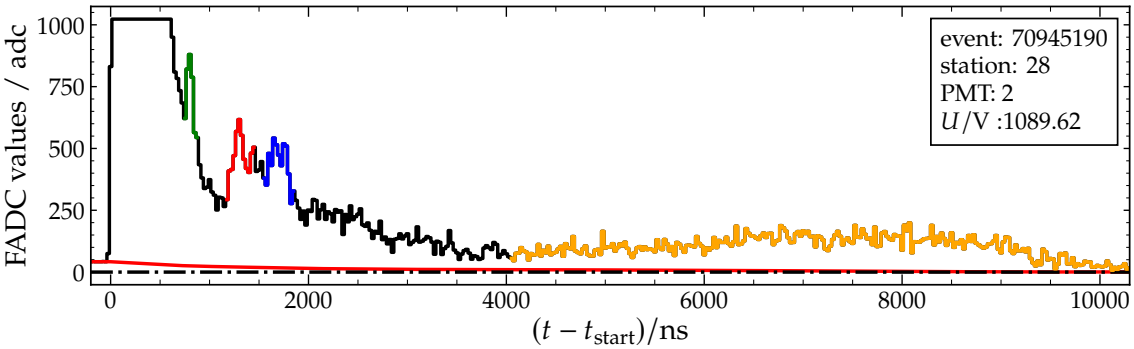

Figure 3.52: An example of a high-gain trace, taken by PMT 3 of station 28 during normal operation. The single (green), as well as the twin (red and blue) peaks and the long wave (yellow), are visible. Note the saturation of the high gain at the beginning of the trace. Time t is shifted to begin at start time t_{start}.

3.4. Understanding Delayed Peak Structures in WCD Traces

In highly saturated WCD traces, specific peaks are consistently observed after the bulk of the shower signal. An example trace is shown in Fig. 3.52. These peaks can be divided into three categories: a *single peak*, shown in green, *twin peaks*, shown in red and blue, and a *long wave*, shown in orange. The peaks themselves appear at characteristic times: about 800 ns after the start of the saturated signal for the single peak, 1.3 µs and 1.6 µs for the twin peaks, while the wave starts at around 4 µs and lasts until the end of the trace. A possible explanation for these peaks could be the afterpulsing of the PMTs due to ionized particles in them. Several studies on afterpulses in the PMTs have been performed, comparing the afterpulse rate to the manufacturer specifications [74, 75, 76]. It is of interest to further analyze these peaks and determine if they originate from afterpulsing effects and how large the impact of these effects is on the total signal of the traces. By measuring saturated traces generated in a laboratory environment, it shall be tested whether the UUB electronics and/or front end are responsible for the appearance of these features.

3.4.1. Discarding Electronics as the Source of Peak Structures

The measurement setup is shown in Fig. 3.53. To generate a signal that saturates the UUB electronics a Philips PM 5715 pulse generator with a 1 Hz to 50 MHz range is used. The signal input is a box function with variable pulse width and height. First, the pulse generator is connected to a LeCroy 9344 oscilloscope to properly adjust the width and height of the pulse. After the adjustment, the oscilloscope is disconnected and the UUB is directly connected to the pulse generator. For analysis, a set of 200 traces is then recorded with the UUB. The high gain saturates at about 60 mV. Three different voltages (125 mV, 2 V, and 4V) and four different pulse widths (200 ns, 400 ns, 600 ns, and 800 ns) are chosen for the measurement. Before the traces can be analyzed, the raw UUB traces have to be filtered, since an oscillation of 214 kHz of unknown origin is visible in these traces. Since no shielding of the UUB is used in the experimental setup, this wave

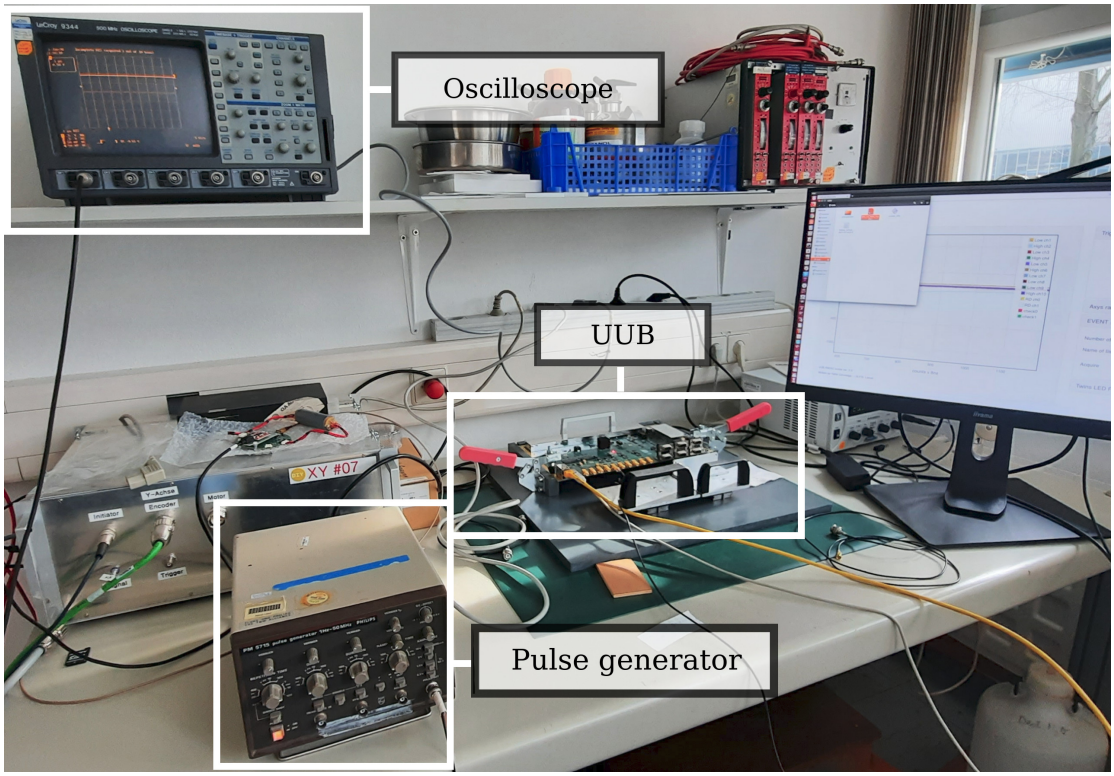

Figure 3.53: Measurement setup in the laboratory. A Philips PM 5715 pulse generator (bottom), LeCroy 9344 oscilloscope (top left), and a UUB in a test stand (middle). The traces were taken via the built-in web interface of the UUB and written on a USB stick.

could be caused by external interference. A detailed explanation of the procedure for determining the oscillation and filtering the traces is given in Appendix A.4.

In comparing the UUB traces with the output of the pulse generator as shown by the oscilloscope, a significant difference can be observed. While the pulse from the function generator quickly recovers to its original baseline, the UUB trace shows a persistent undershoot lasting long after the original pulse from the function generator. This is an expected behavior of the UUB electronics, where the recovery time of this undershoot is expected to be about 100 µs for the high gain.

None of the features shown in Fig. 3.52 are present in the traces taken with the function generator in the lab setup with the UUB. It was ruled out that the UUB electronics are causing these multiple-peak features. However, the interaction between the PMT base and electronics or afterpulsing in the PMT could be the source for these peaks.

3.4.2. Timing of peaks

Particles from gaseous impurities can be ionized in the PMTs and traverse back to the Cathode, where they start a second electron cascade, leading to delayed peaks after the main signal. Over the years, various studies with PMTs have been performed to better understand which ions cause afterpulses [77, 78]. The force

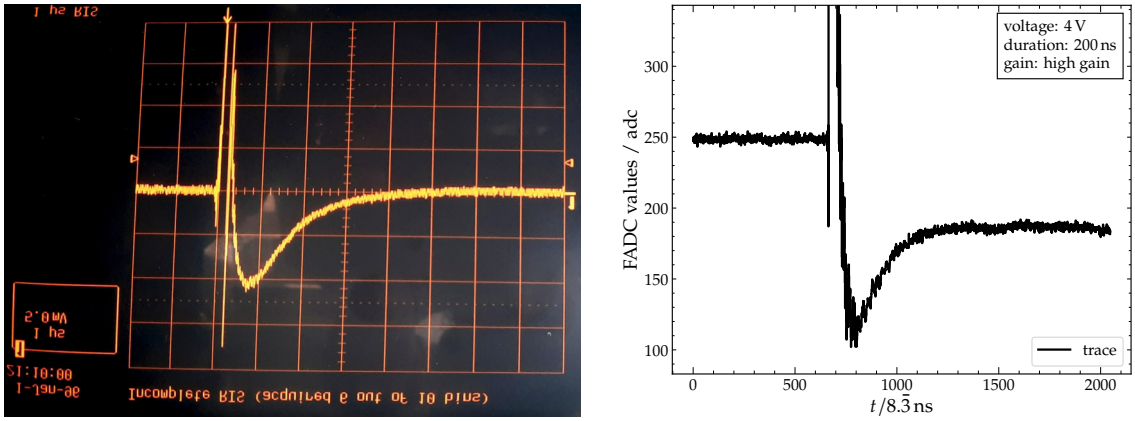

Figure 3.54: *Left:* Pulse from the pulse generator Philips PM 5715 as shown by the oscilloscope LeCroy 9344. Note that the image of the oscilloscope is flipped around the horizontal axis (inverted) to better match the trace shown on the right. *Right:* Corresponding UUB trace after the cleaning procedure.

F on an atom at position x with mass m and charge q in an electric field with strength E is $F = m\,\ddot{x} = q\,E$. The mean field strength in a potential drop U over a distance s is $E = U/s$. From these equations the transition time τ of the ion can be approximated by

$$\tau = \sqrt{\frac{2s^2 m}{qU}} = a\sqrt{1/U}\sqrt{A/Z}, \tag{3.34}$$

with the voltage U of the PMT, and the atomic mass A and charge Z of the ion. A data set of 1 751 981 saturated high-gain traces taken between the years 2009 and 2022 is used. The traces are scanned for the occurrence of the single and twin peaks and the wave. To detect a peak in the trace, a rising and falling edge must be determined before and after the peak maximum. To have a rising edge, the criterion is set to have an increase of 110 adc over the range of 6 time bins. Then, the maximum of the trace is identified in a range of 12 time bins from the beginning of the rising edge. For the falling edge, a decrease of 150 adc over the range of 10 time bins is needed after the maximum bin. These numbers have been chosen arbitrarily by looking at traces, with small, identified peak structures of interest. In the next step, only events are selected, where all three peaks have been identified to be present in a trace, which leaves a set of 33 837 traces. The timing t' of the peak relative to the start of the signal t_{start} is calculated with

$$t' = t - t_{\text{start}}. \tag{3.35}$$

Fig. 3.55-left shows the temporal distribution of the peaks for all events, where all three trace peaks have been found. Maxima in the distribution can be seen around the expected timing of the single and twin peaks.

From Eq. (3.34) it becomes evident, that the timing of afterpulsing peaks should depend on the high voltage of the PMT. Differences in voltage would thus lead to a shift in the timing of the trace peaks. Fig. 3.55-right shows the distribution of the voltage of the PMTs for the recorded traces. The average PMT voltage $\langle U \rangle$ is calculated to be around 1108 V.

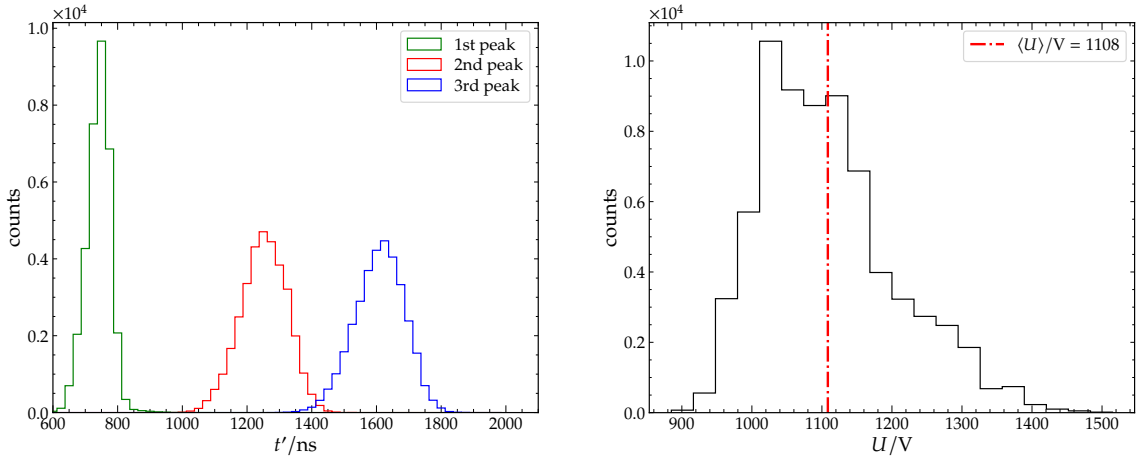

Figure 3.55: *Left:* Distribution of the timing of the single (green) and twin peaks (red and blue). For these distributions, 33 837 HG traces have been used, where all three peaks were identified. *Right:* The distribution of the voltages of all events of the data set. The mean operation range is about 1108 V.

Table 3.3: The mean transition time $\langle\tau\rangle$ as well as its standard deviation $\sigma(\tau)$ calculated from the normalized temporal distributions of Fig. 3.57.

Peak	$\langle\tau\rangle$/ns	$\sigma(\tau)$/ns
1st	737	26
2nd	1246	49
3rd	1602	51

Since τ is proportional to $1/\sqrt{U}$, it can be checked if this applies to the timing of the peaks. The correlation between the peak timing and the voltage is shown in Fig. 3.56 for the single and twin peaks. The timing of the peaks is first binned for different values of U and then a function of the form

$$f(U) = k/\sqrt{U} \tag{3.36}$$

is fitted to the data points. For higher values of the voltage between the cathode and the first dynode in the PMT, the acceleration of the ions increases, resulting in a decrease of their transition time. Thus, the timing t' of the peaks is normalized so that the resulting timing t^* is equivalent to the time observed with the mean high voltage $\langle U\rangle$ applied, i.e.

$$t^* = t'\sqrt{U/\langle U\rangle}. \tag{3.37}$$

Fig. 3.57 shows the distribution of t' (shaded area) and t^* (solid lines). The width of all distributions decreases. This is an indication that the positions of the peaks indeed depend on the high-voltage setting and thus indicates that the peaks indeed originate from PMT afterpulsing.

The mean as well as the standard deviation of the transition time from the single and twin peaks is given in Table 3.3.

A second method to determine the timing of the peaks is to normalize the time of all traces to t^*, further normalize them by scaling with inverse total charge q_{tot},

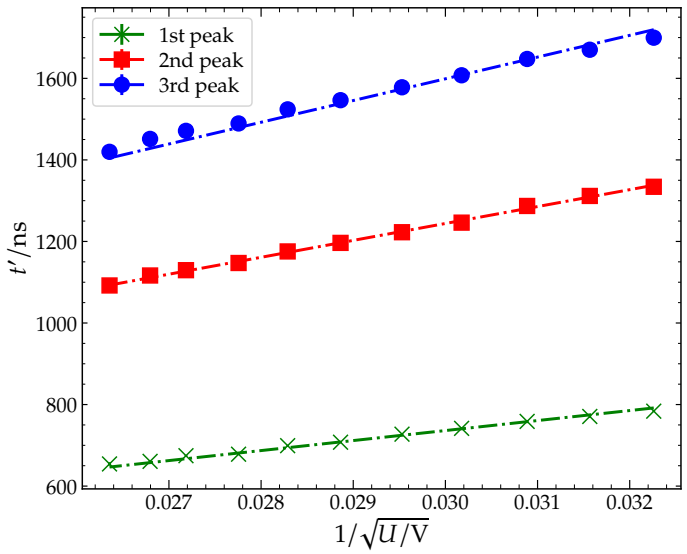

Figure 3.56: The dependence of the timing $t' = t - t_{\text{start}}$ of the peaks on the high voltage U of the PMT. The single peak is depicted with green crosses, and the twin peaks are shown as red squares and blue circles, respectively. The transition time of an ion in a PMT is proportional to $1/\sqrt{U}$. This proportionality function is fitted to the data points and plotted as dash-dotted lines.

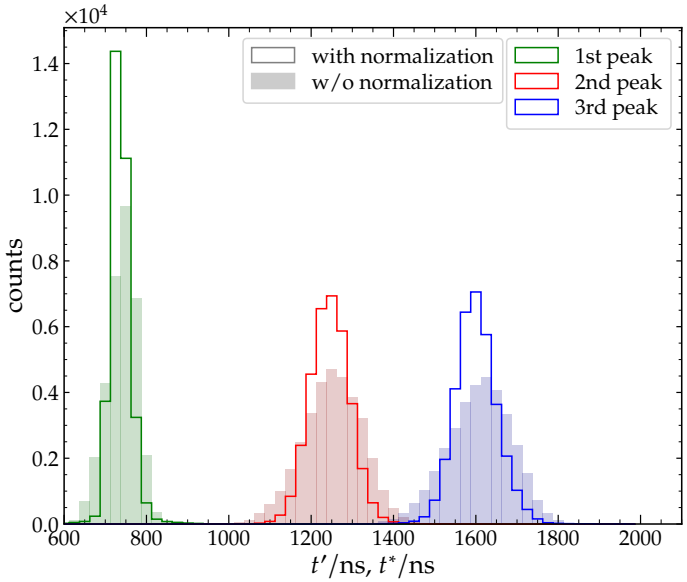

Figure 3.57: Comparison of the original distribution of the timing $t' = t - t_{\text{start}}$ of the peaks (shaded area) and the normalized timing t^* (solid lines). See the text for normalization details. The narrowing of the distributions with the normalization is an indication that the peaks are caused by PMT afterpulsing.

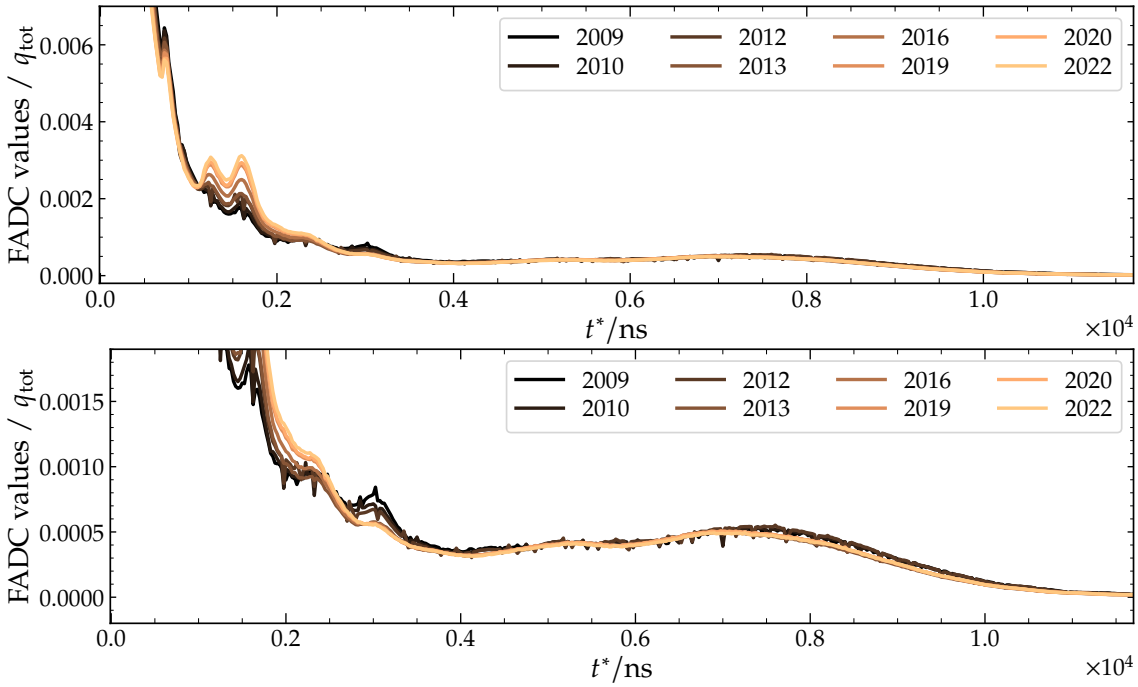

Figure 3.58: *Top:* From the full data set, the traces are stacked in normalized time t^*. The resulting trace is then normalized by the total charge q_{tot} of the trace. The single peak, as well as the twin peaks, are clearly visible. The amplitude of the twin peaks is increasing with the years. *Bottom:* A zoom on the upper plot to show other structures in the trace. A second set of twin peaks is visible at around 2300 ns and 3000 ns, as well as a twin peak structure in the long wave at the end of the trace.

and then stack them. This allows us to use the full data set of 1 751 981 traces to produce a mean trace. The resulting stacked traces are shown in Fig. 3.58 for several years. In the upper plot, the single peak as well as the twin peaks are visible. Over the years the amplitude of the twin peaks has visibly increased. The lower plot shows the same traces but with a zoomed y scale to better highlight the features after the region of the twin peaks. A second set of twin peaks is visible between times 2300 ns and 3000 ns. The wave also seems to contain a two-peak structure. By fitting a Gaussian function to the single and twin peaks, the position of the maximum of the peaks can be estimated as $\tau = (733 \pm 3)$ ns for the single peak and as $\tau = (1234 \pm 3)$ ns and $\tau = (1590 \pm 2)$ ns for the twin peaks.

The relative proportions of times τ of the peaks can now be used to determine which of the candidate ions could be responsible for this afterpulsing. Eq. (3.34) shows that the ratios of various τ values depend only on the square root of the ratio of atomic mass A and ion charge Z. The relative proportions of τ for $\{H^+ : He^{++} : He^+\}$ ions are thus $\{1 : 1.414 : 2\}$. These values can be compared with the measured ratios from Table 3.3 which yield $\{1 : 1.69 \pm 0.08 : 2.17 \pm 0.09\}$.

3.4.3. Analyzing the Celeste Data

For the vertical laser event, the CLF and XLF lasers are connected to the nearest SD station with an optical fiber so that the laser shot, observed by FD, also produces

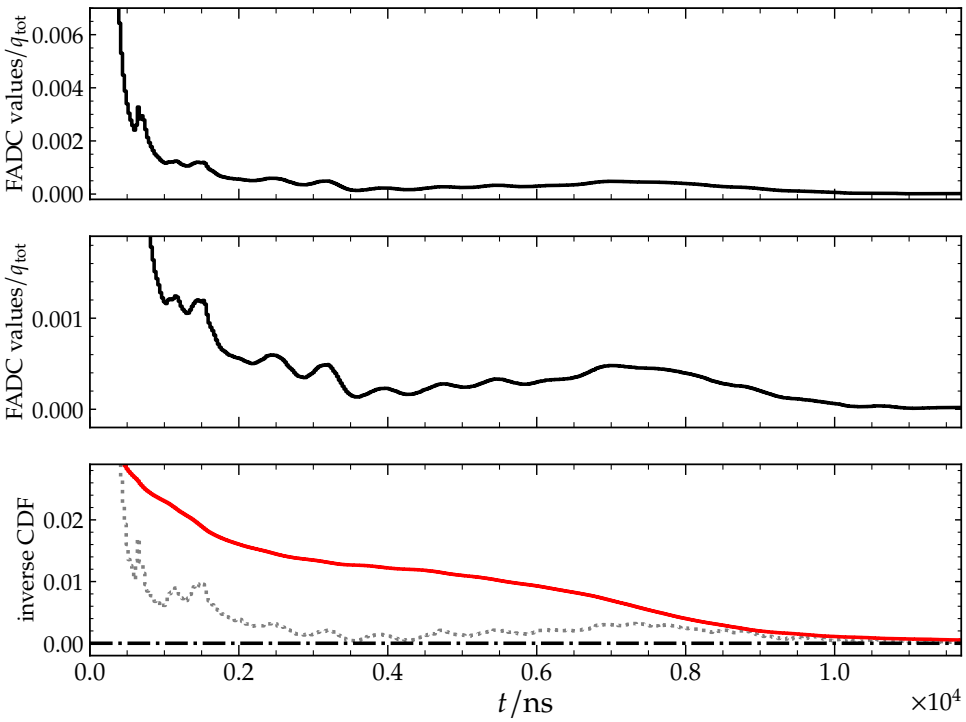

Figure 3.59: *Top:* Stacked trace of the Celeste data set comprising only traces formed by a fraction of the CLF laser light, redirected directly into WCD volume. Similar features are observed as in Fig. 3.58, which strongly indicates that they originate from PMT afterpulsing. *Middle:* A zoom on the upper plot to show other structures in the trace. *Bottom:* The fraction of the integrated signal of the stacked trace. The wave accumulates around 1.5% of the total signal.

an SD trigger. This is achieved by beam-splitter optics which redirect some of the laser light into the tank, allowing for an investigation of the timing offset between the FD and SD [79]. In the case of the CLF, the laser is linked to the Celeste SD station. Celeste traces from such laser events are produced under very controlled circumstances with a relatively constant number of photons. They are a very suitable additional source of useful traces for the afterpulsing analysis. This data set includes only traces with the laser light without any shower particles. The data set contains 274 024 events acquired between 2004 and 2021. Following the same procedure as before, the traces are first normalized by their total charge q_{tot}, and subsequently stacked together. The resulting stacked trace is shown in Fig. 3.59. This trace displays similar characteristics as that shown in Fig. 3.58, specifically the single and twin peaks as well as the wave. All exhibited features within the traces of the Celeste data set can be explained with the PMT afterpulsing, as no air showers are involved.

3.4.4. Impact of Peaks on Integrated Signals

To determine the charge contained in a given peak in the traces where all three peaks are present, a fixed narrow range around the maximum of the corresponding peak is integrated. However, this is merely an approximation of the charge

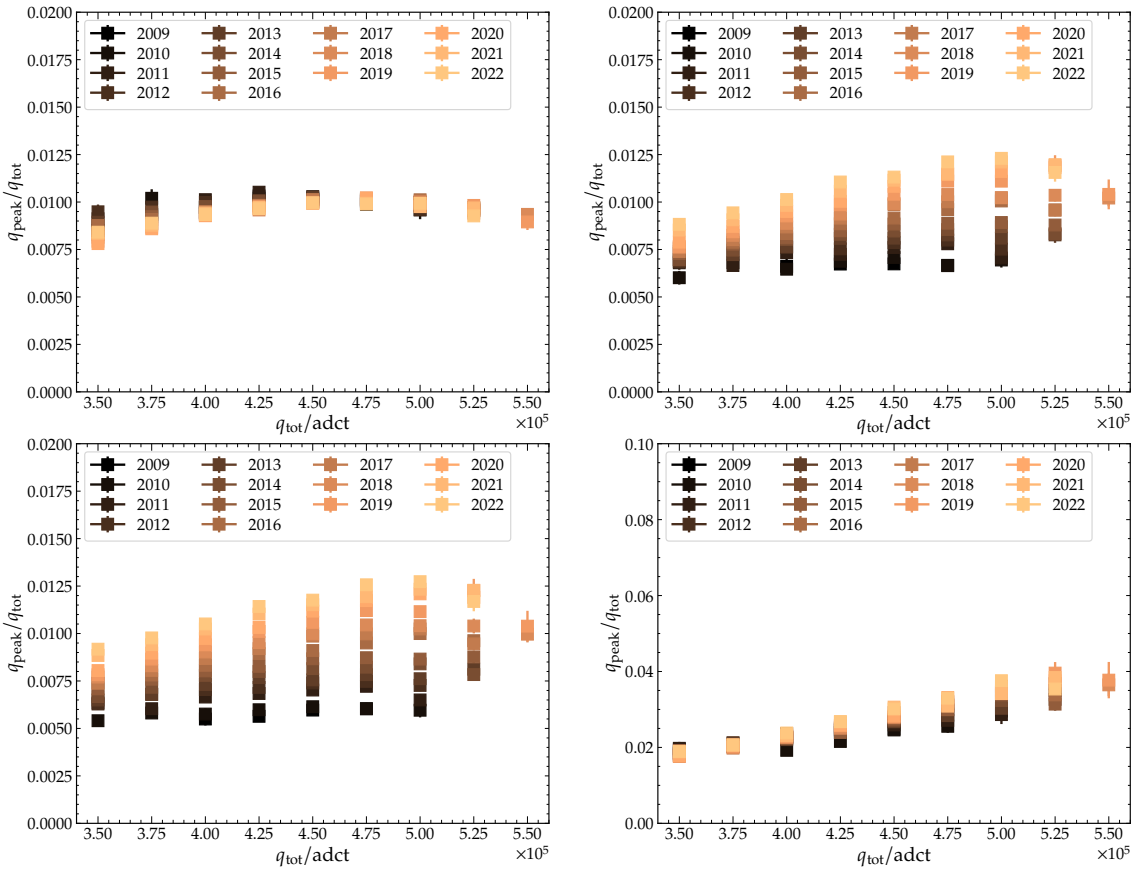

Figure 3.60: Evolution of the ratio between the charge of the peaks q_{peak} and the total LG-trace charge q_{tot}. Note that the LG traces can be saturated, which makes it impossible to obtain an exact ratio. The ratios are shown for different years, each denoted by a different color. The *top-left* plot shows the charge ratio for the single peak while the *top-right* and *bottom-left* plots correspond to the charge ratios of the twin peaks. The ratio of the wave charge is shown on the *bottom-right* plot.

contained in the peaks. To acquire a more accurate estimation, the underlying background signal should be subtracted from the region of the peaks. However, for this quick and simple analysis the approximate determination of the charge is used. The total charge is calculated by integrating the full LG trace. As shown in the stacked traces of Fig. 3.58, the relative strength of the twin peaks increases with time.

Fig. 3.60 shows the ratio between the peak charges q_{peak} and the total LG-trace charge q_{tot} for the single and twin peaks as a function of q_{tot}. The ratio q_{peak}/q_{tot} for the single and twin peaks is between 0.5% and 1.25%. For the wave, the ratio is between 2% and 4%. As some LG traces may be saturated, the LG charge q_{tot} is only a rough estimate and the actual ratios may be smaller. While the charge of the single peak shows no increase, with time the charge of the twin peaks and the wave are clearly increasing.

Fig. 3.61 shows a vertical slice for different years from Fig. 3.60. The relative strength of the twin peaks (red, blue) changes with time, while the strength of the single peak (green) remains constant throughout the years. This supports

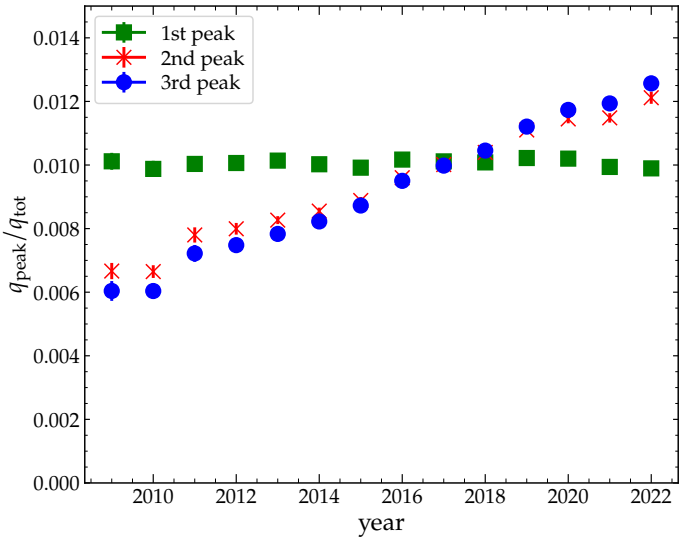

Figure 3.61: The ratio between the charge of the peaks q_{peak} and the total charge of the LG trace q_{tot}. The ratio of the single peak remains constant over time, while the ratio of the twin peaks increases in the same time period. The twin peaks may be produced by atmospheric helium diffusing into the PMT over time, resulting in an increase of the afterpulsing.

the previous hypotheses of afterpulsing caused by atmospheric helium, which can diffuse into a PMT and lead to an increase in the charge of the twin peaks over time. The relative strength of the single peak remains constant. Its origin could be hydrogen. Because of the wide time distribution, one can not reliably associate any single ion with the wave feature, which could be just a superposition of multiple afterpulses originating from the dynodes where the electric-potential differences and distances are not as well defined as in the case of the photocathode and first dynode.

3.4.5. Conclusions

The single and twin peak structures, as well as the wave feature encountered in the traces depicted in Fig. 3.52 are determined to likely originate from the afterpulsing of PMTs. Relative comparisons of the timing of the peaks with predicted values indicate that the single peak may be caused by the afterpulsing from hydrogen ions while the twin peaks are possibly produced by the afterpulsing from helium ions. The wave could be a superposition of afterpulses originating from heavier ions and/or originating from dynode internals, due to its wide time distribution. The afterpulses account only for a small fraction of the total signal between 0.5% and 4% in a typical trace, where it should be noted that this fraction should be considered only as a conservative estimate.

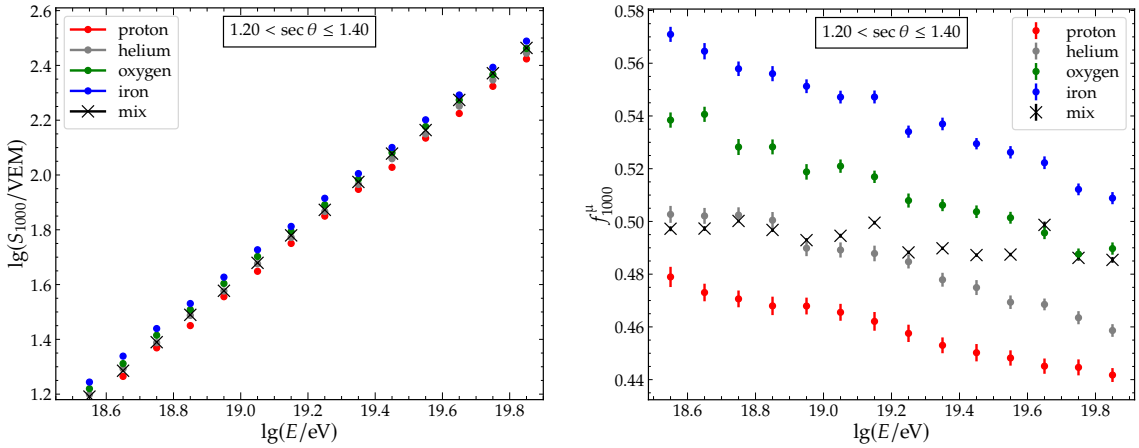

Figure 3.62: *Left:* The shower size S_{1000}, estimated by using the average of a dense ring of 12 stations at a distance of 1000 m from the shower axis, as a function of the primary energy for different primaries. S_{1000}, assuming the AugerMix composition [80], is shown with black crosses (mix). *Right:* The muon fraction f^{μ}_{1000} for each primary slightly decreases as a function of the energy of the primary. When assuming the AugerMix composition, f^{μ}_{1000} shows a relatively constant behavior due to the shift to heavier primaries with increasing energy.

3.5. SD-only Estimate of the Apparent Muon Deficit

Due to the modifications of the baseline algorithm and the determination of the gain ratio in the previous sections, the systematic bias was reduced from 6.5% to approximately 0.3% for measurements with the UB. Having identified and eliminated the primary sources of bias in signal estimation, one can now estimate the apparent muon deficit using only the SD and compare the findings with the results of Ref. [10]. Contrary to the estimation using hybrid measurements, the SD-only estimate allows to cover a wide energy range from $10^{18.5}$ eV up to $10^{20.0}$ eV. The developed improvements on the signal reconstruction also impact the shower-size estimator S_{1000} differently for simulations and measurements. Therefore, the impact of these improvements on the estimation of the apparent muon deficit shall also be compared.

3.5.1. The simulation dataset

A dataset of 58 468 simulated showers from the *Napoli* library [81] of Corsika simulations [82] was used. Primary particles included proton, helium, oxygen, and iron; energies ranged from $10^{18.5}$ to 10^{20} eV and zenith angles ranged from 0° to 60°. Additionally, a ring of 12 dense stations at 1000 m from the shower axis was simulated to get an accurate Monte-Carlo estimate of S_{1000}. For each of these 12 stations, the total signal S is calculated as

$$S = S_{\mu} + S_{\mathrm{em}} + S_{\mathrm{had}}, \tag{3.38}$$

using the the component signals S_{μ}, S_{em} and S_{had} of the component traces. Each component trace contains solely the signals of the particle type they describe.

Finally, S_{1000} is calculated as the average of the 12 dense stations. Fig. 3.62-left shows the average $\lg(S_{1000}/\mathrm{VEM})$ for each primary particle as a function of the logarithmic energy for a zenith range $\sec\theta \in [1.2, 1.4]$. Additionally, the average shower size for the AugerMix composition is calculated and shown using the results of a combined mass composition and cross section fit [80]. Furthermore, the ratio between the average S_μ and S is defined for each dense ring as the muon fraction of the shower at 1000 m, $f^\mu_{1000} = \langle S_\mu \rangle / \langle S \rangle$. In Fig. 3.62-right, f^μ_{1000} is plotted as a function of the logarithmic energy for $\sec\theta \in [1.2, 1.4]$, along with values obtained when assuming the AugerMix composition.

3.5.2. Estimating the muon deficit

For the analysis, 6 191 151 SD events of the Phase I measurements taken between 2004 and 2022 are used. Only showers with reconstructed primary energies greater than $10^{18.5}$ eV and zenith angles between 0° and 60° are considered. Both the simulation and measurement data sets were reconstructed twice. The first reconstruction utilized the OG baseline algorithm without any gain-ratio corrections. In contrast, the second reconstruction utilized the KG baseline algorithm with the corrections performed to the online estimate of the ratio between HG and LG. For both simulations and measurements, the ratio $S^{\mathrm{KG}}_{1000}/S^{\mathrm{OG}}_{1000}$ is calculated between the new shower size S^{KG}_{1000}, retrieved by using the KG reconstruction, and the old shower size S^{OG}_{1000}, retrieved by using the OG reconstruction. S_{1000} obtained from fitting the LDF to the station signals for the measurements is used. For the simulations, the average signal of the dense stations as an estimation for S_{1000} is used.

This ratio is shown as a function of S^{OG}_{1000} in Fig. 3.63-left for showers with $\sec\theta$ between 1 and 1.2 (almost vertical) and in Fig. 3.63-right for showers with $\sec\theta$ between 1.8 and 2 (more inclined). The plots demonstrate that for the measurements, the ratio increases with the shower size of the OG reconstruction, and this increase becomes slightly steeper with larger zenith angles. In simulations, the ratio of S^{KG}_{1000} and S^{OG}_{1000} changes differently than in measurements. For more inclined showers, the ratio is only slightly increased for shower sizes below 20 VEM; for almost vertical showers, below 80 VEM. Above these shower sizes, the ratio increases steeply to around 8%. The increase can be attributed to the shift from HG to LG signals. This shift occurs due to the saturation of the UBs of the stations, which was previously discussed in Section 3.1. The plots demonstrate that comparing measurements with simulations will yield different results for OG and KG reconstructions. The ratios for the full range of zenith bins in $\sec\theta$ are given in Appendix A.5.

Comparisons of measurements and simulations can be used to estimate the magnitude of the muon deficit using only the SD. However, this calculation relies on certain assumptions. Firstly, is is assumed that the electromagnetic component in the simulations is correct

$$S^{\mathrm{sim}}_{\mathrm{em}} = S^{\mathrm{meas}}_{\mathrm{em}}. \tag{3.39}$$

Additionally, the accuracy of the energy scale is assumed, which is the justification for pairing reconstructed SD energies of measurements with Monte-Carlo

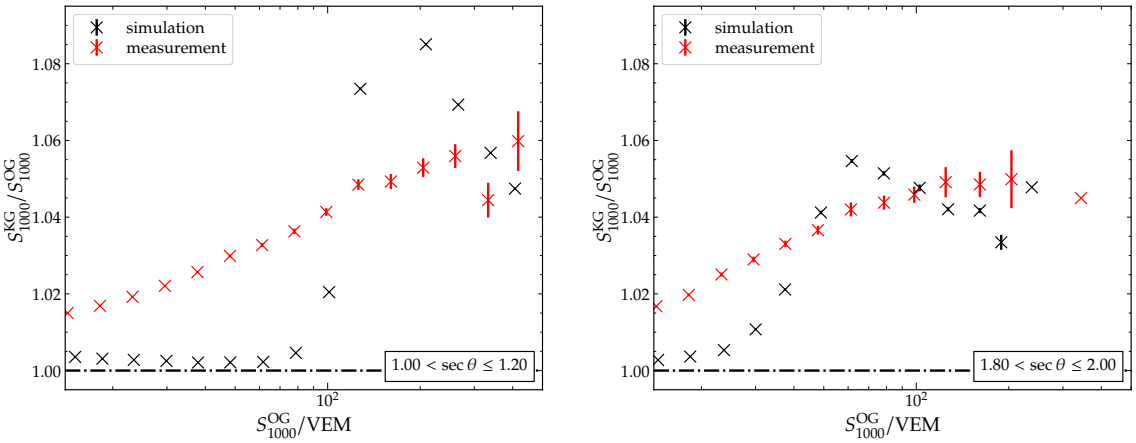

Figure 3.63: The ratio $S^{KG}_{1000}/S^{OG}_{1000}$ between the new shower size S^{KG}_{1000}, retrieved by using the KG reconstruction, and the old shower size S^{OG}_{1000}, retrieved by using the OG reconstruction for simulations (black) and measurements (red) for sec θ between 1 and 1.2 (left) and sec θ between 1.8 and 2 (right). In simulations, the ratio increases steeply by up to 8% at the change from HG to LG signals as dense stations are used to calculate S_{1000}. The ratio increases gradually with S^{OG}_{1000} for the measurements, where S_{1000} is obtained from the LDF fit.

energies of the simulations

$$E_{MC} = E_{SD}. \tag{3.40}$$

These assumptions allow us to define an estimate of the muon deficit D_μ as

$$\begin{aligned} D_\mu &= \frac{1}{f^\mu_{1000}} \left(\frac{S^{meas}_{1000} - S^{sim}_{1000}}{S^{sim}_{1000}} \right) \\ &= \left(\frac{S^{meas}_{1000} - S^{sim}_{1000}}{S^{sim}_{1000,\mu}} \right) \\ &= \frac{1}{S^{sim}_{1000,\mu}} \left(S^{meas}_{1000,\mu} + S^{meas}_{1000,em} + S^{meas}_{1000,had} - S^{sim}_{1000,\mu} - S^{sim}_{1000,em} - S^{sim}_{1000,had} \right), \end{aligned}$$

using the shower size from measurements S^{meas}_{1000} and simulations S^{sim}_{1000}, as well as the muon fraction f^μ_{1000}, which was previously determined from the simulations. Using the assumptions from Eq. (3.39) and Eq. (3.40), this equation simplifies to

$$D_\mu = \frac{S^{meas}_{1000,\mu} - S^{sim}_{1000,\mu}}{S^{sim}_{1000,\mu}}. \tag{3.41}$$

D_μ thus indicates the necessary increase of the muonic signal of the simulations to match the measurements.

To obtain D_μ for the full range of zenith angles, D_μ is calculated for different zenith bins, ranging from 1 to 2 in sec θ with a step of 0.2. Then, a weighted average relative to the number of events in each zenith bin for each energy is calculated. The plots of D_μ for individual zenith bins are given in Appendix A.5.

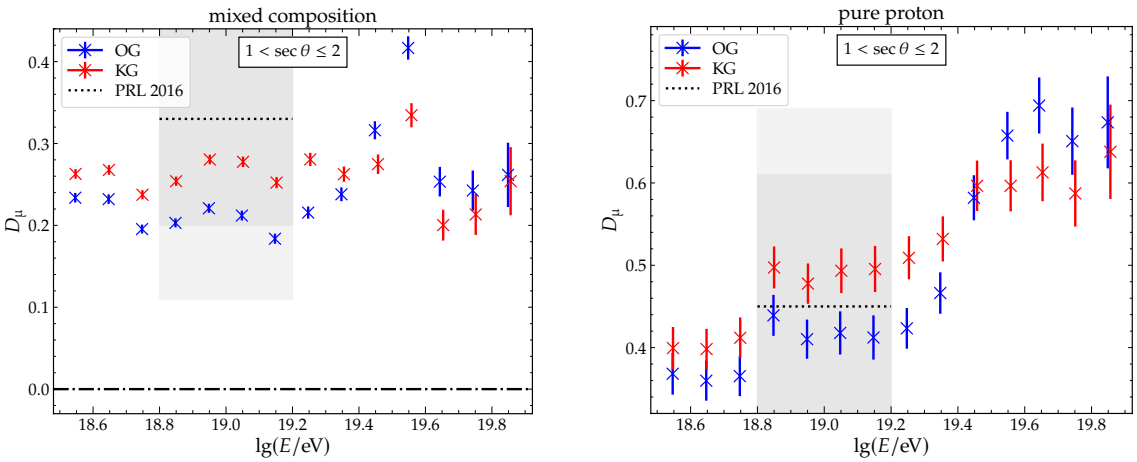

Figure 3.64: D_μ indicates muon deficit, assuming a correct energy scale and a correct electromagnetic signal in the simulations. In comparison, the hadronic scaling factor $R_{\rm had}$ of Ref. [10] is shown with the dotted line and the grey areas indicating the statistical and systematic uncertainties. Assuming the AugerMix composition (left), at energies up to $10^{19.4}$ eV an increase in the estimated muon deficit between 2 to 7 percentage points can be obtained using the KG reconstruction. When a pure proton composition is assumed (right), at energies up to $10^{19.4}$ eV an increase in the muon deficit between 1 and 9 percentage points can be estimated The difference between the KG and OG reconstruction is reversed at higher energies, and a decrease in the muon deficit between 1 and 8 percentage points for the AugerMix composition and a decrease between 3 and 8 percentage points for the pure proton composition can be estimated.

Fig. 3.64-left displays D_μ for both OG and KG reconstructions for various bins of the reconstructed shower energy and the complete range of zenith angles under the assumption of the AugerMix composition of primaries, estimated from Auger's $X_{\rm max}$ measurements [80], for the calculation of f^{μ}_{1000}. One can compare D_μ with the hadronic scaling factor $R_{\rm had}$ of Ref. [10] assuming

$$R_{\rm had} \stackrel{\wedge}{=} D_\mu + 1. \tag{3.42}$$

However, in Ref. [10], $R_{\rm had}$ is estimated using exclusively the muons that originate from the hadronic shower component. In contrast, D_μ is calculated using f^{μ}_{1000}, which includes all muons without respect to their particle history. The hadronic scaling factor $R_{\rm had}$ of Ref. [10] is shown with the dotted line and the grey areas indicating the statistical and systematic uncertainties. The SD-only estimation of D_μ reproduces the estimation of the muon deficit of Ref. [10] within its statistical and systematic uncertainties. Using the KG reconstruction leads to an increase in D_μ by between 2 to 7 percentage points for primary energies from $10^{18.5}$ eV to $\sim 10^{19.4}$ eV. Consequently, an *increase* in the muon deficit in this energy range is expected. At higher energies, the opposite is true, where the difference in D_μ between the KG and OG reconstructions is reversed, and the KG reconstruction results in an *decrease* of D_μ between 1 and 8 percentage points. The sudden decrease in D_μ at an energy of approximately $10^{19.6}$ eV results from a sudden change in the estimated mass-composition fractions in this region, which directly influences the Monte-Carlo shower size of the AugerMix composition as well as

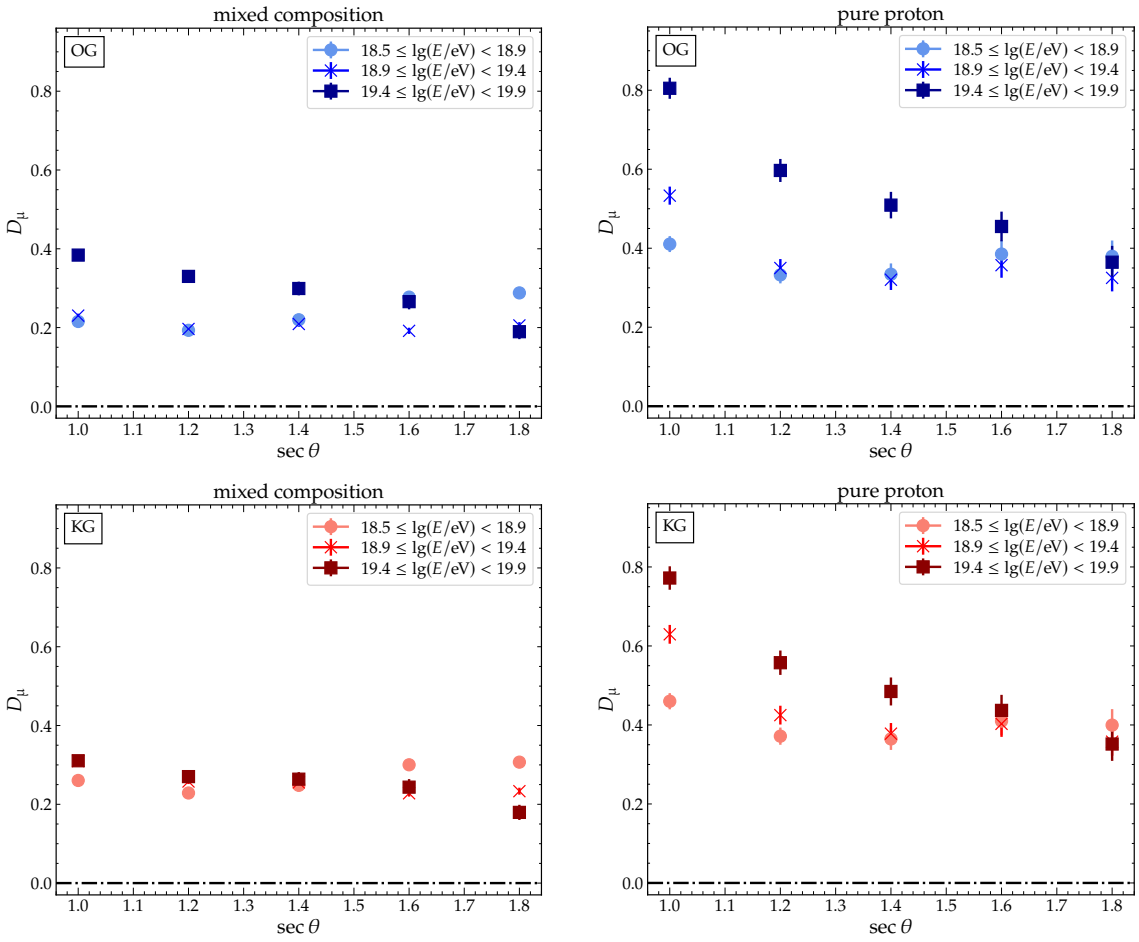

Figure 3.65: D_μ ranges between 19% and 38% for all energy bins when assuming the AugerMix composition and using the OG reconstruction (top-left). In contrast, D_μ decreases in the highest energy bin from almost 80% to 36% over sec θ when assuming a pure proton composition (top-right). Using the KG reconstruction for the AugerMix (bottom-left) and pure proton composition (bottom-right) decreases D_μ in the energy bins above $10^{19.4}$ eV, while increasing D_μ in the lower energy bins. Using the AugerMix composition and KG reconstruction, D_μ is almost constant over sec θ in all energy bins, which could be interpreted as support for the assumptions that the electromagnetic shower component, mixed mass composition, and energy scale are correct.

f^{μ}_{1000}. This change is also visible in Fig. 3.62-right at the same energy.

Additionally, D_μ is calculated assuming a pure proton composition of the primary particles in all energy bins. The weighted average of D_μ for all zenith angles is shown in Fig. 3.64-right. D_μ increases with energy from around 40% up to 70%. Since the muon content of an air shower increases with the mass of the primary particle, the increase of D_μ with energy disfavors a pure proton mass composition. Similarly to the differences in D_μ when using the KG or OG reconstruction for the AugerMix composition, an increase of D_μ between 1 and 9 percentage points can be estimated at energies up to $10^{19.4}$ eV when using the KG reconstruction. The difference is reversed at energies above $10^{19.4}$ eV, where D_μ decreases between 3 and 8 percentage points compared to the OG reconstruction.

D_μ is shown for zenith angles between 1 and 2 in $\sec\theta$ for three energy bins in Fig. 3.65-top for the OG reconstruction and in Fig. 3.65-bottom for the KG reconstruction. D_μ increases from ~ 21% to ~ 29% for the AugerMix composition OG calculation (Fig. 3.65-top-left) with increasing $\sec\theta$ in the lowest energy bin. At the highest energy, D_μ decreases from ~ 38% to ~ 19%. Also, the decrease of D_μ with $\sec\theta$ can be seen for the pure proton composition (Fig. 3.65-top-right). In the lowest energy bin, D_μ ranges between ~ 33% and ~ 41%, and it decreases from ~ 80% to ~ 36% with $\sec\theta$ in the highest energy bin. Comparing the KG with the OG reconstruction, the dependence of D_μ on $\sec\theta$ for all energy bins is smaller for the KG reconstruction. D_μ increases from ~ 26% to ~ 31% for the AugerMix composition KG calculation (Fig. 3.65-bottom-left) with increasing $\sec\theta$ in the lowest energy bin. At the highest energy, D_μ decreases from ~ 31% to ~ 18%. Similarly, the decrease of D_μ with $\sec\theta$ can be seen for the pure proton composition (Fig. 3.65-bottom-right). In the lowest energy bin, D_μ ranges between ~ 36% and ~ 46%, and it decreases from ~ 77% to ~ 35% with $\sec\theta$ in the highest energy bin. This near lack of a zenith dependence for the AugerMix composition KG calculation could be interpreted as support for the assumptions that the electromagnetic shower component, mixed mass composition, and energy scale are correct.

3.5.3. Conclusions

An SD-only approach was used to investigate possible differences in the muon content of simulated and measured air showers. Due to the improvements in the baseline estimation and the resulting changes in the signal calculation, an *increase* in the muon deficit between 2 and 7 percentage points is expected for energies between approximately $10^{18.5}$ eV and $10^{19.4}$ eV, while a *decrease* in the muon deficit of up to 8 percentage points is expected for energies above approximately $10^{19.4}$ eV. For the analysis, assumptions were made about the correctness of the energy scale and the simulated electromagnetic shower component. Under the assumption of the AugerMix composition, the overall muon deficit is estimated to be 18% to 31%, which is in good agreement with the results of Ref. [10]. Further improvements to the analysis can be made in the future by including an electromagnetic scaling parameter for the zenith dependence of the measurements, as well as allowing changes to the energy scale.

Chapter IV

Characterizing the Neutron Component of Air Showers

Simulations of extensive air showers have demonstrated that neutrons with a broad energy spectrum can reach the ground with delays of up to several seconds after the initial shower front [39, 83]. In Ref. [42], using the Fluka simulation framework, it was demonstrated that the shape of the neutron energy spectrum varies based on both arrival-time relative to the shower signal and distance from the shower axis. Fig. 4.1 shows simulated neutron spectra of Ref. [42] for three different arrival-time intervals and three distance bins. The spectrum of "early" neutrons (arriving between 0 and 5 µs after the shower signal) extends to higher energies when compared to the "late" neutrons (arriving between 5 and 11 µs after the shower signal). At energies below $\approx$ 1 MeV mainly neutrons with arrival-times beyond 11 µs arrive on the ground. Furthermore, closer to the shower axis, a larger ratio of high-energy neutrons is expected.

Since neutrons are neutral particles, they can only produce a signal in the SSD through elastic or inelastic scattering with nuclei in the scintillator material. The detection efficiency of the SSD for neutrons is expected to span over a wide energy range starting from a few MeV [42]. Between 2019 and 2021, delayed pulses were observed in the SSD time traces during measurements at the PPA [84]. Similarly, the time traces of the scintillation detectors of the Telescope Array experiment exhibit late pulses [85].

In this chapter, SSD measurements of late pulses are studied and an estimation of the possible contribution of neutrons to the signal in the WCD is given. In Section 4.1, late pulses observed in the SSD that do not exhibit a corresponding signal in the WCD are analyzed. The time structure of these pulses, their distribution in arrival time relative to the shower signal, and the spectrum of pulse amplitudes are characterized to rule out PMT afterpulsing and electronic noise as possible sources. To compare the SSD measurements of these late pulses with air shower simulations, the implementation of hadronic interactions in $\overline{\text{Off}}\underline{\text{line}}$ is described in Section 4.2. In Section 4.3, the characterization of the late neutron component of air showers is continued. To this end, their lateral distributions are analyzed and comparisons are drawn between the measured signal spectra,

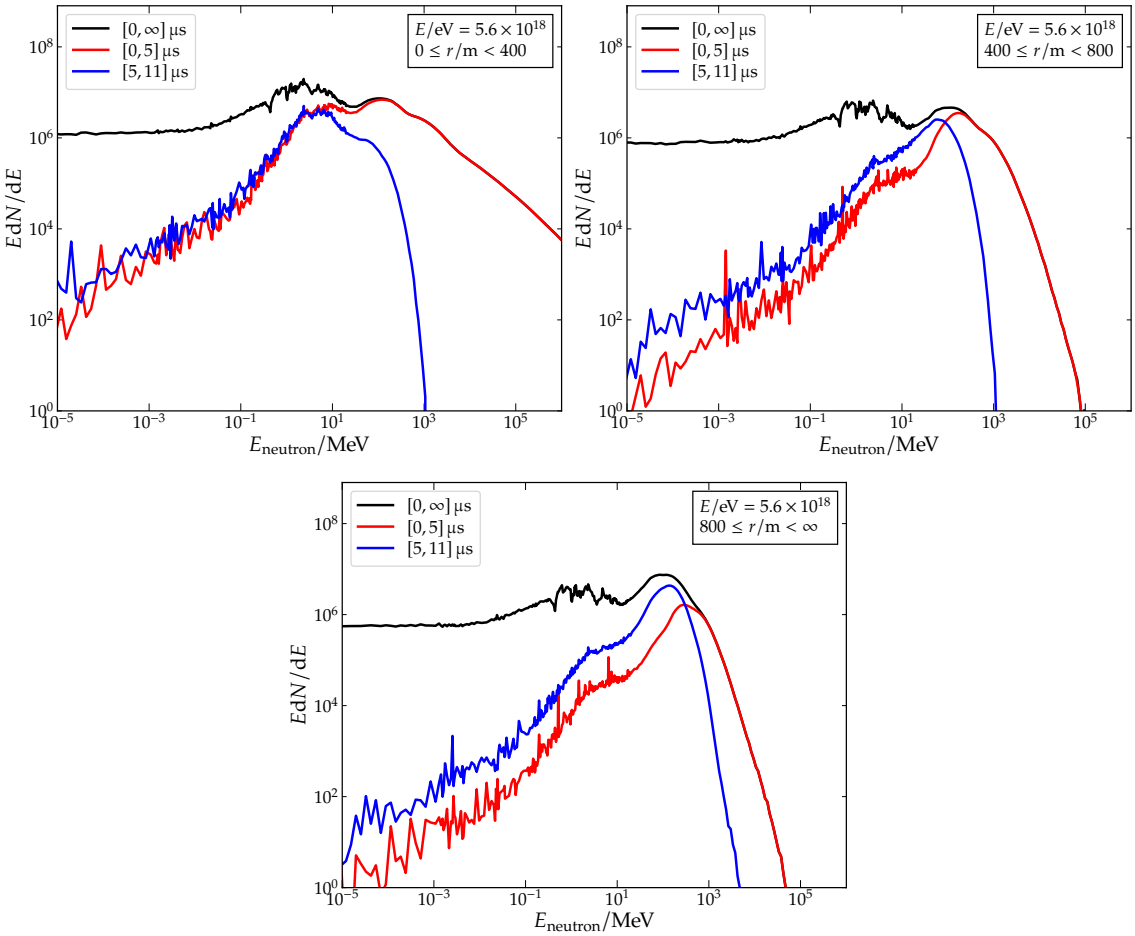

Figure 4.1: The neutron energy spectra for different arrival-times and distances from the shower axis. *Top-left:* For a distance range between 0 and 400 m from the shower axis. *Top-right:* For distances between 400 and 800 m from the shower axis. *Bottom:* The energy spectra for distances above 800 m from the shower axis. The effective range of the neutron energy spectrum extends to larger energies closer to the shower axis. "Early" neutrons, which arrive between 0 and 5 µs (red), also extend to higher energies when compared to "late" neutrons which arrive between 5 and 11 µs (blue). When including all arrival-times (black), it becomes evident that most neutrons with low energies arrive with delays exceeding the observable time-window of the SSD. The data of the spectra is from Ref. [42].

assumed spectral shapes, and spectra from air shower simulations. In Section 4.4, the contribution of neutrons to WCD signals is estimated and the implications for the apparent muon deficit are discussed.

4.1. Subluminal Pulses in the SSD

The measurement of EAS and the disentanglement of their components is crucial for testing hadronic interaction models at ultra-high energies. Since these models are designed to describe the measurements from particle accelerators, they must be extrapolated when simulating EASs, since the initial cosmic rays can surpass the energy of human-made particle accelerators by several orders of magnitude. An EAS can be broken down into three components: the electromagnetic, the muonic and the hadronic shower components. The WCD has a higher sensitivity to the muonic shower component than the SSD of the AugerPrime upgrade. The SSD is planned to enhance the SD with a higher sensitivity to the electromagnetic component. From the hadronic shower component, the only relevant massive and neutral particles that are stable long enough to reach the ground are neutrons. Low-energy massive particles arrive at the ground with a significant delay relative to the shower front [38]. Such subluminal particles were measured and documented in 1984 by Linsley with the Volcano Ranch experiment [17]. Neutron simulations of EASs have demonstrated that particles with a broad energy spectrum could reach the ground with possible delays of up to several seconds after the initial shower front [39, 83]. Since neutrons are neutral particles, they can only produce a signal in the SSD by elastic and inelastic scattering with other nuclei of the scintillator material. The optimal operation range of the SSD is expected to extend from several MeV to approximately 100 MeV. Below 0.7 MeV, the detection probability for neutrons in a scintillator falls below 0.001%. Above 100 MeV, the efficiency to detect neutrons is around 2.3% [42]. With the SSD measurements in the PPA, delayed pulses were detected in the time traces [84].

Fig. 4.2 displays the WCD and SSD traces for a given station of an event in the PPA. The initial shower signal is visible in both detectors at $t_{\text{start}} = 0$, and it decreases over a period of 2.5 µs. The SSD trace exhibits three distinct pulses, occurring approximately 5, 6, and 8.5 µs after the initial signal, which are not visible in the WCD. Since the SSD area does not fully overlap with the WCD area, these pulses could originate from particles passing the SSD at a certain angle. However, these pulses can also be attributed to subluminal particles elastically scattering with protons of the scintillator material. Further evidence is the amplitude of the pulses, which exceeds the MIP_{peak} signal a muon could produce on average. These late pulses are analyzed in the following, and the first measurement of the pulse spectrum and lateral distribution of neutrons, which are likely candidates for these subluminal pulses, is presented.

4.1.1. Data Collection and Simulation Assumptions

The available data of the AugerPrime upgrade is used, comprising measurements from the years 2020 through 2024. The minimal reconstructed shower energy is set to $\lg(E/\text{eV}) = 18.0$. This provides a set of 199 973 events with 613 794 traces for analysis. Throughout the analysis, the data is binned in three energy bins, $18.0 \leq \lg(E/\text{eV}) < 18.5$, $18.5 \leq \lg(E/\text{eV}) < 19.0$, and $19.0 \leq \lg(E/\text{eV}) < 19.5$. Furthermore, zenith angle bins ranging from 1.0 to 2.0 in $\sec\theta$ with steps of 0.2 are used. 60 000 showers are simulated for comparison, using the *Napoli* library

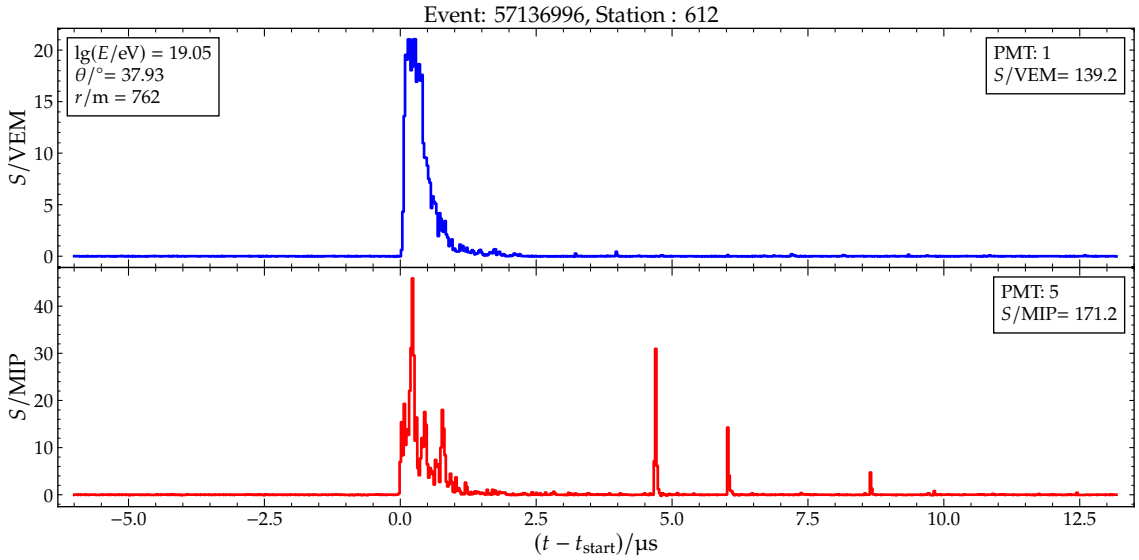

Figure 4.2: WCD and SSD traces are shown for a station participating in an event of the PPA. The time t is adjusted to commence at the start time t_{start}, which corresponds to the estimated start of the passage of the shower front. Three large, late pulses are notable in the SSD trace. The delayed arrival of the pulses and their absence in the WCD implies that slow neutrons probably cause them.

of Corsika simulations [81]. Dense rings with 4 stations at 200, 600, and 1000 m from the shower axis were included in the simulation to improve statistics. The events consist of a mixture of 4 primary particles (proton, helium, oxygen, iron) in a 1:1:1:1 ratio. They are distributed uniformly over $\sin^2\theta$, with θ ranging from 0 to 60°, and energy, ranging from $\lg(E/\text{eV}) = 18.0$ to $\lg(E/\text{eV}) = 19.5$. The utilized hadronic interaction model is Epos-LHC and the hadron energy cut-off in the simulated showers is set at 20 MeV. $\overline{\text{Off}}\underline{\text{line}}$ is utilized for the detector simulation and shower reconstruction. Previously, hadronic interactions were not implemented in the $\overline{\text{Off}}\underline{\text{line}}$ detector-response simulation. However, the work on including these processes in the simulation framework is discussed in Section 4.2.

This analysis aims to characterize the subluminal pulses, determine if they could originate from detector or electronics effects as opposed to a physical origin from EAS and compare them with simulations. First, the region of full trigger efficiency of the stations is determined from simulations. The range of distances r to the shower axis where the trigger efficiency of the array is 100% is determined. For zenith angles from 1.0 to 2.0 in sec θ, all stations will trigger up to 1000 m from the shower axis as shown in Fig. 4.3. The maximum distance where all stations trigger increases with energy, reaching beyond 1600 m from the shower axis at high energies.

Traces from the high-gain of the SSD PMT that are not baseline-saturated are selected with the previously defined cuts applied to the measurements and simulations. On each trace, a simple pulse-finding algorithm is applied. The minimal charge of a pulse from a single photoelectron is about 0.05 $\text{MIP}_{\text{charge}}$ [86]. In Section 3.2.4 the standard deviation σ of the baseline was determined to be

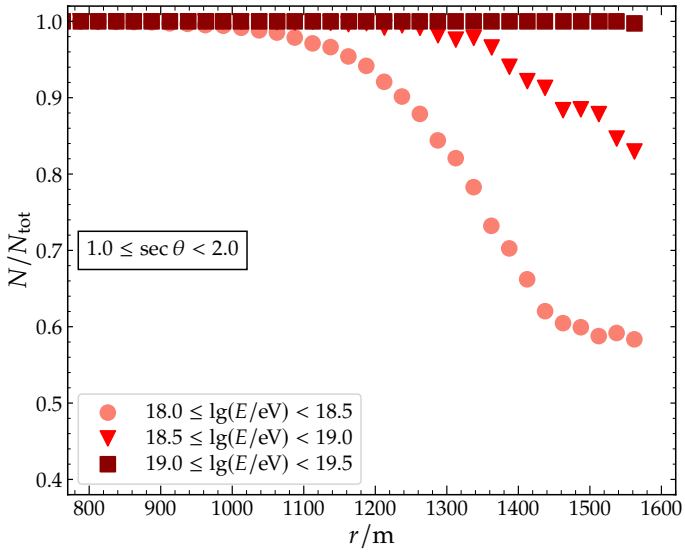

Figure 4.3: *Left:* The fraction of triggered stations N relative to the total number of stations N_{tot} from simulated events based on the distance r from the shower axis provides an approximation of the range of full trigger efficiency.

2 adc, which corresponds to $0.08\,\text{MIP}_{\text{peak}}$. This allows using $3\sigma = 0.24\,\text{MIP}_{\text{peak}}$ as a criterion for defining a minimum pulse height in the traces. However, there is the problem of oscillations with the baseline in the traces of the SSD for the UUB electronics, as was previously discussed in Section 3.2.4, which might lead to a miscounting of small pulses when subtracting the baseline. The amplitude of the oscillations can be roughly estimated to be about 6 ADC or $\approx 0.24\,\text{MIP}_{\text{peak}}$. Using the criteria of 3σ gives a threshold of at least $0.72\,\text{MIP}_{\text{peak}}$. Therefore, the pulse start $t_{\text{pulse}}^{\text{start}}$ is defined when a bin T_i at the time t_i in the trace surpasses a conservative value of $0.8\,\text{MIP}_{\text{peak}}$ and the end $t_{\text{pulse}}^{\text{end}}$ is defined when T_i drops below $0.8\,\text{MIP}_{\text{peak}}$ for two consecutive bins in a row. $t_{\text{pulse}}^{\text{start}}$ and $t_{\text{pulse}}^{\text{end}}$ are defined relative to the signal start time t_{start}, determined by the WCD

$$t_{\text{pulse}}^{\text{start, end}} = t_i - t_{\text{start}}. \tag{4.1}$$

The pulse duration Δt_{pulse} is then determined as the difference between the start and end bin (including the latter). The charge S_{pulse} for each pulse is obtained as the integral from the start to the stop bin. If a pulse is large enough to saturate the trace, the low-gain is used instead to estimate S_{pulse}.

Pulses that arrive after 5 µs are defined as subluminal particles, which are potential candidates for a new, delayed shower component. This time threshold is selected arbitrarily. Nevertheless, neutrons are assumed to dominate the shower signal at a distance of 1000 m from the shower axis after 5 µs [39]. Pulses occurring before the actual start time $t_{\text{pulse}}^{\text{start}} < 0\,\mu\text{s}$ of the shower are classified as pulses originating from the background and considered not causally connected to the shower in question.

To obtain an initial estimate of the rate of late pulses from electrons and muons,

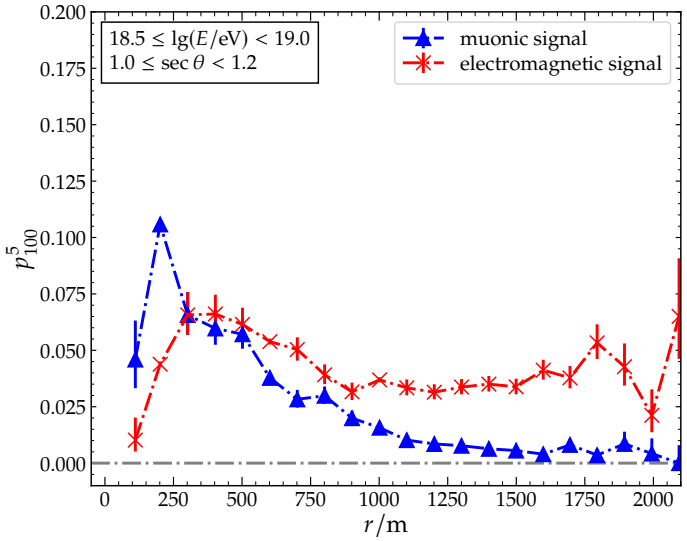

Figure 4.4: The fraction p^5_{100} of simulated traces that do not reach 100% of their integrated signal within 5 µs. Beyond about 1000 m muonic traces hardly show any signal beyond 5 µs, whereas approximately 3.5% of the electromagnetic traces exhibit delayed signal contributions.

the time at which the integrated signal of simulated traces reaches 100% is calculated first. The total is divided into electromagnetic and muonic components. Then, the fraction p^5_{100} of traces that do not reach 100% of the integrated signal within 5 µs is determined and plotted as a function of the distance r in Fig. 4.4. Up to about 700 m the muonic and electromagnetic particles produce signals after 5 µs, between 5 and 11% of the simulated traces. At larger distances, p^5_{100} decreases for muons below 1% and is around 3.5% for the electromagnetic component. This non-hadronic background has to be taken into account when searching for hadronically produced, late pulses and will be discussed in more detail in the next section.

4.1.2. Analysis of Pulses

General observations

As the next step, the pulses of the measurements are analyzed. Fig. 4.5-left shows the signal S_{pulse} for each pulse and its start time $t^{\text{start}}_{\text{pulse}}$. Likewise, Fig. 4.5-right displays the duration Δt_{pulse} of each pulse. Before the shower signal, a few pulses can be observed at times when $t^{\text{start}}_{\text{pulse}} < 0$, likely caused by atmospheric muons. At $t^{\text{start}}_{\text{pulse}} = 0$, the shower signal produces a wide distribution in S_{pulse} and Δt_{pulse}. Most pulses occur within approximately 3.5 µs. However, a pulse rate significantly higher than the rate at $t^{\text{start}}_{\text{pulse}} < 0$ is still visible between 3.5 µs and the end of the trace. These late pulses can reach up to 220 $\text{MIP}_{\text{charge}}$. The average pulse duration Δt_{pulse} is around 0.03 µs, equating to 3 or 4 time bins in the UUB.

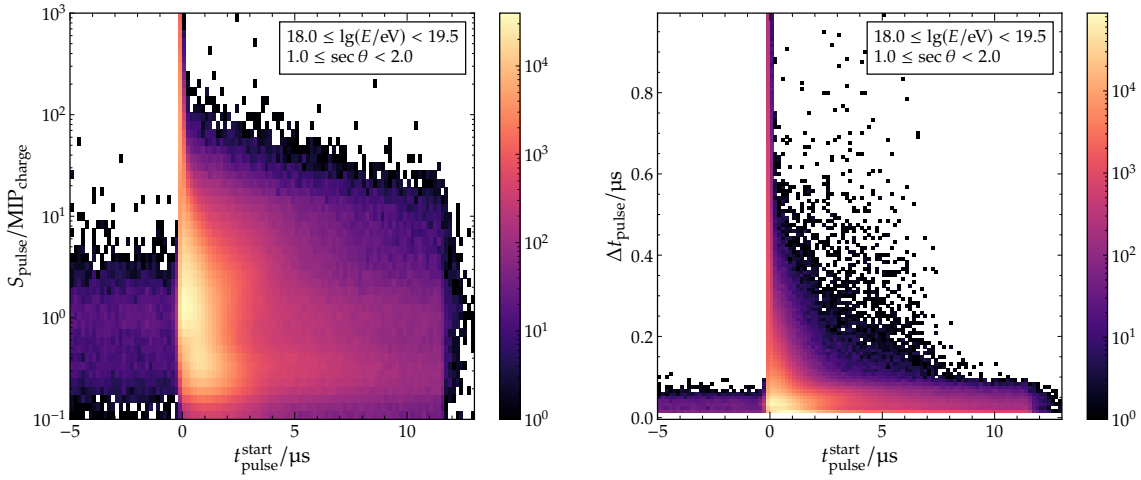

Figure 4.5: *Left:* The distribution of pulses, detected by the pulse-finding algorithm described in the text, is shown as a function of $t^{\text{start}}_{\text{pulse}}$ and pulse charge S_{pulse}. Pulses with $t^{\text{start}}_{\text{pulse}} < 0$ are attributed to atmospheric muons and electrons. At $t^{\text{start}}_{\text{pulse}} \geq 0$, pulses originating from the shower are included. *Right:* The average duration Δt_{pulse} of late pulses with $t^{\text{start}}_{\text{pulse}} \geq 5\,\mu\text{s}$ is approximately 0.03 μs.

Pulse Shape

The late pulses are normalized to their charge and stacked, and the average normalized time structure is calculated. The result is shown in Fig. 4.6. The average pulse shape resembles the response of the SSD to single particles.

Time distribution

For comparison to the measurements, the pulse-finding algorithm is used on the unsaturated muonic, electromagnetic and hadronic traces of the simulated showers discussed in Section 4.1.1. To increase comparability, the simulations are re-weighted to match the energy spectrum and mass composition of the measurements. The spectrum-dependent fractions for mass composition are taken from Ref. [87]. Fig. 4.7 displays the distribution of the reconstructed shower energies obtained from measurements, unweighted and weighted simulations.

The distribution of arrival-times for all pulses is displayed in Fig. 4.8 for stations between 400 and 800 m from the shower axis. The total number of pulses N_{pulses} is normalized to the overall number of traces N_{traces} in each bin. As noted earlier, the simulations include the hadronic shower component only down to particle energies of around 20 MeV. In Section 4.3.3 the maximal possible pulse signal is determined. For a neutron with about 20 MeV this maximal signal is around 11 $\text{MIP}_{\text{charge}}$. The distributions of the simulations and the measurements exhibit agreement for the main shower signal, which starts at 0 μs and extends to several microseconds. The rate of pulses from the electromagnetic and muonic traces drops steeply after the initial shower signal at 0 μs. In the range from 400 to 800 m from the shower axis for pulses above 11 $\text{MIP}_{\text{charge}}$, the background of non-hadronic pulses is around 3%. The remaining 98% of pulses can thus expected to

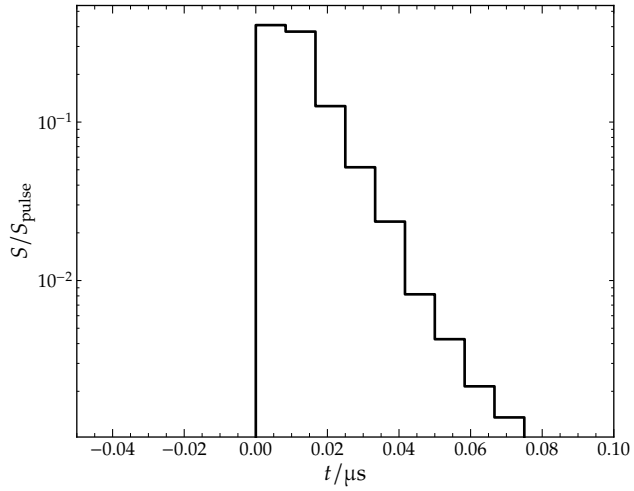

Figure 4.6: All pulses detected by the pulse-finding algorithm arriving at $t_{\text{pulse}}^{\text{start}} \geq 5\,\mu s$ are normalized to their integral signals and stacked. The average pulse shape demonstrates that these detected late pulses are dominantly particle-like rather than resulting from electronic noise.

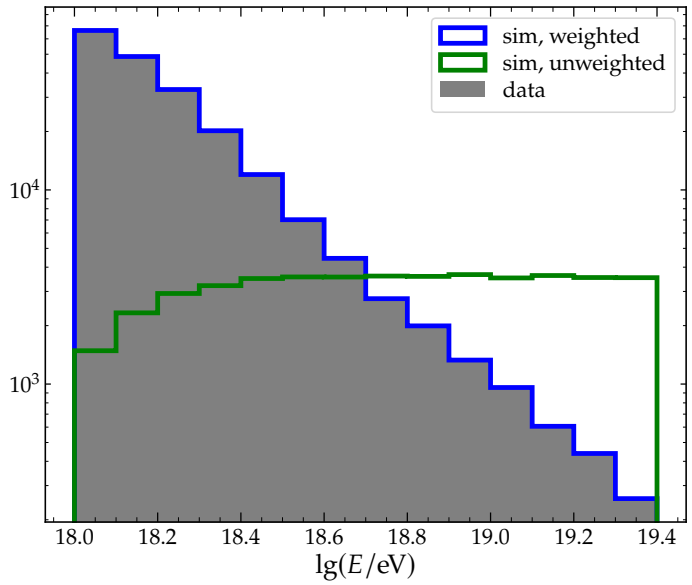

Figure 4.7: The events of the simulated data set require re-weighting to match the energy energies and mass composition of the observed measurements.

be of hadronic origin. Depending on the zenith angle, the fraction of muonic and electromagnetic pulses past 5 µs ranges between 1 and 15%. The distributions, as well as the estimated background of muonic and electromagnetic pulses for different bins in the distance and also shower energy and zenith angle, as well as pulse signal, can be found in Appendix B.1.

For pulses that are observed either alone (blue) or with a second (red) or third (orange) pulse in the same trace, the arrival-time distribution is shown in Fig. 4.9-left. The shape of the arrival-time distributions of single pulses does not differ

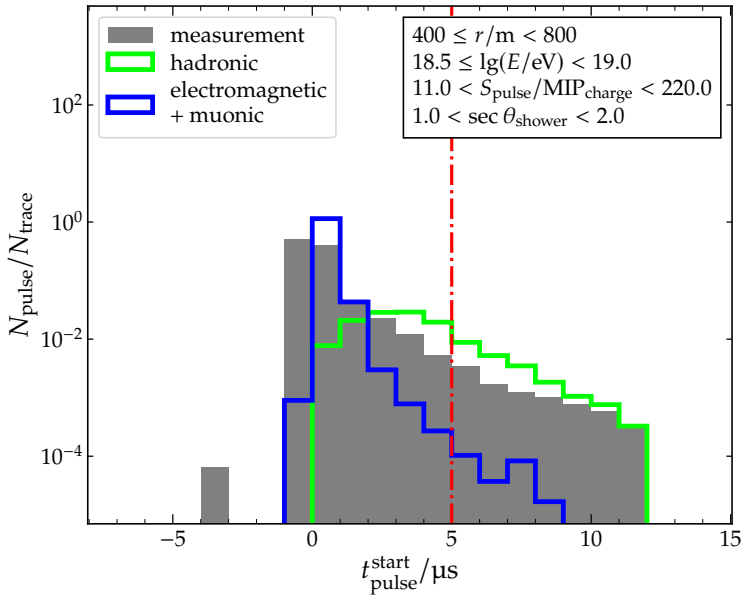

Figure 4.8: The time distribution of the number of pulses N_{pulse}, normalized to the total number of traces N_{trace}. The rate of pulses from the electromagnetic and muonic traces drops steeply after the initial shower signal at 0 µs. 5 µs past the start of the shower signal, around 3% of the pulses from the electromagnetic and muonic traces contribute to the total pulse rate.

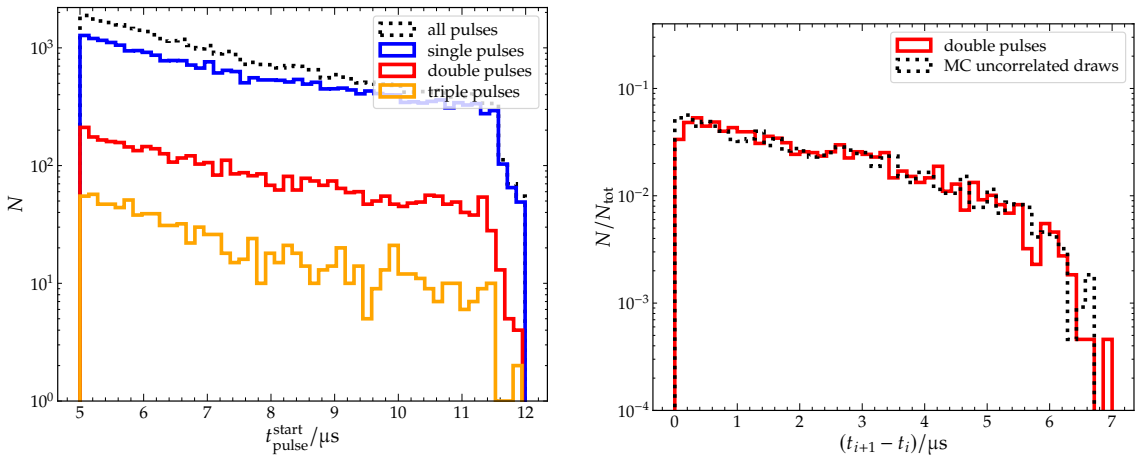

Figure 4.9: *Left:* The arrival-time distribution of measured single (blue), double (red) or triple (orange) pulses in all traces. *Right:* The time difference $(t_{i+1} - t_i)$ between the arrival-times of double pulses (red) does not differ from the difference between randomly selected, uncorrelated pulses (black).

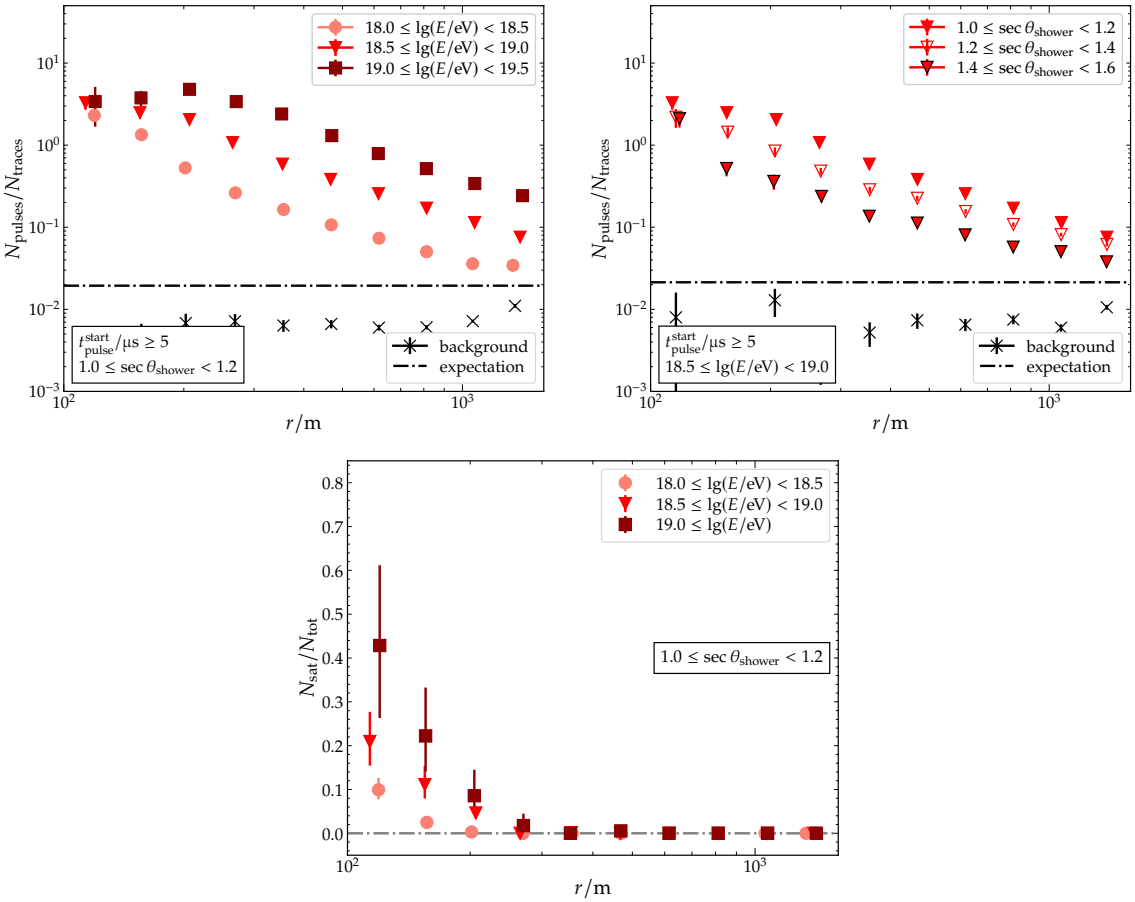

Figure 4.10: *Left:* Pulses that are counted after 5 µs are considered as candidate pulses. The average amount of candidate pulses per trace increases with energy and decreases with distance to the shower axis. *Right:* With increasing sec θ the pulse rate decreases. The background pulse rate (dashed line) is approximately one atmospheric muon occurrence in every 20 traces. *Bottom:* The fraction of stations with a saturated baseline $N_{\text{sat}}/N_{\text{tot}}$ increases closer to the shower axis, leading to a reduced estimation of the pulse rate in this region.

from the shapes of the distribution when two or three pulses arrive in the traces. It can be further determined if the arrival-times of double pulses are correlated with each other. For this, the time difference $(t_{i+1} - t_i)$ between the arrival-times of each pair of double pulses is calculated and plotted in Fig. 4.9-right. In comparison, random pairs of pulses are drawn from the time distribution of single pulses. The distribution of time differences between these uncorrelated draws and the double pulses align. Therefore, it can be concluded that there is no correlation in the arrival-times of multiple pulses.

Pulse rates

All late pulses are counted for various distances from the shower axis, and the average amount of pulses N_{pulses} per trace is calculated as shown in Fig. 4.10-left for events between 1.0 and 1.2 in sec θ. In the energy range from lg(E/eV) = 18.5

to 19.0 and at a distance of 1000 m from the shower axis, a total of 1310 late pulses in 7268 traces is counted, which gives an expected pulse rate of around 18 % per trace. At approximately 600 m, this rate increases to 43 % with a total of 1049 late pulses in 2439 traces. In the lower energy range from $\lg(E/\mathrm{eV}) = 18.0$ to 18.5 at 1000 m 5189 late were observed in a total of 84 676 traces, which gives a rate of 9 %. At 600 m, there is a respective increase up to 13 % with 3769 late pulses in 28 656 traces. All background pulses (pulses that arrive before the shower signal) are also counted. Their rate is calculated, and then normalized to the counting window of the late pulses. At the closest distances to the shower axis, the late pulse rate exceeds the background pulse rate by over two orders of magnitude. As was shown before, the pulse rates do not only contain pulses from a possible hadronic component, but also are contaminated with pulses from the muonic or electromagnetic component, which is here not included in the background estimation. This additional background is dependent on the zenith angle, shower energy, and the pulse signal. A simplified theoretical estimate of the background rate can be made by accounting for random atmospheric muons as a contributing factor to the background pulses. Assuming the rule of thumb rate of one muon per 20 traces, the expected pulses per trace roughly align with the observed rate of background pulses. In Fig. 4.10-right, the pulse rate is shown for the fixed energy range from $\lg(E/\mathrm{eV}) = 18.5$ to 19.0 and bins in sec θ and it can be seen that the pulse rate is decreasing with increasing sec θ of the shower. At distances below 200 m to the shower axis, the rate appears to be constant. This can be explained by the saturation of the baseline as shown in Fig. 4.10-bottom. The fraction of stations with a saturated baseline $N_{\mathrm{sat}}/N_{\mathrm{tot}}$ rapidly increases, starting at around 200 m from the shower axis. Since pulses can not be reliably counted in traces with a saturated baseline, a lower counting rate in this region is expected.

Pulse Spectrum

The individual charges of all pulses that arrive after 5 µs are measured to obtain a pulse spectrum. Fig. 4.11 illustrates the pulse spectrum for measurements and simulations, normalized to the number of traces N_{trace}. The measurements reveal a deficit of pulses in the simulations with pulse charges S_{pulse} from approximately 220 MIP down to 0.8 MIP.

In Fig. 4.12, the measured pulse spectrum can be further separated into bins of energy, shower zenith angle, and distance. To compare the shape of the different pulse spectra, the number of pulses N_{pulse} is normalized to the total amount of pulses N_{tot} in the corresponding bin. The shape of the pulse spectrum appears to be independent of energy (Fig. 4.12-left). Similarly, when separating the spectra for different bins of shower zenith angles no apparent dependency on the shape of the pulse spectrum is visible (Fig. 4.12-right). However, with increasing distance to the shower axis, a softening of the spectrum can be observed, as well as a cut-off of the pulses above $10\,\mathrm{MIP}_{\mathrm{charge}}$.

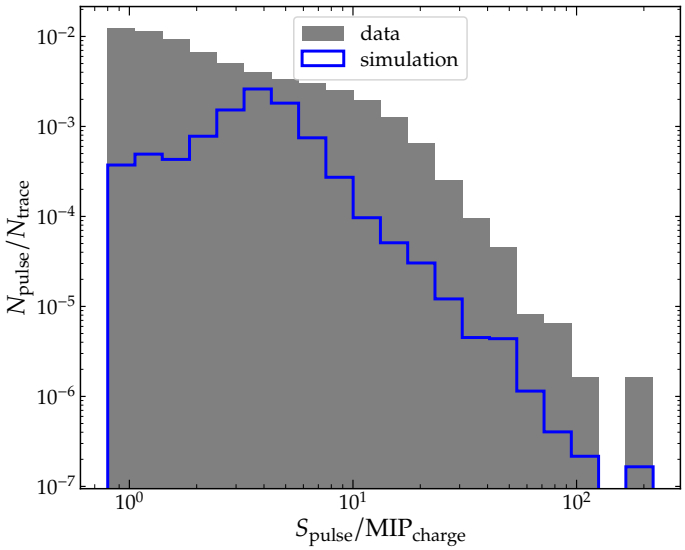

Figure 4.11: There is a deficit of pulses N_{pulses} in simulations compared to the measurements for all pulse charges. The simulations and measurements comprise pulses of the electromagnetic, muonic, and hadronic components after 5 µs. It should be noted that the latter simulation is incomplete as it does not account for neutrons or hadrons below 100 MeV.

Afterpulsing behaviour

To eliminate afterpulsing as a probable source of the pulses, it is helpful to check for correlations between the number of pulses and the total signal in the trace. A qualitative sketch of the expected lateral dependencies of the shower signal S for the electromagnetic shower component and neutrons is shown in Fig. 4.13-left. For simplification, the muonic shower component is left out. The electromagnetic component is the dominant contribution to the total shower signal close to the shower axis. The ratio of the electromagnetic shower component to the total shower signal decreases with increasing distance to the shower axis. The number of afterpulses, denoted by N_{pulses}, depends directly on the total signal of the trace, denoted by S_{tot}. Therefore, the ratio $N_{\mathrm{pulses}}/S_{\mathrm{tot}}$ should remain constant as a function of r.

A contradictory behavior can be observed in Fig. 4.13-right. However, this could also be caused by the widening of the shower signal with distance, which would push the afterpulses to later times. The ratio between the signal from neutrons and the electromagnetic component would be expected to increase with the distance to the shower axis, as qualitatively depicted in Fig. 4.13-left. A corresponding rise could be anticipated for the ratio $N_{\mathrm{pulses}}/S_{\mathrm{tot}}$ if the late pulses derive from neutrons.

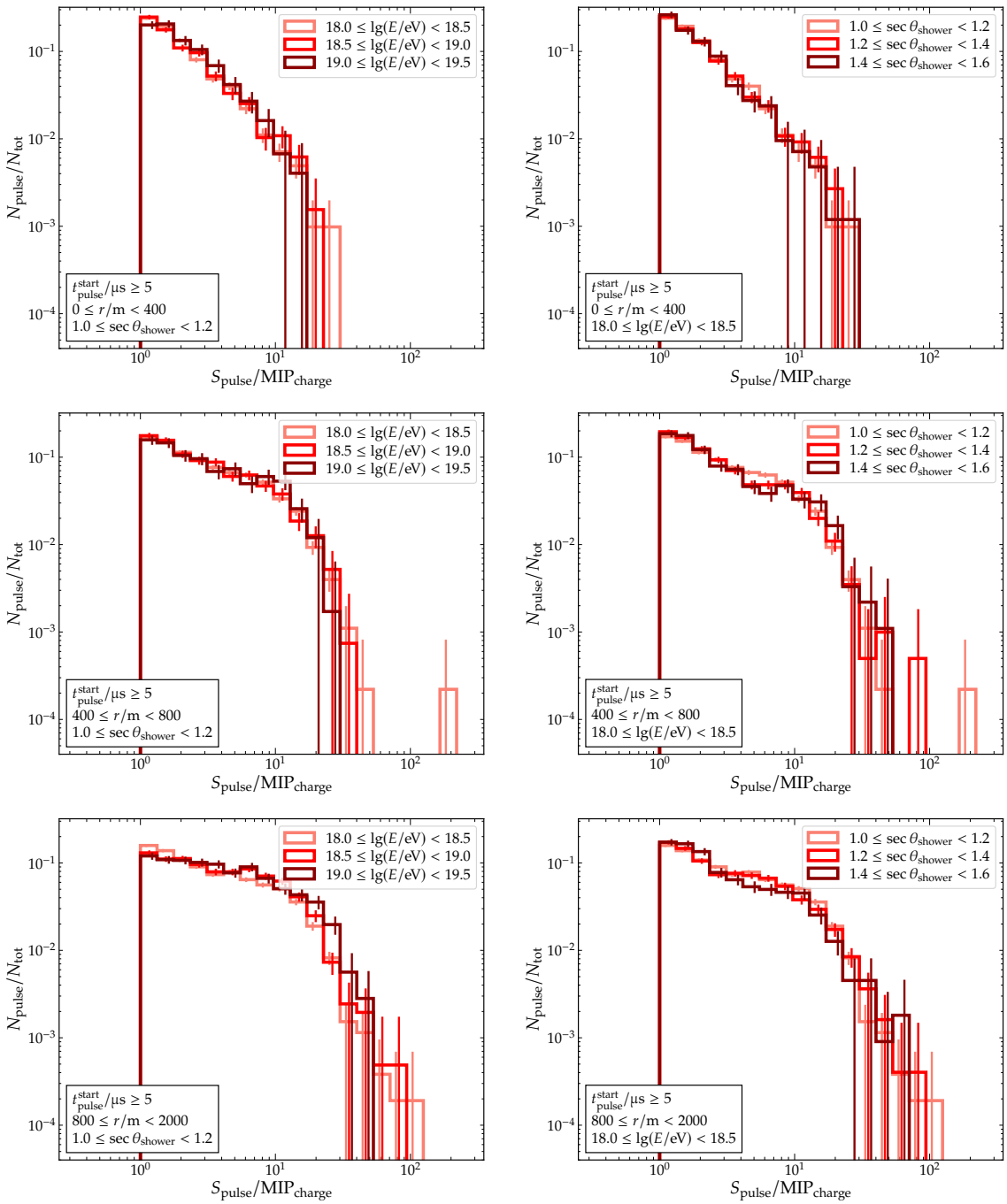

Figure 4.12: The number of pulses N_{pulse} of the pulse spectra are normalized to the total amount of pulses N_{tot} in the corresponding bin, to allow for a comparison of the shape in different bins of energy (left), shower zenith angle (right) and distance. At distances between 0 and 400 m (top) to the shower axis, the observed pulse spectrum reaches up to 50 $\text{MIP}_{\text{charge}}$. The spectrum becomes softer with increasing distance to the shower axis (center), and a cut-off appears around 10 $\text{MIP}_{\text{charge}}$. Between 800 to 2000 m (bottom), the pulse charges reach up to 100 $\text{MIP}_{\text{charge}}$.

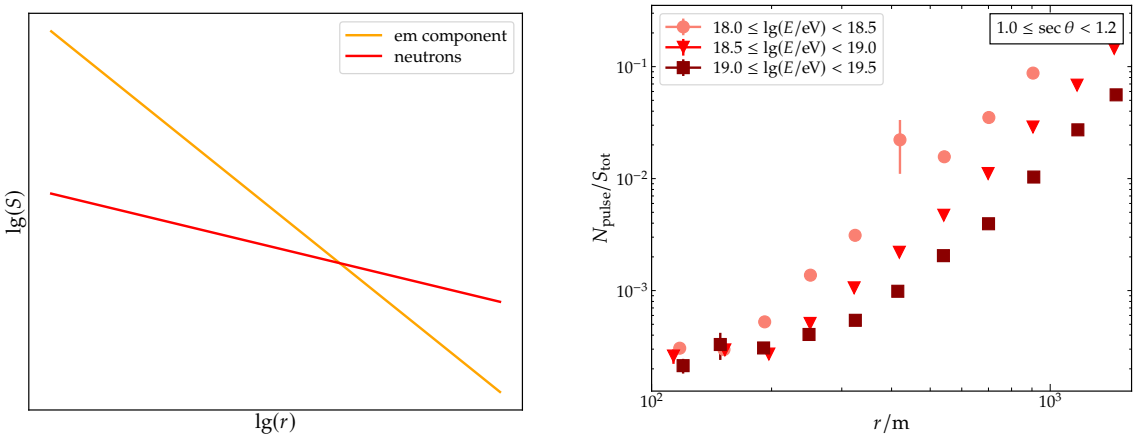

Figure 4.13: *Left:* Qualitative depiction of the relative contributions from the electromagnetic shower component and neutrons to the total signal S in traces relative to the distance r from the shower axis, but the ratio of neutrons to S should increase with distance. The electromagnetic component dominates the signal near the shower axis. *Right:* The ratio between the pulse count N_{pulses} after 5 µs and the total signal of the trace S_{tot} increases with distance r from the shower axis. Should the pulses derive from afterpulsing, this ratio would remain unchanged.

4.2. Adding Hadronic Processes and Quenching to Simulations

Following the prior observations, delayed pulses were characterized in the SSD traces that may originate from neutrons. The main process of a neutron to create a signal in the SSD is by elastic or inelastic scattering with the nucleons of the SSD, leading to secondary charged particles that can ionize the material. Comparisons with simulations that do not incorporate neutrons in simulated detector signals exhibit an excess in the data by over two orders of magnitude in the rate of pulses at the distances nearest to the shower axis. However, due to current technical limitations, neutrons can only be simulated down to an energy of about 20 MeV in air shower simulations with Corsika and the `G4StationSimulator` module of Offline does not include any hadronic physics models from Geant4 that would be relevant for neutron simulations at this time. Therefore, the physics processes used in the `G4StationSimulator` module of Offline are modified to include hadronic interactions. Due to the high energy losses per track length of heavy particles in the scintillator, the resulting light yield from these particles is reduced, and quenching must also be added to the simulations.

4.2.1. Hadronic Processes

Geant4 handles the WCD and SSD physics processes in Offline using physics lists. These lists initialize all relevant physics processes, including electromagnetic processes, muon decay, and optical processes such as Cherenkov radiation. Geant4 includes several reference physics lists for hadronic interactions. Three of the most common reference lists are *QGSP-BIC*, *QGSP-BERT*, and *FTFP-BERT* [88]. The lists are stated to differ primarily in the high-energy hadronic interactions on the order of tens of GeV. In the detector simulations, however, interactions of the order of MeV are of interest. Therefore, one can assume using any of these models should be suitable, but confirmation is necessary in the future. Each list has an extension of a high-precision neutron model for neutron energies below 20 MeV, indicated by an additional *HP* tag. In the following analysis of this work, the *QGSP-BIC* model is used. Since mainly the elastic and inelastic scattering processes of neutrons are of interest, these processes are included separately in the existing physics list of the `G4StationSimulator` module in Offline.[1]

A simple simulation is conducted to test the possible impact of including elastic and inelastic hadronic processes in the simulations. 800 000 vertical particles are injected into the SSD and WCD and count the number of photoelectrons N_{pe} generated by each particle. This is done for electrons and muons with an initial energy of 1 GeV and for protons and neutrons with an initial energy of 50 MeV. Fig. 4.14 shows the impact of hadronic interactions on simulations. The distribution of N_{pe} is not changing for electrons and muons, which is expected since the hadron physics processes should not affect them. Without hadronic processes, the distribution of N_{pe} ranges from approximately 160 to 340 photoelectrons for

[1] The processes in question are *HadronElasticPhysics* and *HandronPhysicsQGSP_BIC*.

protons due to ionization of the scintillator material. Enabling hadronic interactions for the protons results in an additional distribution of N_{pe} ranging from 0 to over 600 photoelectrons. Since neutrons can only deposit energy in the scintillator through elastic or inelastic scattering, no photoelectrons can be seen in the simulations without hadronic interactions. When hadronic interactions are included in the simulations, the distribution of the number of photoelectrons increases from 0 to about 600.

Similarly to the SSD, the photoelectron distributions for the WCD in Fig. 4.15 are compared. As for the SSD, no change in the distribution of N_{pe} for electrons and muons is expected and observed. For protons and neutrons, however, while no photoelectrons were produced before, the switch to simulating hadronic interactions results in an increasing number of N_{pe} which can reach up to about 20 photoelectrons in the case of 50 MeV protons or even 40 photoelectrons in the case of neutrons with an energy of 50 MeV.

4.2.2. Quenching

In addition to the hadronic interactions, which are significant for protons and neutrons in the SSD, ionization quenching is another effect that is relevant for

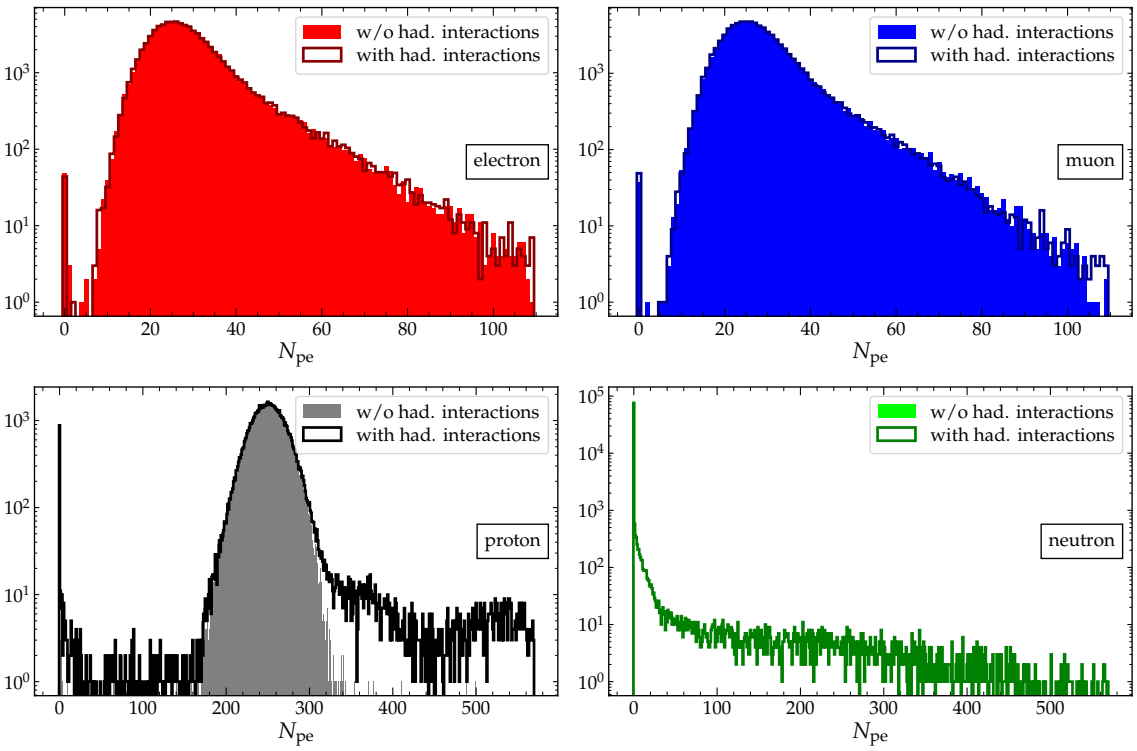

Figure 4.14: The number of photoelectrons N_{pe} generated by single particles injected vertically into the SSD at random positions. The distributions for 1 GeV electrons and 1 GeV muons are shown in the *top-right* and *top-left* respectively. The distributions for 50 MeV protons and neutrons are shown in the *bottom-left* and *bottom-right*. The solid bars show the distributions, where hadronic interactions have not been simulated and the outlines show the distributions, where the *QGSP BIC* model was used.

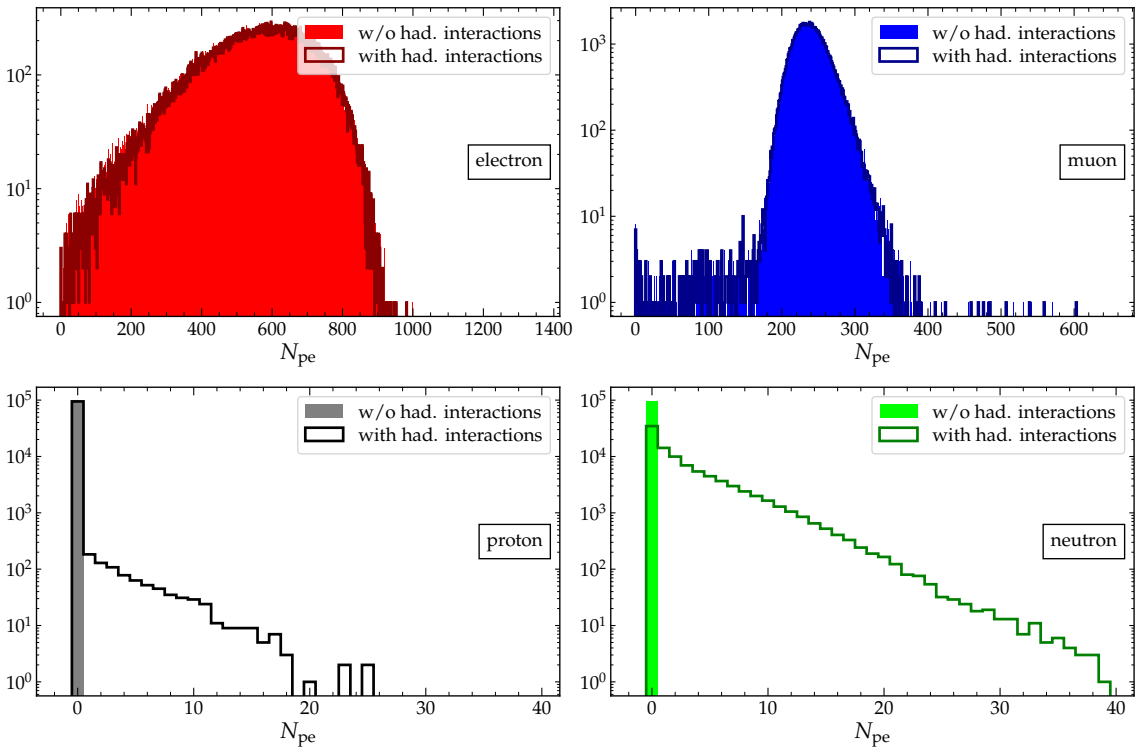

Figure 4.15: The number of photoelectrons N_{pe} generated for single particles injected vertically into the WCD at a random positions. The distributions for 1 GeV electrons and 1 GeV muons is shown are shown in the *top-left* and *top-right* respectively. The distributions for 50 MeV protons and neutrons are shown in the *bottom-left* and *bottom-right*. The solid bars show the distributions, where hadronic interactions have not been simulated and the outlines show the distributions, where the *QGSP BIC* model was used.

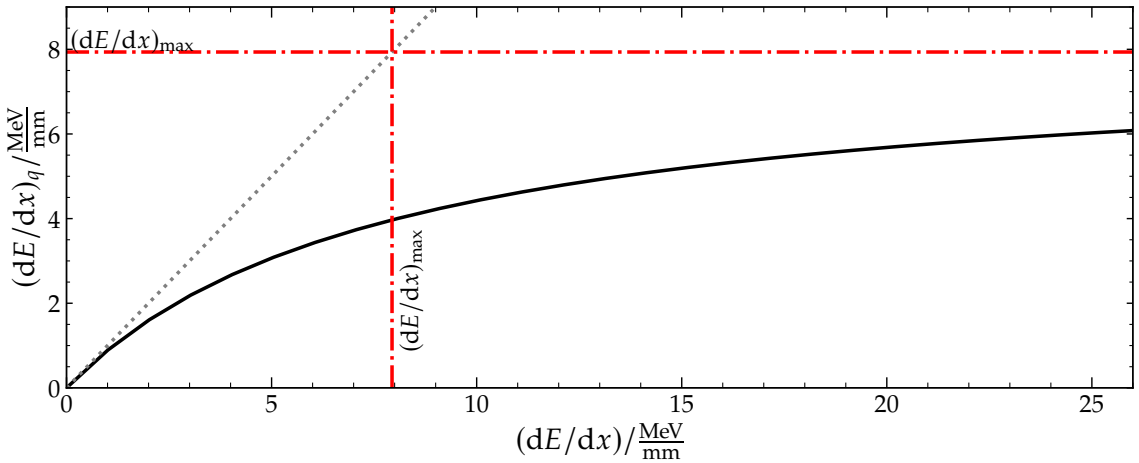

Figure 4.16: The quenched energy deposit $(dE/dx)_q$ of a scintillator exhibits non-linear behavior, with an upper limit of $(dE/dx)_{max}$. At $dE/dx \ll (dE/dx)_{max}$, $(dE/dx)_q$ shows roughly linear behavior.

heavy particles. When particles deposit their energy in a scintillator through ionization, the energy is typically transferred to a primary fluorophore via a dipole-dipole interaction known as the Förster mechanism. Fluorophores are added to the scintillator to increase light yield, shift the wavelength of emitted photons, and enhance scintillation speed [89].

The dependence of the light yield L (per track segment $\mathrm{d}x$) on the energy deposit per track segment $\mathrm{d}E/\mathrm{d}x$ can be approximated, using Birks' law [90]

$$\mathrm{d}L/\mathrm{d}x = \epsilon_{\mathrm{sc}} \frac{\mathrm{d}E/\mathrm{d}x}{1 + kB\,\mathrm{d}E/\mathrm{d}x}. \tag{4.2}$$

where ϵ_{sc} is the scintillation efficiency, k is the probability of quenching and B is the Birks' proportionality coefficient. The relation between the light yield and the energy deposit is thus not linear for large energy deposits, i.e. the yield is "quenched". Equivalently one can say that the quenched energy deposit $(\mathrm{d}E/\mathrm{d}x)_{\mathrm{q}}$ has an upper limit $(\mathrm{d}E/\mathrm{d}x)_{\mathrm{max}}$ such that

$$(\mathrm{d}E/\mathrm{d}x)_{\mathrm{q}} = \frac{\mathrm{d}E/\mathrm{d}x}{1 + \frac{\mathrm{d}E/\mathrm{d}x}{(\mathrm{d}E/\mathrm{d}x)_{\mathrm{max}}}}, \tag{4.3}$$

where $(\mathrm{d}E/\mathrm{d}x)_{\mathrm{max}}$ is the equivalent inverse of the Birks' kB constant. It describes the loss scale, where the transition from the linear behavior between the light yield and energy deposit, $(\mathrm{d}E/\mathrm{d}x)_{\mathrm{q}} = \mathrm{d}E/\mathrm{d}x$, changes to non-linear behavior and finally quenching (plateauing) of the light yield to constant $(\mathrm{d}E/\mathrm{d}x)_{\mathrm{q}} \approx (\mathrm{d}E/\mathrm{d}x)_{\mathrm{max}}$. For polystyrene-based scintillators, the maximal quenched energy deposit per track segment is typically $(\mathrm{d}E/\mathrm{d}x)_{\mathrm{max}} \approx 8\,\mathrm{MeV/mm}$ [89].

Birks' law describes quenching through the creation and capture of excitons. Chou extended Birks' Law by adding a bi-molecular quenching term that considers the interaction between two excited molecules [91]. Hong *et al.* proposed another extension of Birks' law by differentiating between electronic and nuclear energy loss [92]. As in Birks' law, electronic energy loss leads to excitation and ionization. At low energies, elastic collisions between the ion and the scintillator material cause nuclear energy loss [93]. Yoshida *et al.* combined the models of Chou and Hong *et al.* by including the bi-molecular quenching term for electronic energy loss [94]. Voltz *et al.* [95] presented a different approach. The scintillation light emission, which occurs through prompt and delayed fluorescence in the highly ionized central region of the particle track, is quenched. δ-rays that are energetic enough to leave the core region can ionize additional scintillator molecules, providing an unquenched contribution to the light yield. While Birks' law is still commonly used, measurements with various scintillators have demonstrated its inability to accurately predict the light yield across the entire range of $\mathrm{d}E/\mathrm{d}x$ [96]. However, other models also fall short of fully predicting the quenching of different scintillators for different ionizing particles [97]. For scintillators based on polyvinyltoluene[2], the light yield of recoil protons below 1 MeV is smaller than predicted by Birks' law. This difference increases up to 35%

[2]The scintillators of the SSD are polystyrene-based.

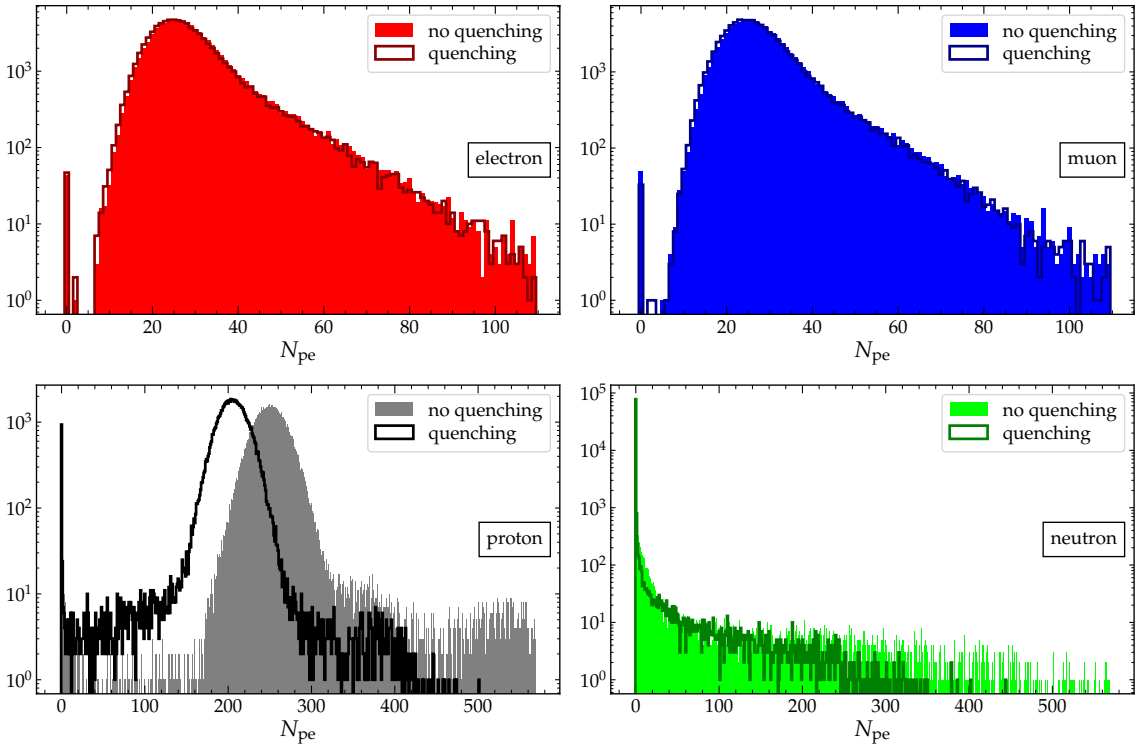

Figure 4.17: The number of photoelectrons generated by single particles injected vertically into the SSD at random positions. The distribution for 1 GeV electrons and 1 GeV muons are shown in the *top-left* and *top-right* respectively. The distributions for 50 MeV protons and neutrons are shown in the *bottom-left* and *bottom-right*. The solid bars show the distributions with no quenching used in the SSD simulations and the outlines show the distributions where Birk's law for quenching was used.

for lower proton energies. For protons with energies above 1 MeV, the light yield is approximately 10% higher.

Dedicated laboratory measurements with the polystyrene-based scintillators of AugerPrime are necessary to implement quenching correctly in the SSD simulations. However, Birks' law with $(\mathrm{d}E/\mathrm{d}x)_{\mathrm{max}} \approx 8\,\mathrm{MeV/mm}$ [89] as a first approximation is used. Various experiments have determined parameters ranging from around 7 MeV/mm to 50 MeV/mm for polystyrene based scintillators [98, 99, 100, 101, 96]. The simulations of injecting single particles are repeated as in Section 4.2.1 and the simulations are compared with and without simulating quenching in the SSD, leaving the hadronic interactions switched on for both simulation runs. Electrons and muons exhibit minimal energy loss per track length in the scintillator, resulting in $(\mathrm{d}E/\mathrm{d}x)_{\mathrm{q}}$ roughly equivalent to $\mathrm{d}E/\mathrm{d}x$. Fig. 4.17 shows a slight shift in the mean of the distributions for electrons and muons, with a reduction from 29.5 to 28.8 photoelectrons for electrons and from 28.7 to 28.1 photoelectrons for muons. However, there is a noticeable reduction of the photoelectron counts in the distributions of N_{pe} for protons and neutrons.

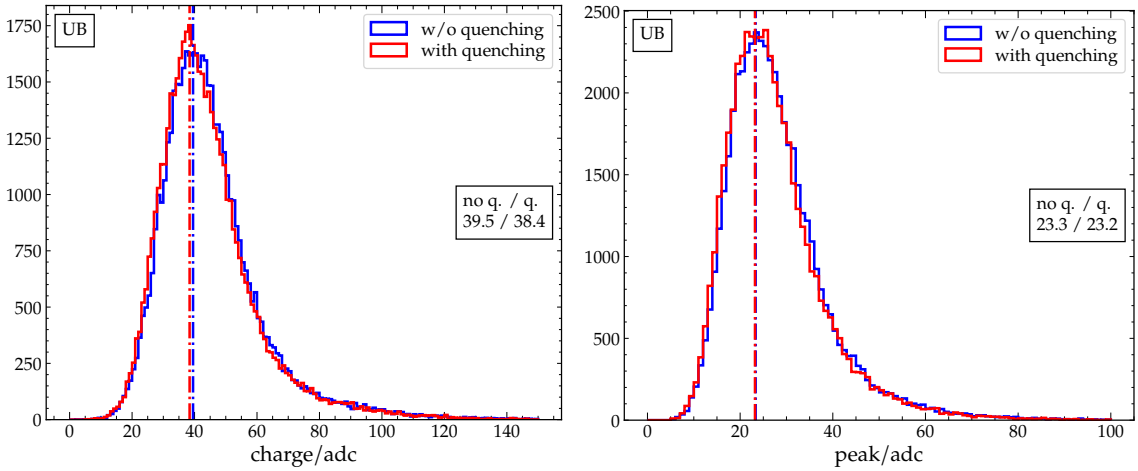

Figure 4.18: *Left:* Histograms of the charge generated by vertical muons used for calibrating the simulated MIP charge for the UB. When simulating quenching in the scintillator, the MIP charge decreases by around 2.8%. *Right:* The simulated MIP peak for the UB decreases by 0.4% when enabling quenching.

4.2.3. Re-calibration of MIP

Even if it is only minimal, quenching impacts the signal produced by muons. To re-calibrate the $\text{MIP}_{\text{charge}}$ and MIP_{peak} of the SSD for the UB and UUB simulations, the `SdSimulationCalibration` module of Offline is used. A 1 GeV muon is injected 50 000 times at a fixed position[3] in the SSD and the charge and peak height of the FADC trace is calculated. The distributions of the charges and peaks with and without quenching are shown in Fig. 4.18 for the UB and in Fig. 4.19 for the UUB. The peaks of the distributions are fitted and used to calibrate the $\text{MIP}_{\text{charge}}$ and MIP_{peak}. If quenching is used in the scintillator simulations, the $\text{MIP}_{\text{charge}}$ of the UB and UUB decreases by 2.8%. Similarly, the MIP_{peak} decreases by 0.4% for the UB and 1.8% for the UUB.

WCD and SSD station signals of 2000 simulated showers of the *Napoli* library [81] of Corsika simulations [82] are further analyzed with primary energies between 10^{19} and $10^{19.5}$ eV. The station signals without simulated quenching $S^{\text{no q.}}$ are compared with the signals when simulating quenching $S^{\text{q.}}$ and the MIP charge is re-calibrated. Hadronic interactions are not simulated in either simulation. The signals without simulation of hadronic interactions $S^{\text{no had.}}$ are also compared to those with the simulation of hadronic interactions $S^{\text{had.}}$. For this comparison, quenching is enabled in both simulations. Fig. 4.20-left shows the average ratio $\langle S_i^{\text{q.}} / S_i^{\text{no q.}} \rangle$ between the simulations with and without quenching as a function of the average station signal without quenching. The SSD signals S_{SSD} above 5 MIP increase between 1.9% and 3%. The WCD signals S_{WCD} remain unchanged above 2 VEM since quenching only affects the SSD. A significant increase in the ratio is visible when the signal of WCD is below 2 VEM and the signal of SSD is below 5 MIP. It is important to note that this artifact can appear when calculating a ratio

[3] This fixed position is where the produced mean charge is equal to the mean charge of a uniform injection across the complete active area of the scintillator.

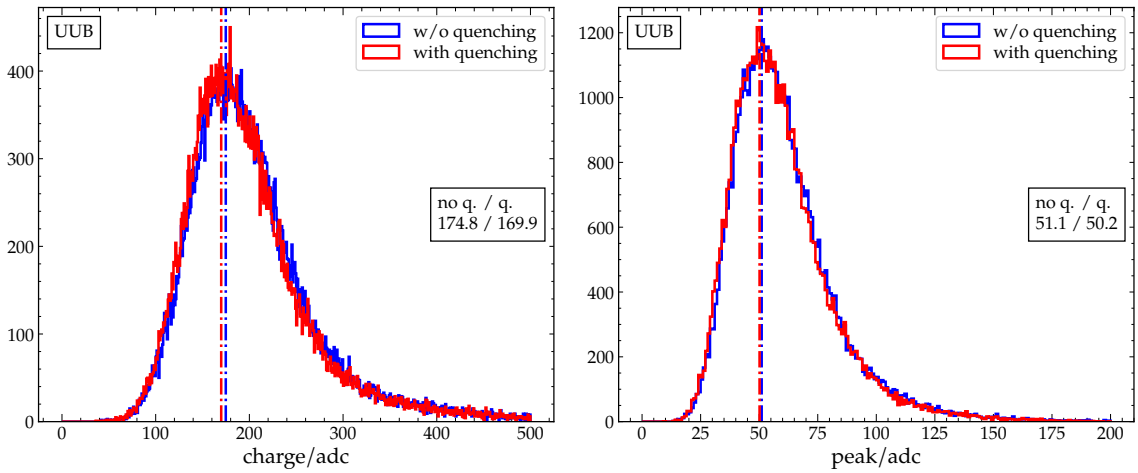

Figure 4.19: *Left:* Histograms of the charge generated by vertical muons used to calibrate the simulated MIP charge for the UUB. When simulating quenching in the scintillator, the MIP charge decreases by around 2.8%. *Right:* The simulated MIP peak for the UUB decreases by 1.8% when enabling quenching.

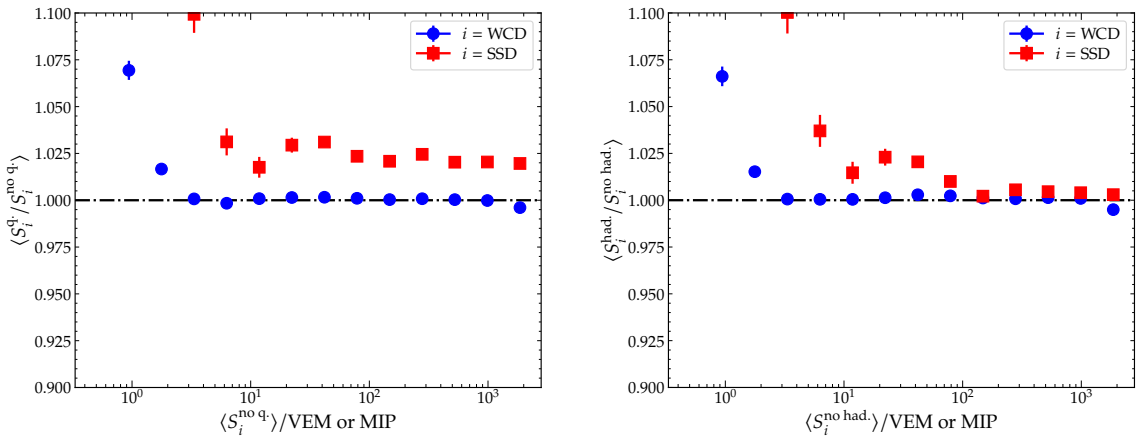

Figure 4.20: *Left:* The average ratio $\langle S_i^{\text{q.}}/S_i^{\text{no q.}}\rangle$ of signals of the WCD (blue circles) and SSD (red squares) as a function of the average signal without quenching $S_i^{\text{no q.}}$, when no hadronic interactions are simulated. The SSD signal $S_{\text{SSD}}^{\text{q.}}$ increases between 1.9% and 3% due to the recalibration of the MIP charge and the addition of quenching. *Right:* When simulating hadronic interactions, $S_{\text{SSD}}^{\text{had.}}$ increases by up to 3% compared to the signals without simulated hadronic interactions $S_{\text{SSD}}^{\text{no had.}}$ in the region between 6 and 100 MIP. For both simulations, quenching is enabled.

of two variables while binning in one of them. Fig. 4.20-right shows the average ratio $\langle S_i^{\text{had.}}/S_i^{\text{no had.}}\rangle$ between the simulations with and without hadronic interactions as a function of the average station signal without hadronic interactions. In the range between 6 MIP and 100 MIP, $S_{\text{SSD}}^{\text{had.}}$ is increased by up to 3% compared to $S_{\text{SSD}}^{\text{no had.}}$. The WCD signals remain unchanged.

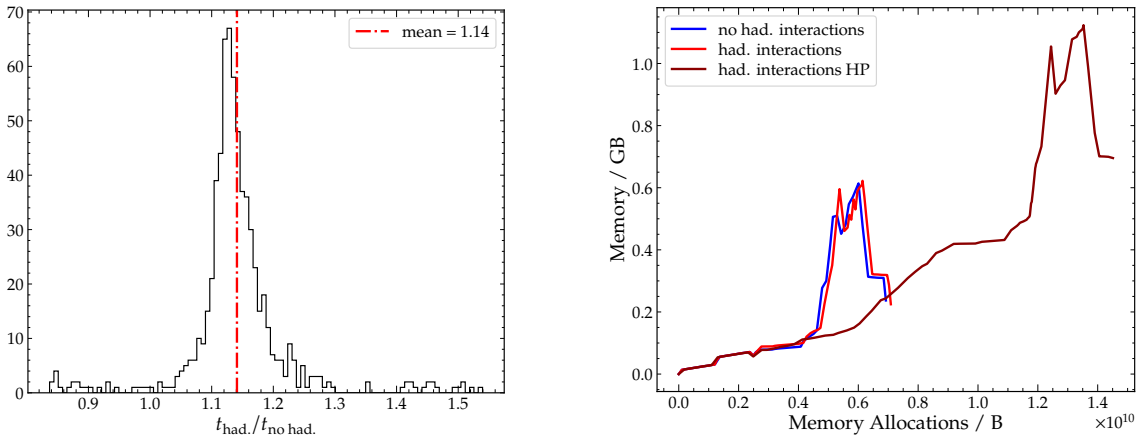

Figure 4.21: *Left:* The ratio of runtimes with and without simulating hadronic interactions. On average, the runtime increases by 13% when using hadronic interactions. *Right:* The memory usage as a function of the allocated bytes during program execution. A minor increase may be observed when simulating hadronic interactions. However, switching to the *HP* model of simulating hadronic interactions almost doubles the memory usage.

4.2.4. Computational Benchmarks

Examining changes in computational demands is necessary before incorporating the simulation of hadronic interactions into the official simulation software framework. The runtime and memory usage when simulating hadronic interactions is compared to simulations without hadronic interactions. The average runtime increases by 13% when simulating hadronic interactions, as shown in Fig. 4.21-left. Fig. 4.21-right shows a slight increase in memory usage when simulating hadronic interactions. Using the *HP* model increases the memory usage and runtime by almost 100%. The reasons for this increase are, as of now, not yet fully understood. Comparing the *HP* model with the regular model, only a minor difference for neutrons with energies of 2 MeV could be determined. Therefore, it is decided not to use the *HP* model but instead the regular one.

4.2.5. Conclusions

The Geant4 physics list in $\overline{\text{Off}}\underline{\text{line}}$ was extended to include the hadronic processes of elastic and inelastic scattering from the *QGSP BIC* model. This makes it possible to investigate neutron signals by simulating surface detector responses to simulated air showers. Additionally, Birks' law with a quenching parameter of $(\mathrm{d}E/\mathrm{d}x)_{\text{max}} \approx 8\,\text{MeV/mm}$ was added as a first step to include quenching in the simulation of the scintillator. This can be improved by measuring the quenching of the scintillators and comparing the measurements with different quenching models. Also, the MIP charge and peak were re-calibrated since quenching reduces light yield in the SSD, albeit the changes are small for muons and electrons with typical energies. Tests with shower simulations have shown a slight increase in memory consumption and runtime when simulating hadronic interactions.

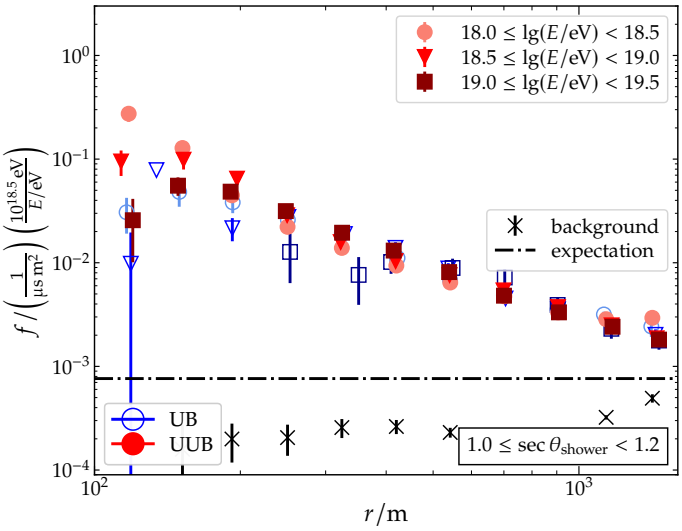

Figure 4.22: The rate of late pulses is normalized to the duration of the counting window, the SSD detector area and the shower energy, resulting in the pulse rate density f. Since the observed rates for the UB (blue, open markers) and the UUB (red, solid markers) are the same, detector effects can be ruled out as the origin for these pulses. The rates for different energies are very similar, making late neutrons the most favorable candidates.

4.3. The Late Neutron Component in Extensive Air Showers

Counting subluminal neutron-pulses presents numerous challenges. Arrival-times at the ground can range from a few nanoseconds to several seconds, yet the traces are limited to 17 µs for the UUB. Discriminating individual neutron-pulses from those of the electromagnetic and muonic shower components is complicated. As employed before in Section 4.1.1, a time threshold of 5 µs after the start of the signal is used to detect potential pulses from neutrons, as they are expected to be the dominant contributors to the signal beyond this point [39]. The shower signal begins at approximately 6 µs, narrowing the search window for neutron-pulses to roughly 6 µs. As a result, only a fraction of neutron-pulses are identified, and missing pulses should be estimated before and after the search window. The abundance of measured pulses was shown previously Fig. 4.8, compared to simulations without a hadronic component. From these plots, estimates about pulses beyond the counting window can be calculated. However, estimates before the counting window are more difficult to estimate. Therefore, the full analysis is limited to the counting window of pulses between 5 and 11 µs after the main shower signal. Further, pulses are counted as neutrons that passed the pulse thresholds of $0.8\,\mathrm{MIP_{peak}}$ and $0.8\,\mathrm{MIP_{charge}}$ in order to avoid the counting of electronic noise due to oscillations of the baseline in the SSD.

4.3.1. Lateral Distribution of Neutrons

The rate of late pulses from Fig. 4.10 is normalized to the area A_{SSD} of the SSD and the length of the pulse counting window. This will show how many pulses are counted per µs and m^2 in the fixed counting window. Since the pulse rate depends

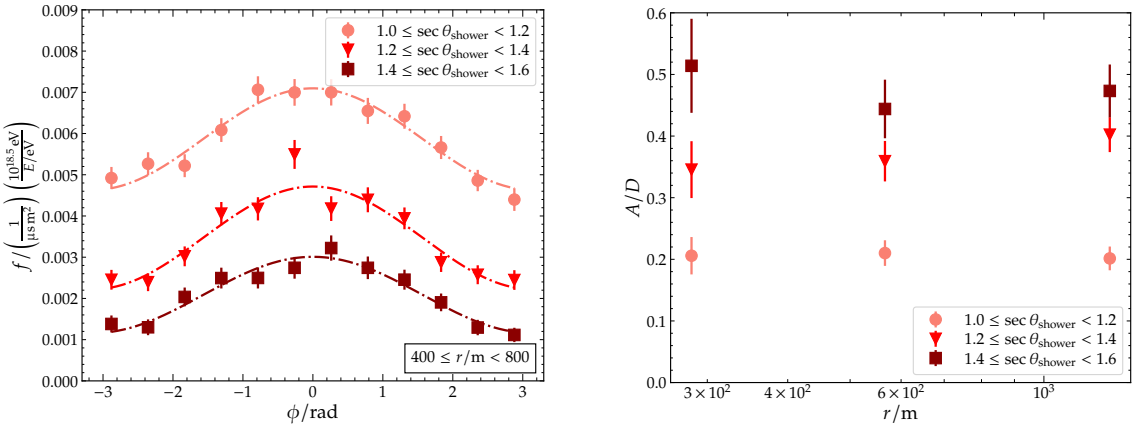

Figure 4.23: *Left:* The pulse rate density f for stations at different azimuthal positions relative to the shower axis. At $\phi = 0$ rad, the station is located toward the incoming trajectory of the shower axis. Thus, incoming particles have to pass through less atmosphere, and the attenuation is expected to be smaller. The dash-dotted line shows a fit of a sinusoidal function to the data. *Right:* The amplitude A and offset D of the fit are used to calculate the relative amplitude A/D of the azimuthal asymmetry. With increasing distance to the shower axis and increasing inclination of the shower, A/D is increasing due to stronger attenuation effects.

on the energy, the rate is normalized to the energy bin from $10^{18.5}$ eV to $10^{19.0}$ eV. Fig. 4.22 shows the normalized pulse rate, or pulse rate density f, for showers between 1.0 and 1.2 in $\sec\theta$ since the rate is also dependent on the inclination of the shower. The rate of background pulses arriving before the shower signal and the expected rate based on the assumption of one atmospheric muon per 20 traces are also included. The normalized rates almost overlay perfectly with each other for each energy bin. In the region of closer than 200 m to the shower axis, the rate at the highest energy bins starts to deviate due to saturation effects in the traces, which lead to a miscounting of the pulses (see Section 4.1). Further away from the shower axis, the pulse rate is slightly higher in the highest energy bins compared to the bins of lower shower energies. This effect reverses around 900 m from the shower axis, where the pulse rate is larger in the lower energy bins than in the higher energy bins. From Ref. [42], the number of neutrons at the ground is expected to scale almost linear with energy due to the strong attenuation in the atmosphere. Furthermore, pulse measurements of the PPA dataset are added to Fig. 4.22, which utilizes UB electronics contrary to the UUB electronics of the AugerPrime dataset. The plot shows that the normalized distributions for both electronics are very similar. This further proves that the observed pulses are not a side effect of the detector electronics but rather physical particles.

Furthermore, the azimuthal dependence of the pulse rate density is analyzed. Fig. 4.23-left shows f as a function of the azimuthal station position relative to the shower axis for stations between 400 and 800 m. Due to a bias in the reconstructed position of the shower core from the WCD measurements, a bias in the azimuthal station position is expected [84]. However, this bias is ignored in the following analysis. At $\phi = 0$ rad, the station is located toward the incoming trajectory of the shower axis called the *upstream* position. At $\phi = \pm\frac{\pi}{2}$ rad, the

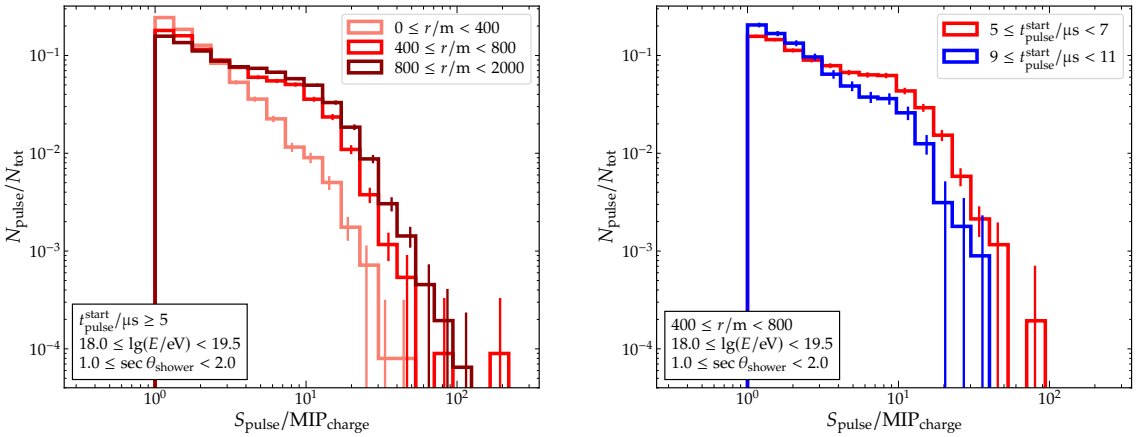

Figure 4.24: *Left:* The measured pulse spectrum for different distance bins. These three spectra are used for any further analysis. *Right:* When binning the pulse spectrum for different pulse arrival-times, the spectrum, containing earlier (5 and 7 μs) pulses, reaches to larger S_{pulse} than when considering later (9 and 11 μs) pulses. This trend corresponds to the expectation that neutrons, arriving earlier, have larger energies than neutrons arriving later on the ground.

station is located opposite of the incoming trajectory of the shower axis called the *downstream* position. Particles that reach the stations in the upstream region have to pass through less atmosphere in inclined showers than in the downstream region. Therefore, the sinusoidal behavior in Fig. 4.23-left is expected due to the attenuation of f towards the downstream region. A function of the form

$$f(\phi) = D + A\cos\phi, \tag{4.4}$$

with the offset D and the amplitude A is fit for each shower zenith angle and distance bin. To exclude the above-mentioned saturation effects, the distance bins are chosen from 200 to 400 m, 400 to 800 m, and 800 to 2000 m. Then, the relative amplitude of the azimuthal asymmetry is calculated as A/D and shown in Fig. 4.23-right for different zenith angle bins. A/D increases with larger sec θ_{shower} due to the increased difference of the traversed atmosphere in the upstream and downstream regions. For vertical showers, ($1 \leq \sec\theta_{\text{shower}} < 1.2$) no increase in A/D with distance to the shower axis is to be expected since the attenuation effects of the upstream and downstream regions should be minimal. However, with increased inclination of the shower, a small increase of A/D with distance can be observed.

4.3.2. The Neutron-Pulse Spectrum

The rate of late pulses heavily depends on the distance to the shower axis, the inclination of the shower, and its energy (see Fig. 4.10). However, it has been shown that the shape of the spectrum of these pulses is almost independent of shower energy and inclination and mainly depends on the distance to the shower axis (see Fig. 4.12). Therefore, the entire energy and zenith range of the measurements is used and only the distance to the shower axis is binned for the

spectra, as shown in Fig. 4.24-left. At larger distances from the shower axis, the spectrum becomes harder compared to closer distances.

In Fig. 4.24-right, the pulse spectrum for distances between 400 and 800 m is divided into two late-pulse arrival-time windows. The rate of pulses with an S_{pulse} above 5 $\text{MIP}_{\text{charge}}$ is larger for pulses between 5 and 7 µs than for pulses between 9 and 11 µs. Neutrons with higher energies undergo less elastic scattering and thus are expected to arrive earlier than low-energy neutrons.

4.3.3. Creating a Neutron-Pulse Library

Current air shower simulations with Corsika do not contain neutrons simulated down to the lowest energies. If one wants to predict the measurements of late pulses from simulated neutron energy spectra, a library of neutron-pulses has to be created for different neutron energies. In Section 4.2, the Offline framework was extended by adding hadronic interactions and quenching to the detector simulations, enabling us to study the expected detector response to neutrons under various conditions. Simulations of single neutrons injected in the SSD at fixed values of their energy E_{neutron} and their impact zenith angle $\sec\theta_{\text{particle}}$ are performed for different quenching parameters $(\mathrm{d}E/\mathrm{d}x)_{\text{max}}$ of the SSD. The resulting neutron-pulses S_{neutron} in the SSD are then evaluated using the same pulse-finding algorithm used for the neutron measurements. In addition, a modified version of this algorithm is run with lower thresholds for pulse detection to catch the most pulses, down to a pulse height of 0.24 MIP_{peak}. For each combination of energy, zenith angle, and quenching bins, 500 000 neutrons are simulated. Energies between 1 MeV and 4700 MeV in 54 logarithmic bins are chosen and for $\sec\theta_{\text{particle}}$ values between 1.0 and 2.0 in steps of 0.1 are used. Further, 2 more bins at 70° and 80° are added, to cover some of the very inclined angles. The values of $(\mathrm{d}E/\mathrm{d}x)_{\text{max}}$ are chosen based on the maximum possible range of values given in Section 4.2. 7 MeV/mm is used as the minimum value, 8 MeV/mm as the standard value and 50 MeV/mm as the maximum value. Additionally, 9 MeV/mm is added as an extra value for quenching and an infinitely large $(\mathrm{d}E/\mathrm{d}x)_{\text{max}}$ corresponding to no quenching.

In each bin, the probability p_{det} of a neutron to create a detectable signal is evaluated. The probability of a neutron interacting with the nucleons of the SSD is directly proportional to the track length in the detector. Fig. 4.25-left shows p_{det} normalized by $\sec\theta_{\text{particle}}$ as a function of E_{neutron} for three different bins of $\sec\theta_{\text{particle}}$. p_{det} increases from 2% up to around 5% for neutrons with energies between 1 and 3 MeV. Between 3 MeV and ~200 MeV, p_{det} then decreases again to about 2%. This behavior is also seen in Ref. [42]. However, with even higher E_{neutron}, the results deviate from Ref. [42] and instead of an expected slight increase, p_{det} increases strongly again. This effect can be explained by the presence of the WCD in the simulations. Due to the presence of the WCD, neutrons can undergo additional elastic or inelastic scattering in the water and get scattered back into the SSD, thus increasing the chance of interactions. As a cross-check, one set of neutron simulations is repeated, simulating only the SSD and not the WCD underneath it. Fig. 4.25-right compares the simulations with

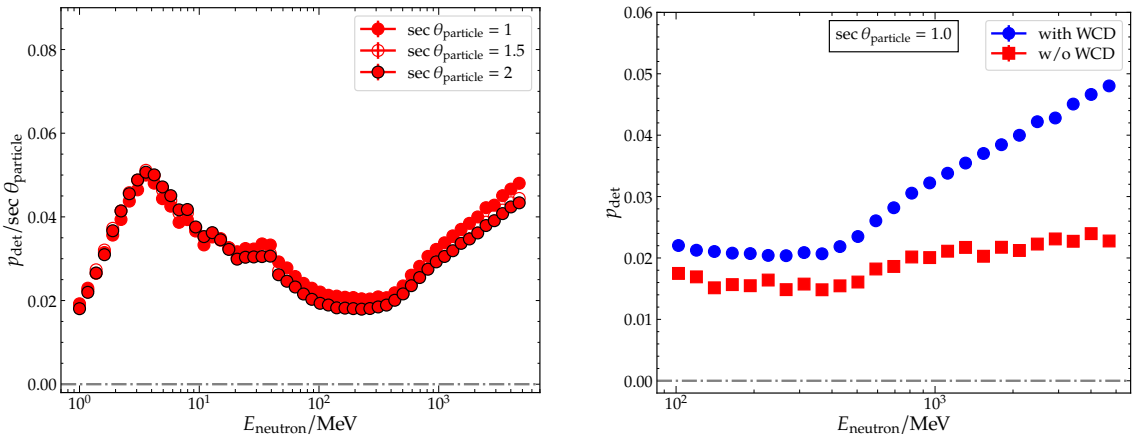

Figure 4.25: *Left:* The probability p_{det} of a neutron to create a detectable signal scales with sec θ_{particle}. *Right:* At large E_{neutron}, p_{det} increases due to neutrons back-scattering from the WCD into the SSD.

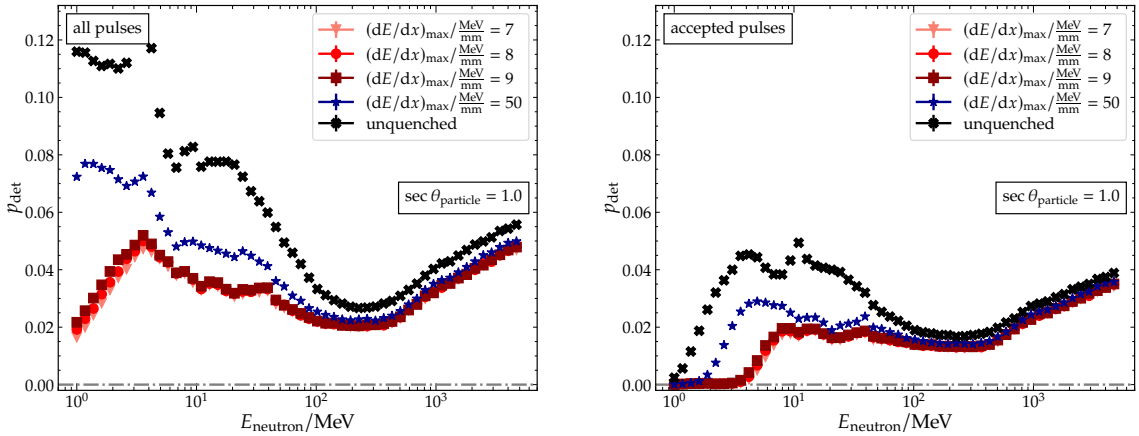

Figure 4.26: *Left:* The probability p_{det} of a neutron to create a detectable signal is also dependent on the quenching of the SSD. For larger $(dE/dx)_{max}$ or no quenching, the signals of the pulses increase, leading to an increase of p_{det}. *Right:* Since thresholds of 0.8 $\text{MIP}_{\text{charge}}$ and 0.8 MIP_{peak} are set in the pulse-finding algorithm, p_{det} for accepted pulses is decreased.

and without the WCD. The increase of p_{det} when the WCD is present is reduced when not simulating the WCD.

p_{det} is also expected to change when using different values for $(dE/dx)_{max}$. The larger $(dE/dx)_{max}$, the less the signal will get reduced due to quenching, increasing p_{det} since more pulses can now be measured. Fig. 4.25-left shows only small differences for p_{det} for quenching values between 7 and 9 MeV/mm. At 50 MeV/mm p_{det} notably increases at lower E_{neutron}. This difference is even more increased when using simulations with no quenching. In Fig. 4.25-right, p_{det} is also calculated for the pulses that pass the neutron-pulse thresholds of 0.8 MIP_{peak} and 0.8 $\text{MIP}_{\text{charge}}$ for comparability with the measurements. p_{det} is lower for these accepted pulses than for all pulses that can be measured. On average, the probability of a neutron producing a pulse that satisfies the pulse thresholds is around 1.6%. Neutrons with energies below 10 MeV do not produce

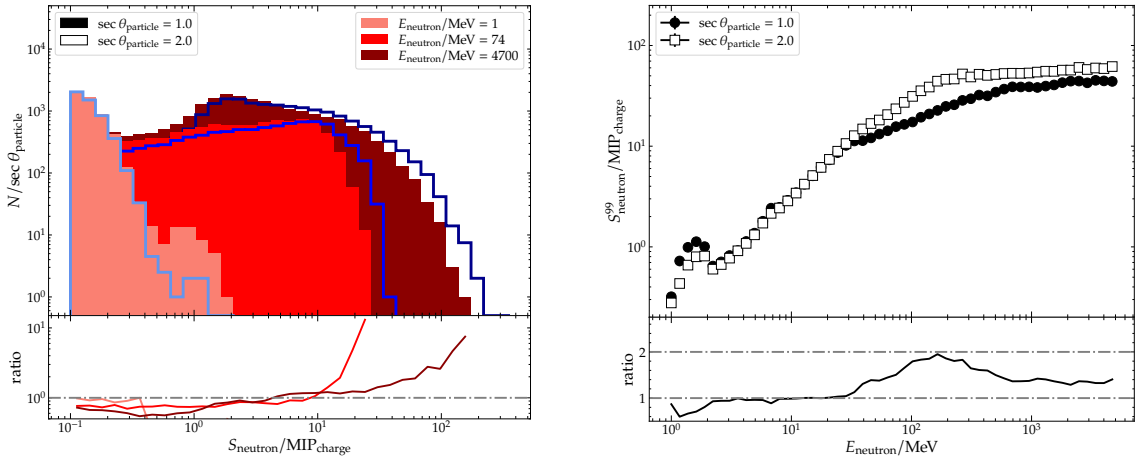

Figure 4.27: *Left:* Neutrons at different energies can create wide distributions of possible S_{neutron}, which are dependent on sec θ_{particle}. Low S_{neutron} are shifted with increasing sec θ_{particle} to larger S_{neutron}, creating a deficit of S_{neutron} below 10 MIP$_{\text{charge}}$. *Right:* The 99% percentile of pulse signals S^{99}_{neutron} after simulating 500 000 neutrons scales linear with energy. At larger E_{neutron}, S^{99}_{neutron} reaches a plateau.

large enough pulses to satisfy the neutron-pulse thresholds, and p_{det} becomes almost 0 at lower energies. For increased $(\mathrm{d}E/\mathrm{d}x)_{\text{max}}$, the neutron-pulses at low energies are slightly larger, lowering the threshold energy to 5 MeV.

The distribution of the signal S_{neutron} of simulated neutron-pulses is shown for 3 energy bins in Fig. 4.27-left for a sec θ_{particle} of 1.0 and 2.0 For a better comparison of the shapes of the distributions, the number of pulses N in each bin is normalized by sec θ_{particle} to account for the detection efficiency. Below is the ratio between N for the zenith angle bins at the different E_{neutron}. For each E_{neutron}, the maximal pulse signal a neutron of this energy can reach is also determined. As an estimate for this maximal signal, the 99% percentile S^{99}_{neutron} is determined for each distribution. S^{99}_{neutron} is shown in the upper part of Fig. 4.27-left, as well as the ratio between both values for different zenith angle bins in the lower part. Higher energetic neutrons have more energy available to transfer to other particles, thus resulting in the increase of S^{99}_{neutron} proportional to E_{neutron}. This is mostly valid as long as the outgoing particles of the interaction are still contained within the volume of the scintillator. At around 200 to 300 MeV, the maximum transferred energy becomes so large that the outgoing particles can exit the scintillator, thus leading to the plateau in S^{99}_{neutron}. In this energy region the ratio between S^{99}_{neutron} for the two zenith angle bins becomes around 2, which reflects the difference in the path length of a particle traversing the SSD with sec θ_{particle} of 1 or 2. This also can explain part of the shift from a negative to a positive ratio in Fig. 4.27-left. A neutron of any energy E_{neutron} can create a large range of S_{neutron}. With increasing zenith angle, the maximum of the range of S_{neutron} becomes higher and the distribution gets larger. Since there is a fixed number of 500 000 neutrons for each energy, the amount of N in the bins of S_{neutron} becomes smaller.

Fig. 4.28-left shows the distribution S_{neutron} for a quenching constant of 8 MeV/mm

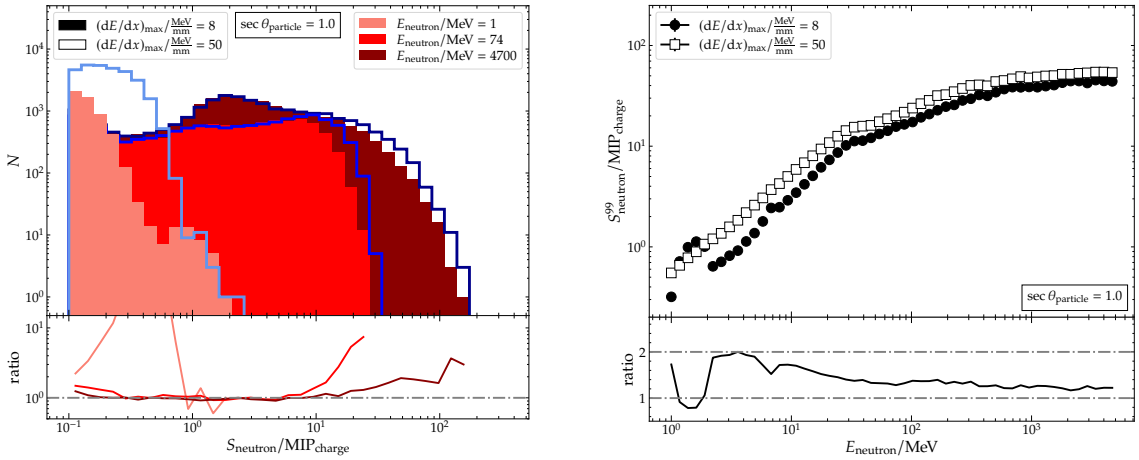

Figure 4.28: *Left:* Contrary to the change in the distributions of $S_{neutron}$ depending on the zenith angle of the neutrons, the shape of the $S_{neutron}$ distributions changes less with $(dE/dx)_{max}$. At low $E_{neutron}$, the amount of pulses is increased for larger $(dE/dx)_{max}$, due to the increased p_{det}. *Right:* The 99% percentile $S^{99}_{neutron}$ of pulse signals after simulating 500 000 neutrons for different $(dE/dx)_{max}$ increases by about 25% when changing from 8 MeV/mm to 50 MeV/mm.

and 50 MeV/mm and Fig. 4.28-right shows the maximum $S_{neutron}$ that are reached after simulating 500 000 neutrons as a function of $E_{neutron}$. With a larger $(dE/dx)_{max}$, the attenuation of the signal is reduced and a larger $S^{99}_{neutron}$ can be reached. The increase is around 25% and can be seen equally for almost all neutron energies.

4.3.4. Forward-Folding Neutron Energy Spectra

Since the simulated neutron-pulse library contains not only the distributions of $S_{neutron}$ for different $E_{neutron}$, $\sec\theta_{particle}$, and $(dE/dx)_{max}$ but also the detection probability of the pulse-finding algorithm, this library can now also be used to forward-fold the neutron-pulse spectra. First, an arbitrary input neutron energy spectrum is determined. For each energy bin, a scaling factor is determined from the input spectrum and then a scaled pulse spectrum of the simulated library is added to the total pulse spectrum.

The resulting pulse spectrum is normalized to the total pulses for comparison with the measurements. Different pulse spectra are shown for three arbitrary input energy spectra in Fig. 4.29. For the incident angles of the neutrons, a $\sec\theta_{particle}$ of 1.0 is chosen and a quenching value of 8 MeV/mm. As the functional form, a simple power-law ansatz of the form

$$dN/dE \propto E^{\gamma},\ \gamma \in \{0, 1, -1\} \tag{4.5}$$

is used. The left plots of Fig. 4.29 show the input energy spectra along with the chosen sampling. The right plots show the resulting pulse spectra and compare them to the measurements for pulses between 400 and 800 m from the shower axis. Next, the G-value is estimated, which is derived in Ref. [102] as the Poisson likelihood

$$G = 2\sum_i N_i^{sim} - N_i^{meas} + N_i^{meas}\ln(N_i^{meas}/N_i^{sim}). \tag{4.6}$$

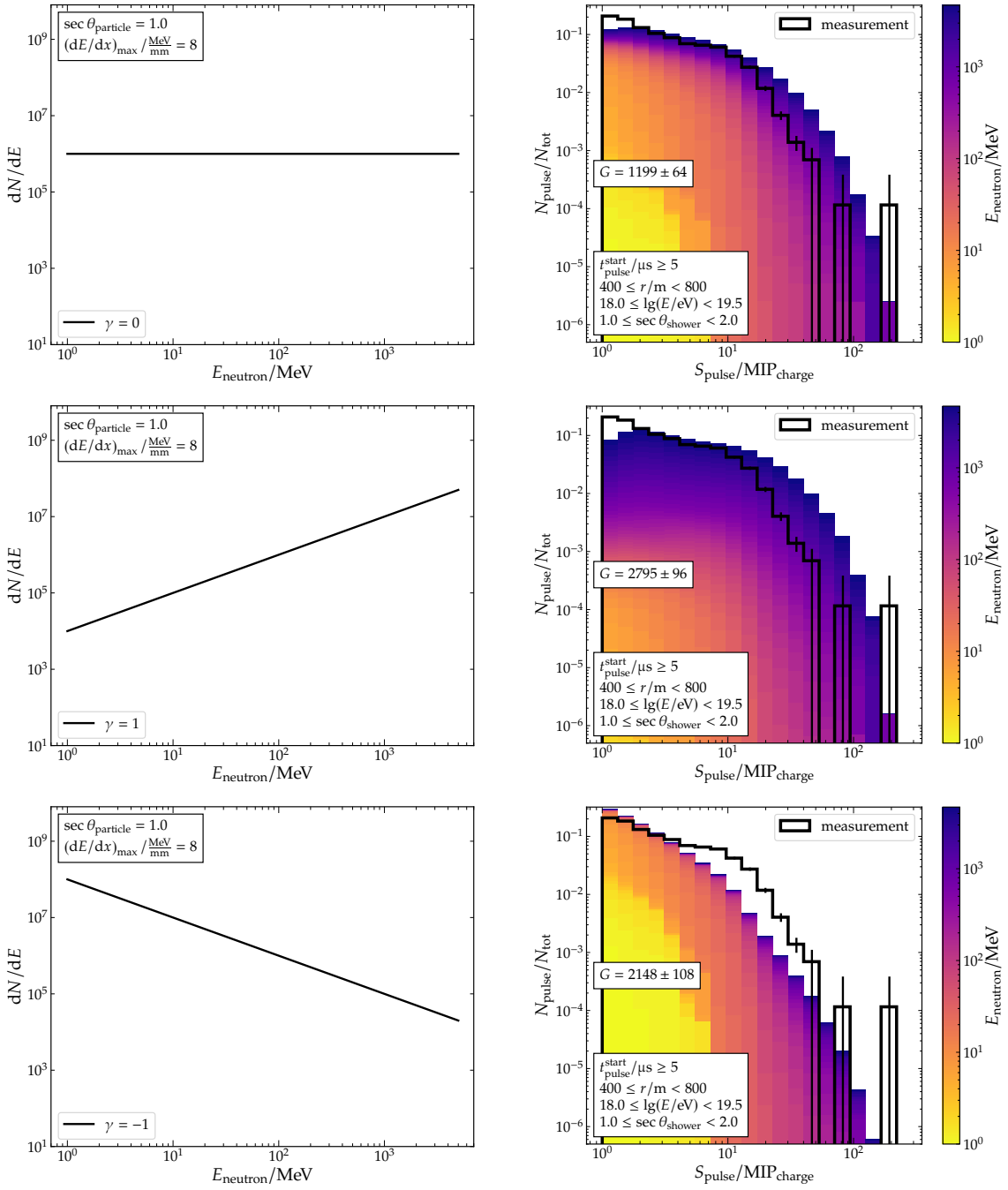

Figure 4.29: The simulated neutron library is sampled from an input energy spectrum (left plots) using a simple power-law with different indices γ. The resulting pulse spectra (right plots) can then be compared with the measured pulse spectrum. The contribution of each neutron energy is color-coded to visualize its relative contribution to the full spectrum.

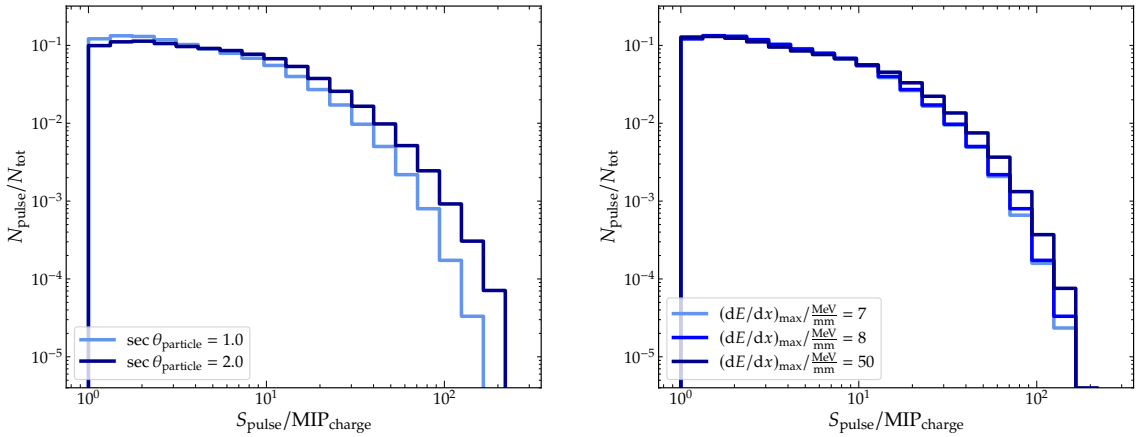

Figure 4.30: *Left:* The influence of $\sec\theta_{\text{particle}}$ to the forward-folded pulse spectrum is compared, using an input energy spectrum of the form E^0 and the two incident neutron angles at $\sec\theta_{\text{particle}}$ 1 and 2. The larger maximum signal at 2 leads to a similar increase at the upper end of the pulse spectrum. *Right:* Similar the influence of $(\mathrm{d}E/\mathrm{d}x)_{\text{max}}$ is compared for 3 different parameters. Due to quenching, a slight increase is observed in the maximal observed neutron-pulse signal. Therefore, a slight variation of the resulting pulse spectrum for different $(\mathrm{d}E/\mathrm{d}x)_{\text{max}}$ can be seen.

N_i^{sim} and N_i^{meas}, correspond to N_{pulses} in each bin i of the simulated or measured pulse spectrum. To calculate G, N_{tot} of the simulated pulse spectrum is normalized first to N_{tot} of the measurements. The measured distribution gets bootstrapped 10000 times, and G is calculated for each distribution. The average G and its standard deviation are then given in the right plots of Fig. 4.29.

From these three plots, a strong dependency of the pulse spectrum on the shape of the input spectrum can be concluded.

The dependency of the pulse spectrum on $\sec\theta_{\text{particle}}$ and $(\mathrm{d}E/\mathrm{d}x)_{\text{max}}$ is checked for an input energy spectrum with $\gamma = 0$. Fig. 4.30-left compares the measured and simulated pulse spectrum with two incident particle angles at $\sec\theta_{\text{particle}} = 1$ and 2. As it was shown in the previous section in Fig. 4.27, the spectrum becomes harder for larger $\sec\theta_{\text{particle}}$, while the number of small pulses slightly reduces. However, it is important to note that a single arrival angle for all neutrons at all energies is incorrect. Different distributions of arrival angles are expected for each neutron at a specific energy and distance to the shower axis. A description of these distributions using air shower simulations is given in Appendix B.2. A single incident angle for all neutrons is kept for simplicity. In Fig. 4.30-right, the comparison for three quenching bins at 7, 8, and 50 MeV/mm is shown. Similarly, a more minor dependency on $(\mathrm{d}E/\mathrm{d}x)_{\text{max}}$ than the changes in $\sec\theta_{\text{particle}}$ can be seen. Since the quenching factor of the used scintillators is unknown, the previously chosen value of 8 MeV/mm is kept and the literature values of 7 and 50 MeV/mm are used as maximum errors.

Next, more modifications are added to the shape of the input spectrum. Instead

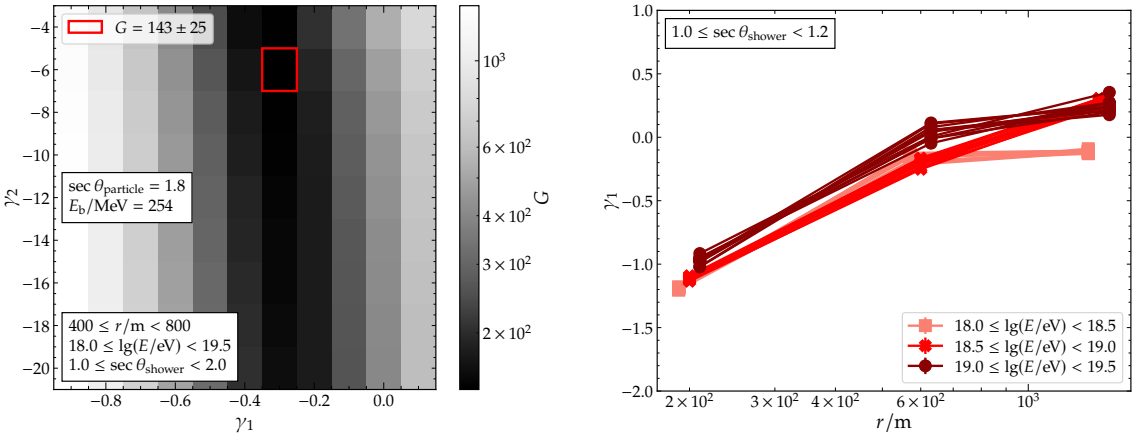

Figure 4.31: *Left:* A scan of G for fixed parameters $\sec\theta_{\text{particle}}$ and E_b for certain shower bins. The global minimum is given with a red square. While for γ_1, an apparent convergence to an optimal value can be seen, γ_2 appears to have only minor importance to the convergence of the minimum G. *Right:* The optimal γ_1 parameters depend on the distance r to the shower axis. Multiple values of γ_1 are given for various $\sec\theta_{\text{particle}}$ for each distance.

of a simple power-law ansatz, a broken power-law of the form

$$\frac{\mathrm{d}N}{\mathrm{d}E} \propto \left(\frac{E_\text{neutron}}{E_\text{b}}\right)^{-\gamma_1} \left\{\frac{1}{2}\left[1+\left(\frac{E_\text{neutron}}{E_\text{b}}\right)^{1/\Delta}\right]\right\}^{(\gamma_1-\gamma_2)\Delta}, \tag{4.7}$$

is used with the spectral indices γ_1 and γ_2 and the transitionpoint between these two at the energy E_b. The Δ factor is used to describe the smoothness of the transition and is set to 0.1. It can now be attempted to find the optimal simulation parameters γ_1, γ_2, E_b, and $\sec\theta_{\text{particle}}$ for different bins in shower zenith angle, energy, and distance to the shower axis of the measurements by minimizing the G-value. In Fig. 4.31-left, an example scan of G for varying γ_1 and γ_2 parameters is shown for a fixed E_b and $\sec\theta_{\text{particle}}$. The global minimum is marked with a red square. While the γ_1 parameter converges to a minimum value at 0.3, for γ_2, no clear minimum is found. Similarly, the other parameters E_b and $\sec\theta_{\text{particle}}$ are found with no apparent convergence to a minimum. This behavior is assumed to be due to correlations between these parameters. A further example of this is shown in Fig. 4.31-right. The optimal γ_1 is shown as a function of distance r to the shower axis for different bins in shower energy and zenith angle. Also, the optimal γ_1 is added for various $\sec\theta_{\text{particle}}$ between 1 and 2, indicated by the extra lines and markers. γ_1 shows a clear dependence on r, while the different $\sec\theta_{\text{particle}}$ appear to have no significant influence on the absolute value of γ_1. Also, the other parameters E_b and γ_2 show no clear dependency on either r or $\sec\theta_{\text{shower}}$.

A new input energy spectrum can be forward-folded using the previously determined optimal parameters for a broken power-law. The shape of the energy spectrum is given in Fig. 4.32-top-left and the resulting pulse spectrum in Fig. 4.32-top-right. With the assumption of an incident particle angle of $\sec\theta_{\text{particle}} = 1.8$ and the parameters $\gamma_1 = -0.3$, $\gamma_2 = -6$, and $E_\text{b} = 254\,\text{MeV}$, the shape of the

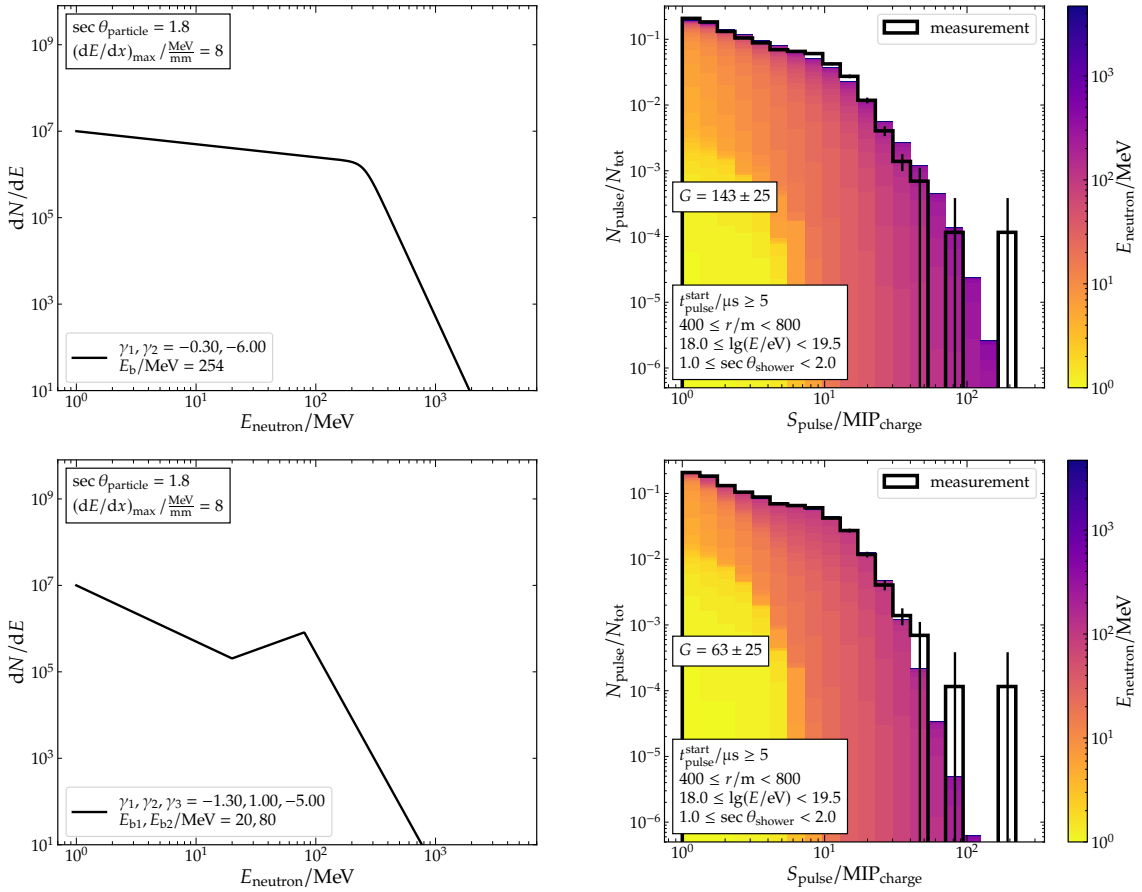

Figure 4.32: *Top:* Using the shape of a broken power-law for the input energy spectrum (left) can yield a quite well-fitting pulse spectrum (right). *Bottom:* This can be further improved by adding more spectral indices and transition points to the energy spectrum.

measured pulse spectrum is reasonably well reproduced. The fit of the pulse spectrum can be further improved by adding more spectral features to the energy spectrum. Fig. 4.32-bottom-left shows an input energy spectrum with three different spectral indices changing from $\gamma_1 = -1.3$ over $\gamma_2 = 1$ to $\gamma_3 = -5$ and two transition points at $E_{\text{b1}} = 20\,\text{MeV}$ and $E_{\text{b2}} = 80\,\text{MeV}$. The resulting pulse spectrum in Fig. 4.32-bottom-right is further improved and mimics the shape of the measured spectrum exceptionally well.

An energy spectrum from Ref. [42], shown in Fig. 4.33-left, which was simulated using Fluka, is forward-folded. The simulation describes an energy spectrum of neutrons in a vertical shower with an energy of $5.6 \times 10^{18}\,\text{eV}$ at an atmospheric depth of about $878\,\text{g/cm}^2$, corresponding to about the same depth as in the measurements. The spectrum includes all downward-going neutrons in a distance range between 400 m and 800 m to the shower axis and an arrival-time between 5 µs and 11 µs. Further, 8 MeV/mm is used as previously for the quenching constant. The angular distribution of the neutrons is assumed to be isotropic

$$\frac{\mathrm{d}N}{\mathrm{d}\cos\theta} = \text{const.} \quad . \tag{4.8}$$

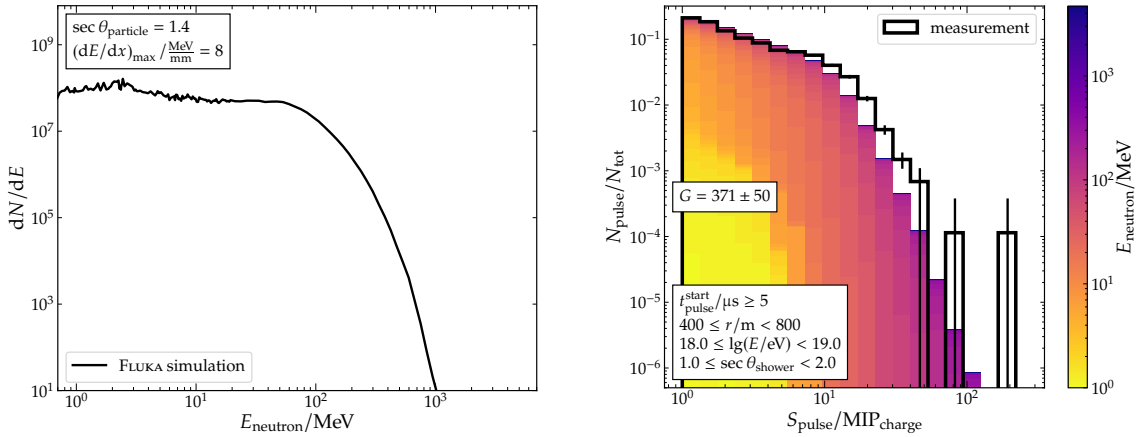

Figure 4.33: *Left:* Input energy spectrum of neutrons, obtained from dedicated simulations using FLUKA. *Right:* The forward-folded pulse spectrum agrees well with the measurements up to pulses of a few $\text{MIP}_{\text{charge}}$. At higher pulses, the amount of pulses from the measurements is larger than that of the simulations.

This distribution can be projected now onto a plane and thus

$$\frac{\mathrm{d}N}{\mathrm{d}\theta} \propto \sin\theta\cos\theta. \tag{4.9}$$

An average arrival angle can now be calculated to

$$\langle\theta\rangle = \frac{\int_0^{\frac{\pi}{2}} \theta\frac{\mathrm{d}N}{\mathrm{d}\theta}\,\mathrm{d}\theta}{\int_0^{\frac{\pi}{2}} \frac{\mathrm{d}N}{\mathrm{d}\theta}\,\mathrm{d}\theta} = \frac{\frac{\pi}{8}}{\frac{1}{2}} = \frac{\pi}{4}, \tag{4.10}$$

which corresponds to an average angle of $\sec\theta_{\text{particle}} = 1.4$ ($\hat{=}$ 45°). The binning of the measurements is also adjusted to match the parameter space of the simulations as agreeably as possible. The range of the measurements is set to include pulses between 400 and 800 m to the shower axis. Next, the energy range is limited from 10^{18} to 10^{19} eV and the zenith angle range from 1 to 2 in $\sec\theta_{\text{shower}}$. Fig. 4.33-right shows the forward-folded spectrum compared to the measurements. The shape of the measured pulse spectrum is matched quite well, with some differences at the largest pulses above around 8 $\text{MIP}_{\text{charge}}$. Assumptions on quenching and incident neutron angles are currently used, which result in systematic errors in the shape of the simulated spectrum. Two resulting forward-folded pulse spectra for the assumption of $\sec\theta_{\text{particle}} = 1$ and $\sec\theta_{\text{particle}} = 5.8$ ($\hat{=}$ 80°) for a comparison to the measurements are given in Fig. 4.34-left. The dependence of the spectral shape on $\sec\theta_{\text{particle}}$ becomes distinct above around 8 $\text{MIP}_{\text{charge}}$ and the tail of the pulse spectrum fits better for larger $\sec\theta_{\text{particle}}$. Therefore, the forward-folded pulse spectrum could be further improved by using a more complex angular distribution of neutrons instead of a single average angle. Fig. 4.34-right shows a similar comparison for different values of $(\mathrm{d}E/\mathrm{d}x)_{\text{max}}$. The absolute differences are smaller than for the variation of $\sec\theta_{\text{particle}}$ and the larger tail of the measured pulse spectrum cannot be explained by quenching.

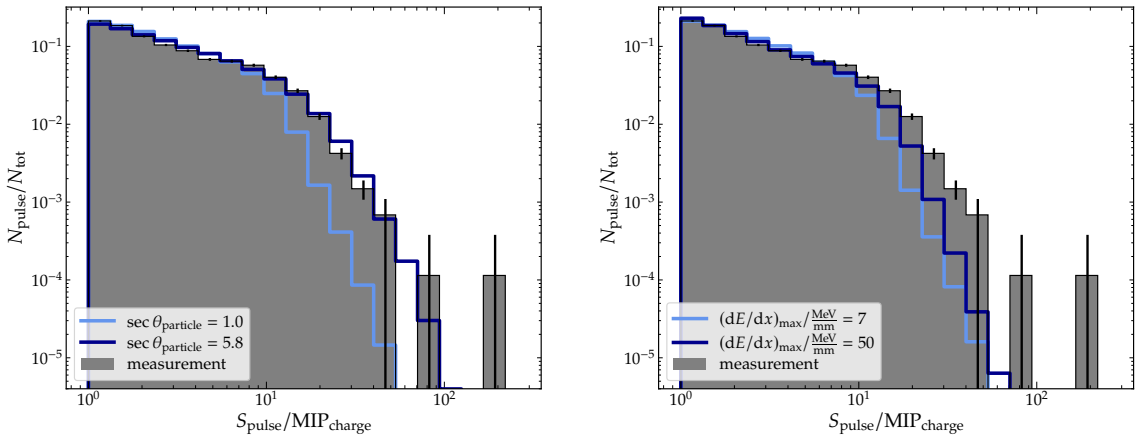

Figure 4.34: *Left:* The largest uncertainties in the forward-folded spectrum simulations arise from the assumption on $\sec\theta_{\text{particle}}$. However, the measurements are within the assumption of $\sec\theta_{\text{particle}} = 1$ and $\sec\theta_{\text{particle}} = 2$. *Right:* A variation of $(\mathrm{d}E/\mathrm{d}x)_{\text{max}}$ will not change the tail of the simulated pulse spectrum enough to match the measurements better.

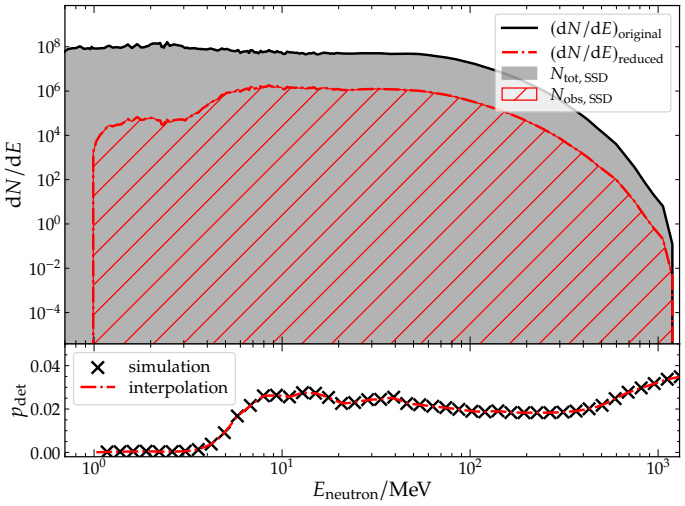

Figure 4.35: The reduced spectrum, shown in red, can be obtained by combining the original spectrum with the energy-dependent detection probability p_{det} for neutrons. Integrating the reduced spectrum will give $N_{obs,\,SSD}$, which is the observed number of pulses in the detector. The ratio between the original and reduced spectrum can then be used to estimate the total number of neutrons in the SSD, $N_{tot,\,SSD}$.

4.4. Impact of Neutron Signals in the WCD

In the previous section, the measurements of late pulses in the SSD that likely originate in large part from neutrons were analyzed. Forward-folding simulated neutron energy spectra from air shower simulations with Fluka using a dedicated neutron-pulse library was in acceptable agreement with the measurements. Therefore, the information from the measurements and the neutron simulations can now be combined to derive the number of neutrons arriving at the detector and estimate the possible signal induced by neutrons in the WCD.

First, the number of observed pulses from the SSD measurements $N_{obs,\,SSD}$ is calculated, using the information from Fig. 4.22. The pulse rate density $f \approx 0.01 \left(\frac{1}{\mu s\,m^2}\right)$ of pulses above 1 MIP_{charge} in the SSD at 400 m from the shower axis at a shower energy E of $10^{18.5}$ eV is chosen for the following calculations. Using the surface area of the SSD $A_{SSD} = 3.84\,m^2$ and $T_{obs} = 6\,\mu s$ as the average observable time of traces after 5 µs , one obtains

$$N_{obs,\,SSD} = f A_{SSD} T_{obs} \approx 0.2 \tag{4.11}$$

as the number of detected pulses. As previously shown in Section 4.3.3, only a fraction of neutrons will deposit a large enough signal to trigger the pulse-finding algorithm. This probability p_{det} of a neutron to create a detectable signal also depends on the neutron energy. Therefore, the total number of neutrons arriving at the SSD $N_{tot,\,SSD}$ can be expressed as

$$N_{tot,\,SSD} = R_{SSD} N_{obs,\,SSD}, \tag{4.12}$$

with the scaling factor R_{SSD} that takes the neutron energy dependent p_{det} into

account. $N_{\text{tot, SSD}}$ and $N_{\text{obs, SSD}}$ can be rewritten as

$$N_{\text{tot, SSD}} = \int_{1\,\text{MeV}}^{\infty} (\mathrm{d}N/\mathrm{d}E)_{\text{original}}\ \mathrm{d}E \tag{4.13}$$

and

$$N_{\text{obs, SSD}} = \int_{1\,\text{MeV}}^{\infty} (\mathrm{d}N/\mathrm{d}E)_{\text{reduced}}\ \mathrm{d}E \tag{4.14}$$

where $(\mathrm{d}N/\mathrm{d}E)_{\text{original}}$ is the neutron energy spectrum and $(\mathrm{d}N/\mathrm{d}E)_{\text{reduced}}$ the observed energy spectrum after folding-in the detection probability

$$(\mathrm{d}N/\mathrm{d}E)_{\text{reduced}} = p_{\text{det}}\,(\mathrm{d}N/\mathrm{d}E)_{\text{original}}\,. \tag{4.15}$$

$N_{\text{obs, SSD}}$ was determined on the rate of pulses above 1 $\text{MIP}_{\text{charge}}$. In Fig. 4.27, it was shown that neutrons with an energy of 1 MeV would barely produce a maximum signal of 1 $\text{MIP}_{\text{charge}}$. Therefore, it can be assumed that only the energy spectrum above 1 MeV will contribute to $N_{\text{obs, SSD}}$. Fig. 4.36 shows the relation between the total and the observed neutron numbers and the energy spectra. The ratio between the integrated spectra above 1 MeV can then be used to calculate R_{SSD}. Using

$$R_{\text{SSD}} = \frac{\int_{1\,\text{MeV}}^{\infty} (\mathrm{d}N/\mathrm{d}E)_{\text{original}}\ \mathrm{d}E}{\int_{1\,\text{MeV}}^{\infty} (\mathrm{d}N/\mathrm{d}E)_{\text{reduced}}\ \mathrm{d}E}, \tag{4.16}$$

one will get for the total number of neutrons arriving between 5 and 11 µs at the SSD $N_{\text{tot, SSD}} \approx 12$. This number can now be scaled to a total number of neutrons arriving at the WCD using

$$N_{\text{tot, WCD}} = N_{\text{tot, SSD}}\,(A_{\text{WCD}}/A_{\text{SSD}}) \approx 31. \tag{4.17}$$

For a shower with a primary energy of $10^{18.5}$ eV, around 31 neutrons are expected from the entire neutron energy spectrum in the WCD between 5 and 11 µs. Similarly, the number of neutrons between 0 and 5 µs can be obtained by determining a factor from the integrals of the early and late neutron energy spectra, resulting in ≈ 45 neutrons for the WCD and ≈ 17 for the SSD.

Following the approach of Section 4.2.1, neutrons with varying energies are injected in the WCD and the resulting number of photoelectrons is converted to $\text{VEM}_{\text{charge}}$. As a scaling factor, the peak in Fig. 4.15-top-left is determined with a Skew-Normal distribution to be ~234. For each neutron energy, the mean of the signal distribution is then calculated as the average expected $\text{VEM}_{\text{charge}}$ per neutron. Fig. 4.36 shows the average expected $\text{VEM}_{\text{charge}}$ for neutrons at different energies. Below an energy of 10 MeV, the average expected $\text{VEM}_{\text{charge}}$ for neutrons drops below ~10^{-4} $\text{VEM}_{\text{charge}}$. As a last step, the total signal contribution of neutrons in the WCD is sampled from the neutron energy spectrum, using the previously determined $N_{\text{tot, WCD}}$ and the conversion of E_{neutron} to $\langle S_{\text{neutron}} \rangle$. Bootstrapping this procedure 10 000 times gives a total signal estimation in the WCD of (0.004 ± 0.002) $\text{VEM}_{\text{charge}}$ for neutrons arriving between 5 and 11 µs

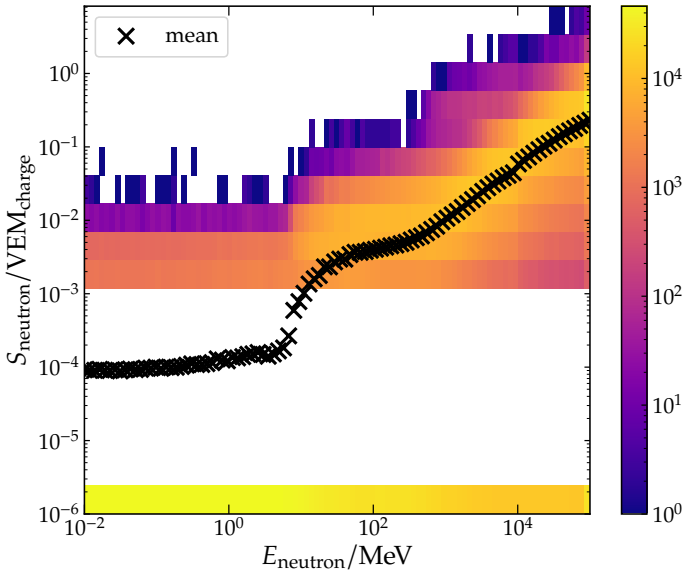

Figure 4.36: For each neutron energy, the number of photoelectrons in the WCD is determined and converted to the integrated signal S_{neutron} in $\text{VEM}_{\text{charge}}$. Similarly to the simulations with the SSD, the signals have a large spread. The mean of the signals $\langle S_{\text{neutron}} \rangle$, including the cases where no photoelectrons were created, is given with the black crossed markers.

and $(0.009 \pm 0.004)\,\text{VEM}_{\text{charge}}$ for neutrons arriving between 0 and 5 µs. From simulated showers at an energy of $10^{18.5}$ eV, the average signal in the WCD at 400 m from the shower axis is around $(525 \pm 219)\,\text{VEM}_{\text{charge}}$. Therefore, the signal from neutrons cannot explain the discrepancy of 15 to 30% in the signal size between simulations and measurements, which has been determined in Refs. [10, 15].

Chapter V

Outlook and Summary

The study of ultra-high-energy cosmic rays allows for the probing of hadronic interactions at energies far exceeding those accessible by human-made accelerators. However, these studies rely on indirect methods, specifically through the analysis of extensive air showers produced by these cosmic rays. A significant tension exists between measurements and simulations, with the measured abundance of muons exceeding predictions from the most current interaction models. This thesis aims to not only contribute to a better understanding of this muon puzzle but also to offer an initial exploration into the measurement of neutrons and their contribution to the total WCD signal using the new scintillation detectors that are part of the AugerPrime upgrade at the Pierre Auger Observatory.

Before any comparisons can be made between measurements and simulations regarding the muon and neutron content of air showers, it is important to understand the detectors and the processing of their recorded data, as well as identify and resolve any potential sources of bias. The algorithm to determine the baseline of the time traces from the PMTs of the WCDs and SSDs was reworked entirely. The baseline-finding algorithm was redesigned to incorporate a realistic model of the PMT response, making it robust to early or late signal contributions in the trace and to account for the natural undershoot that follows large signals. Additionally, the algorithm was adapted to handle the differing behaviors of the UB and UUB electronics used to record the PMT output. These improvements reduced biases from the baseline determination, lowering the discrepancies in the signal estimation from about 6% to 10% down to approximately 1.5% at the transition from signals recorded with the HG channel of the PMT to the LG channel. The remaining bias in LG signals recorded with the UB was traced back to systematic errors in the estimation of the gain ratio, which differs between PMTs and can fluctuate over time. To address this, a database was created comprising the information on the bias in the gain ratio of each PMT for each year of data-taking, enabling corrections to be applied to the LG signals. For the UUB, only the electronic components determine the gain ratio, which is chosen to correspond approximately to a factor of 32. However, a 2.2% discrepancy was observed between this fixed value and estimations using air shower measurements from the AugerPrime dataset. It was subsequently shown that using the gain

ratio determined by an online algorithm of the local station software reduces the discrepancy between the HG and LG signals to about 0.5%.

Resolving the biases in the gain ratio and improving the baseline-finding algorithm also allowed for the indntification of distinct peak structures in the traces of the WCD and delayed pulses in the SSD. For the WCD, these peak structures were determined to largely originate from the afterpulsing of the PMTs using a special dataset of measurements of laser light injected into one tank. An attempt was made to establish a possible correlation between the timing of these distinct pulses and specific ions within the PMT that could be responsible for their occurrence. Furthermore, a conservative estimate of the contribution of afterpulses to the total signal of WCD traces was calculated to be between 0.5% and 4%.

With these improvements to the data quality, an alternative method for estimating the apparent muon deficit using only SD measurements was explored. Using the measurements of the WCD allows not only to cover a wide energy range from $10^{18.5}$ eV up to $10^{20.0}$ eV but also significantly increases the exposure due to the 100% up-time of the SD. As a result of the improvements in the baseline and gain ratio estimation and the subsequent changes to signal magnitudes, changes in the estimation of the muon deficit were analyzed. For the analysis, assumptions were made about the correctness of the energy scale and the simulated electromagnetic shower component. The SD-only approach was found to be consistent with previous measurements of the apparent muon deficit, estimated to be approximately 18 to 31%. At energies below approximately $10^{19.4}$ eV the muon deficit increased between 2 and 7 percentage points, while at larger energies, the deficit decreased up to 8 percentage points.

With the new AugerPrime upgrade, complementary measurements from WCDs and SSDs can help disentangle the muonic and electromagnetic components of extensive air showers. This will provide a better insight into the muonic signal in the WCD and thus improve the understanding of the muon deficit further. By applying a matrix formalism [62], it becomes possible to separate the muonic and electromagnetic signals of the combined WCD and SSD measurements. However, this method is only effective if the signals from the WCD and SSD differ significantly due to their distinct responses to shower particles. In Appendix C.1, the potential for increasing the signal difference between the detectors by adding shielding on top of the SSDs is explored.

An effort was made to estimate the potential contribution of neutrons in air showers to the apparent missing signal in simulations. For this, measurements from the new AugerPrime SSD dataset were analyzed. Late pulses observed in the SSD time traces were studied, revealing rates up to three orders of magnitude higher than the expected background pulses, which are due to uncorrelated particles with the shower signal. Simulations of air showers showed that the fraction of pulses from muonic and electromagnetic components ranged from 1% to 15%, depending on the primary energy, zenith angle, and distance from the shower axis. Additionally, the signal spectrum of the late pulses was examined, and its shape appeared to be largely independent of both primary energy and zenith angle. However, a hardening of the spectrum was observed with increasing distances from the shower axis. This hardening could originate from the limitation of the

time window in the traces, where the delayed pulses are counted. Furthermore, the Offline simulation and reconstruction software framework was extended to include hadronic processes such as elastic and inelastic scattering and a basic implementation of quenching effects in the scintillator simulations using Birks' law. Using this updated Offline framework, a simulation library was created with the SSD signal responses for neutrons at different energies and impact angles. The energy-dependent efficiency of the SSDs for detecting neutrons and the signal variation for different quenching factors and angular distributions were studied. By forward-folding arbitrary neutron energy spectra using the neutron-pulse library, it was shown how the neutron-pulse spectrum depends on the shape of the neutron energy spectrum and that AugerPrime is sensitive to the shape. A comparison between the SSD measurements and FLUKA simulations of a neutron energy spectrum of Ref. [42] showed agreement at first order. Consequently, the simulated neutron energy spectra, using the SSD measurements of late pulses, were used to calculate the total number of neutrons of different energies expected in the WCD. This was then used to estimate the possible contribution of neutrons to the total WCD signal. The resulting contribution was found to be negligible with respect to explaining the apparent muon deficit.

The measurement of late pulses in the SSD of the AugerPrime upgrade indicates that the neutron component of air showers could be further studied in the future at the Pierre Auger Observatory. While the rate of late pulses is likely too low to allow for an event-by-event analysis at primary energies below $10^{19.5}$ eV, the cumulative data of the expanding PhaseII dataset can be used for further study and to compare predictions from various hadronic interaction models regarding the neutron content of air showers.

Appendix A

Improvements to SD Signals & Impact on the Apparent Muon Deficit

A.1. Fit Function

In the upper figures of Fig. 3.21 of Section 3.1.3, the bias $\langle S/S_{\mathrm{mc}}\rangle - 1$ of the estimated signal S relative to the true signal S_{mc} is fitted to an ad-hoc empirical Gauss function of the form

$$f_{\mathrm{bias}}(S) = a + \frac{b}{\sqrt{2\pi}\sigma}\exp\left(-\frac{(\lg(S/\mathrm{VEM}) - \mu)^2}{2\sigma^2}\right). \tag{A.1}$$

The fit parameters for both algorithms and gains are given in Table A.1.

The lower figures of Fig. 3.21 show the relative uncertainty $\sigma(S/S_{\mathrm{mc}})$ of the estimated signal S fitted to an ad-hoc empirical broken power-law of the form

$$f_{\mathrm{res}}(S) = \exp(g(S)), \qquad \text{where} \qquad g(S) = \begin{cases} a & ; S < b \\ a - c\lg(x/b) & ; S \geqslant b \end{cases}. \tag{A.2}$$

The fit parameters for both algorithms and gains are given in Table A.2.

A.2. Signal Cut

Since the amplitude of the undershoot is proportional to the size of the signal that precedes it, a small signal will not produce a significant undershoot and thus the decay time can not be determined reliably. To determine a reasonable cut on the preceding signal, the full procedure of Section 3.2.1 is repeated. At first, for all traces, the signal charge q_{c} of the trace is approximately determined as

$$q_{\mathrm{c}} = \sum_{i=0}^{t_1}(T_i - B_{\mathrm{front}}). \tag{A.3}$$

The end of the integration t_1 is chosen as the first bin after the trace maximum, where the trace becomes negative with 0.5 µs added to exclude potential signal

Table A.1: Fit parameters and errors of the fitted Gauss function $f_{\text{bias}}(S)$ for description of biases.

algorithm	gain	a	b	μ	σ
OG	HG	$(-6.5 \pm 0.3)\times10^{-4}$	$(-7.7 \pm 0.9)\times10^{-3}$	0.49 ± 0.04	0.47 ± 0.02
OG	LG	$(7.5 \pm 0.2)\times10^{-3}$	$(2.7 \pm 0.1)\times10^{-2}$	2.1 ± 0.008	0.33 ± 0.008
KG	HG	$(8.7 \pm 1.4)\times10^{-5}$	$(3.3 \pm 1.2)\times10^{-4}$	0.41 ± 0.04	0.19 ± 0.03
KG	LG	$(3.5 \pm 1.2)\times10^{-4}$	$(-1.1 \pm 0.2)\times10^{-2}$	1.7 ± 0.06	0.41 ± 0.04

Table A.2: Fit parameters and errors of the broken power-law $f_{\text{bias}}(S)$ for description of the relative resolutions.

algorithm	gain	a	b/VEM	c
OG	HG	-4.15 ± 0.02	4.9 ± 0.1	0.91 ± 0.01
OG	LG	-2.98 ± 0.02	203 ± 7	1.13 ± 0.03
KG	HG	-4.39 ± 0.02	4.4 ± 0.1	0.77 ± 0.01
KG	LG	-3.67 ± 0.02	96 ± 4	0.74 ± 0.01

contributions of the shower. A cut value for q_c is then chosen to study the development of the decay times. In Fig. A.1-left the distribution of all fitted decay times is shown for three different cuts on q_c. With an increasing cut on minimal q_c, the amount of fits with very long decay times seems to be reduced. Since the amplitude of the undershoot correlates with the signal size, the decay of the undershoot becomes more visible and easier to fit. The most probable decay time is estimated for each distribution of decay rates of individual PMTs. In the last step, the average of the individual PMT decay times is calculated. Fig. A.1-right shows the calculated average decay times as well as the standard deviation for increasing cut on q_c. With increasing signal size the mean decay rate decreases from $r\Delta t = 2.2\times10^{-4}$ down to approximately $r\Delta t = 1.8\times10^{-4}$.

A.3. Identification of "bad" PMTs

The two parameters I_u and $r\Delta t$ of the trace fits from Section 3.2.1 can be used not only to check if the fit was successful but also to identify "bad" PMTs. Fig. A.2-top left shows the distribution of both fit parameters I_u and $r\Delta t$ for each individual trace in a scatter plot. Most of the fits are in the lower right quadrant, which is the expected region for the two fit parameters when the trace has a normal shape and the fit was successful. Due to the expected undershoot, the parameter I_u is negative and the recovery of the undershoot is given by a positive rate $r\Delta t$. Outliers can be read off of the plot as deviations from the densest accumulation of data points in the upper right and lower left quadrant, as well as a second distribution to the right of the main group. The outliers in the upper right and lower left quadrants can be attributed to traces with a long, anomalous tail after the signal. Two example traces for both quadrants are shown in Fig. A.2-top left and Fig. A.2-bottom right, where either a successful fit of the long tail is

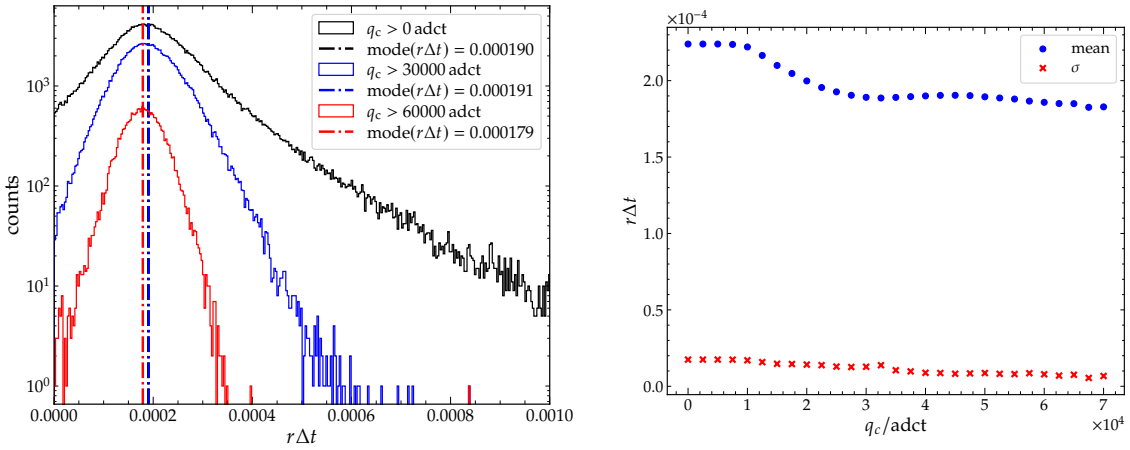

Figure A.1: *Left:* Binned distribution of the decay rates $r\Delta t$ for various cuts on the signal charge q_c of the trace. The cut removes cases where the undershoot is small and thus the decay is hard to observe. This cut effectively cleans the data set so that only well-resolved decay of the undershoot is fitted. *Right:* The mean and standard deviation σ of the determined constant universal decay rate $r\Delta t$ for various cuts on the signal charge q_c of the trace. The mean of the universal decay rate decreases from $r\Delta t = 2.2{\times}10^{-4}$ down to approximately $r\Delta t = 1.8{\times}10^{-4}$ with an increasing cut on q_c.

performed, or the fit fails due to the long tail of the trace. For these two cases, two PMTs of two separate stations (PMT 2 of station 1815 and PMT 2 of station 1840) have been identified to repeatedly show such anomalous behavior and have been removed from the data set of this analysis. A procedure to identify these PMTs is explained in Ref. [103] and Ref. [104]. In the lower right quadrant a smaller, second distribution can be seen to the right of the main group. This distribution has been identified to originate as well from one single PMT (PMT 3 of station 1839). The decay time of these traces is about $\tau = 10\mu s$, which is over 4 times smaller than expected decay $\tau = 45\mu s$, which was determined for most of the PMTs.

A.4. TRACE CLEANING

The recorded high-gain UUB traces show a baseline oscillation that is not visible on the oscilloscope. Since there is no shielding for the UUB in the measurement setup, possible external disturbances can cause these oscillations. To clean the trace, a fit of the oscillation is performed on the first 560 bins, since they do not contain any signal from the pulse generator. The function used to fit the oscillation is of the form

$$f(t) = A + B\sin(2\pi t/C + D), \tag{A.4}$$

where A is the offset, B is the amplitude, C is the period, and D is the phase. An example fit of the oscillation is shown in Fig. A.3-left. The fit is performed on the data set of 2400 traces and the distribution of periods C is shown in Fig. A.3-right. The most common period is 561 bins ($8.\bar{3}$ ns each) or 4675 µs, corresponding to a frequency of ~214 kHz. Subsequently, a fit of the oscillation is performed on

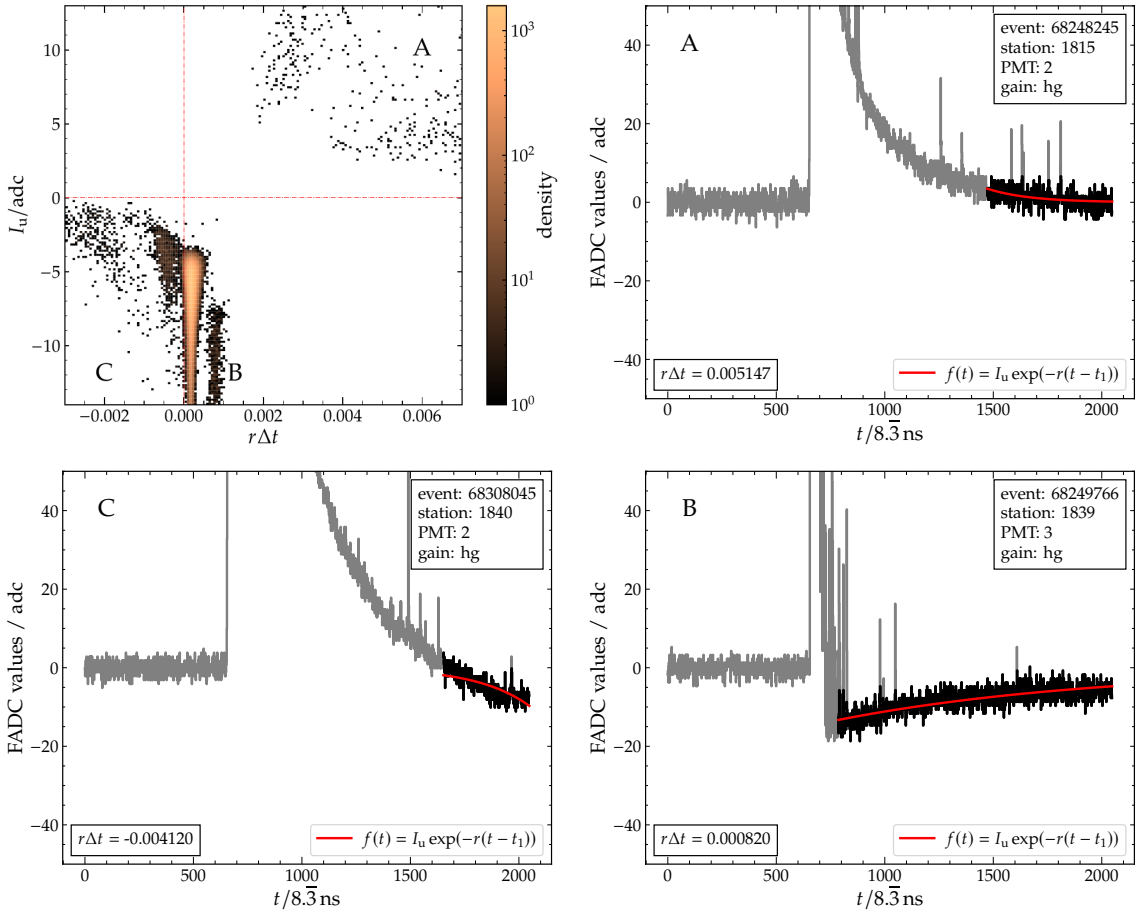

Figure A.2: *Top left:* Distribution of the fit parameters I_u and $r\Delta t$ of the traces. The expected behaviour is located in the lower right quadrant with a negative I_u and a positive decay rate $r\Delta t$. Outliers can be easily identified due to their deviation from the main group. *Top right:* Anomalous trace with a fit of a long tail. The fit parameters are found in this case in the upper right quadrant of the scatter plot. *Bottom left:* Anomalous trace with an unsuccessful fit of a long tail. These fit parameters are found in the lower left quadrant of the scatter plot. *Bottom right:* Trace with an anomalously-fast recovery. These fit parameters can be seen as the second distribution, right to the main distribution in the lower right quadrant.

every trace individually for parameters A, B, and D, while C is kept fixed at the previously determined value of 561 bins. To obtain oscillation free traces. For each trace this fit is then simply subtracted from the original.

A.5. Binned shower size and muon deficit

The ratio $S_{1000}^{\mathrm{KG}}/S_{1000}^{\mathrm{OG}}$ between the new shower size S_{1000}^{KG}, retrieved by using the KG reconstruction and the old shower size S_{1000}^{OG}, retrieved by using the OG reconstruction is shown as a function of S_{1000}^{OG} for different zenith bins, ranging from 1 to 2 in sec θ with a step of 0.2 is shown in Fig. A.4. With increasing zenith angles, the slope of the ratio for measurements becomes steeper. For simulations, the start of the steep increase of the ratio shifts from around 80 VEM at almost

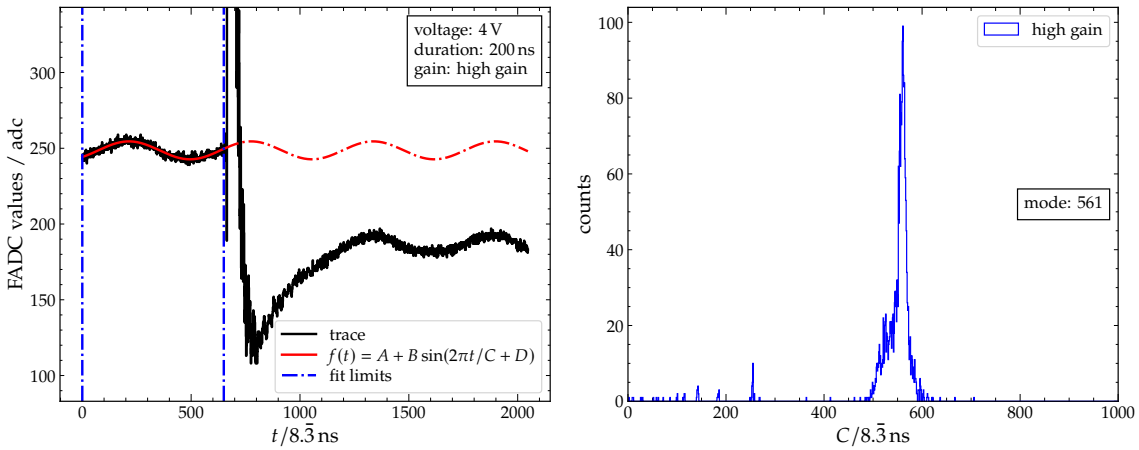

Figure A.3: *Left:* Raw UUB high-gain trace (black) with a fit $f(t)$ to the low-frequency oscillation (red) and its extrapolation (red dot-dashed). The fit was performed only in the time interval denoted with the two vertical dot-dashed blue lines. Peak voltage of the pulse was set to 4 V and the pulse width was 200 ns. *Right:* Distribution of the fitted oscillation periods C which were mainly around 560 bins or 4.7 µs (~214 kHz).

vertical events to about 20 VEM at inclined events. Coupled with the observed changes in S_{1000} for measurements, the change of the muon deficit D_μ is expected to be energy and zenith-dependent when switching from the OG reconstruction to the KG reconstruction.

To obtain the estimation of D_μ for the full range of zenith angles, as shown in Fig. 3.64-left, the average shower size S_{1000} is calculated for the AugerMix composition [80] for different zenith bins, ranging from 1 to 2 in $\sec\theta$ with a step of 0.2, as shown in Fig. A.5. D_μ for each zenith bin is shown in the plots of Fig. A.6. For the zenith angles up to 1.6 in $\sec\theta$, a peak in D_μ around $10^{19.5}$ eV can be seen. This feature disappears at larger zenith angles. This peak can be attributed to the jump of the mass composition around the same energy, as can be seen in Fig. A.5-top. At larger zenith angles, the absolute difference of S_{1000} for different primaries decreases, and the shift becomes smaller, resulting in the disappearance of the jump in D_μ.

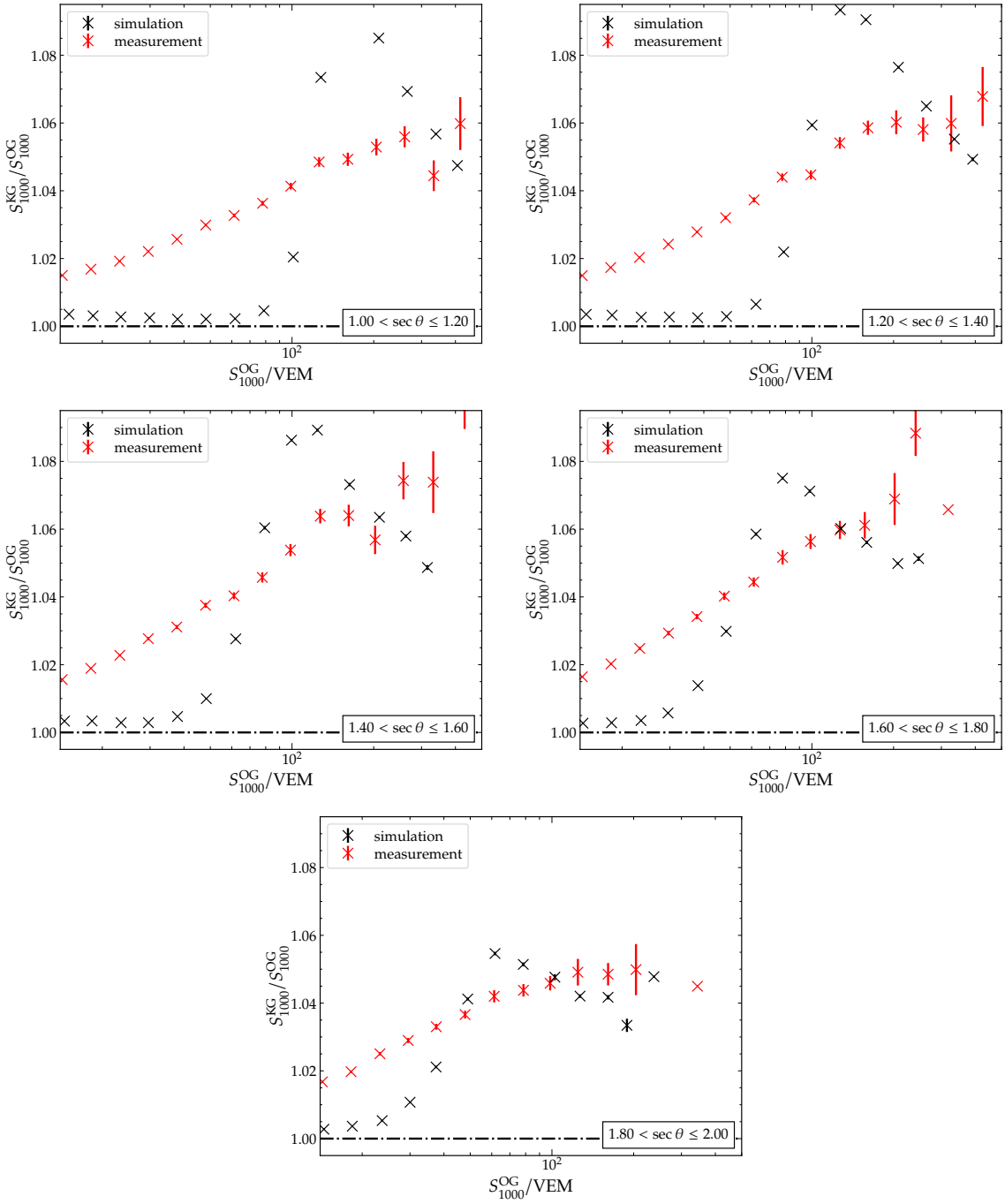

Figure A.4: The ratio $S^{KG}_{1000}/S^{OG}_{1000}$ between the new shower size S^{KG}_{1000}, retrieved by using the KG reconstruction, and the old shower size S^{OG}_{1000}, retrieved by using the OG reconstruction for simulations (black) and measurements (red) for various bins in sec θ between 1 and 2 with a step of 0.2. In simulations, the ratio increases steeply by up to 9% at the change from HG to LG signals. The ratio increases with S^{OG}_{1000} for the measurements.

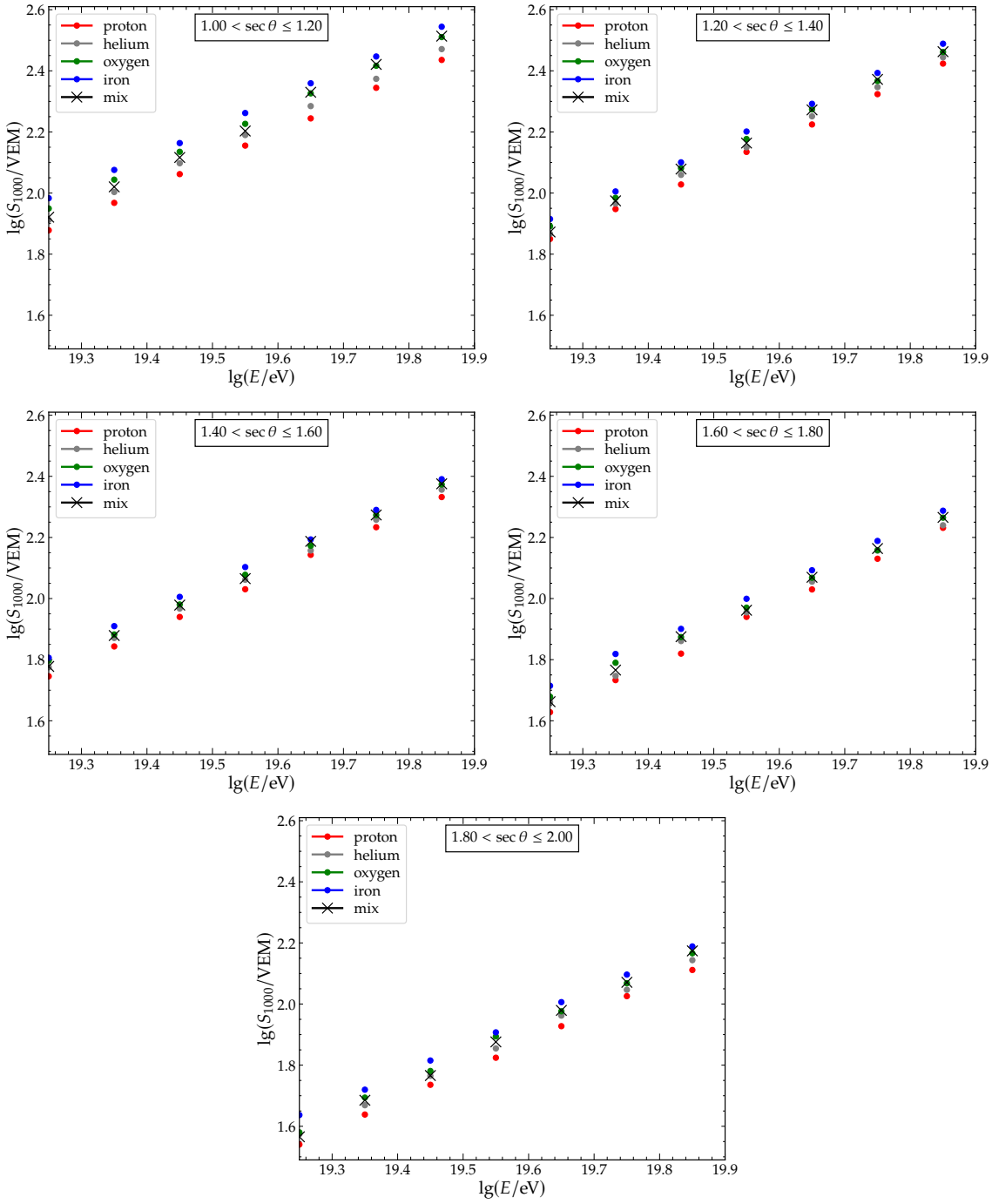

Figure A.5: The shower size S_{1000}, estimated by using the average of a dense ring of 12 stations at a distance of 1000 m from the shower axis, as a function of the primary energy E for different primaries. S_{1000}, assuming the AugerMix composition [80], is shown with black crosses (mix). With larger zenith angles, the absolute difference in the shower size between the different primaries decreases.

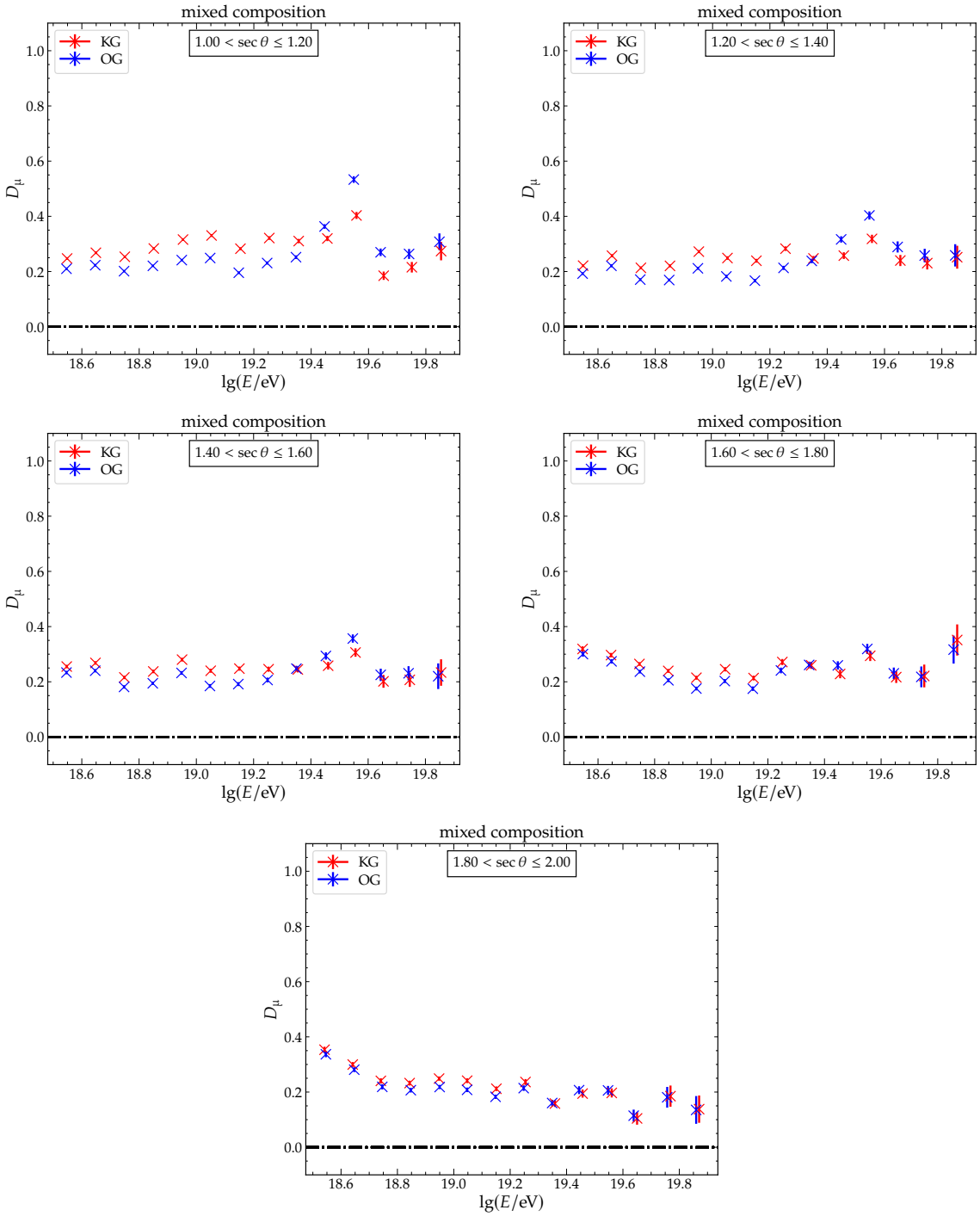

Figure A.6: D_μ indicates muon deficit for the AugerMix composition, assuming a correct energy scale and no change in the electromagnetic signal for different reconstructions. The peak of D_μ around $10^{19.5}$ eV can be attributed to the jump in the composition at this energy. The peak vanishes for larger zenith angles due to the decrease of the absolute difference in the shower size for different primaries as seen in Fig. A.5.

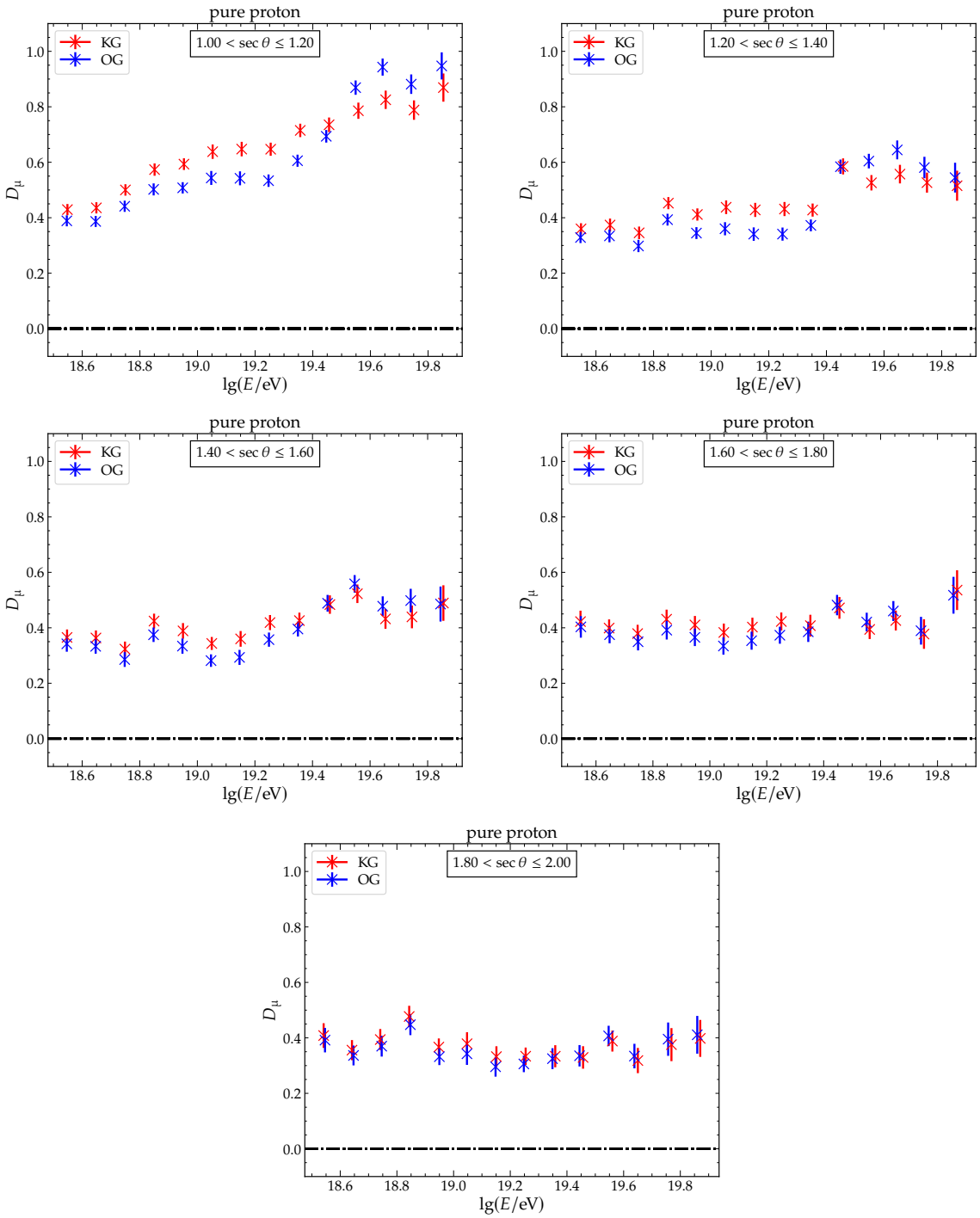

Figure A.7: D_μ indicates muon deficit for a pure proton composition, assuming a correct energy scale and no change in the electromagnetic signal for different reconstructions.

Appendix A. Improvements to SD Signals & Impact on the Apparent Muon Deficit

Appendix B

Characterizing the Neutron Component of Air Showers

B.1. Binned time distributions

The distribution of arrival-times for all pulses is displayed in the following plots for stations between 0 to 400 m, 400 to 800 m and 800 to 2000 m from the shower axis, for shower zenith angles between 1.0 to 1.2, 1.2 to 1.4 and 1.4 to 1.6 in $\sec\theta_{\text{shower}}$. The total number of pulses N_{pulses} is normalized to the overall number of traces N_{traces} in each bin. These simulations include the hadronic shower component only down to particle energies of around 20 MeV. Pulses with a signal above 11 $\text{MIP}_{\text{charge}}$ can only be created from neutrons with an energy equal to or larger than 20 MeV. The simulations are further separated into pulses recorded from the hadronic traces (green) and the electromagnetic and muonic traces (blue). The plots give the fraction of the simulated pulse rate past 5 µs compared to the measurements. This value is the non-hadronic background in the measurements for the electromagnetic and muonic components. In each figure, along the horizontal axis, the distributions are binned in the pulse signal for the three bins of 0.8 to 3 $\text{MIP}_{\text{charge}}$, 3 to 11 $\text{MIP}_{\text{charge}}$ and 11 to 220 $\text{MIP}_{\text{charge}}$. The vertical axis shows the three energy bins from 10^{18} to $10^{18.5}$ eV, $10^{18.5}$ to 10^{19} eV and 10^{19} to $10^{19.5}$ eV.

For the highest energy bin from 10^{19} to $10^{19.5}$ eV and the distance bin from 0 to 400 m,

B.2. Neutron arrival angle distribution

10000 proton showers with primary energies between $10^{18.5}$ eV and $10^{19.0}$ eV were simulated, using the *Napoli* library of Corsika simulations [81]. They are uniformly distributed over $\sin^2\theta$, ranging from 0 to 60° In addition, dense rings of 4 stations were simulated at distances of 200, 400, 600, 800 and 1000 m from the shower axis. Each neutron processed by the `G4StationSimulator` module of Offline was recorded and the information about its arrival angle and energy was

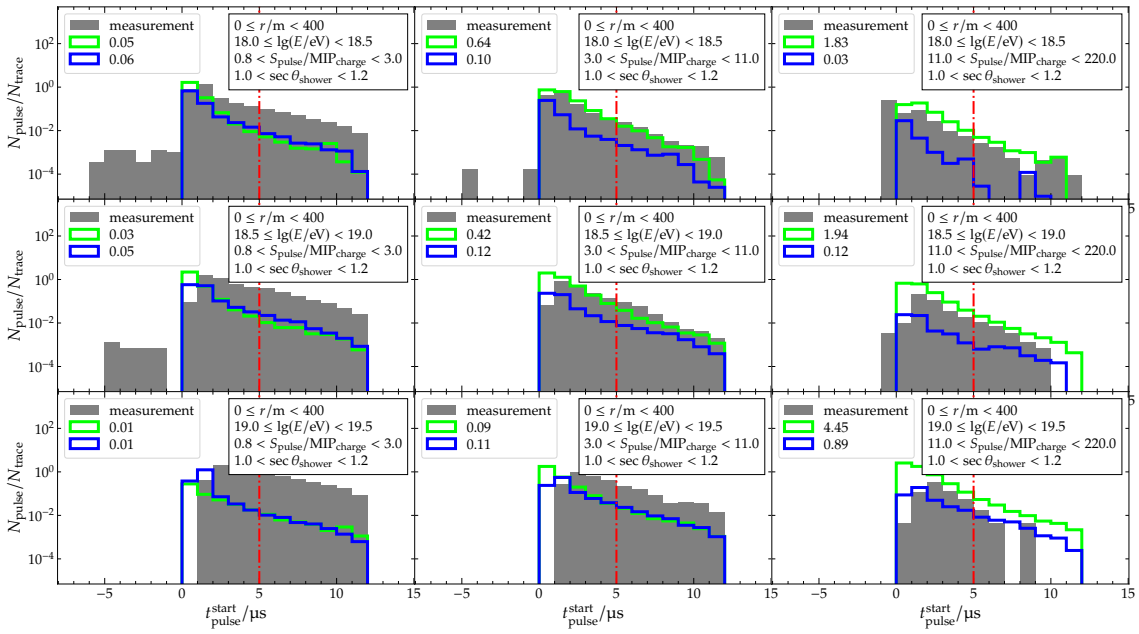

Figure B.1: Pulse rate as a function of the time in the trace, relative to the start of the shower signal, for a shower between 1.0 and 1.2 in $\sec\theta_{\text{shower}}$ and distances between 0 and 400 m to the shower axis. The fraction of the simulated hadronic pulse rate past 5 µs compared to the measurements is given in green and for the electromagnetic and muonic in blue.

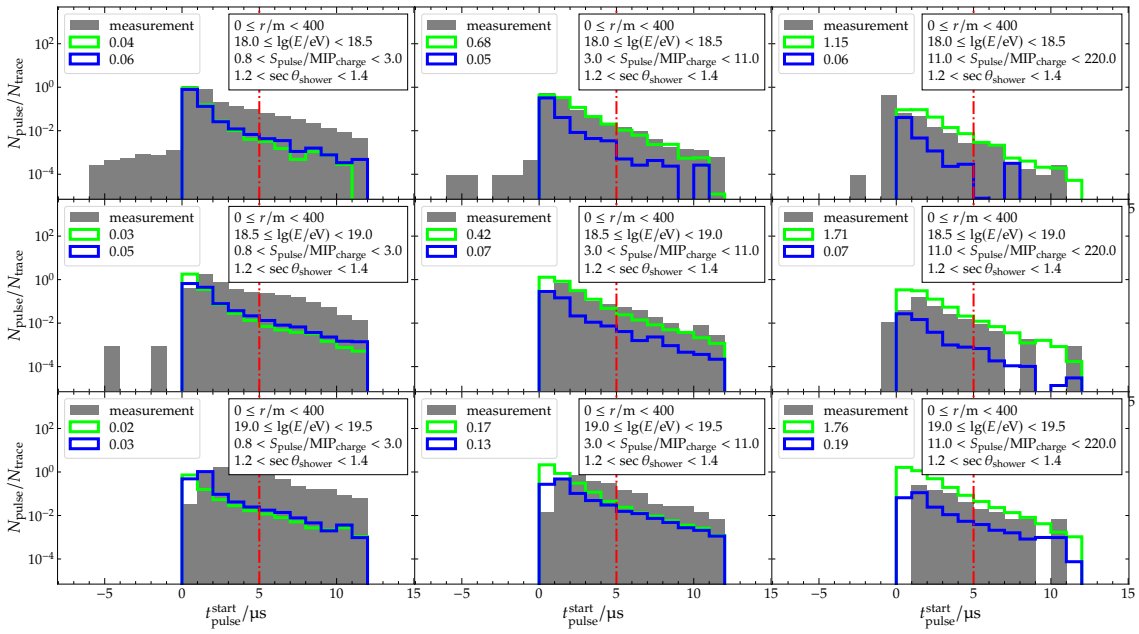

Figure B.2: Pulse rate as a function of the time in the trace, relative to the start of the shower signal, for a shower between 1.2 and 1.4 in $\sec\theta_{\text{shower}}$ and distances between 0 and 400 m to the shower axis. The fraction of the simulated hadronic pulse rate past 5 µs compared to the measurements is given in green and for the electromagnetic and muonic in blue.

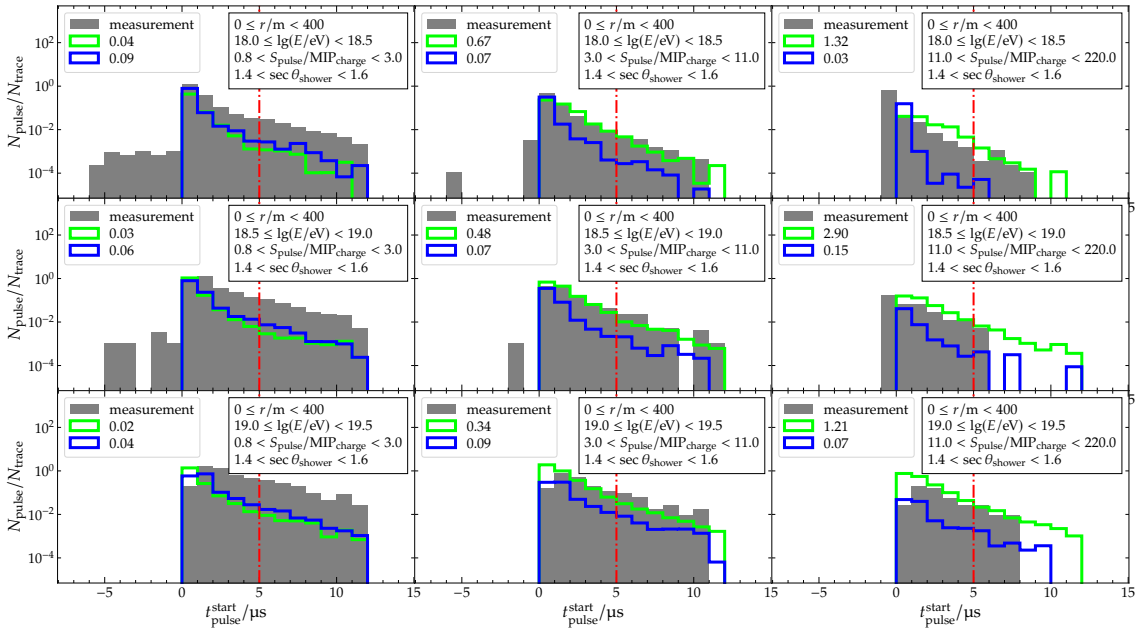

Figure B.3: Pulse rate as a function of the time in the trace, relative to the start of the shower signal, for a shower between 1.4 and 1.6 in sec θ_{shower} and distances between 0 and 400 m to the shower axis. The fraction of the simulated hadronic pulse rate past 5 µs compared to the measurements is given in green and for the electromagnetic and muonic in blue.

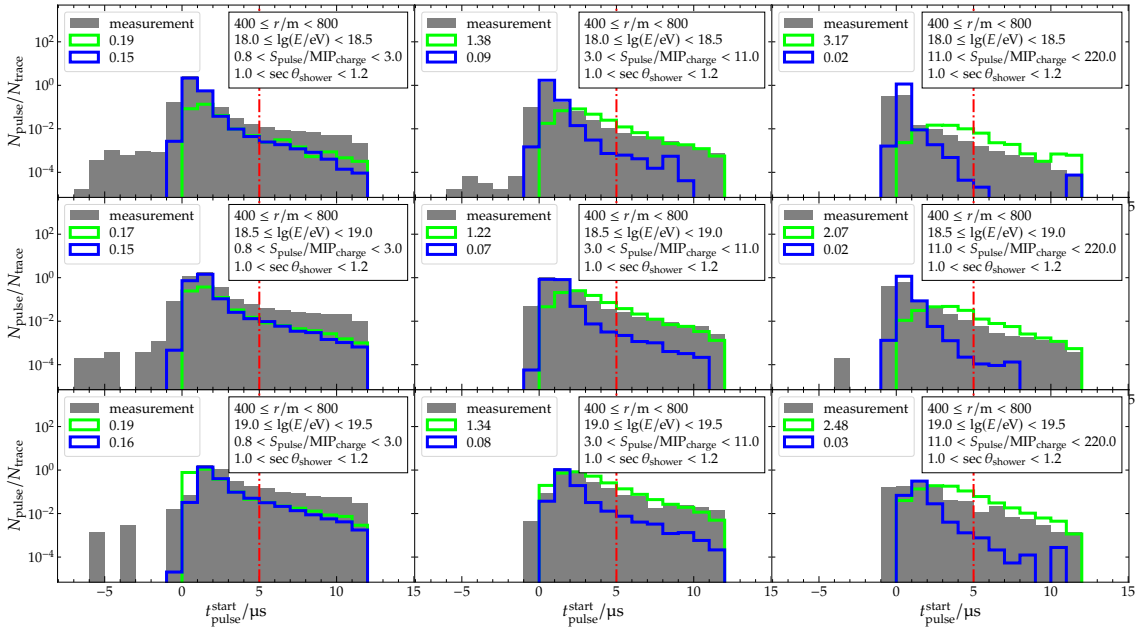

Figure B.4: Pulse rate as a function of the time in the trace, relative to the start of the shower signal, for a shower between 1.0 and 1.2 in sec θ_{shower} and distances between 400 and 800 m to the shower axis. The fraction of the simulated hadronic pulse rate past 5 µs compared to the measurements is given in green and for the electromagnetic and muonic in blue.

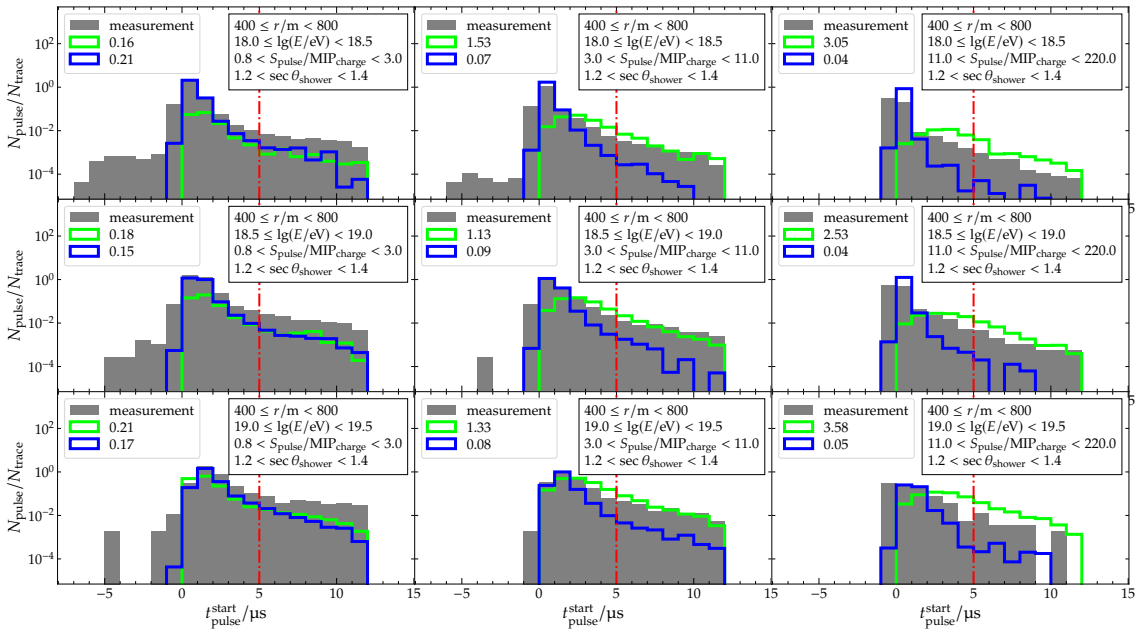

Figure B.5: Pulse rate as a function of the time in the trace, relative to the start of the shower signal, for a shower between 1.2 and 1.4 in $\sec\theta_{\text{shower}}$ and distances between 400 and 800 m to the shower axis. The fraction of the simulated hadronic pulse rate past 5 µs compared to the measurements is given in green and for the electromagnetic and muonic in blue.

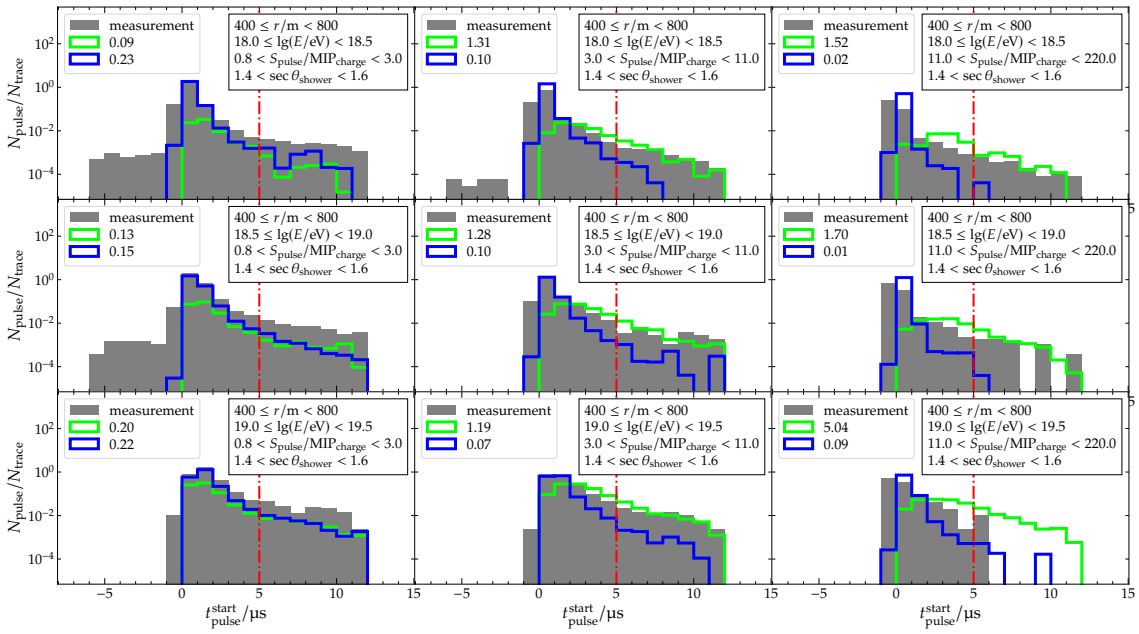

Figure B.6: Pulse rate as a function of the time in the trace, relative to the start of the shower signal, for a shower between 1.4 and 1.6 in $\sec\theta_{\text{shower}}$ and distances between 400 and 800 m to the shower axis. The fraction of the simulated hadronic pulse rate past 5 µs compared to the measurements is given in green and for the electromagnetic and muonic in blue.

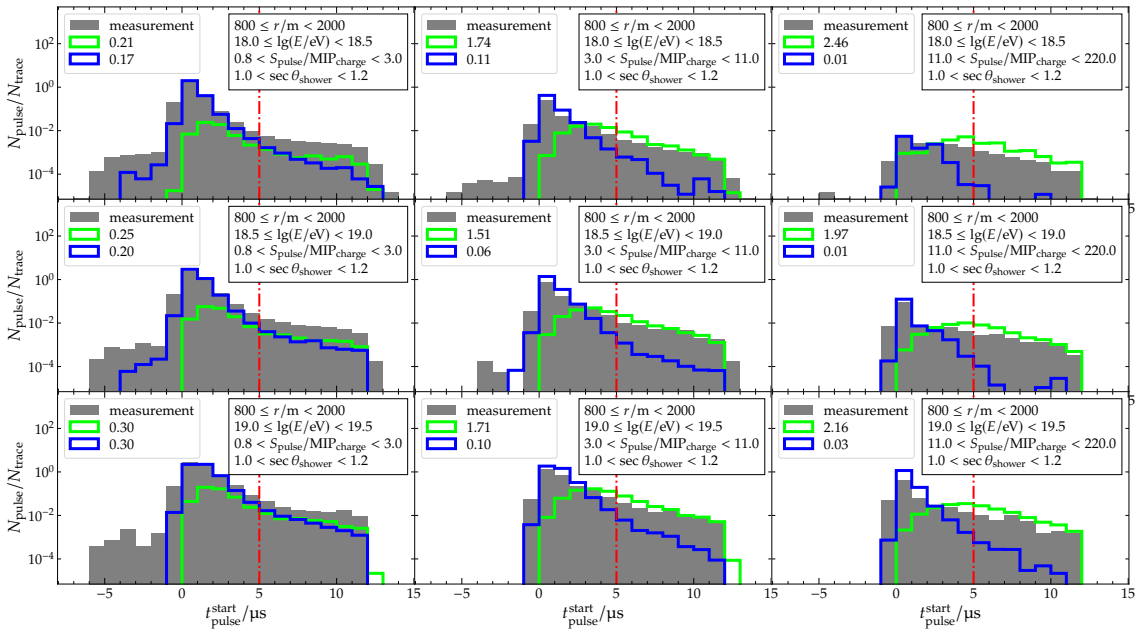

Figure B.7: Pulse rate as a function of the time in the trace, relative to the start of the shower signal, for a shower between 1.0 and 1.2 in $\sec\theta_{\text{shower}}$ and distances between 800 and 2000 m to the shower axis. The fraction of the simulated hadronic pulse rate past 5 µs compared to the measurements is given in green and for the electromagnetic and muonic in blue.

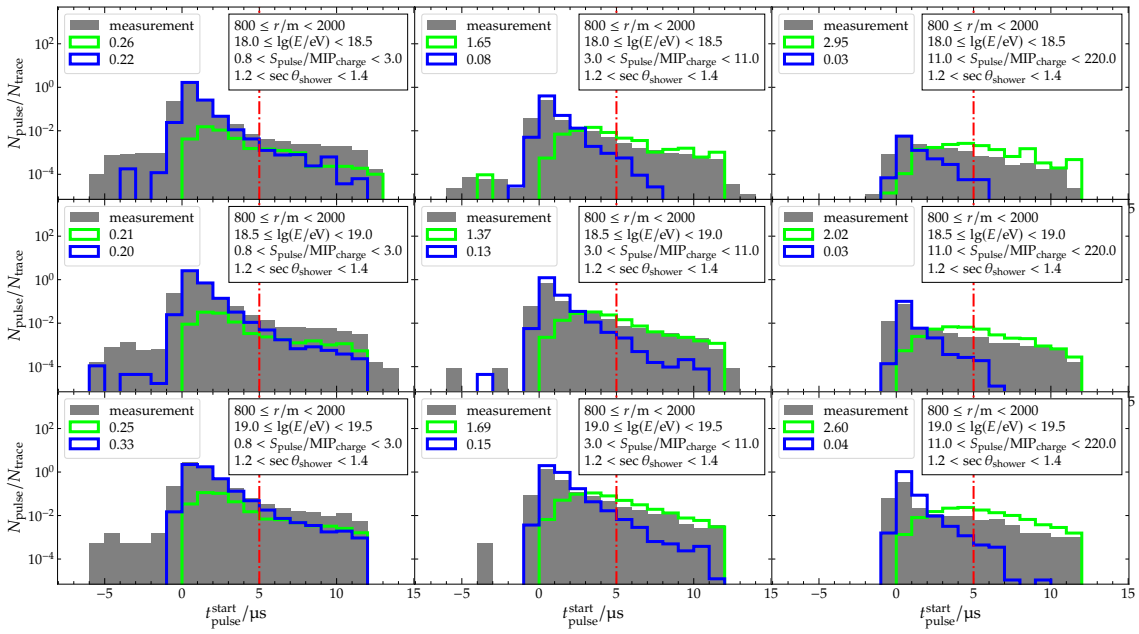

Figure B.8: Pulse rate as a function of the time in the trace, relative to the start of the shower signal, for a shower between 1.2 and 1.4 in $\sec\theta_{\text{shower}}$ and distances between 800 and 2000 m to the shower axis. The fraction of the simulated hadronic pulse rate past 5 µs compared to the measurements is given in green and for the electromagnetic and muonic in blue.

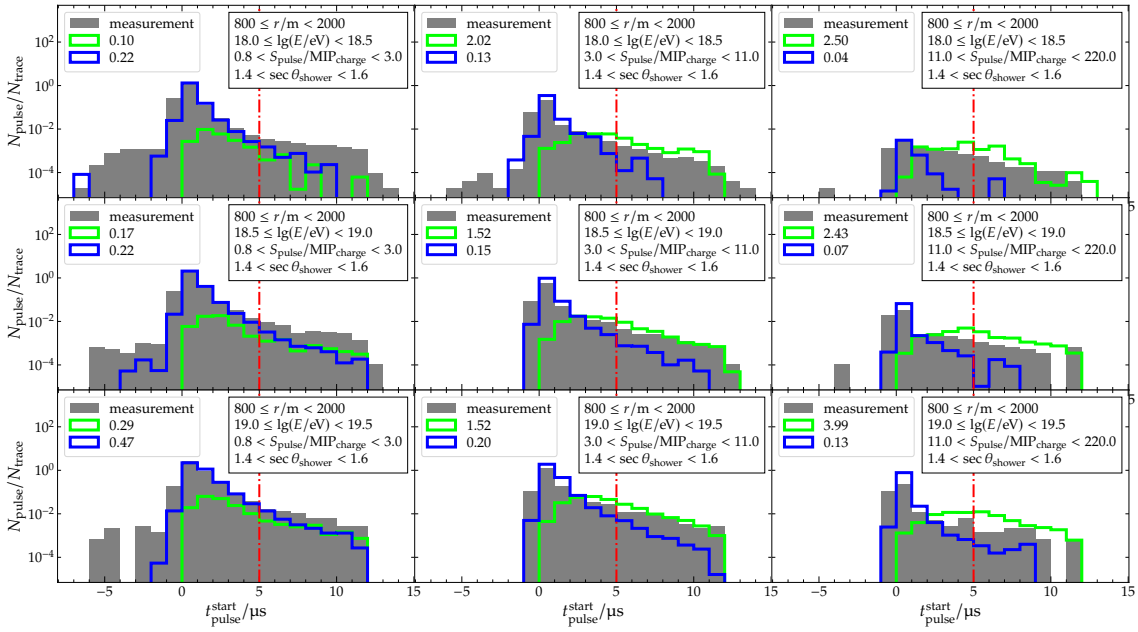

Figure B.9: Pulse rate as a function of the time in the trace, relative to the start of the shower signal, for a shower between 1.4 and 1.6 in sec θ_{shower} and distances between 800 and 2000 m to the shower axis. The fraction of the simulated hadronic pulse rate past 5 µs compared to the measurements is given in green and for the electromagnetic and muonic in blue.

saved. The angular distribution for different energies at various distances to the shower axis is shown in Fig. B.10. For neutrons with energies above ≈ 1000 MeV, the arrival angles tend to align with the direction of the shower axis. As the energy of the neutron decreases, the angular distribution becomes increasingly isotropic, an effect that is more prominent at greater distances from the shower axis.

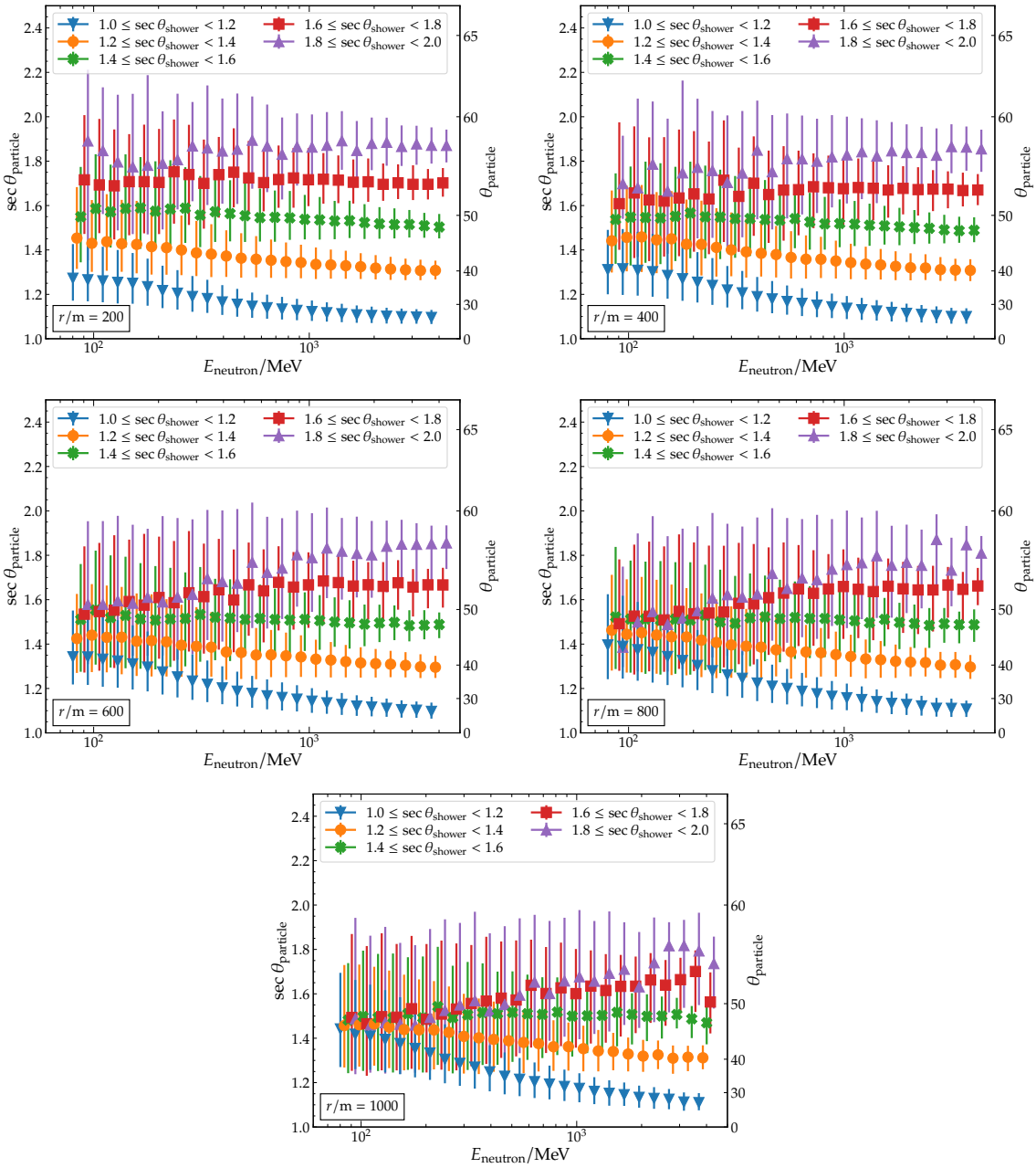

Figure B.10: The angular distribution of neutrons, binned for different shower angles and distances from the shower axis. At low neutron energies, their angular distribution is isotropic. The larger the neutron energy, the more the arrival angles of the neutrons align with the direction of the shower axis.

Appendix B. Characterizing the Neutron Component of Air Showers

Appendix C

Outlook

C.1. Enhancement of Photon Signals through Shielding on SSDs

The goal of the AugerPrime upgrade is to disentangle the muonic and electromagnetic components of extensive air showers, which will enhance the ability to study ultra-high-energy cosmic ray composition and hadronic interaction effects at the highest energies. This is achieved by complementing the existing *Water-Cherenkov Detectors* (WCDs) with additional *Scintillator Surface Detectors* (SSD) to better identify air-shower particles [105].

The SSDs are more sensitive to the electromagnetic component than to the muonic component. Electrons and positrons penetrate only a few centimeters into the WCDs, leaving a faint signal, whereas muons can traverse the detectors fully, producing a larger signal. However, the particles of the electromagnetic and muonic components traverse the SSDs completely, producing equal signals. To produce a signal in the detectors, the photons of the electromagnetic component need to undergo pair production or Compton scattering. Since the SSDs are mounted on top of the WCDs, both detectors measure the same portion of the air shower. By combining the complementary measurements from the two detectors, the accuracy of the reconstructed composition of extensive air showers might improve significantly because of the differences in the measured signals. In this note, we evaluate the possibility of additionally increasing the magnitude of the difference between both detector signals by simulating enhanced shielding on top of the SSD to increase the probability of photon conversion and, thus, the electromagnetic signal in the SSD. From these simulations, we will deduce the signal changes and whether the signal from photons can be increased significantly.

C.1.1. Simulation setup

The simulation dataset was created using a Corsika shower library with fixed energies and zenith angles. The library parameters are listed in Table C.1. For each combination of parameters, 120 showers are simulated. Two dense station rings are added, consisting of 12 stations at a distance of 600 m and 24 stations at a

Table C.1: Fixed library of Corsika simulations with different combinations of parameters. For each combination, 120 events were simulated.

primary	proton, iron
hadronic interaction model	Epos-LHC
lg(E/eV)	18.5, 19.0, 19.5, 20.0
θ/°	0, 12, 22, 38, 48, 56

distance of 1000 m from the shower axis. An iron shielding of a variable thickness x_{shield} is simulated on top of the SSD for each primary, zenith angle and energy combination with

$$x_{\text{shield}}/\text{mm} \in \{1, 2, 3, 4, 5, 10, 18\}.$$

Likewise, lead instead of iron is added as shielding in the simulations, with

$$x_{\text{shield}}/\text{mm} \in \{0.7, 1.4, 2.1, 2.8, 3.5, 6.9, 14.4\},$$

to match the same column density X_{shield} of iron in g/cm^2. The column density can be calculated as

$$X_{\text{shield}} = \int_0^{x_{\text{shield}}} \rho(x)\,\mathrm{d}x = \rho\, x_{\text{shield}}, \tag{C.1}$$

using the density of iron, $\rho_{\text{iron}} = 7.874\,\text{g/cm}^3$, or the density of lead, $\rho_{\text{lead}} = 11.4\,\text{g/cm}^3$. Thus, when comparing the different shielding materials, we will use

$$X_{\text{shield}}/(\text{g/cm}^2) \in \{0.8, 1.6, 2.6, 3.1, 3.9, 7.9, 14.2\}.$$

To simulate the shielding on top of the SSD, the detector properties in Geant4 must first be modified. A rectangular prism of iron or lead is added to the SSD to cover the entire SSD area, including the non-active area, as shown in Fig. C.1. For technical reasons, the center of this rectangular prism was set to 1.1 cm above the center of the SSD bars, regardless of the thickness of the simulated shielding volume.

Further, we fix the physics seeds to minimize fluctuations in the simulations of the same shower for different shielding. This ensures that every particle is injected at its same location in the detector for each iteration of different shielding simulations.

C.1.2. Impact on component signals

The total signal measured by each detector $S_{\text{WCD / SSD}}$ is divided into the muon, electron and photon components. We calculate the average component signals $S^i_{\text{WCD / SSD}}$ in the WCD and the SSD for each dense station ring at 600 m and 1000 m for different primaries, energies, zenith angles, and shielding materials. In this analysis, we present the results for a proton primary with an energy of $10^{19.5}$ eV and a zenith angle of 38° for the dense station ring at 600 m.

The energy spectra of muons, electrons, positrons, and photons at the ground of the simulations are shown in Fig. C.2. A minimum energy cut is applied

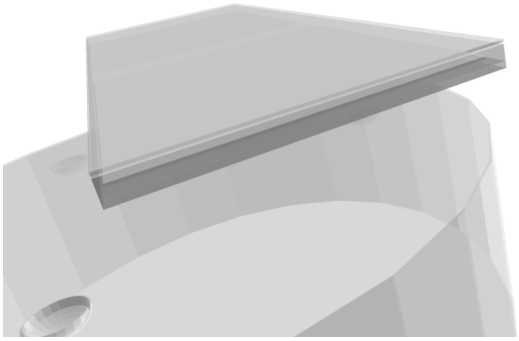

Figure C.1: Visualization of volumes defined in Geant4. A volume corresponding to 10 mm of lead can be seen atop the SSD.

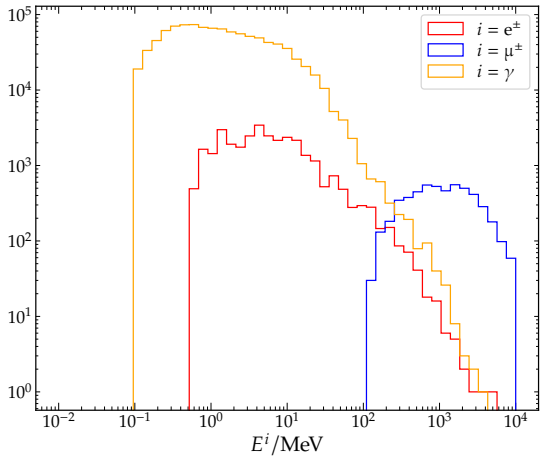

Figure C.2: The energy spectra of electrons and positrons (red), muons (blue) and photons (yellow) that reach the detector. The amount of photons at the ground is over ten times larger than that of electrons and positrons.

for each component to increase computing efficiency in Offline. The simulated spectra indicate that the number of photons at the ground is more than ten times greater than the number of electrons and positrons. However, photons must undergo either pair production to form an electron-positron pair or Compton scattering to produce a signal in the SSD or WCD. The most probable interaction process for photons with energies up to 10 MeV is Compton scattering, while above 10 MeV, pair production becomes dominant [89].

The number of photons in the dense ring of stations at 600 m is evaluated for one event. Additionally, the amount of photoelectrons that originate from photons N_{PE} created in the SSD at different thicknesses of iron shielding is calculated. The histogram of photons at certain energies is shown in Fig. C.3-left. Most photons have energies up to 10 MeV, which will mainly produce a signal in the detectors through Compton scattering. Fig. C.3-right displays the average N_{PE} for various iron shielding thicknesses, binned for the various photon energies. If

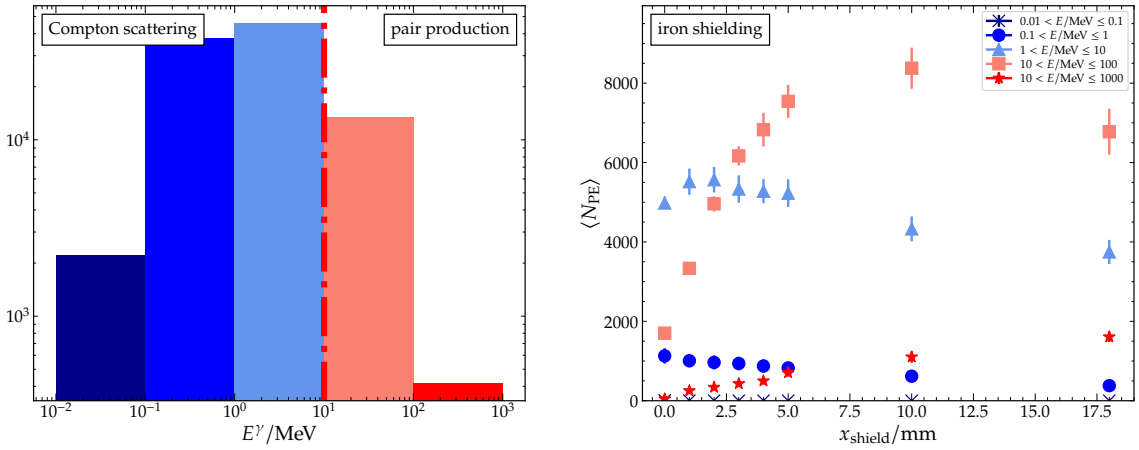

Figure C.3: *Left:* Energy histogram of photons for 5 ranges of energies. Up to 10 MeV the main interaction process of photons is through Compton scattering (blue bars). Above this energy, pair production becomes available and the main conversion process (red bars). *Right:* The average number of photoelectrons $\langle N_{\mathrm{PE}} \rangle$ produced in the SSD from photons for various layers of iron shielding x_{shield}. Photoelectrons originating from photons with energies up to 10 MeV (blue markers) are the dominant contribution when there is no shielding. With increasing shielding thickness, $\langle N_{\mathrm{PE}} \rangle$ from photons above 10 MeV (red markers) increases significantly.

there is no additional shielding, the primary contribution to the photon signal in the SSD stems from photons with energies between 1 and 10 MeV. However, as iron shielding is added to the SSD, N_{PE} of the photons above 10 MeV increases. N_{PE} of photons below 10 MeV decreases since the photons are more likely to stop in the shielding material. At $x_{\mathrm{shield}} = 3\,\mathrm{mm}$, N_{PE} above 10 MeV surpasses N_{PE} with energies between 1 and 10 MeV, becoming the dominant contribution to the photon signal.

Fig. C.4-left shows the absolute change of S^i_{SSD} in the SSD for different X_{shield} of iron and lead shielding. The change of S^i_{SSD} relative to the component signal without shielding $S^i_{\mathrm{SSD}}(0)$ is shown in Fig. C.4-right. The muonic signal $S^{\mu^\pm}_{\mathrm{SSD}}$ remains stable throughout the iron and lead shielding range with a slight increase of around 3% at $X_{\mathrm{shield}} = 14.2\,\mathrm{g/cm^2}$. The electron signal $S^{e^\pm}_{\mathrm{SSD}}$ decreases by approximately 80% for both iron and lead at the largest X_{shield}. The photon signal $S^{\gamma}_{\mathrm{SSD}}$ increases by 70% for iron and by 105% for lead when $X_{\mathrm{shield}} = 3.9\,\mathrm{g/cm^2}$. At larger X_{shield}, the increase of $S^{\gamma}_{\mathrm{SSD}}$ relative to $S^{\gamma}_{\mathrm{SSD}}(0)$ is 50% for iron and 40% for lead shielding. This corresponds to the increase of N_i from photons converted by pair production through the shielding as shown in Fig. C.3-right.

Similar to the plots for the SSD, the absolute change of the WCD component signals S^i_{WCD} for different X_{shield} of iron and lead shielding is shown in Fig. C.5-left, and the change of S^i_{WCD}, relative to the component signal without shielding $S^i_{\mathrm{WCD}}(0)$, is depicted in Fig. C.5-right. $S^{\mu^\pm}_{\mathrm{WCD}}$ remains unchanged throughout the entire range of iron and lead shielding, with a minimal reduction of less than 1% at the largest X_{shield}. $S^{e^\pm}_{\mathrm{WCD}}$ is reduced with increasing X_{shield} of the

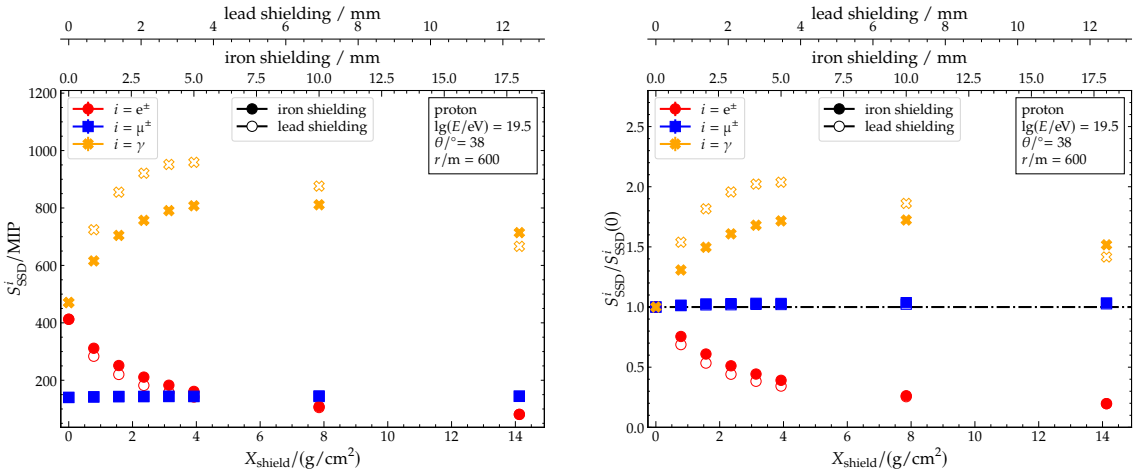

Figure C.4: *Left:* The absolute change of S^i_{SSD} in the SSD for different X_{shield} of iron (filled markers) and lead (hollow markers) shielding. With no shielding, the electrons and positrons (red) and the photons (yellow) contribute almost equally to the total signal. *Right:* The change of S^i_{SSD} relative to the component signal without shielding $S^i_{SSD}(0)$. By increasing the shielding $S^{e^{\pm}}_{SSD}$ decreases while S^{γ}_{SSD} firstly increases and $S^{\mu^{\pm}}_{SSD}$ remains almost constant.

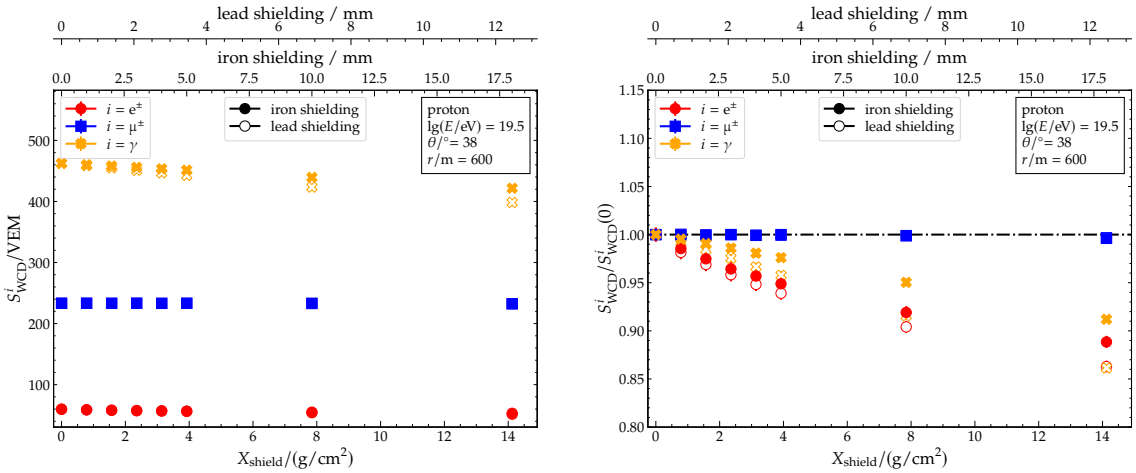

Figure C.5: *Left:* The absolute change of S^i_{WCD} in the WCD for different X_{shield} of iron (filled markers) and lead (hollow markers) shielding. *Right:* The change of S^i_{WCD}, relative to the component signal without shielding $S^i_{WCD}(0)$ shows a decrease in the signal for all components with increasing shielding.

shielding material by 11% for iron and 14% for lead. Similarly, S^{γ}_{WCD} is reduced by approximately 9% and 14% for iron lead shielding, respectively.

C.1.3. Impact on total signals

The signals from the muon, electron, and photon components are combined to obtain the total signals S_i. Similarly to the analysis of the components, the results for a proton primary with an energy of $10^{19.5}$ eV and a zenith angle of 38° for the dense station ring at 600 m are shown. Fig. C.6-left shows the absolute change of S_i

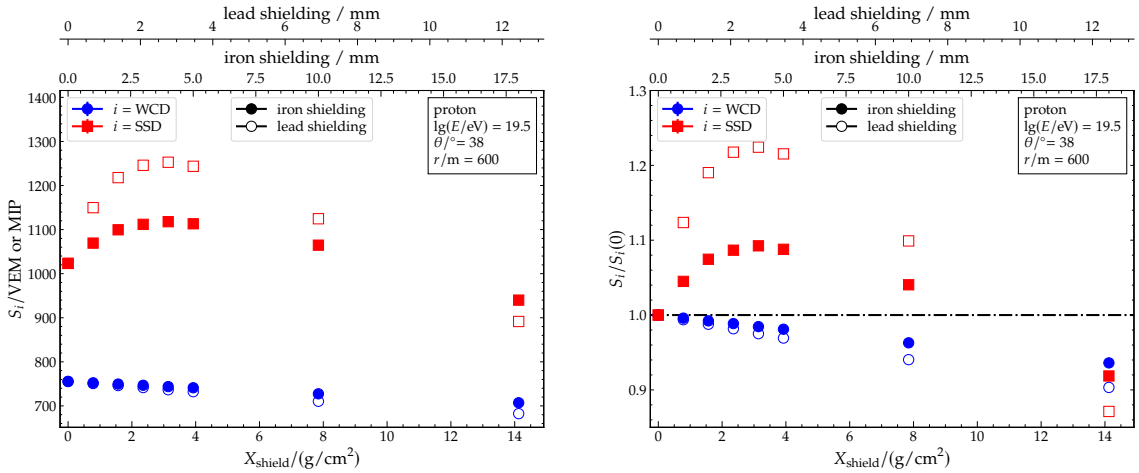

Figure C.6: *Left:* The absolute change of S_i in the WCD (blue) and SSD (red) for different X_{shield} of iron (filled markers) and lead (hollow markers) shielding. *Right:* S_{SSD} increases significantly, relative to the total signal without shielding $S_{\text{SSD}}(0)$ up to $X_{\text{shield}} = 3.1\,\text{g/cm}^2$ due to the boost of the signal from converted photons. At larger X_{shield} the increase becomes smaller and eventually S_{SSD} decreases relative to $S_{\text{SSD}}(0)$.

for different X_{shield} of iron and lead shielding. The change of S_i, relative to the total signal without shielding $S_i(0)$, is depicted in Fig. C.6-right. S_{SSD} increases by 9% for iron and 22% for lead shielding at $X_{\text{shield}} = 3.1\,\text{g/cm}^2$. As iron (lead) shielding further increases, S_{SSD} gradually reduces to 92% (87%) of $S_{\text{SSD}}(0)$ at the largest X_{shield}. Appendix C.1.2 shows that the change in S_{SSD} is due to the different behavior of the component signals. The muon component remains unaffected by the shielding, while the shielding causes additional conversion of photons through pair production, resulting in an increase in the total electromagnetic signal that exceeds the losses from the electron-positron component. However, as X_{shield} increases, S_{SSD} decreases again.

S_{WCD} decreases linearly to about 5% at the largest X_{shield} for iron. An equivalent lead shielding reduces S_{WCD} by about 10%. Although the shielding converts more photons and increases the SSD signal, it only reduces the WCD signal. This is because the energy of the additional electrons and positrons from the pair production is insufficient to reach the WCD or boost the photon signal therein.

C.1.4. Impact on the reconstruction of component signals using the matrix formalism

We have now demonstrated that additional shielding on top of the SSD will significantly increase the conversion of photons through pair production, thus increasing S_{SSD}. However, S_{WCD} is slightly reduced with shielding. Therefore, it is of interest to test the impact of shielding on the reconstruction of shower properties. With the combination of two signals from a multilayered detector, the muonic and electromagnetic components of extensive air showers, which are sensitive to the mass of the primaries, can be estimated [62]. Using the measured signals from WCD and SSD, a method was developed to disentangle the

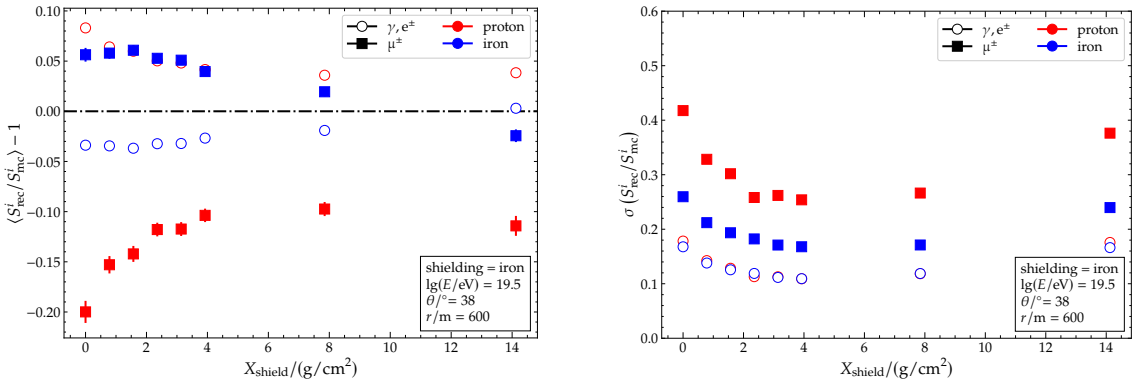

Figure C.7: *Left:* The bias of S^i_{rec} relative to S^i_{mc} decreases for the electromagnetic signal (hollow markers) and muonic signal (filled markers) with increasing X_{shield} by almost 50% in proton (red) and iron (blue) showers. *Right:* The resolution $\sigma(S^i_{rec}/S^i_{mc})$ decreases by up to 60% with increasing shielding.

electromagnetic and muonic components of S_{WCD}, called *matrix formalism* [106]. This matrix formalism has been studied throughout the past [107, 108, 109] and recently revised in Ref. [110]. Following the elaboration from Ref. [110], a matrix relating S_{WCD} and S_{SSD} with the muonic components $S^{\mu^\pm}_{WCD}$ and $S^{\mu^\pm}_{SSD}$ can be written as

$$\begin{pmatrix} S^{\mu^\pm}_{WCD} \\ S^{\mu^\pm}_{SSD} \end{pmatrix} = \begin{pmatrix} \alpha & -\beta \\ -\frac{\alpha(1-\alpha)}{\beta} & 1-\alpha \end{pmatrix} \begin{pmatrix} S_{WCD} \\ S_{SSD} \end{pmatrix}. \tag{C.2}$$

Parameters α and β are defined as

$$\alpha = \frac{S^{\mu^\pm}_{WCD} S^{\mu^\pm}_{SSD} - S^{\mu^\pm}_{WCD} S_{SSD}}{S_{WCD} S^{\mu^\pm}_{SSD} - S^{\mu^\pm}_{WCD} S_{SSD}}, \tag{C.3}$$

and

$$\beta = \frac{S^{\mu^\pm}_{WCD} S^{\mu^\pm}_{SSD} - S_{WCD} S^{\mu^\pm}_{WCD}}{S_{WCD} S^{\mu^\pm}_{SSD} - S^{\mu^\pm}_{WCD} S_{SSD}}. \tag{C.4}$$

By measuring S_{WCD} and S_{SSD}, the muonic and electromagnetic signal in the WCD can now be calculated using the α and β parameters as

$$S^{\mu^\pm}_{WCD} = \alpha\, S_{WCD} - \beta\, S_{SSD}, \tag{C.5}$$

and

$$S^{\gamma e^\pm}_{WCD} = S_{WCD} - S^{\mu^\pm}_{WCD}. \tag{C.6}$$

For each combination of energy, zenith angle, distance of the dense ring and shielding, an average α and β is calculated for an equal mix of proton and iron primaries. Using Eq. (C.5) and Eq. (C.6), the reconstructed WCD component signals $S^i_{rec} \triangleq S^i_{WCD}$ are obtained and compared with the simulated signals S^i_{mc} for different X_{shield}.

Fig. C.7-left shows the bias $\langle S^i_{rec}/S^i_{mc}\rangle - 1$ of S^i_{rec} relative to S^i_{mc} for iron shielding of varying thickness. Fig. C.7-right shows the resolution $\sigma(S^i_{rec}/S^i_{mc})$. For a proton

primary, the bias of $S^{\mu^\pm}$ decreases from about −20% to −10%, and the bias of $S^{\gamma e^\pm}$ decreases from approximately 8% to 4% for increasing X_{shield}. For an iron primary, the biases of $S^{\mu^\pm}$ and $S^{\gamma e^\pm}$ are smaller than for the proton primary. Up to $X_{\text{shield}}/(\text{g/cm}^2) = 1.6$, the bias of $S^{\mu^\pm}$ and $S^{\gamma e^\pm}$ minimally vary around 6% and −3%. With increasing X_{shield}, the bias reduces to −2.5% for $S^{\mu^\pm}$ and 0.5% for $S^{\gamma e^\pm}$. At $X_{\text{shield}}/(\text{g/cm}^2) = 4$ resolution of $S^{\gamma e^\pm}$ decreases for both primaries equally from 18% to 11%. The resolution of $S^{\mu^\pm}$ decreases from 42% to 25% for a proton primary and from 26% to 17% for iron. For larger X_{shield}, the resolution of $S^{\gamma e^\pm}$ and $S^{\mu^\pm}$ increases for both primaries.

C.1.5. Conclusions

We have shown that most of the signal from photons to the electromagnetic component in the SSD originates from photons up to 10 MeV. Thus, these photons will produce a signal in the SSD through Compton scattering. When added, photons above 10 MeV are more likely to undergo conversion through pair production processes, resulting in an increase in the signal from photons. Although the signal from electrons and positrons decreases with shielding, the more significant increase from photons compensates for this, resulting in an overall signal increase in the SSD by over 9% (20%) for 4 mm (3.5 mm) of iron (lead) shielding. However, adding shielding will then lead to a decrease in the SSD signal. The signal in the WCD remains mainly unaltered by shielding, as the primary signal contribution originates from the muonic shower component. Consequently, the increased signal in the SSD can significantly reduce the bias and resolution discrepancies between the reconstructed muonic signal and the Monte Carlo signals in the WCD by up to 50% to 60% when using the matrix formalism.

Bibliography

[1] V. F. Hess, *Über Beobachtungen der durchdringenden Strahlung bei sieben Freiballonfahrten*, *Physikalische Zeitschrift* **13** (1912) 1084.

[2] N. G. A. De Angelis and S. Stramaglia, *Domenico Pacini, the forgotten pioneer of the discovery of cosmic rays*, 1002.2888.

[3] P. Auger, P. Ehrenfest, R. Maze, J. Daudin and A. F. Robley, *Extensive cosmic ray showers*, *Rev. Mod. Phys.* **11** (1939) 288.

[4] J. Linsley, *Evidence for a primary cosmic-ray particle with energy* 10^{20} *ev*, *Phys. Rev. Lett.* **10** (1963) 146.

[5] HIRES collaboration, *Detection of a cosmic ray with measured energy well beyond the expected spectral cutoff due to cosmic microwave radiation*, *Astrophys. J.* **441** (1995) 144 [astro-ph/9410067].

[6] Telescope Array collaboration, *The Cosmic Ray Energy Spectrum Observed with the Surface Detector of the Telescope Array Experiment*, *Astrophys. J. Lett.* **768** (2013) L1 [1205.5067].

[7] Pierre Auger collaboration, *Features of the Energy Spectrum of Cosmic Rays above 2.5×10*^{18} *eV Using the Pierre Auger Observatory*, *Phys. Rev. Lett.* **125** (2020) 121106 [2008.06488].

[8] EAS-MSU, IceCube, KASCADE Grande, NEVOD-DECOR, Pierre Auger, SUGAR, Telescope Array, Yakutsk EAS Array collaboration, *Working Group Report on the Combined Analysis of Muon Density Measurements from Eight Air Shower Experiments*, *PoS* **ICRC2019** (2020) 214 [2001.07508].

[9] H. Dembinski, J. Arteaga-Velázquez, L. Cazon, R. Conceição, J. Gonzalez, Y. Itow et al., *Report on tests and measurements of hadronic interaction properties with air showers*, *EPJ Web Conf.* **210** (2019) 02004.

[10] Pierre Auger collaboration, *Testing Hadronic Interactions at Ultrahigh Energies with Air Showers Measured by the Pierre Auger Observatory*, *Phys. Rev. Lett.* **117** (2016) 192001 [1610.08509].

[11] Pierre Auger collaboration, *Muons in Air Showers at the Pierre Auger Observatory: Mean Number in Highly Inclined Events*, *Phys. Rev. D* **91** (2015) 032003 [1408.1421].

[12] Pierre Auger collaboration, *Direct measurement of the muonic content of extensive air showers between* $\mathbf{2 \times 10^{17}}$ *and* $\mathbf{2 \times 10^{18}}$ *eV at the Pierre Auger Observatory*, *Eur. Phys. J. C* **80** (2020) 751.

[13] Pierre Auger collaboration, *Inferences on mass composition and tests of hadronic interactions from 0.3 to 100 EeV using the water-Cherenkov detectors of the Pierre Auger Observatory*, *Phys. Rev. D* **96** (2017) 122003 [1710.07249].

[14] Pierre Auger collaboration, *Measurement of the Fluctuations in the Number of Muons in Extensive Air Showers with the Pierre Auger Observatory*, *Phys. Rev. Lett.* **126** (2021) 152002 [2102.07797].

[15] Pierre Auger collaboration, *Testing hadronic-model predictions of depth of maximum of air-shower profiles and ground-particle signals using hybrid data of the Pierre Auger Observatory*, *Phys. Rev. D* **109** (2024) 102001 [2401.10740].

[16] Pierre Auger collaboration, *The Pierre Auger Cosmic Ray Observatory*, *Nucl. Instrum. Meth. A* **798** (2015) 172 [1502.01323].

[17] J. Linsley, *Subluminal pulses from cosmic ray air showers*, *J. Phys. G* **10** (1984) L191.

[18] S. Mollerach and E. Roulet, *Progress in high-energy cosmic ray physics*, *Prog. Part. Nucl. Phys.* **98** (2018) 85 [1710.11155].

[19] C. Evoli, *The cosmic-ray energy spectrum*, Dec., 2020. 10.5281/zenodo.4396125.

[20] KASCADE collaboration, *KASCADE measurements of energy spectra for elemental groups of cosmic rays: Results and open problems*, *Astropart. Phys.* **24** (2005) 1 [astro-ph/0505413].

[21] KASCADE Grande collaboration, *Kneelike structure in the spectrum of the heavy component of cosmic rays observed with KASCADE-Grande*, *Phys. Rev. Lett.* **107** (2011) 171104 [1107.5885].

[22] K. Greisen, *End to the cosmic ray spectrum?*, *Phys. Rev. Lett.* **16** (1966) 748.

[23] G. T. Zatsepin and V. A. Kuzmin, *Upper limit of the spectrum of cosmic rays*, *JETP Lett.* **4** (1966) 78.

[24] F. W. Stecker, *Photodisintegration of ultrahigh-energy cosmic rays by the universal radiation field*, *Phys. Rev.* **180** (1969) 1264.

[25] J. W. Cronin, *Ultra high energy cosmic rays*, *Nuclear Physics B - Proceedings Supplements* **97** (2001) 3.

[26] A. A. Watson, *High-energy cosmic rays and the Greisen–Zatsepin–Kuz'min effect*, *Rept. Prog. Phys.* **77** (2014) 036901 [1310.0325].

[27] E. Fermi, *On the Origin of the Cosmic Radiation*, *Phys. Rev.* **75** (1949) 1169.

[28] R. J. Protheroe, *Acceleration and interaction of ultrahigh-energy cosmic rays*, astro-ph/9812055.

[29] E. Fermi, *Galactic Magnetic Fields and the Origin of Cosmic Radiation.*, *Astrophys. J.* **119** (1954) 1.

[30] R. D. Blandford and J. P. Ostriker, *Particle Acceleration by Astrophysical Shocks*, *Astrophys. J. Lett.* **221** (1978) L29.

[31] F. M. Rieger, V. Bosch-Ramon and P. Duffy, *Fermi acceleration in astrophysical jets*, *Astrophys. Space Sci.* **309** (2007) 119 [astro-ph/0610141].

[32] A. Achterberg, Y. A. Gallant, J. G. Kirk and A. W. Guthmann, *Particle acceleration by ultrarelativistic shocks: Theory and simulations*, *Mon. Not. Roy. Astron. Soc.* **328** (2001) 393 [astro-ph/0107530].

[33] A. M. Hillas, *The Origin of Ultrahigh-Energy Cosmic Rays*, *Ann. Rev. Astron. Astrophys.* **22** (1984) 425.

[34] R. Alves Batista et al., *Open Questions in Cosmic-Ray Research at Ultrahigh Energies*, *Front. Astron. Space Sci.* **6** (2019) 23 [1903.06714].

[35] W. Heitler, *The quantum theory of radiation*, vol. 5 of *International Series of Monographs on Physics*. Oxford University Press, Oxford, 1936.

[36] J. Matthews, *A Heitler model of extensive air showers*, *Astropart. Phys.* **22** (2005) 387.

[37] A. Haungs et al., *KCDC - The KASCADE Cosmic-ray Data Centre*, *J. Phys. Conf. Ser.* **632** (2015) 012011 [1504.06696].

[38] V. C. Tongiorgi, *Neutrons in the extensive air showers of the cosmic radiation*, *Phys. Rev.* **75** (1949) 1532.

[39] A. D. Erlykin, *The neutron 'thunder' accompanying large extensive air showers*, *Nucl. Phys. B Proc. Suppl.* **175-176** (2008) 330 [hep-ph/0612118].

[40] Y. V. Stenkin, D. D. Dzhappuev and J. F. Valdes-Galicia, *Neutrons in extensive air showers*, *Phys. Atom. Nucl.* **70** (2007) 1088.

[41] A. Shepetov et al., *Measurements of the low-energy neutron and gamma ray accompaniment of extensive air showers in the knee region of primary cosmic ray spectrum*, *Eur. Phys. J. Plus* **135** (2020) 96 [1912.13173].

[42] M. Schimassek, R. Engel, A. Ferrari, M. Roth, D. Schmidt and D. Veberič, *Neutron Production in Simulations of Extensive Air Showers*, 2406.11702.

[43] A. Ferrari, P. R. Sala, A. Fasso and J. Ranft, *FLUKA: A multi-particle transport code (Program version 2005)*, .

[44] H. Schraube, J. Jakeš, A. Sannikov, E. Weitzenegger, S. Roesler and W. Heinrich, *The cosmic ray induced neutron spectrum at the summit of the zugspitze (2963m)*, *Radiation Protection Dosimetry* **70** (1997) 405.

[45] P. Goldhagen, M. Reginatto, T. Kniss, J. Wilson, R. Singleterry, I. Jones et al., *Measurement of the energy spectrum of cosmic-ray induced neutrons aboard an er-2 high-altitude airplane*, *Nuclear instruments & methods in physics research. Section A, Accelerators, spectrometers, detectors and associated equipment* **476** (2002) 42.

[46] Pierre Auger collaboration, *The Surface Detector System of the Pierre Auger Observatory*, *Nucl. Instrum. Meth. A* **586** (2008) 409 [0712.2832].

[47] Pierre Auger collaboration, *The Fluorescence Detector of the Pierre Auger Observatory*, *Nucl. Instrum. Meth. A* **620** (2010) 227 [0907.4282].

[48] Pierre Auger collaboration, *The Pierre Auger Observatory Upgrade - Preliminary Design Report*, 1604.03637.

[49] Pierre Auger collaboration, *Trigger and Aperture of the Surface Detector Array of the Pierre Auger Observatory*, *Nucl. Instrum. Meth. A* **613** (2010) 29 [1111.6764].

[50] Pierre Auger collaboration, *The front-end electronics for the Pierre Auger Observatory surface array*, *IEEE Trans. Nucl. Sci.* **51** (2004) 413.

[51] Pierre Auger collaboration, *New Electronics for the Surface Detectors of the Pierre Auger Observatory*, *PoS* **ICRC2019** (2021) 370.

[52] B. G. Keilhauer, *Investigation of atmospheric effects on the development of extensive air showers and their detection with the Pierre Auger Observatory*, Ph.D. thesis, 2004. 10.5445/IR/4512003.

[53] Pierre Auger collaboration, *Scintillator detectors of AugerPrime Scintillator detectors of AugerPrime*, *PoS* **ICRC2017** (2018) 390.

[54] Pierre Auger collaboration, *First results from the AugerPrime engineering array*, *PoS* **ICRC2017** (2018) 449.

[55] A. Taboada, *Analysis of the First Data of the AugerPrime Detector Upgrade*, Ph.D. thesis, KIT, 2020.

[56] Pierre Auger collaboration, *AugerPrime Surface Detector Electronics*, *JINST* **18** (2023) P10016 [2309.06235].

[57] Pierre Auger collaboration, *HEAT – Enhancement Telescopes for the Pierre Auger Southern Observatory*, in *30th International Cosmic Ray Conference*, 7, 2007.

[58] Pierre Auger collaboration, *The AMIGA muon detectors of the Pierre Auger Observatory: overview and status*, in *33rd International Cosmic Ray Conference*, 2013.

[59] Pierre Auger collaboration, *The AMIGA underground muon detector of the Pierre Auger Observatory - performance and event reconstruction*, *PoS* **ICRC2019** (2021) 202.

[60] Pierre Auger collaboration, *A Large Radio Detector at the Pierre Auger Observatory - Measuring the Properties of Cosmic Rays up to the Highest Energies*, *PoS* **ICRC2019** (2021) 395.

[61] M. Stadelmaier, R. Engel, M. Roth, D. Schmidt and D. Veberič, *Model of the response of surface detectors to extensive air showers based on shower universality*, *Phys. Rev. D* **110** (2024) 023030.

[62] A. Letessier-Selvon, P. Billoir, M. Blanco, I. C. Mariș and M. Settimo, *Layered water Cherenkov detector for the study of ultra high energy cosmic rays*, *Nucl. Instrum. Meth. A* **767** (2014) 41 [1405.5699].

[63] B. C. Manning, *Event Reconstruction with the AugerPrime Upgrade*, Ph.D. thesis, Adelaide U., 2024.

[64] P. Sánchez Lucas, *The ⟨Δ⟩ Method: An estimator for the mass composition of ultra-high-energy cosmic rays*, Ph.D. thesis, U. Granada, 2016.

[65] Q. Luce and I. Lhenry-Yvon, *Saturation and estimation of the signal on high and low-gain channel*, Auger internal note GAP-2017-024, 2017.

[66] P. Billoir, *FADC trace cleaning in Surface Detector through a segmentation procedure*, Auger internal note GAP-2005-074, 2005.

[67] A. Bueno, P. Sánchez-Lucas and A. A. Watson, *The Delta-Method revisited*, Auger internal note GAP-2013-078, 2013.

[68] Q. Luce and I. Lhenry-Yvon, *A modified baseline estimation and signal selection in FADC traces of SD Detectors within CDAS*, Auger internal note GAP-2016-044, 2016.

[69] S. Maldera and G. Navarra, *Restoring the SD PMT signals through the Laplace transforms* , Auger internal note GAP-2005-006, 2005.

[70] B. Genolini, T. Nguyen Trung and J. Pouthas, *Base line stability of the Surface Detector PMT base*, Auger internal note GAP-2003-051, 2003.

[71] Funk Experiment collaboration, *Limits from the Funk Experiment on the Mixing Strength of Hidden-Photon Dark Matter in the Visible and Near-Ultraviolet Wavelength Range*, *Phys. Rev. D* **102** (2020) 042001 [2003.13144].

[72] Z. Szadkowski and K.-H. Kampert, *Analysis of the SD-PLD firmware and implications to physics data*, Auger internal note GAP-2006-027, 2006.

[73] P. S. Allison, X. Bertou and C. Grunfeld, *Pulse shape agnostic methods of measuring the dynode-anode ratio*, Auger internal note GAP-2004-033, 2023.

[74] S. Coutu, J. Beatty, E. Fantozzi and J. Hartshorn, *Surface Detector PMT Tests*, Auger internal note GAP-1999-045, 1999.

[75] D. Barnhill, K. Arisaka, A. Tripathi, T. Ohnuki, B. Garcia, F. Suarez et al., *Results of Testing Pre-Production and Production PMTs For the Surface Detector in the New PMT Test Facility in Malargüe*, Auger internal note GAP-2003-037, 2003.

[76] S. Atulugama and S. Coutu, *Afterpulsing of Surface Detector Photonis XP1805 Photomultiplier Tubes*, Auger internal note GAP-2005-100, 2005.

[77] G. A. Morton, H. M. Smith and R. Wasserman, *Afterpulses in photomultipliers*, *IEEE T. Nucl. Sci.* **14** (1967) 443.

[78] P. B. Coates, *The origins of afterpulses in photomultipliers*, *J. Phys. D Appl. Phys.* **6** (1973) 1159.

[79] C. F. Medina Hernandez, *The Central Laser Facility at the Pierre Auger Observatory. Studies of the atmospheric vertical aerosol optical depth and other applications to cosmic ray measurements*, Ph.D. thesis, Colorado School of Mines, 2017.

[80] O. Tkachenko, *Measurement of the Composition of Cosmic Rays and the Properties of Hadronic Interactions at Ultrahigh Energies with the Pierre Auger Observatory*, Ph.D. thesis, Karlsruhe Institute of Technology, 2024.

[81] "http://natter.na.infn.it:18501/."

[82] D. Heck, J. Knapp, J. N. Capdevielle, G. Schatz and T. Thouw, *CORSIKA: A Monte Carlo code to simulate extensive air showers*, .

[83] M. Schimassek, *Extending the Physics Reach of the Pierre Auger Observatory using Low-Level Trigger Data*, Ph.D. thesis, Karlsruhe Institute of Technology, 2022.

[84] Pierre Auger collaboration, *Reconstruction of Events Recorded with the Water-Cherenkov and Scintillator Surface Detectors of the Pierre Auger Observatory*, *PoS* **ICRC2021** (2021) 218.

[85] Telescope Array collaboration, *An extremely energetic cosmic ray observed by a surface detector array*, *Science* **382** (2023) abo5095 [2311.14231].

[86] A. Streich, *Performance of the Upgraded Surface Detector of the Pierre Auger Observatory*, Ph.D. thesis, Karlsruher Institut für Technologie (KIT), 2023. 10.5445/IR/1000158193.

[87] Pierre Auger collaboration, *Studies of the mass composition of cosmic rays and proton-proton interaction cross-sections at ultra-high energies with the Pierre Auger Observatory*, *PoS* **ICRC2023** (2023) 438.

[88] Geant4 collaboration, *Guide for physics lists*, https://geant4-userdoc.web.cern.ch/UsersGuides/PhysicsListGuide/html/index.html.

[89] Particle Data Group collaboration, *Review of Particle Physics*, *PTEP* **2022** (2022) 083C01.

[90] J. B. Birks, *Scintillations from organic crystals: Specific fluorescence and relative response to different radiations*, *Proc. Phys. Soc. A* **64** (1951) 874.

[91] C. N. Chou, *The nature of the saturation effect of fluorescent scintillators*, *Phys. Rev.* **87** (1952) 904.

[92] J. Hong, W. Craig, P. Graham, C. Hailey, N. Spooner and D. Tovey, *The scintillation efficiency of carbon and hydrogen recoils in an organic liquid scintillator for dark matter searches*, *Astroparticle Physics* **16** (2002) 333.

[93] H. Paul, *Nuclear stopping power and its impact on the determination of electronic stopping power*, *AIP Conference Proceedings* **1525** (2013) 309 [https://pubs.aip.org/aip/acp/article/pdf/1525/1/309/12019358/309_1_online.pdf].

[94] S. Yoshida, T. Ebihara, T. Yano, A. Kozlov, T. Kishimoto, I. Ogawa et al., *Light output response of kamland liquid scintillator for protons and 12c nuclei*, *Nuclear Instruments and Methods in Physics Research Section A: Accelerators, Spectrometers, Detectors and Associated Equipment* **622** (2010) 574.

[95] R. Voltz, J. L. da Silva, G. Laustriat and A. Coche, *Influence of the Nature of Ionizing Particles on the Specific Luminescence of Organic Scintillators*, *The Journal of Chemical Physics* **45** (1966) 3306.

[96] T. Pöschl, D. Greenwald, M. J. Losekamm and S. Paul, *Measurement of ionization quenching in plastic scintillators*, *Nucl. Instrum. Meth. A* **988** (2021) 164865 [2007.08366].

[97] T. A. Laplace, B. L. Goldblum, J. A. Brown, G. LeBlanc, T. Li, J. J. Manfredi et al., *Modeling ionization quenching in organic scintillators*, *Mater. Adv.* **3** (2022) 5871.

[98] R. Craun and D. Smith, *Analysis of response data for several organic scintillators*, *Nuclear Instruments and Methods* **80** (1970) 239.

[99] V. Tretyak, *Semi-empirical calculation of quenching factors for ions in scintillators*, *Astroparticle Physics* **33** (2010) 40.

[100] L. Reichhart, D. Akimov, H. Araujo, E. Barnes, V. Belov, A. Burenkov et al., *Quenching factor for low energy nuclear recoils in a plastic scintillator*, *Physical Review C* **85** (2011) .

[101] L. Kelleter and S. Jolly, *A mathematical expression for depth-light curves of therapeutic proton beams in a quenching scintillator.*, *Medical physics* (2020) .

[102] S. Baker and R. D. Cousins, *Clarification of the use of chi-square and likelihood functions in fits to histograms*, *Nuclear Instruments and Methods in Physics Research* **221** (1984) 437.

[103] I. Lhenry-yvon, *About bad PMTs : inventory of spurious data remaining after the two first levels of PMT quality cuts*, Auger internal note GAP-2018-022, 2003.

[104] I. Lhenry-yvon and P. Papenbreer, *Bad PMTs: the third levels of quality cuts, tuned for PMT traces analysis*, Auger internal note GAP-2018-029, 2018.

[105] T. Suomijärvi and for the Pierre Auger Collaboration, *The augerprime upgrade of the pierre auger observatory*, *Journal of Physics: Conference Series* **2429** (2023) 012010.

[106] A. Letessier-Selvon and P. Billoir, *Separating the muonic and electromagnetic components of a shower through the matrix formalism for a two-fold detector*, Auger internal note GAP-2015-045, 2015.

[107] D. Schmidt, *Sensitivity of AugerPrime to the masses of ultra-high-energy cosmic rays*, Ph.D. thesis, Karlsruhe Institute of Technology, 2018.

[108] D. Martello, *Considerations about the method of the matrix inversion*, Auger internal note GAP-2019-033, 2019.

[109] M. Pothast, C. Timmermans and S. de Jong, *SSD and WCD signal model*, Auger internal note GAP-2021-058, 2021.

[110] A. M. Payeras, *Potential of the AugerPrime Surface Detector for Composition Studies of High-Energy Cosmic Rays*, Ph.D. thesis, Universidade Estadual de Campinas, 2023.

Acknowledgements

I want to express my gratitude to the two reviewers of this thesis, Prof. Dr. Ralph Engel and Dr. Federico Sanchez, for enabling me to write this thesis and allowing me to participate in the joint double doctoral degree program. It was a unique experience that I will remember forever. My biggest thanks go to my supervisors: To Dr. David Schmidt for the endless amount of meetings he had to endure with me to bring this work to fruition and for his trust in me, even when I was in doubt. To Dr. Darko Veberič, for his incredible help in fighting against Offline, English grammar and mathematical formalisms. And finally, to Dr. Markus Roth for his support and always having an open ear for any concerns or wishes. I also want to thank Sabine Bucher, Anna Friedrich, Marie-Christine Mundt, Kathrin Link, Tadeo Lopez, and Doris Wochele for their outstanding organizational and logistical support.
My deepest gratitude goes to my family; to my parents Brigitte and Hans-Werner and my brother Andreas, for their infinite support and love. I'm genuinely thankful for my most treasured love, Olena Tkachenko, who was with me in my happiest moments and helped me through all challenging times. I am deeply grateful to all the people with whom I shared an office over the years and contributed to a very comfortable environment: Allan Payeras, Fabio Convenga, Paul Filip, Thomas Fitoussi and Alexander Streich. To Martin Schimassek, with whom I shared very enjoyable lunch breaks and who provided me with lots of useful information. To Flavia Gesualdi and her family, who greatly helped me to find a place in Buenos Aires. To Luca Deval, Fiona Ellwanger, Steffen Hahn and Maximilian Stadelmaier for the good discussions and enjoyable moments. To Kathrin Bismark, Max Büsken, Berenika Čermáková, Chloé Gaudu, Sara Martinelli and Christoph Schäfer for the good company and pleasant atmosphere.
I owe a special thanks to Emily Martins, my PhD buddy, for her never-ending help and support. To my Argentinian friends Carmina Bertolli, Gabriel Brichetto, Joaquin De Jesus, José Ochoa and Ezequiel Rodriguez, for the wonderful moments and experiences. And to Varada Varma, Marina Scornavacche and Fernando Golan, who helped me to "survive" Buenos Aires and greatly contributed to this amazing experience.
Also, I would like to thank Alfredo Ferrari for all his support and helpful explanations during the final month of my thesis. And, of course, to all people within the Pierre Auger Collaboration that were not mentioned here.

Erklärung

Karlsruhe, den 21.10.2024

Erklärung der selbständigen Anfertigung meiner Dissertationsschrift

Hiermit versichere ich, dass ich die Dissertationsschrift mit dem Titel

The Muon Puzzle and the Neutron Component in Extensive Air Showers

selbständig und ohne unerlaubte fremde Hilfe verfasst habe. Dabei habe ich keine anderen, als die von mir angegebenen Hilfsmittel benutzt.

Tobias Schulz